AN EXPERIMENTAL INVESTIGATION OF THE GRAZING FLOW IMPEDANCE DUCT AT THE UNIVERSITY OF FLORIDA FOR ACOUSTIC LINER APPLICATIONS

By

BRANDON L. BERTOLUCCI

A DISSERTATION PRESENTED TO THE GRADUATE SCHOOL
OF THE UNIVERSITY OF FLORIDA IN PARTIAL FULFILLMENT
OF THE REQUIREMENTS FOR THE DEGREE OF
DOCTOR OF PHILOSOPHY

UNIVERSITY OF FLORIDA

2012

In dedication to my parents.

ACKNOWLEDGMENTS

This project is only possible due to the helpful and continuing guidance of my advisors, Dr. Louis Cattafesta and Dr. Mark Sheplak whom provided mentorship and lead me in this process. I would like to extend my gratitude to the rest of my committee: Dr. Balachandar, Dr. David Arnold (ECE), and Michael Jones at NASA LaRC. This project would not be possible without the donation of the GIT facility from NASA LaRC. I would specifically like to thank Michael Jones, Carroll Harrison, and Brian Howerton for their continued support over the past four years.

The physical construction and machining of the tunnel was accomplished by primarily by Rafferty Machine and Tool, TMR Engineering, and Mark Hurm and Co. I would like to thank Wayne Willis for his fiberglass work. Much of the design and construction was accomplished by a series of undergrads whose assistance was invaluable; thank you all. University of Florida staff Jeff Studstil and Mark Reidy's support was well beyond expectation and were extremely helpful.

Many whiteboard markers came and went through thoughtful discussions with my colleagues as they helped me iron out the details of the project and steer me down the correct path. I would like to specifically thank Dr. Fei Lui providing many hours of discussion. Additionally, my peers in the Interdisciplinary Microsystems Group (IMG) were indispensable, including: Dr. Ryan Holman, Dr. Vijay Chandrasekharan, Dr. Chris Bahr, Dr. Drew Wetzel, Dr. Jessica Meloy, Miguel Palaviccini, Matias Oyarzun, Nik Zawodny, Ashley Jones, and John Griffin.

Furthermore, I would like to extend appreciation to Jason June for the tremendous help he provided in my final year. He will be taking the project over and I can not imagine more capable hands. Also, a special thanks to Katie Reed, her patience and support were a constant source of strength and motivation throughout the years.

TABLE OF CONTENTS

LIST OF TABLES

LIST OF FIGURES

Abstract of Dissertation Presented to the Graduate School
of the University of Florida in Partial Fulfillment of the
Requirements for the Degree of Doctor of Philosophy

AN EXPERIMENTAL INVESTIGATION OF THE GRAZING FLOW IMPEDANCE DUCT AT THE UNIVERSITY OF FLORIDA FOR ACOUSTIC LINER APPLICATIONS

By

Brandon L. Bertolucci

December 2012

Chair: Louis Cattafesta III
Cochair: Mark Sheplak
Major: Aerospace Engineering

Acoustic liners remain the standard method for reducing environmental noise emanating from aircraft engine nacelles. To aid in liner testing and development, facilities capable of accurately educing the acoustic impedance in the presence of mean flow analogous to an aircraft engine are required. A facility was built to facilitate novel design approaches and studies into fundamental acoustic liner flow physics.

This thesis details the design, testing, and implementation of the Grazing Flow Impedance Duct (GFID) as an experimental test bench capable of educing the impedance of an acoustic liner. Each component of the facility is discussed detailing the specific features applicable toward the facility as a grazing flow acoustic test bench. Characterization of both the underlying fluid dynamics and acoustics are tested to determine the abilities and inherent limitations associated with the facility. Comparisons are made to similar facilities. Finally, an acoustic liner provided by NASA is tested under grazing flow conditions and the impedance educed by applying the single mode method with favorable results. The thesis ends with an exploratory investigation of the drag impact of an acoustic liner through three indirect velocity profile methods.

CHAPTER 1
BACKGROUND AND MOTIVATION

Concerns of health and general population annoyance due to aircraft noise grow as population centers expand and air traffic becomes a larger part of daily life, increasing environmental noise pollution. Aircraft noise is presented and discussed in the context of the noise sources and current abatement strategies detailing improvements made through implementation of acoustic liners. The effectiveness of acoustic liners require detailed evaluation via experimental facilities necessitating a fundamental understanding of both acoustic and fluid dynamic physics as well as the facilities themselves. The chapter concludes with an outline of this thesis on the development and testing of of the Grazing Flow Impedance Duct (GFID) experimental acoustic liner flow facility for research on acoustic liners and liner technology.

1.1 Aircraft Noise Issues

Aircraft noise has long been a problem for communities near airports. As population centers continue to expand and airport communities grow, new restrictions and subsequent abatement procedures applied to aircraft noise have increased substantially.

Studies have found that as many as 70% of the people living within flight corridors are bothered by aircraft generated noise (Bronzaft & Ahern 1998). The need for aircraft noise abatement has also been linked to several community health concerns. Over the last thirty years, significant research has been conducted on possible side effects of living near airports, including low birth weights (Knipschild *et al.* 1981), increased levels of unemployment (Kryter 1990), and childhood cognition performance (Stansfeld *et al.* 2005). Such hazards have prompted both regional and national fines to be implemented to airlines which do not meet restrictions. There are instances, such as the case of the Boeing 707, where the cost to retrofit the design to attain proper noise level certification became cost prohibitive, and operation of the aircraft was discontinued (Smith 2004). Such fines

and restrictions necessitate airlines, aircraft manufacturers, and component contractors to consider new technologies to decrease environmental noise pollution.

As illustrated in Figure 1-1, federal noise restrictions currently in Stage 4 are periodically reviewed and altered to maintain community noise standards. However, these restrictions do not extend far enough into the future for adequate planning of future aircraft and advanced technologies. NASA, in conjunction with aircraft and engine companies, has defined goals for aircraft noise to assist in future technology and noise testing development, where "N+1" refers to models being released prior to the conclusion of the FAA Stage 4 standards.

Aircraft noise, regardless of its source, has three potential observer groups: aircraft passengers and crew, airport staff including maintenance and support personnel, and flight-path communities. The noise most pertinent to the passengers and airport staff is that generated by the jet exhaust, internal combustion, airframe noise, and structural vibrations of aircraft components (Powell & Fields 1991). General aircraft noise suppression benefits all parties involved as total noise is reduced over time by identifying dominant noise sources and applying appropriate reduction measures.

While the reasons for aircraft noise abatement are numerous, the methods for noise level reduction remain an ongoing and complicated endeavor for engineers. Over the years, issues associated with aircraft noise have had a large impact on many aspects of modern life. Aircraft noise has influenced city planning for flight corridors and has shaped aspects of modern aircraft design, such as the number, size, and placement of engines, as well as the angle of descent and takeoff (Smith 2004). To better understand the mechanisms behind aircraft noise, the issue is approached on two fronts by the engineering community. Investigations separate the noise generated by the airframe from the noise radiated from the propulsion system. A breakdown of each source and its origins is presented below along with sources of generated noise.

1.2 Types of Aircraft Noise

Separating aircraft noise into different types allows the sources of each to be investigated independently, as well as to establish priorities for current and future research. The aircraft noise sources of the airframe and propulsion systems are both actively studied for noise level reduction. Unique source characteristics contribute to noise source identification and future abatement procedures while presenting challenges for engineers. A basic overview of the generation of each noise source is discussed, and current noise abatement procedures are described.

Airframe noise is a result of the passage of air interacting with physical structures on the aircraft (Smith 2004). Any structure in the path of the flow which causes a sudden or abrupt change in flow direction has the potential to create pressure fluctuations. Due to external structures of various sizes, from landing gear, wings, and control surfaces, as well as the fuselage itself, the generated frequencies span the full range of human sound perception; thus airframe noise is categorized as both tonal and broadband in nature (Smith 2004).

The noise emanating from the airframe has been experimentally found to be highest for ground-based observers during approach conditions when additional, less aerodynamic components, come into effect (Motsinger & Kraft 1991). Figure 1-2 presents an illustration of an airplane with labeled sound-generating sources. Components designed to increase drag, such as flaps and slats, provide a necessary stability condition for control during landing by reducing overall speed. However, these components directly generate additional aerodynamic sound capable of propagating to an observer (Smith 2004). Furthermore, the landing gear are also deployed at this time, generating additional noise. By design, landing gear are generally not streamlined for aerodynamic performance and increase the overall noise signature of the airframe by as much as 10 dB (ref 20 μPa) (Smith 2004). Landing gear noise is generally characterized by low frequency sound propagating both into the passenger cabin and externally over long distances (Smith 2004).

While airframe noise is dominant during approach for landing, propulsion noise dominates at takeoff when engine power is maximum (Smith 2004). Propulsion noise is associated with any power system that propels the aircraft forward. The current investigation will focus on the modern high bypass turbofan engine, housed in what is commonly referred to as an engine nacelle, while forgoing external propellor driven systems. Thus, the generated noise is a combined result of turbomachinery noise and resultant exhausting jet as well as the bypass fan and ducting systems. The engine bypass ratio (BPR) defines the relationship between the mass of cooler air directed around the core engine to the mass of air passing through the core (Mattingly 1996).

Jet noise in modern turbofan engines is a combination of turbulent mixing and, in some cases, shock system inefficiencies (Smith 2004). Jet wake characteristics have changed dramatically over the years due to design modifications to engine construction. The high bypass ratio, commonly found in modern aircraft engines for added fuel efficiency, separates the incoming air into two parts. Figure 1-3 illustrates a high bypass ratio engine with the flow of air displayed in blue and the acoustic sources and direction of noise propagation indicated in yellow. A portion of the incoming air is directed through the engine where it is compressed, heated, and accelerated rearward, generating forward thrust. Surrounding this hot jet, the remaining majority of the air is steered around the core engine remaining relatively cold, forming an outer concentric shear flow.

Bypass ratios of passenger aircrafts have steadily increased since their introduction, raising fuel efficiencies and lowering jet noise (Smith 2004). The Rolls-Royce Trent 1000 engine requisitioned for the Boeing 787 has a bypass ratio of 11, doubling values of only 4-6 typically found in 1970's models (Nayfeh *et al.* 1975). Goals for ultra-high BPR's nearing 20 by the year 2020 are in view (Guynn *et al.* 2009).

Without the influence of high velocity turbulent structures found in the high speed jet, the large bypass air generates low frequency broadband noise (Smith 2004). The air directed into the core engine receives a tremendous velocity gain ($450 - 700\ m/s$)

generating small-scale turbulent eddies producing loud, higher frequency broadband noise (Smith 2004). The cold, slower bypass air and hot, faster turbine exhaust combine and mix downstream of the exhaust plane, generating additional high intensity sound over a wide frequency range (Nayfeh *et al.* 1975). Although still a source of noise generation, the bypass system has been the highest contributor to the decrease in jet engine noise (Smith 2004). However, while noise will decrease with increased BPR, tradeoffs of increased engine drag, weight, and installation issues become apparent. Optimal BPR have been estimate around 11-14 (Daggett *et al.* 2003). Basic steps toward noise abatement of jets are presented in section 1.4.

When the first jet engine was introduced on production scale aircraft, jet noise was the dominant propulsion noise source in what is now referred to as a "pure jet" configuration, that is, no bypass system. However, instituting a bypass system lead to lower specific fuel consumption, and fan noise was subsequently identified as a noise source (Nayfeh *et al.* 1975). Since that time, the upstream fan and compressor stages have garnered a considerable proportion of the focus of aircraft noise abatement research for a multitude of reasons. The inclusion of the bypass system allowed for a significant reduction of jet speed, reducing the levels of jet noise. Lighthill (1952) proposed that jet sound intensity scales as V^8, but this relation drops to a V^3 relation for jet velocities greater than approximately 400 m/s (Dowling & Williams 1983). The change in scaling comes from a breakdown in the assumption of the low speed jet; as the jet becomes supersonic the ratio of the source dimension to acoustic wavelength is no longer small and can no longer be considered compact (Dowling & Williams 1983). The effective perceived noise level, in units of EPNdB, is a subjective measure of the perceived effect of aircraft noise on humans (Smith 2004). Since the 1960's, combined noise levels from the engine have dropped more than 20 EPNdB as a result of the high bypass ratio engine currently used in modern aircraft design (Casalino *et al.* 2007). Thus it can be stated that the

largest reductions in jet noise are on the engine designs with the largest bypass ratios (Marsh 1968).

The introduction of the engine air bypass system reduced overall jet noise levels by decreasing the jet speed. However, the large fan stage necessary for the bypass now generated additional noise at non-negligible levels. The fan noise was discovered to produce more "annoying" tones compared to the broadband howl of the "pure-jet", reminiscent of past propellor-driven transport (Smith 2004). Clinical investigations have demonstrated that humans are most sensitive to frequencies between $2 - 4\ kHz$ even though the ear is generally capable of discerning frequencies between $20\ Hz - 20\ kHz$ (Kryter 1959). Fans generate high-intensity tones within the sensitive frequency range capable of propagating to external observers due to several inherent geometric and installation reasons discussed in the following sections (Marsh 1968).

The noise measured within the fan stage, that is any region prior to the compressor as illustrated in Figure 1-3, is a combination of broadband and high intensity sound. The broadband source is due to noise emanating upstream from the combustion chamber. In addition, jet noise will propagate upstream via the nacelle boundary layer or if operated at subsonic "off-design" conditions. (Smith 2004).

The frequencies observed in the fan stage are found to originate from several sources. The dominant noise source stems from the interaction of the fan stage endured swirling air with the exit guide vanes downstream. The appropriately named blade passage frequency (BPF) is equal to the product of fan blade rotation frequency and the number of blades present (Motsinger & Kraft 1991). The turbulent vortices generated from the trailing edges and standoff shock waves at the tips of the fan blades can propagate both upstream (forward of the engine) and downstream, incorporating in with the jet noise (Smith 2004). In the multiple fan stages of early bypass engine designs, vortical interactions would combine to generate new tones based on the sutm and difference frequencies of the multiple stages, as well as the combined harmonics (Nayfeh *et al.* 1975).

While the BPF may be the dominant frequency within the fan stage, several sources related to the engine design and manufacturing also add to the overall noise level and sound signature. Fan blades themselves, regardless of installation uniformity, suffer wear and are deformed due to rain, hail, birds, and debris. Eventually, no two fan blades are identical as minor differences alter flow structures that generate noise. While the measured frequencies may be dominated by the BPF, the intensities of each as well as additional noise specific to a particular blade may therefore change (Smith 2004).

Inlet boundary layer symmetry is also important for noise generation. If the developing boundary layer has any azimuthal dependance such that any two blades are subject to dissimilar inlet flow conditions, additional forces are introduced and pressure fluctuations will arise (Smith 2004). Current practice dictates that the inlet flow should be both axisymmetric and as "clean" as possible, accomplished by ensuring the nacelle inlet is free of any support structures or sharp corners which may cause irregular flow patterns (Nayfeh *et al.* 1975). Such changes in design and the awareness of the tones has spurred interest in the area of engine inlet noise suppression, nearly universally through the implementation of acoustic liners.

1.3 Acoustic Liners Within Aircraft Engine Nacelles

Fan noise within engine nacelles has gained much attention over the years. One particular area of research focuses on suppression of the fan noise through implementation of acoustic liners within the nacelle walls. The acoustic liners reduce noise by altering the boundary contrition at the interior wall decreasing the amplitude of an incident sound wave (Motsinger & Kraft 1991).

The effectiveness of an acoustic liner is determined by measuring incoming and outgoing sound waves through an area where the acoustic lining is used at one or more boundaries. This is generally quantified in the form of the specific acoustic impedance, defined as the ratio of the effective sound pressure acting on a surface, to the particle velocity through the surface area (Beranek 1996).

The use of liners for noise level suppression is not unique to the aerospace industry, and in fact, has been effectively implemented in several industries where noise restrictions and sound levels pose annoyance, health, and/or safety risks. Acoustic wall treatment and liners have been routinely used successfully on turbomachinery (Smith 2004), automotive exhaust systems (Dokumaci 2005) and are prevalent in many architectural designs (Egan 2007).

However, unlike industrial or architectural acoustic liner use, the aircraft engine may present the harshest environment of all. Such liners must maintain effectiveness over a broad range of conditions. The engine nacelle can be subjected to temperature ranges of -50°C to +500°C leading to harsh freeze-thaw cycling of amassed water. The potential for fire exists if fuel or oil mixtures become entrained near a heat source. In addition to stringent environmental conditions, the liners must maintain structural rigidity of the nacelle while minimizing weight. Furthermore, liners should require little or no maintenance over the lifespan of the nacelle (Smith 2004).

Depending on their physical construction, acoustic liners can be broadly divided into two main categories, locally reacting and bulk reacting (Nayfeh *et al.* 1975). Figure 1-4 illustrates liners commonly used on modern aircraft. The construction of the liner defines the liner type by constraining particle velocity normal to the surface for locally reactive (Motsinger & Kraft 1991). These liners are generally a honeycomb structure of cellular separations where each cell is oriented normal to the wall of the duct. A perforated or wire-mesh face sheet rests on the face of the cell with the base of the cell attached to a rigid plate creating a cellular sandwich of the three components (Motsinger & Kraft 1991). A bulk reacting liner replaces the cellular honeycomb structure with a thick homogeneous fiber panel between the face-sheet and the rigid backplate, allowing for transverse progression of sound (Motsinger & Kraft 1991).

To understand how an acoustic liner suppresses noise, it is important to understand how acoustic waves propagate within a nacelle. As an acoustic wave advances away from

a noise generating source in an enclosed duct, acoustic energy striking a boundary can result in energy loss associated with either the reflection or absorption of the incident wave (Ingard 1994). Acoustic reflections arise as a result of impedance discontinuities (Blackstock 2001). Acoustic absorption ultimately converts the acoustic energy incident on the nacelle surface to another domain, such as heat or stored energy (Ingard 1953).

Modification of a local acoustic field on a surface is made possible through two potential mechanisms. The first is destructive interference of the incident acoustic wave by tuning the reactive physical characteristics of the cavity to a specific frequency termed the resonant frequency. This is accomplished by designing the cavity depth to be 1/4 the wavelength (λ) of the incident acoustic wave. The subsequent reflection off the cavity base will cause destructive interference at the cavity opening (Nayfeh *et al.* 1975). The propagating pressure wave through the duct is then met by an acoustic sink at the boundary and sound reflection is drastically reduced (Nayfeh *et al.* 1975). The second mechanism for suppression reduces incident pressure by means of viscous resistance in which acoustic energy is converted into heat at the orifice. This viscous effect reduces the particle velocity at the entrance to the cavity thus weakening the acoustic wave (Smith 2004). The two mechanisms can complement one another, albeit at disparate levels depending on design, to form an array of cells that coat the interior of a nacelle.

A locally reactive liner is typically best suited for a specific tone or a narrow band of frequencies near the design frequency of the resonator, generally covering one octave (Motsinger & Kraft 1991). The reactive mechanism for reducing the sound intensity is most effective when the cavity depth is near $\lambda/4$ of the incident pressure wave but proves ineffective to those frequencies of which little to no destructive interference occurs. Frequency and wavelength are related through

$$\lambda = \frac{c_0}{f}, \tag{1–1}$$

where c_0 is the local speed of sound.

The perforate-sandwich construction of the locally reactive liner described earlier is denoted as a single degree-of-freedom (SDOF) liner where the facesheet and cavity are generally lumped as a single degree-of-freedom. This concept can be expanded to a larger range of frequency suppression if a porous septum sheet is used in the place of the original sound hard bottom plate exposing a second cavity tuned to a dissimilar frequency. The lower cavity becomes a second degree-of-freedom and thus the moniker, 2DOF, is commonly used. The range of effective suppression can be designed to cover up to two octaves in contrast to the characteristic single octave coverage of typical SDOF liners (Motsinger & Kraft 1991). A schematic of the resistive and reactive mechanism is illustrated in Figure 1-5.

Bulk reacting liners are unconstrained by the cellular divisions of locally reactive liners, consequently allowing for transverse wave progression (Nayfeh *et al.* 1975). Generally isotropic materials, bulk reacting liners are designed for general use applications such as suppression of multiple or broadband frequencies. In contrast to locally-reactive liners suppressing a specific tone or a narrow frequency range, bulk reacting liners can suppress up to three octaves, however less effectively than either SDOF or 2DOF liners (Nayfeh *et al.* 1975). Bulk reacting liners dissipate energy through viscous resistance as kinetic energy is lost to intra-matrix collisions (Nayfeh *et al.* 1975). Although widely used in many industries, adoption of bulk liners within the aerospace field has been hindered due to the limited effectiveness, inherent risks associated with fuel absorption, and risk of failure through abrasion (Motsinger & Kraft 1991).

Both types of liners rely on a sound wave interacting with the boundaries as it propagates through the engine nacelle duct. Multiple reflections within a duct increase the effectiveness of a liner as each interaction with a duct dissipates additional acoustic energy. For this reason, longer regions of liners, such as in the bypass duct systems, are the most effective at suppressing noise, as there are multiple opportunities for energy conversion

(Smith 2004). However, enhanced noise suppression via lengthening the interior ducts necessitates a weight penalty, leading to excess material and fuel costs (Smith 2004).

1.4 Aerodynamic and Acoustic Performance of Liners

Although liners have greatly reduced the noise level from engine nacelles, additional research is required within the aerospace and aeroacoustic communities. With any new technology, wide scale implementation should be weighed against disadvantages associated with its application. Disadvantages associated with acoustic liners stem from design constraints on nacelle size, drag penalty, and liner property testing.

As previously mentioned, SDOF locally reactive liners are most effective when the cavity depth is tuned to a given frequency. However, the $\lambda/4$ design on cavity depth necessarily increases the external diameter of the nacelle. This additional thickness increase over unlined ducts increases material costs, drag, takeoff weight, and reduces nacelle ground clearance (Motsinger & Kraft 1991). For a standard Boeing 777 engine, the lowest BPF value lies in the 630 and 800 Hz 1/3 octave band range (Bielak *et al.* 1999). Theoretical suppression of these frequencies would add over a foot to the nacelle diameter of an unlined duct. Restrictions on overall size restrict frequency suppression to those frequencies most sensitive to human hearing, limiting full noise suppression (Smith 2004).

In addition, the drag penalty associated with acoustic liners has been investigated in the past but still remains a topic of interest due to increasing fuel costs (Wolter 2005). The overall size of an aircraft's engine is a direct function of the bypass ratio, a mechanism designed to increase fuel performance. The viscous drag penalty associated with acoustic liners during flight conditions is a function of the wetted area, that is the liner material in direct contact with the moving fluid. Thus, decreased jet noise due to increased bypass ratios causes a non-trivial drag penalty (Smith 2004). Facility experiments are necessary for performing liner drag studies as well as development of intelligent design tools and novel measurement techniques to reduce the drag penalty while maintaining and enhancing acoustic suppression performance.

1.5 Acoustic Liner Test Facilities

Many issues of nacelle flow fields and noise mechanisms have been presented to illustrate current challenges a modern aircraft engine presents to engineers. This thesis covers the mathematical models, design, and testing procedures for an aeroacoustic wind tunnel facility for grazing flow acoustic liner testing. The following section will present some motivation for a facility as well as some of the design considerations necessary for implementation.

Full-scale engine testing, while possible, presents non-trivial issues related to cost and maintenance, as well as obvious safety and environmental hazards. Noise source identification becomes difficult in full-scale models, where noise reductions from liners near the fan stage can become buried by fluctuations in jet noise, possibly masking key advancements (Motsinger & Kraft 1991). While full-scale testing is performed at certain facilities, the majority of liner testing is achieved in well controlled acoustic laboratories for better source control (Smith 2004). A brief overview of facility components and a review of past and current liner test facilities are presented in Chapter 3.

A facility designed for the acquisition of acoustic liner impedance measurements, specifically those pertaining to the suppression of aircraft engine noise, should provide a representative environment of true flight conditions as well as the ability to control the acoustic and fluid conditions. The test environment can be characterized by three primary components: the acoustic source, the test section for sample placement and testing, and the acoustic termination (Melling & Doak 1971).

Achieving the high intensity acoustic field of the engine can be accomplished with multiple sound sources. The sources should match both the appropriately-scaled frequency content as well as the sound intensity of a nacelle environment (Melling & Doak 1971). Sound pressure levels up to $160; dB$ are ideally required as levels of this magnitude are not uncommon within a nacelle environment (Smith 2004). The extremely high levels of acoustic power promote a nonlinear acoustic response within a nacelle, and can be found

at levels as low as low as 130 dB (Smith 2004). The ability to withstand such high levels without acoustic leakage or other complications, such as source interference, must be considered during the design of the test section and all test components. Additionally, test Mach numbers above $M = 0.5$ should be attained to match full-scale cruise conditions (Smith 2004).

Similar to the acoustic field, the flow field throughout the nacelle, excluding the region under the direct influence of the fan, can be considered as locally two-dimensional for simplicity. Flow speed is primarily related to the acoustic convection effect discussed in Chapter 2. However, the flow should be fed by clean, dry air with minimal turbulent fluctuations (Smith 2004). The facility conditions must be established in a controlled manner such that information regarding acoustic liner impedance under various flow and acoustic conditions can be extracted.

Test sections for liner impedance testing should be designed such that a large range of testing capabilities, including multiple sample sizes and materials, can be investigated without replacing multiple components. Full-scale nacelles can be several meters in diameter and length. The size constraints imposed on a laboratory by a full-scale engine would be too great, and thus smaller, more manageable, wind tunnel assemblies are generally considered. However, the geometry of the tunnel must allow for the physics of a nacelle at flight conditions to be accurately captured (Melling & Doak 1971). For ease of manufacturing and installation, a rectangular cross section is commonly used to allow for flat wall installation and testing procedures.

Using a wind tunnel in contrast to a full-scale engine does present drawbacks on the tested frequencies, which are restricted by the chosen excitation source as well as the geometry of the test facility. Similarly, the tunnel walls should be "sound hard" as to not cause undesirable dissipation of acoustic energy. During liner impedance testing, new materials and methods may require one or more tunnel walls to be replaced. Ensuring the boundaries remain free of discontinuities requires samples be flush mounted to the

wall, thus minimizing reflections from protruding corners and maintaining flow uniformity. As sound propagates and air flows down the duct there are opportunities for reflections and new noise sources to be generated at junctions or area changes. Downstream noise sources have the potential to propagate upstream, contaminating measurements. Upstream propagating noise can be minimized by terminating into an anechoic outlet, where reflections are unable to propagate (Melling & Doak 1971).

Several facilities have been specifically designed and used for the grazing flow impedance testing of acoustic liners allowing for new technologies to be tested and ultimately implemented (Herkes *et al.* 2006). In an effort to upgrade current capabilities and steer liner development, NASA LaRC donated portions of such a facility, to the University of Florida. Such a test capability in a U.S. university lab is rare as most facilities are operated by private companies (Eversman & Gallman 2009), (Yu *et al.* 2008), government agencies (Watson & Jones 2009), or in foreign countries (Auregan & Leroux 2008), (Thiele *et al.* 2008), (Jing *et al.* 2008). University contained facilities allow for an open platform for collaboration and the flexibility for multiple uses. A full comparison of known experimental liner facilities is presented in Chapter 3.

Acoustic liner testing is a small step toward a larger goal of reducing aircraft generated noise. Many advancements are being made to reduce aircraft noise using advanced materials, in-flight trailing edge geometry treatment, and acoustic treatment of landing gear (Herkes *et al.* 2006). The facility proposed in this work is but another tool to help better understand and ultimately reduce fan noise for passengers and the community at large.

1.6 Thesis Outline

The current chapter established basic aircraft noise sources, noise abatement technology, and highlighted some advantages for a university-level test facility. Chapter 2 presents analytical models for understanding the acoustic and fluidic behavior within geometries pertaining to the proposed design. A thorough literature review in Chapter

3 describes current and past facilities. An in-depth comparison at acoustic impedance measurement techniques are also be compared. Chapter 4 describes the design of the proposed facility, contrasting the differences between it and the original Grazing Impedance Tube at NASA Langley Research Center. Chapter 5 lays out a proposed experimental investigation for complete characterization of the tunnel, establishing baseline flow and acoustic performance.

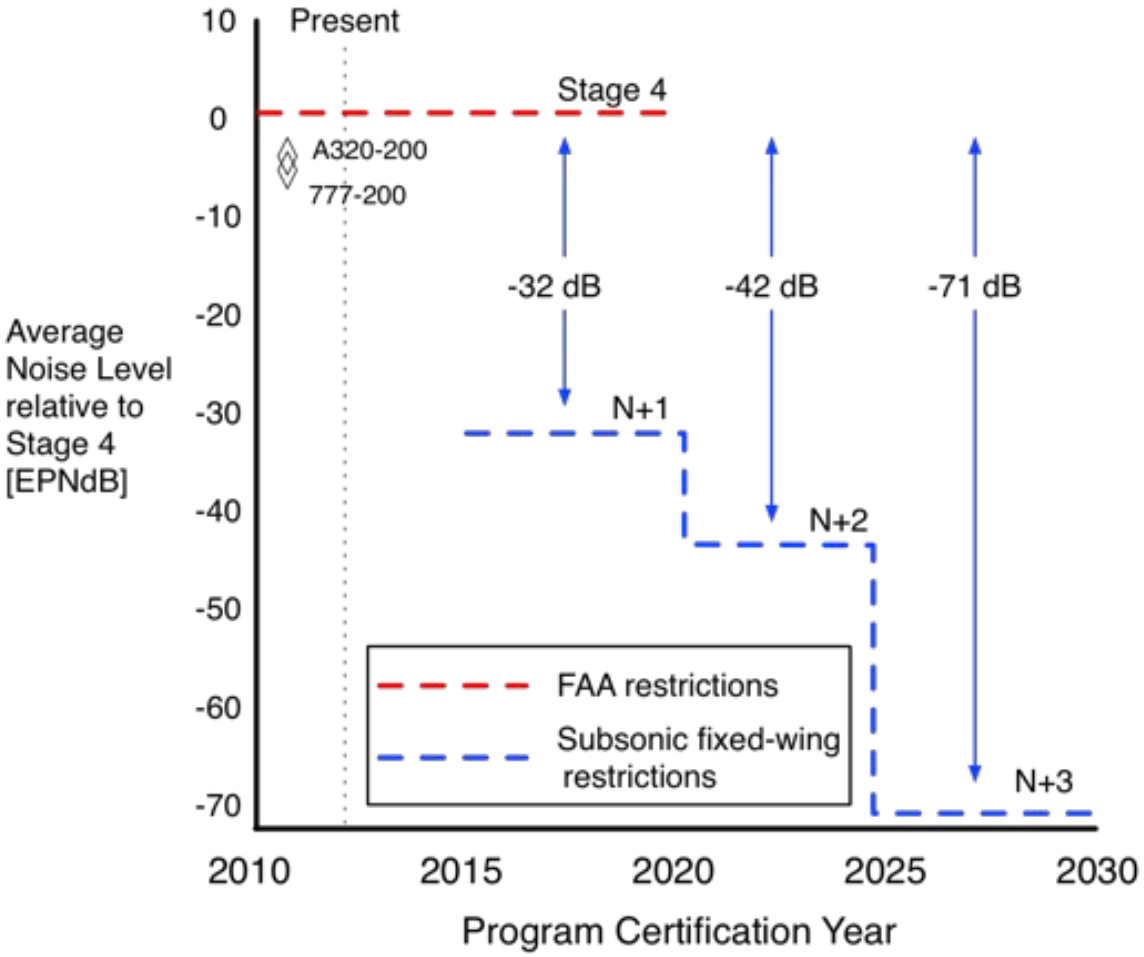

Figure 1-1. Overall noise level goals for future aircraft design. Data based on Environmentally Responsible Aviation (ERA) Project of the NASA Research Opportunities In Aeronautics 2010. Aeronautics Research Mission Directorate.

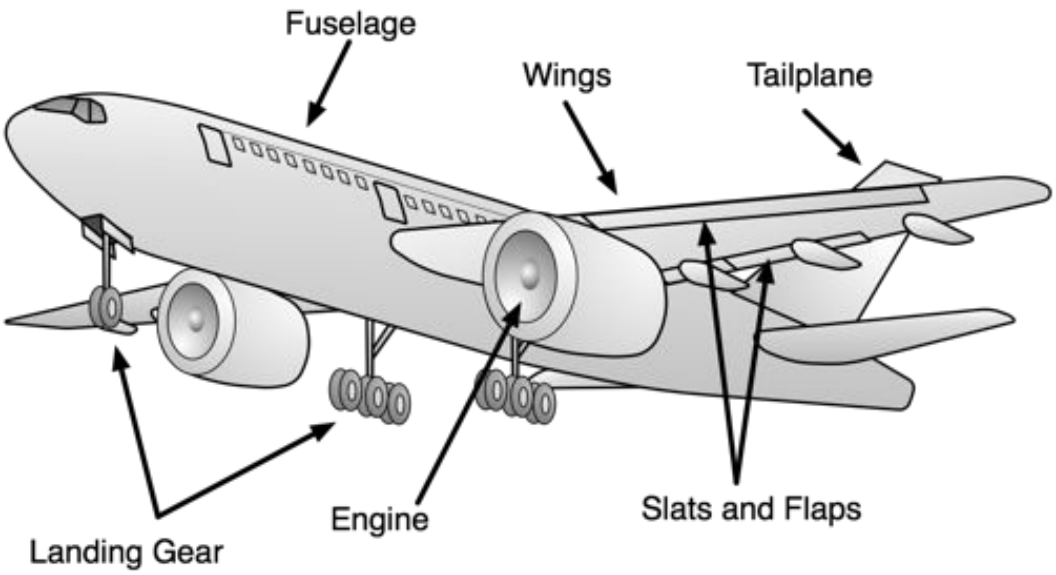

Figure 1-2. Aircraft noise generating sources.

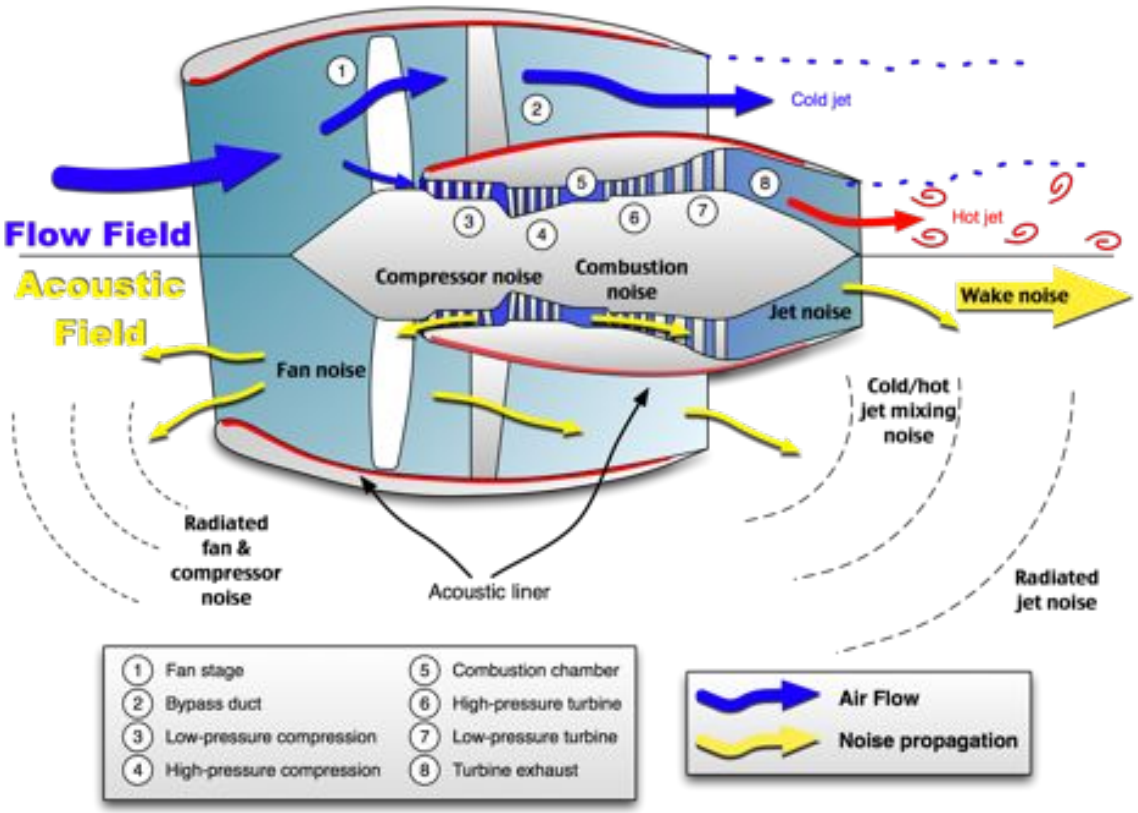

Figure 1-3. High-bypass ratio engine nacelle side view, adapted from Voutsinas, S. G. 2007. Aeroacoustics research in Europe: The CEAS-ASC Report on 2005 highlights. The Journal of Sound and Vibration, Volume 299, (Page 426, Figure 7).

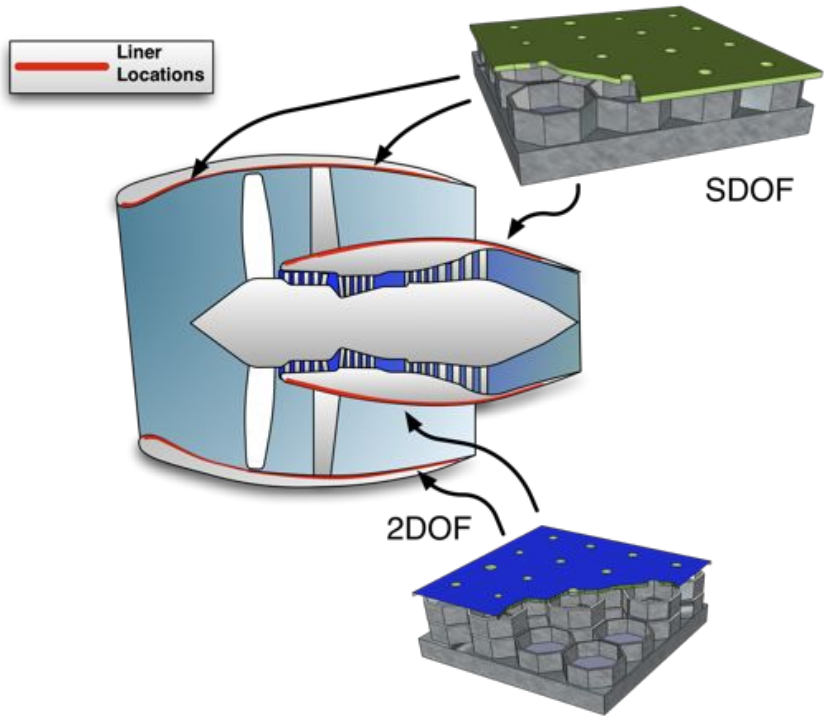

Figure 1-4. Acoustic liner types, adapted from Rolls Royce 1996. The Jet Engine (Page 204, Figure 19-6) Rolls-Royce Technical Publications, England.

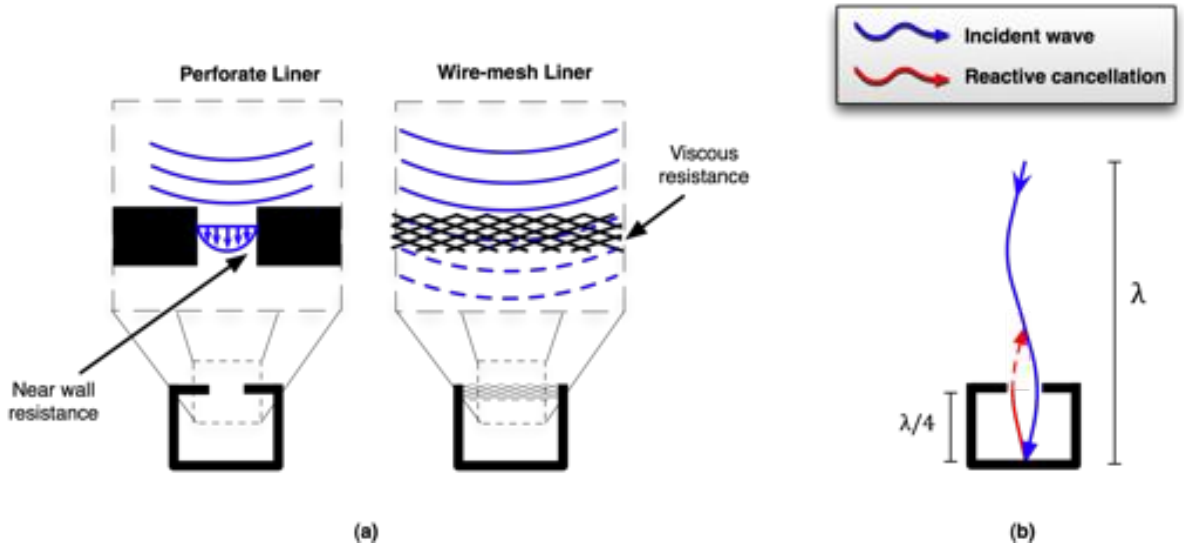

Figure 1-5. A 2-D side view of a single locally reactive liner with (a) resistive and (b) reactive facesheets for acoustic energy conversion, adapted from Smith (2004). Aircraft Noise. Cambridge University Press. (Page 144, Figure 4.26)

CHAPTER 2
THE PHYSICS OF A GRAZING IMPEDANCE DUCT FACILITY

Chapter 1 illustrated the necessity for experimental test facilities to study acoustic liners for aircraft noise reduction. This chapter will present the underlying physics involved with a grazing flow facility, specifically duct acoustics and channel flow. The acoustic analysis consists of three idealized examples: acoustic propagation in a hard-wall duct without flow, duct acoustics with an impedance boundary condition without flow, and finally the acoustic propagation within a bounded moving fluid. A consideration of the fluid physics is accomplished by presenting a review of laminar and turbulent boundary layer theory and scaling analysis, as well as an introduction to turbulent channel flow. Such physical insights are prerequisites to an understanding of the acoustic and flow fields specific to the current facility.

2.1 Introduction to Grazing Duct Flow

The proposed facility seeks to elucidate the underlying physics regarding superimposed acoustic and flow fields. Later chapters will make reference to topics discussed ultimately aiding in the design, implementation, and thorough testing of the GFID facility.

The acoustic field within a closed duct is highly dependent upon source conditions, duct geometry, and boundary conditions. Initially, a hard-walled duct is examined to establish a baseline solution. The hard walls are then replaced with a complex impedance boundary condition to demonstrate the impact on the acoustic field by modifying the boundaries, much like an acoustic liner. Finally, a steady uniform flow is superimposed on the acoustic field to illustrate the effect of a free stream Mach number on acoustic properties. Full derivations of select equations are worked out in Appendix A - C.

The latter half of this chapter provides an in-depth look at the flow field within an enclosed rectangular channel. The analysis focuses on the developing boundary layers within the duct, beginning with a discussion on laminar and turbulent boundary layers as well as turbulence scaling. Viscous effects specific to turbulent channel flow within, such as

corner flows and cross-axis secondary motion, are discussed via the generation and decay of vorticity.

2.2 Duct acoustics

2.2.1 Rigid Wall Analysis in a Quiescent Medium

The propagation of an acoustic wave through a two-dimensional rigid-walled duct of infinite length and width is investigated to establish a baseline solution for propagation without energy loss at the boundaries, illustrated in Figure 2-1a. For simplicity, the acoustic field is assumed to be generated by an upstream time-harmonic source of the form $e^{i\omega t}$, including the simplest case of a single tone. The source is also assumed to be sufficiently far away such that the solution can be considered a "far-field" approximation and thus hydrodynamic effects are assumed to be negligible (Beranek 1996). Acoustic propagation is limited to only "right-running waves", neglecting upstream propagating reflections. This assumption simplifies the solution and is more applicable to the proposed facility where the pressure waves will terminate into an anechoic diffuser. The acoustic field is modeled by an assumed solution of the form

$$p'(x, y, t) = P(x, y, \omega)e^{j\omega t}, \tag{2–1}$$

where the pressure field, $p'(x, y, t)$, is expressed as the product of a frequency and spatially dependent complex amplitude, $P(x, y, \omega)$, with a complex time-harmonic excitation term, $e^{j\omega t}$ (Blackstock 2001).

Assuming the given time harmonic source and an isentropic speed of sound, the pressure wave equation,

$$\nabla^2 P - \frac{1}{c_0}\frac{\partial^2 p}{\partial t^2} = 0, \tag{2–2}$$

can be converted to the frequency domain

$$\nabla^2 P + \kappa^2 P = 0, \tag{2–3}$$

commonly referred to as the Helmholtz equation (Blackstock 2001). Here, $k = \omega/c_0$, represents the acoustic wave number, defined as the ratio of the angular frequency and the isentropic speed of sound. The boundary conditions of zero particle velocity normal to the walls are imposed. Separation of variables is an appropriate approach to the solution of Equation 2–3. The solution to the linear 2^{nd} order homogeneous partial differential equation reduces to transcendental functions in the transverse direction and the sum of complex exponentials in the direction of propagation (Blackstock 2001). The final result represents the superposition of an infinite number of right-running acoustic modes, n, presented in Equation 2–4. A full derivation of the solution is presented in Appendix A.

$$p' = \sum_{n=0}^{\infty} \cos\left(\frac{n\pi y}{b}\right) A e^{-j(\kappa_x)_n x} e^{j\omega t} \tag{2–4}$$

The constant A is a function of the source operating conditions, and b is the duct height. The eigenvalues of Equation 2–4, functions of duct geometry and mode of interest, are representative of the propagating wave number mode,

$$\kappa_y = \frac{n\pi}{b} \qquad \text{for } n = 0, 1, 2, ... \tag{2–5}$$

The total wave number, k, can be decomposed into directional trace wave numbers. The relationship between directional trace wave numbers and the total wave number is commonly referred to as a dispersion relationship

$$k = \sqrt{{\kappa_x}^2 + {\kappa_y}^2}, \tag{2–6}$$

or solved for κ_x as

$$\kappa_x = \sqrt{\left(\frac{\omega}{c_0}\right)^2 - \left(\frac{n\pi}{b}\right)^2}. \tag{2–7}$$

The wave number aligned with the direction of propagation, κ_x, is shown to be dependent upon two terms: the overall acoustic wave number, itself a function of the medium and excitation frequency, and κ_y, a constant defined by duct geometry that is

highly dependent upon the imposed boundary conditions. Various values of these terms allow for the dispersion relationship to be purely real, purely imaginary, or complex.

Via the dispersion relationship for hard-walled ducts, modal wave propagation occurs when the value of κ_x is purely real. However, if κ_x is purely imaginary, the wave is evanescent and decays with increasing downstream distance, x. The third case dictates that, for finite modes associated with complex values of κ_x, the wave may propagate but will eventually attenuate (Blackstock 2001).

For propagating modes, wave numbers defined such that $k > \kappa_y$ designates the frequency value at which higher order modes are supported and are a function of the duct geometry and source excitation frequency (Blackstock 2001),

$$f_n = \frac{nc_0}{2b}. \tag{2–8}$$

The 0^{th} mode is a planar wave in a rectangular duct, one devoid of transverse pressure variations (Blackstock 2001). A higher order propagating mode is first cut-on when the transverse dimension of the duct is equal to an integer number of half-wavelengths. Note that although only the planar mode is supported to propagate in the duct, so called "soft modes" are generated at the leading and trailing edges of an installed acoustic liner, but will evanescently decay (Watson *et al.* 2008).

From a practical standpoint, the spatial dependance of higher order modes within a duct defines the location of possible microphone installation sites for impedance eduction measurements. Due to the size of current microphones and duct geometry, testing is often restricted to frequencies associated with the planar mode.

The cut-on frequency described in Equation 2–8, is limited to ducts with idealized sound hard boundaries (Blackstock 2001). The following analysis specifically investigates duct acoustics under impedance boundary conditions, such as an acoustic liner.

2.2.2 Impedance Boundary Conditions in a Quiescent Medium

The values of κ_x determine which modes are permitted to propagate within a duct. If the value of κ_x can be altered to reduce the amplitude of unwanted modes, then undesirable noise resulting from these modes can be attenuated inside the duct prior to propagating to the surrounding environment. Since κ_x is a function of both κ and κ_y, altering κ_x requires that either the duct geometry or the boundary conditions be modified. Geometries are generally designed for aerodynamic efficiency or structural integrity, generally leaving acoustic mitigation as a secondary concern (Smith 2004). Thus, the boundary condition is usually altered, most commonly through the use of acoustic liners.

A new dispersion relationship can be obtained for different impedance boundaries. While zero particle velocity normal to the wall was imposed for the hard-walled case, the particle velocity is now generalized as a function of the local impedance. A key assumption applied in the analysis of impedance boundary conditions is the acoustic liners are "locally reactive", that is constraining particle motion normal to the surface (Nayfeh *et al.* 1975). The boundary conditions match particle velocity normal to the surface from the momentum equation to the particle velocity imposed by the specific acoustic impedance defined at the boundaries of the imposed liner (Ingard 1999),

$$\frac{1}{-j\omega\rho_0}\frac{\partial p}{\partial y} = \frac{P}{-Z_1}\bigg|_{y=0} \tag{2–9}$$

and

$$\frac{1}{-j\omega\rho_0}\frac{\partial p}{\partial y} = \frac{P}{Z_2}\bigg|_{y=b}. \tag{2–10}$$

A solution is described for two walls separated by distance b with specific acoustic impedance values, Z_1 and Z_2, as shown in Figure 2-1b. It becomes convenient to introduce the inverse of acoustic impedance, admittance, defined by

$$\eta_i = \frac{\rho_0 c_0}{Z_i}. \tag{2–11}$$

To solve the acoustic field when impedance boundaries are specified, a separation of variables technique, similar to the rigid-walled case, is employed. Combining like terms, the ratio of κ_y/k is obtained as a function of the wave number and liner admittance. A full derivation of this result can be found in Appendix B.

$$\left(\frac{\kappa_y}{\kappa}\right) tan(\kappa_y b) = -j\frac{\eta_1 + \eta_2}{1 + \eta_1\eta_2\left(\frac{\kappa}{\kappa_y}\right)^2} \tag{2–12}$$

The above expression is generally solved numerically for the transverse wave number, κ_y, as a function of duct geometry, total wave number, and the liner normalized specific admittance (Ingard 1999). With κ and κ_y known, values for κ_x can be calculated, revealing which modes will propagate and their attenuation. More complex designs can further attenuate undesirable modes by varying liner admittance along the duct length.

The hard-walled and locally reactive liner cases both assume that acoustic propagation is soley a function of the geometry, propagating wave number, and imposed boundary conditions. However, in the effort to further mimic engine nacelle conditions, the effect of the flow of air passing over a liner surface must also be assessed.

2.2.3 The Convective Wave Equation with Uniform Velocity Profile

Both of the presented solutions have been subject to the restriction of zero-mean velocity, simplifying the governing equations necessary for subsequent derivations. However, if a known mean velocity is superimposed with a propagating linear acoustic wave, the resultant field is best described by the convective pressure-wave equation.

$$\frac{\partial^2 p'}{\partial t^2} + c_0^2\frac{\partial^2 p'}{\partial x^2}\left(Ma^2 - 1\right) = -2u_0\frac{\partial^2 p'}{\partial x \partial t}, \tag{2–13}$$

where Ma is the local Mach number, formed by non-dimensionalizing the local mean velocity by the isentropic speed of sound, $M = {}^{u_0}/_{c_0}$. A full derivation of Equation 2–13 is provided in Appendix C. Note that in Equation 2–13, if Ma is zero the classic pressure-wave equation for a quiescent medium is recovered.

The downstream moving fluid convects the acoustic field downstream, increasing the speed at which pressure waves propagate (Nayfeh *et al.* 1975). For a lined duct, the effect of convection decreases the attenuation for downstream traveling waves (Eversman 1991). For upstream acoustic propagation, the opposite is true, and a higher attenuation rate is achieved (Tack & Lambert 1965). In uniform flow, the convection of the acoustic field is the only mechanism for altering the attenuation rate, the influence of which increases with increased free stream Mach number (Eversman 1991).

Note that Equation 2–13 is only valid for uniform flow, but experimental results have found a second attenuation mechanism. The influence of fluid viscosity exhibits a refraction effect, most notably near walls where viscous effects dominate in the boundary layer (Nayfeh *et al.* 1975). For downstream acoustic propagation, the velocity gradient refracts the propagating acoustic front toward the boundaries, increasing the attenuation rate. For upstream propagation, the attenuation rate decreases as acoustic waves converge toward the center (Nayfeh *et al.* 1975).

The two contradictory effects of convection and refraction are strong functions of the wave number. Convective effects are found to influence a large range of frequencies (Nayfeh *et al.* 1975). Conversely, refraction effects are important at higher wave numbers, and thus higher frequencies, notably for $\kappa\delta > 1$, where the boundary layer thickness, δ, is approximately $1/6$ of the acoustic wavelength. Thus, refraction effects become increasingly significant at downstream locations due to boundary layer growth (Tack & Lambert 1965).

The influence of refraction has been demonstrated both experimentally and numerically (Mungur & Gladwell 1969; Tack & Lambert 1965). The refractive effects are based upon viscous dissipation inherent to the boundary layer. The development, structure, and scaling of boundary layers are discussed next.

2.3 Fluid Analysis

In section 2.2.1, the problem of acoustic propagation through a duct was analyzed subject to zero-mean flow to establish a relationship between the acoustic wave number

and the imposed boundary conditions. A uniform velocity profile was then superimposed in section 2.2.3 to describe the impact of a convective medium on liner attenuation. However, the uniform flow profile violates the no-slip boundary condition imposed by viscous interactions of a fluid with a boundary. Disregarding the viscous effects within a fixed area duct allows for some basic physical insight; however, this method of analysis does not fully represent the physics of the problem.

In order to better understand the underlying fluid effects, it is instructive to consider the developing boundary layer on a flat plate under the restrictions of an enclosed channel. Specifically, a rectangular channel is examined because it is consistent with the proposed facility. The study of channel flow can be separated into two distinct topics: the near wall developing boundary layer and secondary flow influenced near the corner regions, specific to enclosed rectangular channel flow.

The two defining topics of boundary layers and channel flow are highly dependent on viscous phenomena. The significance of the viscous forces can be quantified via the Reynolds number

$$Re = \frac{\rho U \ell}{\mu}. \tag{2–14}$$

The Reynolds number is the dimensionless ratio of inertial to viscous forces (Young 1989). In equation 2–14, ℓ is a length scale of interest such as channel height or local boundary layer thickness, while ρ and μ are the fluid density and dynamic viscosity, respectively. Alternatively, the fluid properties can be combined to form the kinematic viscosity, $\nu = \mu/\rho$. The value of the Reynolds number is indicative of flow regime characteristics. Section 2.3.1 discusses the range of different length scales within the boundary layer based upon the Reynolds number.

2.3.1 The Boundary Layer

The boundary layer is a thin region of fluid near a surface dominated by viscous forces. Even for high Reynolds number flows, where inertial effects dominate, the

boundary layer is responsible for viscous drag penalties, vorticity generation, and possible shedding effects (Batchelor 2000).

The boundary layer within a flow is the result of internal stresses induced by intermolecular attractions as fluid particles pass a surface (Schlichting & Gersten 1968). The fluid in direct contact with the surface is subject to the "no-slip condition", and consequently must match the local surface velocity. The dynamic viscosity, μ, is the fluid property responsible for dissipating kinetic energy, thus reducing the local fluid velocity near the wall. At some distance from the body, the influence of viscosity becomes negligible, and the free stream velocity is reached at a distance δ from the wall. Mathematically, δ is defined as the height normal to the surface where the local fluid reaches 99% of the free stream velocity, U_∞ (White 2006).

For a Newtonian fluid in a steady, two-dimensional, incompressible boundary layer, the local wall shear stress, τ_{ji}, can be estimated as the product of the dynamic viscosity and the local velocity gradient at the wall (White 2006),

$$\tau_{ji} = \mu \left(\frac{\partial u_i}{\partial x_j} + \frac{\partial u_j}{\partial x_i} \right) \tag{2–15}$$

Applying Equation 2–15 to the boundary layer in a channel coordinate system, scaling analysis demonstrates that the second term is two orders of magnitude smaller than the first term, $^{\partial v}/_{\partial x} \ll {}^{\partial u}/_{\partial y}$. This leads to an approximation for wall shear stress

$$\tau_w \approx \mu \frac{\partial u}{\partial y}\bigg|_{y=0}. \tag{2–16}$$

Although δ itself can be useful in gauging the influence of viscosity, the displacement thickness, δ^*, and momentum thickness, θ, provide additional insight. The displacement thickness physically represents the distance a streamline is displaced from a surface to match the mass flow of the boundary layer (Panton 2006), and is defined as

$$\delta^* = \int_0^\infty \left(1 - \frac{u(y)}{U_\infty} \right) dy. \tag{2–17}$$

Similar to the displacement thickness, the momentum thickness is also defined by an integral relation

$$\theta = \int_0^\infty \frac{u(y)}{U_\infty}\left(1 - \frac{u(y)}{U_\infty}\right) dy. \tag{2–18}$$

The momentum thickness physically represents the momentum deficit per unit depth caused by the retardation of the fluid within the boundary layer (Tennekes & Lumley 1999). The non-dimensional shape factor, H, allows for comparison of boundary layers and is defined as the ratio of the two preceeding variables,

$$H = \frac{\delta^*}{\theta}. \tag{2–19}$$

Always greater than unity, higher shape factor values indicate near-separation flow. Blasius's solution specifies a constant shape factor value of 2.59 for an idealized laminar boundary layer, higher than the estimate of a turbulent boundary layer of 1.3 based on a $1/7^{th}$ power law (White 2003).

Depending upon the local Reynolds number, the flow is categorized as laminar, transitional, or turbulent. For a given geometry, lower Reynolds number values indicate a greater dependence on viscous effects. The flow regime at low Reynolds numbers is designated laminar to describe the smooth and ordered flow structure. A laminar regime is found at $Re_D < 2,300$ for pipe flow and $Re_x < 500,000$ for flow over a flat plate (White 2003). Here, x is the streamwise distance from the leading edge. The onset of turbulence can be difficult to pinpoint as it is a strong function of surface roughness and initial conditions. Conservative estimates are $Re_D > 4,000$ and $Re_x > 1E6$ for pipe and flat plate flows, respectively (White 2003). The subscript on the "Re" indicates the length or velocity scale used for the specific Reynolds number calculation.

The growth of a laminar boundary layer stems from a combination of the convection of momentum and viscous diffusion away from the surface (Mathieu & Scott 2000). The facility built for this project was designed for speeds above $M = 0.5$ to model the flow inside engine ducts. These Mach numbers are achieved by increasing the free stream

speed, thereby establishing a turbulent flow regime beyond a certain point. Due to their relevance to the present application, turbulent boundary layers are given additional discussion.

2.3.2 Turbulent Boundary Layers

As a fluid propagates downstream, the smooth and ordered flow transforms to one characterized by three-dimensional random fluctuations (Tennekes & Lumley 1999). A turbulent field is highly dependent on local variables including surface roughness, pressure gradients, and even external effects such as local environmental noise (Young 1989). Once the flow becomes unstable and transitions to a turbulent regime, the physical characteristics of the flow, and thus the boundary layer, transform.

Turbulent flow exhibits random motion with a wide range of length, velocity, and time scales. A turbulent flow contains vortical structures referred to as "turbulent eddies" that convect and entrain fluid (Tennekes & Lumley 1999). While laminar boundary layer growth is dictated by viscous diffusion, the faster turbulent boundary layer growth (i.e. increase in $\delta(x)$ with x) stems from the entrainment of high momentum fluid attributed to the turbulent eddies (Mathieu & Scott 2000).

Termed the Reynolds decomposition, the local velocity, $u(x,t)$, at a particular point in space and time can be written as $u_i = \overline{u_i} + u_i'$. More generally, the turbulent velocity field at any given point is the superposition of mean, $\bar{(\ )}$, and fluctuating components, $(\ )'$. On a flat plate, the fluctuating velocity component can be as high as 10% of the free stream velocity in a turbulent flow, resulting in increased boundary layer mixing (Young 1989).

Turbulent flow enhances three-dimensional mixing, which increases the transport of momentum, vorticity, and heat near the surface of a body, leading to a boundary layer with a "fuller" mean velocity profile that entrains high energy fluid found further from the wall, illustrated in Figure 2-2 (Tennekes & Lumley 1999). A fuller boundary layer is quantified by lower H values, defined in Equation 2–19. As a consequence of the no-slip condition, larger near wall velocity gradients are formed, resulting in turbulent boundary

layers having higher mean shear stress values than laminar flows at similar conditions (Mathieu & Scott 2000).

Up to this point, boundary layers have only been discussed in terms of the distance from the origin, x, the height, such as boundary layer thickness, δ, or momentum thickness, θ, which are functions of the normal distance from the wall, y. To quantify the influence of viscous effects within turbulent boundary layers, the length scales previously presented are insufficient. Instead, a non-dimensional viscous length scale is defined,

$$y^+ = \frac{yu^*}{\nu}, \tag{2–20}$$

the ratio of wall-normal distance, y, to a "viscous wall unit". The variable u^* defines the friction velocity,

$$u^* = \sqrt{\frac{\tau_w}{\rho}}, \tag{2–21}$$

a function of the the local shear stress and local fluid density. Similarly, a non-dimensional viscous velocity scale, u^+, is formed by normalizing the local mean velocity by the friction velocity

$$u^+ = \frac{\bar{u}}{u^*}. \tag{2–22}$$

The quantities presented can now be used to analyze the turbulent boundary layer in terms of viscous length and velocity scales.

One particular area of interest is the ability to measure and extract the local shear stress values. For a laminar boundary layer, a good approximation to the local shear stress value is simply Equation 2–16 (Young 1989). However, in a turbulent boundary layer, highly energetic eddies give rise to an additional imparted stress, referred to as turbulent Reynolds stress, $-\rho\overline{u_i' u_j'}$. The total stress throughout a turbulent boundary layer can then be written as

$$\tau_{ij} = \mu\left(\frac{\partial u_i}{\partial x_j} + \frac{\partial u_j}{\partial x_i}\right) - \rho\overline{u_i' u_j'}. \tag{2–23}$$

It is evident that Equation 2–15 is a simplification of Equation 2–23 for when Reynolds stresses are negligible, as is the case of laminar boundary layers.

The turbulent boundary layer can now be subdivided into regions where the local stress is dominated by either turbulent stresses or by viscous stresses, termed the inertial sublayer and viscous sublayer, respectively. The two regions are bridged by the buffer layer, where both the viscous and turbulent stresses play a pivotal role (Schlichting & Gersten 1968).

Defined within the approximate region $y^+ \leq 5$, the viscous sublayer is dominated by viscous effects and is also strongly dependent on surface roughness (Mathieu & Scott 2000). Assuming a smooth surface, the non-dimensional velocity in this region is linearly related to the dimensionless wall unit length scale, i.e. $u^+ \approx y^+$, leading to the alternative designation of "linear sublayer". Strong viscous stresses within this region generate a momentum sink as viscosity suppresses high energy fluid entrainment toward the wall (Tennekes & Lumley 1999).

The buffer layer is generally defined for y^+ values within $5 < y^+ < 30$ (Tennekes & Lumley 1999). Linking the energetic inertial layer and the dissipative viscous sublayer, the buffer layer demonstrates a balance between production and dissipation of turbulent energy, exhibiting maximum turbulent energy production near $y^+ = 15$ (Mathieu & Scott 2000). This energy is generated by the turbulent fluctuations and is appropriately called the turbulent kinetic energy, $\frac{1}{2}\overline{u_i' u_j'}$.

For $y^+ \geq 30$, the inertial sublayer is dominated by turbulent Reynolds stresses. No clear upper limit can be defined as the y^+ range influence widens with increased Reynolds number to approximately $y/\delta = 0.2$ (Mathieu & Scott 2000). Without a strong dissipative viscous effect, the velocity profile can no longer be written simply as a linear function of only one variable, y^+. Alternatively, the velocity profile within this region is well approximated by the "law of the wall",

$$u^+ = \frac{1}{\kappa} \ln y^+ + B \tag{2–24}$$

out to $y/\delta \approx 0.7$ (White 2006). The von Kármán constant κ and B currently adhere to the experimental values of 0.41 and 5.0, respectively. However, values of 0.38 and 4.08 have been suggested for use when $Re_\theta > 10,000$ (White 2006). Denoting the form of the equation, this region is often referred to as the "log layer", although other mathematical models exist (Kays *et al.* 2005).

A similar formula that takes into account all three regions of the turbulent boundary layer simultaneously was developed by Spalding (Spalding 1965),

$$y^+ = u^+ + e^{-\kappa B}\left[e^{\kappa u^+} - 1 - \kappa u^+ - \frac{(\kappa u^+)^2}{2} - \frac{(\kappa u^+)^3}{6}\right]. \tag{2–25}$$

The wall shear stress can then be extracted through the definition of the viscous wall unit and the friction velocity provided by equations 2–20 and 2–21, respectively.

Spalding's equation breaks down at high y^+ values near the wake region, requiring a secondary function for the outer region. Musker (1979) presented an explicit equation that accounts for both the inner and outer regions,

$$u^+ = 5.424\tan^{-1}\left[\frac{2y^+ - 8.15}{16.7}\right] + \log_{10}\left[\frac{(y^+ + 10.6)^{9.6}}{\left((y^+)^2 - 8.15y^+ + 86\right)^2}\right]\ldots$$
$$-3.52 + 2.44\left\{\Pi\left[6\left(\frac{y}{\delta}\right)^2 - 4\left(\frac{y}{\delta}\right)^3\right] + \left[\left(\frac{y}{\delta}\right)^2\left(1 - \frac{y}{\delta}\right)\right]\right\}, \tag{2–26}$$

where $\Pi = \kappa A/2$, Coles Wake parameter, and A is an outer layer variable that is a function of the local pressure gradient. Experimental data in Chapter 4 will be fit to both Equations 2–25 and 2–26 for comparison (White 2006).

The relations for the three inner layer regions have been plotted in Figure 2-3. The horizontal axis, representing the distance from the wall in viscous wall units, is commonly expressed on a logarithmic scale, illustrating the discrepancy in sizes of the sublayers. The height of the viscous sublayer can be less than $1/100^{th}$ of the total boundary layer thickness (Young 1989). As an example, an incompressible flow of air at 100 m/s through a 2 $in.$ square tunnel would have a viscous sublayer of approximately 2.9 μm. The layer's small size hinders accurate experimental sublayer velocity measurements.

Many of the boundary layer approximations and comparisons are applicable to near-wall internal flows as well. However, the influence of multiple confining walls and a corresponding streamwise pressure gradient inherent to internal flows, globally impacts the flow structure and boundary layer characteristics. The following section presents some general channel flow features and their significance to the current research.

2.3.3 Turbulent Channel Flow

The GFID facility combines the flow and acoustic propagation through a square channel in an effort to mimic flight conditions for impedance eduction of acoustic liner samples. Duct geometry has already been shown to influence the acoustic field by limiting the range of supported frequencies. Near wall acoustic refraction by means of viscous effects also influences the propagation and attenuation of acoustic waves, thus ultimately affecting impedance measurements. This section will reveal some of the important characteristics associated with turbulent channel flow. Note that this section specifically deals with flow through channels of finite aspect ratios less than $(1:7)$, where a 2-D assumption is not applicable (Dean 1978).

Fluid flow restricted to an enclosed section shares some characteristics with external boundary layers in terms of development and structure. The pressure within the developing region is nonlinear, allowing the streamwise velocity to only be a function of x. However, unlike boundary layers of an external flow, an enclosed channel is strongly influenced by the necessary driving pressure gradient to overcome viscous losses. Once the flow becomes fully developed, the streamwise pressure gradient becomes constant, driving the flow, and the centerline velocity is no longer a function of downstream distance.

In order to discuss internal flows, new scaling arguments need to be established. Given enough streamwise distance, external boundary layers eventually transition to a turbulent regime (Young 1989). However, for internal flows, the boundary layers from multiple walls ultimately merge, restricting additional boundary layer growth. The influence of viscosity propagates downstream and is distributed toward the duct centerline.

Thus duct width (for 2-D flows) is a more appropriate length scale for internal flows (Gessner 1973; Hoagland 1960). Common practice for turbulent channel flow scaling involves using a combination of geometric and viscous scales, generally hydraulic diameter and either the centerline or integrated bulk velocity (Anselmet *et al.* 2009). The following discussion is based on the GFID square duct geometry.

Channel flow also presents interesting physics from a vorticity perspective. In laminar flows involving incompressible Newtonian fluids, the vorticity transport equation is written as

$$\frac{D\omega_i}{Dt} = \omega_j \frac{\partial u_i}{\partial x_j} + \nu \frac{\partial^2 \omega_i}{\partial x_j \partial x_j}, \tag{2–27}$$

where the vorticity vector, ω_i, is the curl of the vector velocity field, $\nabla \times \overrightarrow{V}$ (Panton 2006). Under further assumptions of steady, fully developed, three-dimensional flow, only the right hand side of Equation 2–27 remains; representing vorticity stretching and diffusion of vorticity, respectively (Panton 2006).

Higher Reynolds number values based on friction velocity, ($Re_{u^*} > 180$), are indicative of fully-developed, three-dimensional, turbulent flow in channels. The turbulent Reynolds stress introduces additional vorticity production terms into Equation 2–27 (Brundrett & Baines 1964). The two additional terms are simplified for rectangular geometry as,

$$\frac{\partial^2}{\partial x_2 \partial x_2}\left(\overline{(u_3')^2} - \overline{(u_2')^2}\right) - \left(\frac{\partial^2}{\partial x_2^2} - \frac{\partial^2}{\partial x_3^2}\right)\overline{u_2' u_3'}. \tag{2–28}$$

Further simplifications can be made by limiting the geometry to a square cross section.. In doing so, the first term of Equation 2–28 drops out as u_2' and u_3' are equivalent (Brundrett & Baines 1964).

The remaining term describes a source of turbulent vorticity production stemming from nonlinear Reynolds stress (Gessner & Jones 1965). Through analysis of the geometry, the Reynolds stress term can be shown to have zero magnitude along any geometric lines of symmetry within the duct, thus generating eight triangular regions of non-zero vorticity production with quadrant symmetry, illustrated in Figure 2-4 (Brundrett & Baines 1964).

These additional production terms generate a flow where the streamwise vorticity, ω_1, is non-zero. Restricting analysis to the geometry mentioned, the definition of $\overline{\omega_1}$ is expressed as

$$\overline{\omega_1} = \frac{\partial \overline{u_3}}{\partial x_2} - \frac{\partial \overline{u_2}}{\partial x_3}. \tag{2–29}$$

Thus, the mean streamwise vorticity, $\overline{\omega_1}$, exists due to mean lateral velocity gradients (Brundrett & Baines 1964). Similar to the turbulent lateral velocities, u_2' and u_3', the mean lateral velocities are restricted to stay within the lines of geometric symmetry (Brundrett & Baines 1964). This establishes secondary flow patterns within the triangular symmetry regions. A qualitative representation of secondary velocity streamlines, or isovels, common to symmetric turbulent duct flow are illustrated in Figure 2-5 (Melling & Whitelaw 1976).

The secondary flow pattern has been experimentally measured and can reach a maximum value of $1 - 3\%$ of the centerline velocity (Gessner *et al.* 1977; Melling & Whitelaw 1976) but demonstrates a global impact on the flow by convecting momentum away from the walls, ultimately impacting the local boundary layer structure (Brundrett & Baines 1964). Along lines of symmetry, there are no walls to retard the flow and thus no vorticity is present (Melling & Whitelaw 1976). However, the convection of momentum causes large gradients of cross-axis shear and vorticity toward the corners (Gessner 1973). The secondary flow acts to maintain stability by convecting momentum from regions of vorticity production toward regions of vorticity diffusion, found near the wall (Brundrett & Baines 1964).

In summary, this chapter presented a review of the acoustic propagation and flow patterns associated with geometry similar to the proposed facility. The analysis of acoustic duct propagation with impedance boundary conditions demonstrated the relationship of propagating wave number and liner impedance values. Chapter 3 will describe published methods used for liner impedance eduction testing. Chapter 3 will also discuss past channel flow experiments to establish baseline test conditions. Such experiments will be outlined in Chapter 5.

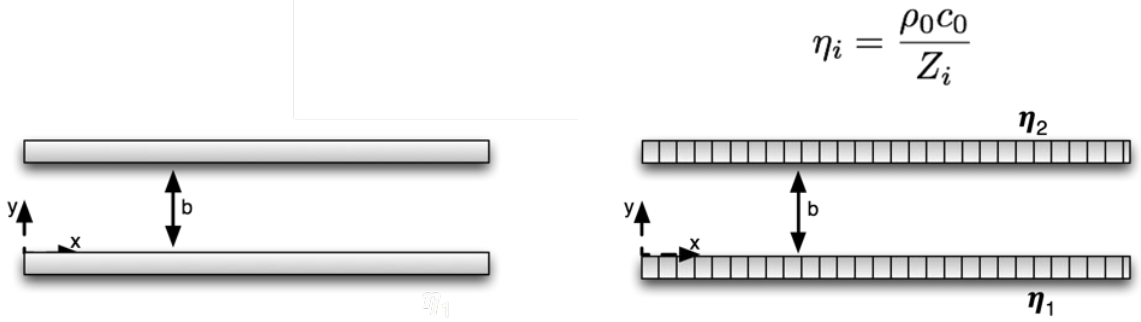

Figure 2-1. a) Two-dimensional sound hard boundary waveguide, and b) Two-dimensional waveguide with locally reactive impedance boundary conditions.

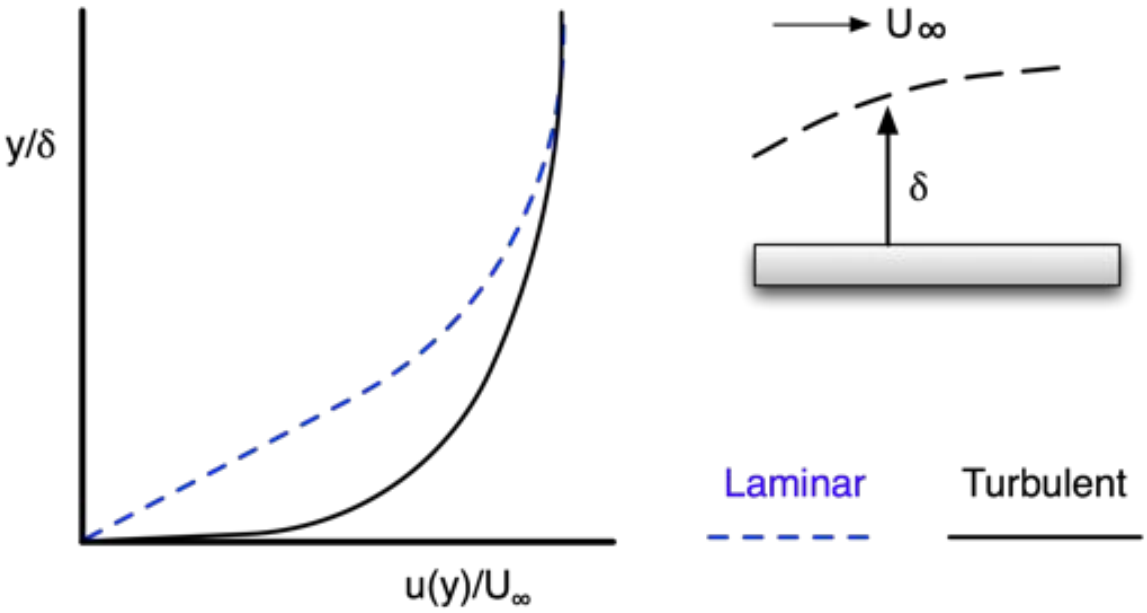

Figure 2-2. Laminar vs. turbulent boundary layer profiles.

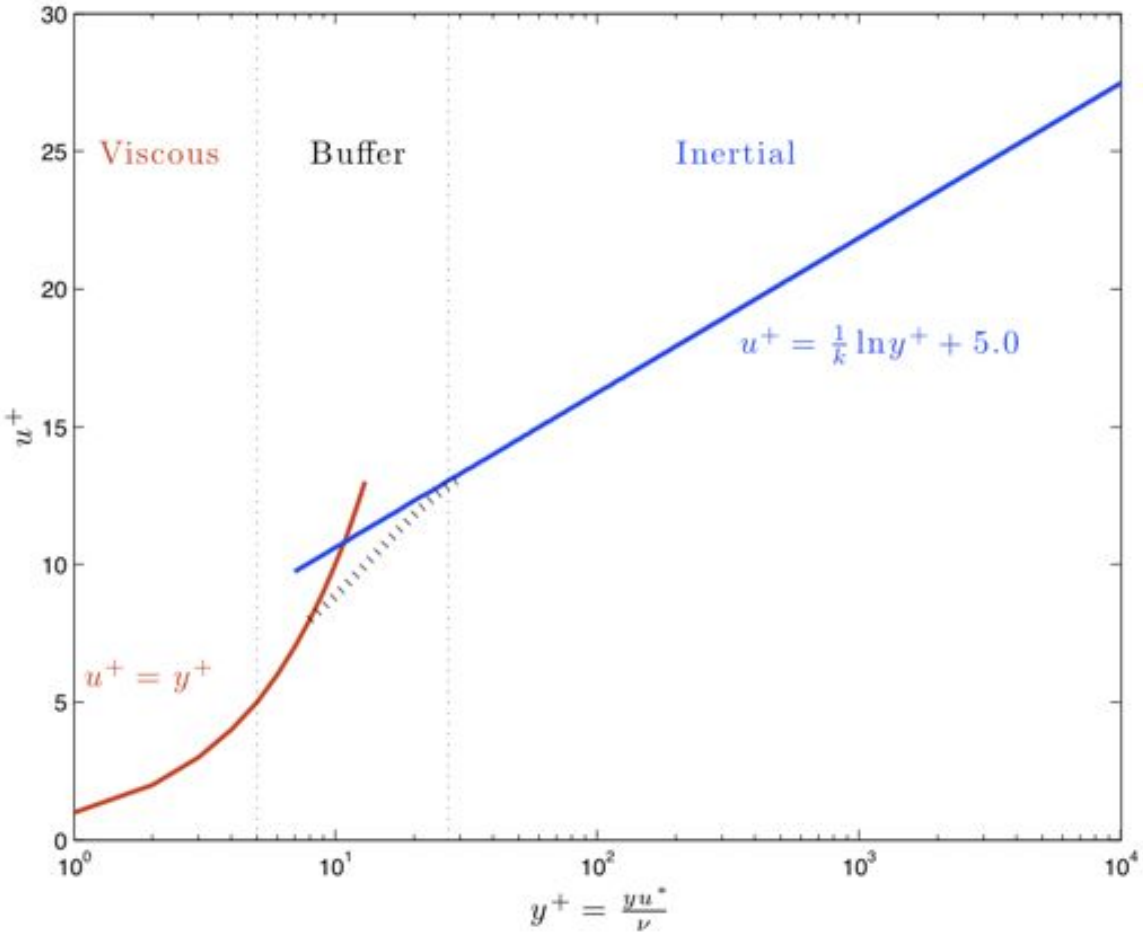

Figure 2-3. Sublayer regions within turbulent boundary layer.

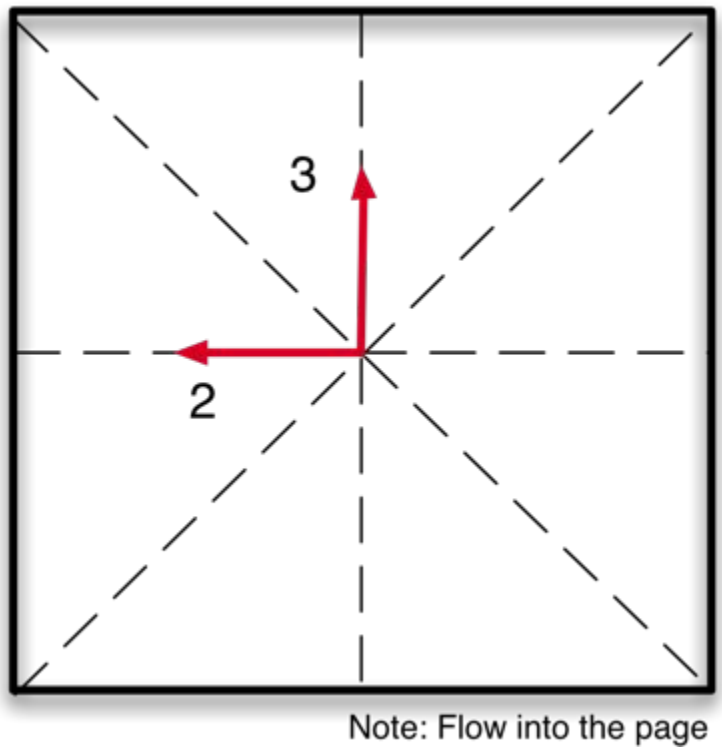

Figure 2-4. Symmetry lines (dashes) separating secondary velocity established by turbulent channel flow, adapted from Gessner, F.B. 1973. The origin of secondary flow in turbulent flow along a corner. Journal of Fluid Mechanics, Volume 58. (Page 8, Figure 5b).

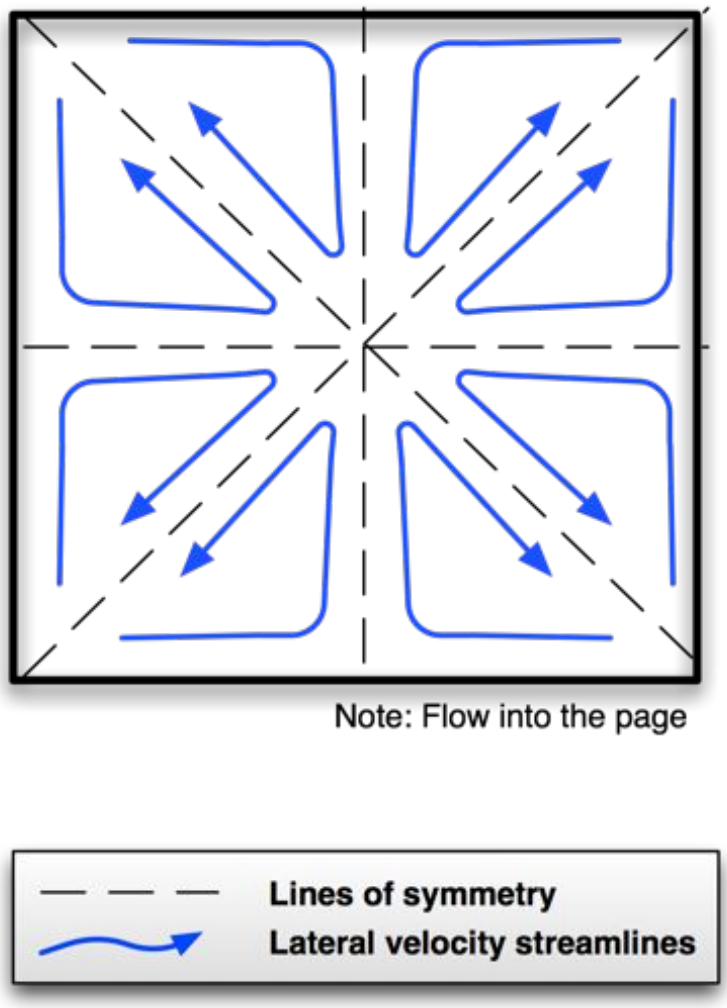

Figure 2-5. Isovel streamlines induced by turbulent channel flow, adapted from Brundrett & Baines (1964).

CHAPTER 3
LITERATURE REVIEW

Past channel and impedance eduction studies and alternative facility details are reviewed with an aim to demonstrate prior achievements and undertakings to clearly establish the fit and necessity of the current facility within the scientific community. This review is divided into three sections: channel flow studies, acoustic liner impedance eduction techniques, and finally a review of known facilities. Section 3.1 outlines channel flow studies and compares them with regards to flow physics and test conditions. Impedance eduction techniques are reviewed in Section 3.2 comparing accuracy, inherent assumptions, and the physical setup of each method. Section 3.3 concludes the chapter with a survey of both past and contemporary facilities used for acoustic liner impedance testing, including a comparison of sizes, achievable velocity range, and sound excitation pressure levels.

3.1 Channel Flow Studies

Due to the inherent rectangular cross section geometry and the speed range of the GFID, a thorough investigation of past turbulent channel flow studies is presented. The significance of turbulent channel flow stems from the differences and possible challenges for which flow through an enclosed duct manifests in contrast to the flow in a full-scale engine for which the facility aims to replicate. The facilities reviewed herein are limited to to those capable of applicable Reynolds and Mach numbers with rectangular geometries similar to the proposed facility.

Considerable knowledge of channel flow physics has been obtained since the inception of the discipline in the late 1920's. Channel flow studies can be broadly categorized by the individual study's end goal. Emerging patterns of three chronological themes appear in regards to experimental channel flow: the identification and measurement of secondary flow patterns, the investigation of the origin of the secondary flow and a shift to high

Reynolds number flows, and finally scaling arguments applicable to turbulent channel flow. A comparison and review of each study is presented with a summarizing table.

3.1.1 Identification and Measurement of Secondary Flow in Channels

Initial experiments on channel flow began unknowingly in 1926 by J. Nikuradse who observed through flow visualization a "waviness" of the lateral velocity in a $(3.5:1)$ aspect ratio rectangular duct. Prandtl, Nikuradse's advisor, postulated the waviness was due to an imbalance of pressure stemming from the presence of the corners which generated a cross-axis secondary velocity component (Hoagland 1960).

Fage (1936) examined the difference in pressure drop between rectangular and circular ducts of equal hydraulic diameter. Through his work measuring streamwise pressure gradients, Fage observed the non-isotropic nature of the turbulent field unique to flow in rectangular ducts (Howarth 1938).

Laufer (1948) performed further channel flow investigations through detailed hot-wire experiments at Reynolds numbers of hydraulic $O(10^4)$. Laufer's tests were carried out in $(12:1)$ aspect ratio channel. Fluctuating velocities were measured to allow for comparison of turbulent energy and length scales across the channel. As hot-wire anemometry was still in its infancy at this time, much of the author's experiments were simply to prove the efficacy of hot-wire as a measurement tool.

From discovery to the initial measurements of the secondary velocity field, Nikuradse, Fage, and Laufer laid the initial groundwork for future fluid dynamic experiments of channel flow. Table 3-1 describes the contributions and specifications of each experimental effort. In an effort to directly compare the studies, the test Reynolds numbers and measurement technique are included. Because Reynolds number can be based on several length and velocity scales, values were recast based on the average, or bulk, velocity, U_b, and the hydraulic diameter, D_h,

$$Re_{D_h} = \frac{U_{av} D_h}{\nu}. \tag{3–1}$$

The hydraulic diameter is defined as a function of the cross-sectional area of the channel, A, and the wetted perimeter, P,

$$D_h = \frac{4A}{P}. \tag{3–2}$$

In studies where the centerline velocity, U_{CL}, was specified in lieu of the average velocity, the approximation $U_{av} = 0.79\, U_{CL}$ proposed by Hoagland (1960) was applied.

3.1.2 Origins of Secondary Flow and High Reynolds Number Studies

After Laufer, there was a paradigm shift from simply being able to measure secondary flows to attempting to explain the origin of the flow patterns through accurate experiments. Hoagland (1960) and Brundrett & Baines (1964) performed thorough experimental investigations using a combination of hot-wire anemometry and pitot tubes. Hoagland's results verified Prandtl's theory of the shape of secondary flow contours, or isovels as an octet set with flow toward the centerline along the diagonal symmetry planes. He concluded that the secondary flow was not caused by an imbalance of pressure and shear, as Prandtl had theorized, but instead by shear gradients at the walls. Brundrett and Baines disagreed with Hoagland on the source of the secondary flow. Their investigation led them to conclude the source of the secondary flow velocity was due to turbulent Reynolds stress near the boundaries. As turbulent Reynolds stress is inherent only to turbulent flow regimes, so to are the secondary flow patterns they generate. They demonstrated via hot-wire anemometry that vorticity production is zero along geometric symmetry lines in a cross-duct plane.

Gessner & Jones (1965) performed hot-wire experiments up to $Re_{D_h} = 3E5$, the highest of any previous study. Their results supported the hypothesis of Brundrett and Baines that the imbalance of turbulent Reynolds stress and lateral static pressure within the duct ultimately induced secondary flow in rectangular channels. The authors also found that shear stress can be considered constant across the duct walls, except in the immediate vicinity of the corner where skewness is highest.

Melling & Whitelaw (1976) subsequently experimentally investigate high Reynolds number channel flow physics. The use of a non-intrusive 2-D laser Doppler velocimetry (LDV) system enabled fluctuating velocity measurements to be made without the alignment and interference issues associated with hot-wire and pitot tube probes. Their results confirmed the prior experimental findings of Gessner & Jones (1965). The use of LDV allowed for similar sample rates and better near wall resolution than hot-wire without the alignment issues common to other methods.

3.1.3 Channel Flow Scaling Arguments

The third major chronological theme revolves around scaling arguments for channel flow. Scaling arguments are often applied in fluid mechanics applications to establish universal equations or models for prediction of engineering quantities such as shear stress and heat transfer. The CFD community uses scaling laws for faster and more robust models and numerical validation.

Leutheusser (1984) performed scaling analysis in turbulent channel flows by applying published data to "Law of the Wall" curve fits for parameter extraction of Equation 2–24, previously discussed in Chapter 2. The author noted that the relation does not match experimental data at distances as far from the wall as that of flow under a zero pressure gradient. Similar power law fits were not able to be applied successfully.

Wei & Willmarth (1989) used a 2-D LDV system to establish Reynolds number scaling of turbulent quantities within channel flow. Noting that most previous studies assumed that within the "inner" region, up to $y^+ < 100$, there existed a Reynolds number independent scaling. The authors demonstrates this assumption is inaccurate, and showed that the maximum value of turbulent intensity profiles was found to increase with Reynolds number. The authors claim that inner law scaling can be demonstrated within $y^+ < 15$ for streamwise velocity fluctuations, although wall-normal fluctuations cannot be scaled using inner variables, which were attributed to the presence of the neighboring walls and vorticity stretching.

Because many of the numerical channel flow studies center on low Reynolds number flows or investigate transitional flow with secondary flow development, these are beyond the scope of the current research. However, Anselmet *et al.* (2009) numerically investigated the development of the ratio of centerline to bulk velocity, U_c/U_b for turbulent channel flow from $Re_{Dh} = 5E3 - 3E4$ for rectangular duct flow of three aspect ratios: $(1.875:1)$, $(1.43:1)$ and $(1:1)$. Noting for the majority of internal flow research that through non-dimensionalization of U_c/U_b, laminar flows through circular pipes and high-aspect ratio 2-D channel flows, the data could collapse via a single function; however a similar collapsing function for noncircular turbulent duct flows had yet to be devised. The authors compared their numerical results with experimental data extracted from the literature, including previously discussed (Melling & Whitelaw 1976). They were able to collapse all of the available data by plotting U_c/U_b, vs $(x/D_h)\,/\,(U_b x/\nu)^{1/5}$ resulting in a slope of 0.185 up to the point of maximum U_c/U_b. While not only defining a useful comparison for new facilities, they were also able to better established a definition for entrance length for aspect ratios less than $(13:1)$ based on measurable quantities for internal turbulent flows. Additionally, these results were established in the absence of including secondary flow effects in their numerical simulations, noting the weak influence of secondary motion on the centerline velocity.

Table 3-1 summarizes turbulent channel flow studies. Via the evolution of turbulent channel flow investigations, an understanding of the underlying assumptions provide checks and aided in the testing and design of the GFID in Chapter 5. Scaling arguments can be used for non-dimensionalizing the channel's developing boundary layers, and streamwise pressure gradients are measured to ensure fully developed flow. With a characterized facility in place, the impedance of an acoustic liner under grazing flow is measured. A review of the current eduction methods are summarized below.

3.2 Impedance Eduction Techniques

Accurate impedance measurements of acoustic liners under grazing flow conditions are vital to effectively reduce aircraft engine noise. Several methods have been developed to determine liner performance characteristics. This section will investigate the techniques used for impedance eduction of locally reactive liners. Many of the techniques are tied closely to the facility in which they are used, as detailed in Section 3.3. The techniques are presented with details concerning the specific method for impedance eduction as well as the underlying assumptions associated with the method.

3.2.1 The *In-situ* Method

Dean (1974) presented a direct technique for measuring the impedance of a liner that has become widely used due to the relative ease of the measurement. An illustration of this method, designated the *in-situ* method due to the intrusive manner of which the microphones are installed, is found in Figure 3-1. This technique is popular due to the relative ease of the experimental setup requiring only two microphones to accurately educe impedance of a locally reactive acoustic liner. The first microphone is flush-mounted with the surface of the liner within the channel subject to grazing flow conditions. The second microphone is mounted within a reactive cavity measuring the pressure of the specific cell under analysis.

The mathematical background of the method will be outlined and relies on the basics of linearly reactive acoustics shared amongst many of the impedance eduction methods. The method is formulated by applying the definition of specific acoustic impedance as the ratio of the acoustic pressure, P, to the acoustic particle velocity, u, at a point.

$$Z = \frac{P_A}{u_A} \tag{3–3}$$

P_A denotes the measured pressure outside of the cavity along the duct wall, as illustrated in Figure 3-2. The particle velocity, u_A, is assumed to be a function of the pressure measured within the cavity, P_B, angular frequency, ω, and the cavity depth, ℓ, of the form

$$u_A = \frac{P_B}{\rho c} i e^{i\omega t} sin(\kappa \ell). \tag{3–4}$$

Substituting Equation 3–4 into Equation 3–3, the impedance can be written in terms of the measured SPL and phase angle between P_A and P_B, ϕ,

$$Z = 10^{\left(\frac{SPL_A - SPL_B}{20}\right)} \frac{\sin\phi - j\cos\phi}{sin(\kappa\ell)}. \tag{3–5}$$

The impedance can be decomposed into real and imaginary components, $Z = R + iX$.

$$R = 10^{\left(\frac{SPL_A - SPL_B}{20}\right)} \frac{\sin\phi}{sin(\kappa\ell)} \tag{3–6}$$

and

$$X = 10^{\left(\frac{SPL_A - SPL_B}{20}\right)} \frac{\cos\phi}{sin(\kappa\ell)} \tag{3–7}$$

The impedance at a point on the liner is the combination of cavity reactance, Z_c, and the surface impedance, Z_s. A single cavity is a closed end tube and thus the impedance, sans resistive losses, is expressed as

$$Z_c = -i\cot(\kappa\ell). \tag{3–8}$$

The surface impedance can now be expressed as a function of the facesheet resistance, R_{fs}, and facesheet reactance (often called mass reactance), X_{fs}, as

$$Z_s = Z_{fs} + Z_c = R_{fs} + iX_{fs} - Z_c. \tag{3–9}$$

Thus the surface impedance is

$$Z_s = R_{fs} + i\left(X_{fs} + \cot(\kappa\ell)\right). \tag{3–10}$$

Hydrodynamic pressure fluctuations can be much larger than the acoustic pressures and as a result the *in-situ* method is limited to grazing flow speeds less than 100 $^{ft}/_{s}$ (30 $^{m}/_{s}$). An obvious downside of using this method is the inherent destruction of the

sample under test due to microphone installation. As described, the method is only applicable to single degree of freedom (SDOF) liner.

3.2.2 Infinite Waveguide Method and Single Mode Method

Armstrong (1974) introduced the "infinite waveguide" method, avoiding any damage to the sample by flush-mounting a microphone in a traversable section on the duct wall opposite the sample. The infinite waveguide method assumes a single dominant mode plane progressive wave within the duct and thus large errors occur if multiple modes are are of near-equivalent magnitude, including reflections from a non-ideal exit termination or evanescent modes generated at the leading and trailing edges of the installed liner. The flow is also assumed to be non-turbulent and uniform across the duct and the liner of unknown uniform impedance. If a single acoustic mode is present over the liner, both the measured SPL and phase at the center of the liner will be linear, indicating a constant impedance value, as illustrated in Figure 3-3.

The infinite waveguide method extracts the impedance of a liner by comparing two microphones. The first is a stationary microphone mounted at the entrance plane of the liners leading edge. The second microphone is traversed along the opposing wall from the reference microphone over the liner. The attenuation between the two microphones is measured and the wavelength is inferred from the data during post-processing as a function of downstream distance.

Jones *et al.* (2001) applied the "infinite waveguide" method under the name "Single Mode Method" (SMM) to distinguish between a comparison method within the same paper capable of handling multiple modes called the the Finite Element Method, discussed below in Section 3.2.3. They also outline a method in a simpler form than Armstrong's that is more applicable to experiments. This method is outlined here.

The axial wavenumber, κ_x, can be decomposed into real, κ_{xr}, and imaginary parts, κ_{xi}, described by Armstrong as the phase velocity parameter and attenuation parameter,

respectively. The dissipation of acoustic within a duct is described by

$$\left|\frac{P(0)}{P(x)}\right| = e^{\kappa_{xi}x} \tag{3–11}$$

and further cast as acoustic power,

$$20\log\left(\left|\frac{P(0)}{P(x)}\right|\right) = 20\log\left(e^{\kappa_{xi}x}\right). \tag{3–12}$$

Note that the left side of Equation 3–12 is already defined in units of dB and therefore can be simplified and written as

$$dB = \kappa_{xi}x20\log\left(e\right). \tag{3–13}$$

Equation 3–13 is solved for the axial wavenumber as a function of the drop in acoustic power per unit distance,

$$\kappa_{xi} = \frac{1}{8.68}\frac{dB}{x}.. \tag{3–14}$$

The analysis of the attenuation parameter is cast in more general terms in combination with the phase velocity

$$\kappa_x = \frac{d\phi(x)}{dx} + \frac{i}{20\log_{10}(e)}\frac{d\mathrm{SPL}(x)}{dx}. \tag{3–15}$$

The axial wavenumber can be assumed constant over the center of the liner and be extracted from the measured SPL and phase decay as measured at discrete microphone locations. The model is only valid for frequencies up to the cut-on frequency, therefore from Equation 2–5 both n and $\kappa_z = 0$. The ratio of transverse wavenumber to the drive wavenumber, κ_y/κ, is a function of axial wavenumber, κ_x, and the mean Mach number, M,

$$\frac{\kappa_y}{\kappa} = \left(\frac{1-\left[(1-M)^2\left(\frac{\kappa_x}{\kappa}\right)+M\right]^2}{(1-M)^2}\right)^{1/2}. \tag{3–16}$$

Equation eq:Ch$_{3S}MM_kyisderivedinAppendixC.Notethatthe^1/_2powerwasabsentfromJoneset\ al.$ (2001), b

$z/\rho_0 c_0$ measured over the central region of a liner under is

$$\zeta = -i\left(\frac{\kappa}{\kappa_y}\right)\left[1-M\left(\frac{\kappa_x}{\kappa}\right)\right]^2\cot\left[2\kappa h\left(\frac{\kappa_y}{\kappa}\right)\right], \tag{3–17}$$

where h, is the duct half-width.

Armstrong (1974) applied his version of the method successfully over a frequency range of $1000 - 2500\,Hz$ and speed of $M = 0.5$. Tests at higher speeds proved difficult to extract the impedance as the uniform flow assumption was invalidated by high shear gradients.

3.2.3 Finite Element Method

In an effort to develop a technique that is less restrictive than the infinite waveguide method and less intrusive than Dean's method, Watson *et al.* (1995) developed a finite element modeling (FEM) method.

An assumed solution to the convective wave equation, Equation 2–13, is iteratively established. The solution procedure matches the experimentally obtained complex pressure amplitude and phase distribution along the duct using the boundary conditions at four duct planes: the source plane, the exit plane, the rigid wall, and the acoustic liner surface.

The source plane boundary condition,

$$p(x = 0, y) = p_s(y), \tag{3–18}$$

is defined at the leading edge plane of the acoustic liner under test and is measured by a stationary reference microphone.

The exit plane, defined at the trailing edge plane of the acoustic liner under test, is a function of the test Mach number, wavenumber, and normalized exit impedance, ζ_{exit},

$$\frac{\partial p(L, y)}{\partial x} = \frac{-i\kappa p(L, y)}{M + \zeta_{exit}}. \tag{3–19}$$

The normalized exit impedance is measured between the test section and the near-anechoic termination during testing. The method was later updated to require only the exit pressure in lieu of the exit impedance (Watson *et al.* 2008).

Between the source and exit planes, the method iteratively solves for the liner impedance by matching the boundary conditions for the rigid wall of zero particle velocity,

$$\frac{\partial p}{\partial y} = 0, \tag{3–20}$$

and the unknown acoustic liner

$$\frac{\partial p(x,0)}{\partial y} = \frac{i\kappa p(x,0)}{\zeta} + 2M\frac{\partial}{\partial x}\left[\frac{p(x,0)}{\zeta}\right] + \frac{M^2}{i\kappa}\frac{\partial^2}{\partial x^2}\left[\frac{p(x,0)}{\zeta}\right]. \tag{3–21}$$

The FEM code assumes a uniform flow profile (slug profile) and thus can be limited by high shear regions near the walls. This method was validated against experimental results (Watson *et al.* 1996) and later optimized (Watson *et al.* 1998). Eversman & Gallman (2009) used a similar FEM model but extend the search parameters to include an effective Mach number and termination impedance to account for shearing and reflection effects. Jones *et al.* (2005) at NASA LaRC released benchmark data for comparison of alternative impedance eduction methodologies.

Jones *et al.* (2001) found that under the correct circumstances of linear sound pressure and phase decay rates across the liner length, the SMM method produced impedance values identical to the FEM model and suggested when appropriate that the computational cost benefits of the SMM model make it a preferable choice.

3.2.4 Finite Element Method with Shear

Many of the models presented in this review assume a uniform flow. Pridmore-Brown (2006) noted that for accurate impedance eduction, the effect of mean shear should be accounted for and neglecting this effect could result in impedance errors of up to 10%. To such an end, a new finite element method with shear (FEMS) code was devised by Watson *et al.* (2001) which accounted for shear effects by means of a cross duct velocity profile, $^{dM}/_{dy}$, and solving the linearized conservation of energy,

$$i\kappa P = M\frac{\partial P}{\partial x} + \rho_0 c_0\left[\frac{\partial U}{\partial x} + \frac{\partial V}{\partial y}\right] = 0, \tag{3–22}$$

the streamwise momentum,

$$i\kappa U = M\frac{\partial U}{\partial x} + \frac{1}{\rho_0 c_0}\frac{\partial P}{\partial x} + \frac{dM}{dy}V = 0, \tag{3–23}$$

and transverse momentum equations,

$$i\kappa V M\frac{\partial V}{\partial x} + \frac{1}{\rho_0 c_0}\frac{\partial P}{\partial y} = 0. \tag{3–24}$$

In the above equations, U and V represent the time-averaged streamwise and transverse velocities, respectively. These equations are solved under similar boundary conditions to the FEM model with an additional constraint for defining the velocity profile at the source plane. The impedance of the liner is attained through iteratively matching the calculated rigid wall pressure to the measured pressure on the rigid wall while matching the liner boundary condition,

$$-\rho_0 c_0 V = \left(1 + \frac{M}{ik}\frac{\partial}{\partial x}\right)\left[\frac{P}{\zeta}\right]. \tag{3–25}$$

In the FEMS method, it is assumed that a transverse variance in shear exists due to the no slip condition and thus cross duct velocities are required as an input (Jones *et al.* 2003).

The FEMS model was demonstrated to work especially well for single mode tests. It was shown that for a single frequency plane progressive wave, the shear effect used in the FEMS model produced higher resistance values than the uniform assumption of the FEM model, though the reactance was found to be virtually identical.

3.2.5 Inverse Semi-Analytical

Elnady *et al.* (2009) presented a simple mode matching scheme referred to as the "inverse semi-analytical technique" (ISA). The method relies on the measurements of four microphones, two upstream (A and B) and two downstream (C and D) of the acoustic liner section. Using a multimodal approach, the test section is divided into three regions: upstream of the liner, over the liner, and downstream of the liner.

An upstream reflection coefficient defined as a function of the upstream transfer function, H_{AB}, the microphone separation distance, s, and the axial wavenumber, κ,

$$R_B = \left(\frac{1 - H_{AB}\dot{e}^{j\kappa_{(+)}s}}{H_{AB}\dot{e}^{-j\kappa_{(-)}s} - 1} \right), \tag{3–26}$$

is used to calculate the amplitude of the dominant right-running mode,

$$a_+^{(1)} = \left(\frac{p_B}{1 + R_B} \right) e^{-j\kappa_{(+)}z_B}. \tag{3–27}$$

a distance Z_B from the leading edge of the liner.

Similarly, a downstream reflection coefficient is defined as a function of the downstream transfer function and the independently measured exit impedance, z_D,

$$R_e^{(1)} = \left(\frac{1 - H_{CD}e^{j\kappa_{(+)}s}}{H_{CD}e^{-j\kappa_{(-)}s} - 1} \right) e^{-j(\kappa_{(+)}\kappa_{(-)})z_D}. \tag{3–28}$$

$a_+^{(1)}$ and $R_e^{(1)}$ are the only inputs to a matrix of amplitudes and mode shape at the leading and trailing edge planes of the liners. The impedance is extracted once the educed pressure field iteratively converges to match the measured modal content under the prescribed boundary conditions. The method also assumes a uniform flow profile and thus increased error is found with high shear flows. The method compared favorably with NASA benchmark data results (Elnady *et al.* 2009).

3.2.6 Grazing Flow Data Analysis

Similar to the original NASA model, a three part FEM model for liner impedance eduction was formulated called the Grazing Flow Data Analysis (GFAZ) program, for use at the former Boeing Wichita facility, now Spirit AeroSystems. The method is based on a microphone traversing along the centerline of the upper wall, opposite the liner under test. Assuming a non-reflective termination condition and a uniform flow assumption, the GFAZ model claims to be capable of solving for up to eight simultaneous propagating modes. Initially, a frequency response function (FRF) based on a pressure field calculated from an assumed impedance value is generated. The impedance value is iterated and

a new pressure field is calculated until the iterated FRF matches the measured FRF from the traversing microphone to within a set tolerance (Gallman & Kunze 2002). The method solves the three regions, upstream, downstream, and across the liner, separately and then matches conditions at the shared boundaries. This process comes at an inherent computational expense.

3.2.7 The Straightforward Method

Many of the eduction methods presented here, such as the FEM, FEMS, GFAZ, and similar numerical schemes are classified as "inverse methods", which use measured pressure at known locations and an assumed pressure field to converge on a solution in order to extract characteristics of the boundary conditions, such as impedance. These methods are computationally expensive but are generally more robust and less restrictive than the alternatives, such as the *in-situ* or infinite waveguide methods (Jing *et al.* 2008).

In contrast, the "straightforward" method, presented by Jing *et al.* (2008), extends the "infinite waveguide" by fitting the measured pressure field over an acoustic liner to a series of equations. As an alternative to the restrictive assumption of linear phase and SPL decay of Equation 3–15, the measured pressure field, $p_u(x, y)$, is assumed to a sum of complex exponentials. Representing left and right running waves as a function of the axial ,$\mu_n^{\pm}$, and transverse wavenumbers, $\beta_n^{\pm}$, as well as complex model amplitudes, $A_n^{\pm}$, the pressure field is defined as

$$p_u(x, y) = \sum_{i=1}^{N} A_n^+ \cos\left(\beta_n^+ y\right) e^{-i\mu_n^+ x} + A_n^- \cos\left(\beta_n^- y\right) e^{-i\mu_n^- x}. \tag{3–29}$$

The axial wavenumber is extracted from Equation 3–29 and then Equations 3–16 and 3–17 are used obtain the to transverse wavenumber and impedance, respectively.

Ideally, any axial wavenumber will allow for impedance extraction, however in practice, a single dominant forward traveling mode provided the higher accuracy. The authors note that unlike other methods which may be sensitive to, or even fail in the presence of upstream reflections, the straightforward method only relies on the dominant

mode wavenumbers. As a result, the method is independent of reflected upstream propagating waves, relaxing the requirement for costly anechoic terminations. This technique performed well compared to the NASA benchmark data (Jing *et al.* 2008).

3.2.8 Laser Doppler Velocimetry Impedance Eduction

Instead of measuring the acoustic pressure within a duct or at the surface of a liner to infer the liner impedance, Minotti *et al.* (2008) demonstrated a laser Doppler velocimetry (LDV) technique to measure particle displacement.

The authors state that particle displacement, derived from instantaneous velocity measurements, reduces error when a highly viscous flow is present. Measurements of particle velocity are used to extract the particle displacement by solving a system of equations relating the acoustic velocity to the acoustic displacement for each coordinate direction.

$$V_{ref\,x}\frac{\partial \chi_x}{\partial x} + i\omega\chi_z = \mathcal{V}'_x + \frac{\partial V_{ref\,x}}{\partial y}\chi_y + \frac{\partial V_{ref\,x}}{\partial z}\chi_z \tag{3–30}$$

$$V_{ref\,x}\frac{\partial \chi_y}{\partial x} + i\omega\chi_y = \mathcal{V}'_y \tag{3–31}$$

$$V_{ref\,x}\frac{\partial \chi_z}{\partial x} + i\omega\chi_z = \mathcal{V}'_z \tag{3–32}$$

The acoustic impedance is then described as

$$Z_n = \frac{p'}{i\omega\chi_n} \tag{3–33}$$

as a function of the time-harmonic pressure, p', and the acoustic displacement of a particle, χ_n, where $n = 1:3$ representing the three cartesian directions.

The LDV signal is referenced to an upstream cone-mounted microphone in the flow to interpret phase information during post-processing, discerning acoustic fluctuations from similar random fluctuations of the turbulent flow. The experiment was limited to 25 $^{m}/_{s}$.

Impedance values were compared to measurements made using Dean's *in-situ* method at three streamwise locations. Similarly, power spectra was compared between the LDV

method and those of an embedded microphone. Both the impedance and spectra results were in good agreement.

All of the previously described methods have focused on impedance eduction techniques by measuring the acoustic pressure or particle displacement near or within the liner section. However, there are two techniques that use different methodologies for liner impedance, using insertion loss and bias flow. While other studies not described here may also demonstrate similar strategies, the two presented, utilized by B.F. Goodrich and General Electric Aircraft Engines, are specifically geared toward design and testing liners for engine nacelles.

3.2.9 Insertion Loss Method

The Insertion loss method (ILM) used by B. F. Goodrich for liner impedance eduction is inherently tied to the facility for which it is employed (Syed *et al.* 2002). The facility, illustrated in Figure 3-4, is further described in Section 3.3. Testing is accomplished by monitoring the ratio of sound pressure levels in upstream and downstream reverberation chambers. Loudspeaker acoustic sources are placed within the upstream chamber. The assumed diffused acoustic fields in each chamber allow for a single measurement of the frequency dependent sound pressure level, $SPL_U(f)$ and $SPL_D(f)$ for upstream and downstream, respectively. The reduction of acoustic power due to the liner, , is defined by the difference in the hard walled "calibration" case and a liner of unknown impedance.

$$IL\ dB(f) = SPL_U(f) - SPL_D(f) \tag{3–34}$$

$$\Delta PWL\ dB(f) = [IL\ dB(f)]_{\text{liner}} - [IL\ dB(f)]_{\text{hard wall}} \tag{3–35}$$

The calibration case defines the coefficients of a 2-D multimodal propagation technique and iteratively solves for insertion loss based on an assumed impedance. The liner impedance is correct when the calculated IL matches the measured IL to within a specified tolerance.

3.2.10 Flow Resistance Method

The dc flow resistance method (FRM) utilized at General Electric is capable of finding the resistance of a perforate or wire-mesh sheet which would normally cover a locally reactive liner (Syed *et al.* 2002). A positive or negative pressure differential is applied across the material section with a superimposed grazing flow along the surface. Through this method the flow resistance is calculated as the ratio of the pressure drop across the sample to the bias flow velocity through the sample Jones *et al.* (2003). Assuming the test sheet is thin, the flow resistance of the liner can be assumed to be equivalent to acoustic resistance. While this method provides fast resistance values, its does not provide insight to the reactance nor any frequency dependence, as no acoustic source is present. This method does however implicitly account for a boundary layer induced by the grazing flow over the liner.

3.2.11 Impedance Eduction Method Summary

The available impedance eduction methods described above can be sorted into three categories: waveguide methods, inverse techniques, and non-traditional methods. The waveguide methods include the infinite waveguide, also known as the SMM, and the more advanced straightforward method. Both assume a fitting function applied to the attenuated complex pressure from which impedance is extracted. Inverse methods, such as the FEM, FEMS, GFAZ and inverse semi-analytical are becoming more popular due in part to increased computations speeds. The remaining non-traditional techniques explore and demonstrate alternative methods for which impedance can be educed, but restrict run conditions. Based on the preceding review, the SMM was chosen for initial application in the GFID due to the balance of simplicity in setup and quickness in educed solution and relative accuracy. The restrictions of the method are accounted for through the use a near-anechoic termination to minimize upstream propagating acoustics and initial low run speeds to better approximate a uniform flow assumption. The modular nature of the facility and the active research in a university setting allow for alternative methods to

easily be applied for future research. Experimental impedance eduction of an acoustic liner under flow is demonstrated in Section 5.4.4.

3.3 Experimental Acoustic Liner Impedance Test Facilities

Toward the project goal of designing an acoustic liner grazing flow test facility for impedance eduction measurements, a look at the underlying components that make up that facility have been investigated. Section 3.1 outlined experimental studies specifically relating to the nature of the flow inside of rectangular channels. Section 3.2 presented the available techniques used to directly or indirectly educe the impedance of an acoustic liner. The section will investigate all past and present experimental flow facilities which were used for liner impedance measurements.

The GFID is part of a university environment, and thus the funding sources, knowledge gained, and publication expectations are different than for a private company. Similarly, international facilities are separated to highlight what is currently available in the US, which is generally easier from a collaboration standpoint. To such effect, the following reviewed facilities, categorized by affiliation, fall into one of four possible groups: international, private industry, educational institutions, and government research facilities.

A total of 19 facilities were found through a thorough literature search. However some are assumed to no longer be in working order or no longer used for impedance measurements. Many facilities share common features, sizes, and run conditions. Some of the facilities have been illustrated at the end of the chapter for visualization purposes to demonstrate the wide range of possible design implementations. Table 3-3 lists all the tunnels, organized by affiliation, listing cross-section sizes for direct comparison.

3.3.1 International Facilities

The first set of facilities investigated are those found outside the United States. A total of five international facilities were found at both the educational (two) and government institutions (three).

University of Maine, France

The University of Maine in La Mans, France operates a flow duct, illustrated in Figure 3-5. The $15 \times 100\,mm$ ($0.59 \times 3.94\,in.$) cross-section duct is fed by an upstream compressor generating flow speeds up to $M = 0.3$ and controlled via feedback from an inline flow rate meter. The tunnel has an anechoic termination at each end of the duct (Auregan & Leroux 2008). Acoustic excitation up to 140 dB between $70 - 3000\,Hz$ is generated by two loudspeakers. Leading edge microphones are positioned $2\,m$ downstream from the compressor to allow for flow development prior to testing (Auregan *et al.* 2004).

National Aerospace Laboratory, The Netherlands

The National Aerospace Laboratory (NLR), an independently-funded technological institute in the Netherlands, maintains the Acoustic Flow Duct facility for acoustic liner impedance studies. The tunnel is a reverberation style facility, similar to the tunnel at Goodrich, both using the insertion loss method for global impedance eduction (Murray *et al.* 2005). Local impedance values are measured via Dean's method. Acoustic excitation via four electrodynamic speakers generate sound pressures of $150\,dB$ up to $6\,kHz$ and test speeds up to $M = 0.8$ are achievable over the $1.05\,m$ long duct with a $150\,mm \times 300\,mm$ ($5.9\,in. \times 11.8\,in$) cross-section. The flow is driven by a downstream vacuum line capable of displacing $14.7\,{}^{kg}/_{s}$ of air (Murray *et al.* 2005).

French national aerospace center, ONERA, France

The French national aerospace center, ONERA, operates the Aero-Thermo-Acoustic Bench (B2A) for acoustic liner measurements, illustrated in Figure 3-6. The blowdown tunnel is capable of $M = 0.5$ flow at temperatures up to $570\,K$ within the $4\,m$ long test section with a $50\,mm \times 50\,mm$ ($1.97\,in. \times 1.97\,in.$) cross-section. The high temperatures are managed by using stainless steel walls and silica optical windows throughout the facility. The optical access allows for impedance measurements via LDV through the dual-window setup. A pair of upstream loud speakers enclosed in pressured chambers provides high sound pressures of $140\,dB$ in the frequency range of $300 - 3000\,Hz$. The tunnel terminates

into a sound proof room via an exponential horn providing a quasi-anechoic termination with reflection coefficients less than 0.2 up to $M = 0.3$. Acoustic liners with up to 100 mm thick can be tested in the lower wall while 10 static pressure ports and two thermocouples record flow conditions (Lavieille *et al.* 2006).

German Aerospace Center, DLR, Germany

The German Aerospace Center (DLR) maintains the Cold Acoustic Test-Rig for liner impedance testing. The tunnel can run in either an 80 mm (3.15 $in.$) square cross-section or a 140 mm (5.51 $in.$) diameter cylinder configuration. Maximum speeds of $M = 0.27$ are obtained only in the square section. Two loudspeakers positioned on opposite ends of the centrally located liner test section provide up to 120 dB of sound pressure over the frequency range of $210 - 2110$ Hz. Impedance eduction is accomplished via the insertion loss method. Acrylic windows provide optically clear test section access for optical based measurements. Both ends of the test rig are attached to near-anechoic terminations Richter *et al.* (2008).

Beijing University of Aeronautics and Astronautics, China

Beijing University of Aerospace and Aeronautics (BUAA) maintains a 40 mm (1.57 $in.$) square duct, 2.1 m long and capable of relatively slow run at speeds of 30 $^{m}/_{s}$. Two upstream loudspeakers provide acoustic excitation. Up to two 130 mm long liners can be simultaneously tested Fung *et al.* (2009).

3.3.2 Domestic Corporate Test Facilities

The remaining facilities are all based in the United States. Facilities within the private sector are capable of testing in-house or patented designs not yet released, or not intended, for the public domain. The publications herein referring to specifications of private sector facilities are generally comparison studies of the the facility or the eduction techniques performed within.

Pratt and Whitney

Marsh (1968) performed several tests on a full scale JT3D-3 turbofan engine to establish baseline numbers. Tests were made using a single 1/4 $in.$ microphone 3 $in.$ downstream of the leading edge along with fan discharge SPL levels of 160 dB. SPL levels were then matched at the Pratt & Whitney Aircraft Facility with three configurations: blow-down type compressed air driven with upstream pulsed jet for noise excitation, vacuum pull-down with two electrodynamic speakers, and vacuum driven with pulsed noise. The facility cross-sectional area was 80 $in.^2$ with multiple test section geometries including a 360° circular duct, 180° semicircle, and a 22° wedge. Velocities up to 300 m/s were tested but the primary focus was at 91 m/s to match landing conditions where fan noise dominates engine jet noise.

Boeing - Wichita / Spirit Aerosystems

Spirit AeroSystems, previously known as the Boeing Commercial Airplane Group, Wichita division, operates two flow ducts. The larger of the two is the Boeing Wichita 6 $in.$ × 6 $in.$ Flow Duct, which is 23.5 $ft.$ long. The 48 $in.$ long test section is located 9 $ft.$ downstream from any curves (18 duct diameters). Flow is supplied by either a 100 or 300 psi source to reach flow speeds up to $M = 0.5$ (Gallman & Kunze 2002). An exit nozzle was designed to reduce upstream reflections. The facility is generally used for testing acoustic liner boundary layer growth, including applying a position or negative pressure to the facesheet called transpiration (Drouin *et al.* 2006).

The Spirit AeroSystems 2 $in.$ × 2 $in.$ flow duct is a newer tunnel designed for acoustic liner impedance eduction. Broadband testing up to 3000 Hz and 150 dB is accomplished via electropneumatic drivers. The tunnel is capable of testing flow speeds up to $M = 0.5$ (Gallman *et al.* 2002). Liners up to eight duct diameters long can be tested with a traversing microphones flush mounted in a Teflon strip to reduce leakage opposite the liner at 79 evenly spaced traverse positions (Eversman & Gallman 2009).

General Electric

The Acoustic Laboratory at General Electric Aircraft Engines (GEAE) was specially designed to measure the flow resistance of a perforate or linear wire mesh acoustic liner facesheet. Because only the facesheet of the locally reactive liner is tested, no information regarding the liner impedance reactive component can be assessed. Illustrated in Figure 3-7, the GE flow duct used a bias flow approach where a positive or negative pressure differential can be applied to the liner under test, forcing the air to be "pushed" or "pulled" through the facesheet. By controlling the vacuum pressure a 2.5 $^{m}/_{s}$ blowing or -1.5 $^{m}/_{s}$ suction velocity could be applied to the sample in the 5.5×5.5 $in.$ test section. Speeds were controlled via an upstream high pressure source allowing for free stream run conditions of $M = 0.8$ to be obtained. This facility contained no acoustic sources, and thus only measures the DC flow resistance (Syed *et al.* 2002). The facility has since been moved to the University of Cincinnati.

Goodrich Corporation

The previously described insertion loss impedance eduction technique introduced the flow duct apparatus at B.F. Goodrich as a double-reverberate chamber design. Although not built, this design was originally conceptualized by Melling & Doak (1971). The design was to be ideal for acoustic testing because the acoustic field inside the chambers can be consider "diffuse" and thus only a single microphone is required to measure the acoustic power (Syed *et al.* 2002). Illustrated in Figure 3-4 the liner test section has a $4\,in. \times 5.5\,in.$ cross-section allowing for testing of liner up to $5.5\,in. \times 24\,in.$. The blower driven design allows for testing up to $M = 0.7$.

United Technologies Research Center

United Technologies Research Center (UTRC) recently built and tested their Grazing Flow Facility (GFF) (Simonich *et al.* 2006). The GFF is a 99 $in.$ long duct with a $2\,in. \times 5\,in.$ cross-section. Speeds of $M = 0.65$ are achieved via the UTRC high pressure system. Dual anechoic terminations upstream and downstream maintain low reflection

coefficients. Acoustic excitation is accomplished via two 150 W compression drivers capable of producing 140 dB, and positioned on either sides of the centrally located liner test section. Acoustic liners up to 12 $in.$ in length were tested via Dean's eduction method. Published baseline noise measurements exhibit a zero velocity noise floor of 45 dB and noise floors of 105 dB and 110 dB for $M = 0.36$ and 0.64, respectively.

3.3.3 Domestic University Test Facilities

As the GFID is installed used in a university environment, specific benefits associated with such an environment make it an attractive location for a liner test facility. These benefits include access to joint research endeavors such as computational modeling, or new acoustic liner technologies as well as additional funding sources that may not be available to the private sector or government agencies. At present, only three universities were found to possess similar facilities.

University of Minnesota

The University of Minnesota built a grazing flow facility to test the attenuation of fiberglass over a range of frequencies. Experiments were performed up to velocities of 75 m/s and frequencies within 2060 Hz. The facility was built with 1.5 $in.$ thick PF615 fiberglass bonded to hard wood panels on opposing walls. Pressure measurements were performed with a small condenser microphone every 5 cm centered over the 1 m of the test section (Tack & Lambert 1965).

University of Cincinnati

The University of Cincinnati maintains the Acoustic Liner Flow Duct, but few details are available in the literature. The tunnel has a 3×5 $in.$ cross-section and is capable to run up to $M = 0.7$ via an upstream high pressure source. Liners up to 24 $in.$ long were tested on one or both sides of the 110 $in.$ long flow duct (Hillereau 2004).

Georgia Tech Research Institute

The Georgia Tech Research Institute (GTRI) houses a test center designated the Liner Flow Duct Facility. The facility, shown in Figure 3-8, is capable of performing

impedance eduction measurements in its 2 $in.$ $\times$ 4.7 $in.$ cross-section tunnel with temperatures up to 1200 $^{\circ}F$ (922 K) and speeds near $M = 0.4$ (Ahuja *et al.* 2000). Four upstream acoustic drivers positioned normal to the flow direction provide sound pressure levels up to 120 dB. The flow duct is capable of housing liners in any of its four walls for maximum flexibility. Combination pitot probe and thermocouples measure velocity and temperature upstream and downstream of the liner in four specified measurement planes (Ahuja *et al.* 2000).

3.3.4 Government Facilities

The Flow Impedance Tube at NASA LaRC

One of the original facilities designed specifically for measurements of acoustic liner impedance was the Flow Impedance Tube (FIT) at NASA LaRC. The tube was constructed of four main stainless steel components listed in downstream order: the acoustic source, an air inlet plenum, the test duct with microphone traverse bar, and finally the anechoic termination. The acoustic source used four to five electrodynamic speakers to generate signals up to 140 dB in a 2 $in.$ diameter circular pipe at frequencies up to 3.4 kHz (Parrott & Lester 1980). The sound would propagate downstream through a circular tube with highly resistive perforated walls that acted as a waveguide. The perforate pipe was encased by a large cylinder into which pressurized air was introduced. The air would then be forced through the walls of the perforate pipe and flow downstream, superimposed upon the generated acoustic field. The tube geometry was converted to a square cross-section for the remainder of the duct, 2 $in.$ $\times$ 2 $in.$ across. The duct was constructed of four duct pieces that could be arranged in any order, a total of 128 $in.$ long, or 64 duct diameters. A traverse bar, controlled by a stepper motor, ran the length of the four piece duct section allowing a microphone to traverse over the sample liners. The duct section terminated into an anechoic termination duct of perforated metal walls backed by bulk absorbing material behind perforate metal. The air line emptied to a vacuum for maximum run conditions of $M = 0.5$.

The Grazing Incidence Tube at NASA LaRC

The traverse bar in the FIT was prone to both acoustic and air leakage. In an effort to update the facility, new components were added including a new test section (Jones *et al.* 2004*a*). The improvements led to the facility being renamed the Grazing Incidence Tube (GIT), illustrated in Figure 3-11. The new test section allowed for liner samples to be installed in the ceiling of the duct for easier installation and microphone cable strain relief. The traverse bar was retained but permanently attached in place to reduce leakage. The single traversing microphone was replaced, as the new test section could hold up to 95 stationary microphones with the capability to simultaneous sample 48 at a time. The additional microphones installed off-center allowing for testing past the first higher-order mode (3.37 kHz), up to 10 kHz. The continued use of the traverse bar as a stationary piece however restricted the test section installation position to be upstream of the ducting, reducing control over liner placement as a function of boundary layer development. For additional control, a suction/blowing device was installed on all four walls upstream of the test section. The device was attached to a vacuum pump that would siphon the near-wall boundary layer away, establishing a known starting point for boundary layer development (Jones *et al.* 2005).

The Grazing Flow Impedance Tube at NASA LaRC

Anticipating the retirement of the GIT, NASA LaRC built a new facility with many improvements based on what was learned through three decades of the FIT and GIT. The GFIT, illustrated in Figure 3-12, has a 50.8 $\times$ 63.5 mm cross section and can test acoustic liners up to 50.8 mm to 609.6 mm long. Up to 18 side-mounted speakers can be used together to generate 150 dB single tone. The system is run by an upstream high pressure source in combination with a downstream vacuum allowing for near atmospheric conditions at the test section up to $M = 0.6$. A downstream anechoic termination with locally reactive acoustic liner walls minimizes upstream reflections while simultaneously slowing the flow by increasing the cross sectional area of the duct. The duct also has

a dual-axis traverse pressure probe to measure the internal flow profile to feed into shear-based eduction models (Jones 2011).

The Curved Duct Test Rig at NASA LaRC

NASA LaRC also actively maintains the Curved Duct Test Rig (CDTR), illustrated in Figure 3-13, demonstrating potential future aircraft engine designs by testing liner impedance around a bend. In an effort to eliminate the line-of-sight noise source from the external environment, future engine designs incorporate a shortened engine nacelle allowing for a reduction in size and weight. The CDTR has two main unique contributions to the liner testing community: the facility allows for modal isolation and liner curvature. The facility is capable of measuring up to $3\,kHz$ at $140\,dB$ via dual source locations within a $M = 0.5$ flow (Jones *et al.* 2006) within a test cross-section of $6 \times 15\ in$. The level of curvature is adjustable, offsetting the incoming and outgoing duct by up to one duct diameter.

3.4 Summary

This chapter has presented a review of three areas of research relevant to the design and future testing of the proposed facility. Section 3.1 presented the evolution of turbulent channel flow studies presenting non-dimensional scaling analysis. A look at acoustic liner impedance eduction methods and mathematical models in Section 3.2 presented several available methods in the literature for experimentally educing the impedance of an acoustic liner under flow. Finally, Section 3.3 reviewed all known grazing flow impedance test facilities for comparison. Several elements of the facilities presented were instrumental in the design of the GFID presented in Chapter 4.

Table 3-1. Channel flow studies

Author(s)	Year	Re_{D_h}	Brief description
Nikurdase	1926		First to note secondary flow effects
Fage	1936	$6.9E4$	Found difference in pressure drop between circular vs. non-circular ducts
Laufer	1948	$3.1E4$	Directly measured secondary flow and turbulent energy
Hoagland	1960	$6.3E4$	Experimentally illustrated isovels
Brundrett & Baines	1964	$4.3E4$	Zero vorticity along symmetry lines
Gessner & Jones	1965	$3.0E5$	Secondary flow stems from relationship of Reynolds and static pressure
Melling & Whitelaw	1976	$4.2E4$	Used LDV to verify past results
Ahmed & Brundrett	1971	$1.65E5$	Demonstrated that wall shear stress was best indicator for fully developed channel flow
Leutheusser	1984	Turbulent	Found "Law of the wall" parameters for channel flow
Wei & Willmarth	1989	$4E4$	Inner law scaling is velocity component specific
Anselmet *et al.*	2009	$3E4$	Collapse of entrance region based on centerline velocity

Table 3-2. Grazing flow impedance eduction techniques

Eduction method	Pros	Cons
In-situ	Simple, direct	Intrusive, damaging
Infinite Waveguide/SMM	Simple and fast	Assumes single dominant progressive mode
FEM	Accurate upon convergence	Computationally expensive
FEMS	Accounts for shearing effects	Computationally expensive
ISA	Few inputs needed	Reliance on convergence decreases speed
GFAZ	Can solve up to eight propagating modes	May not match single mode methods for nonlinear liners
Straightforward	Independent of reflecting waves	Assumes uniform flow
LDV	Non-intrusively measures acoustic particle velocity	Particle based flow turbulence increases uncertainly
ILM	Simple and fast results after proper calibration	Broadband only, must calibrate sample
FRM	Can apply a suction or blowing to alter resistance	Resistance value only, must dismantle sample

Table 3-3. Acoustic liner impedance eduction facilities

Liner test facility	Cross-section ($in. \times in.$)	Max flow speed (M)	SPL (dB)
U. of Maine (France)	0.59×3.94	0.3	140
NLR (Netherlands)	5.9×11.8	0.8	150
ONERA (France)	1.97×1.97	0.3	140
DLR (Germany)	3.15×3.15	0.27	120
BUAA (China)	1.57×1.57	0.09	-
P&W	$80\ in.^2$	0.87	160
Boeing Wichita 6x6	6×6	0.5	160
Spirit AeroSystems 2x2	2×2	0.5	150
GE Aircraft Engine	5.5×5.5	0.8	N/A
B.F. Goodrich	4×5.5	0.7	-
UTRC	2×5	0.64	140
U. of Minnesota	2.2×2.2	0.22	-
U. of Cincinnati	3×5	0.7	N/A
GTRI (Georgia Tech)	2×4.7	0.4	120
FIT @ NASA LaRC	2×2	0.5	140
GIT @ NASA LaRC	2×2	0.5	140
GFIT @ NASA LaRC	2×2.5	0.6	150
CDTR @ NASA LaRC	6×15	0.5	140

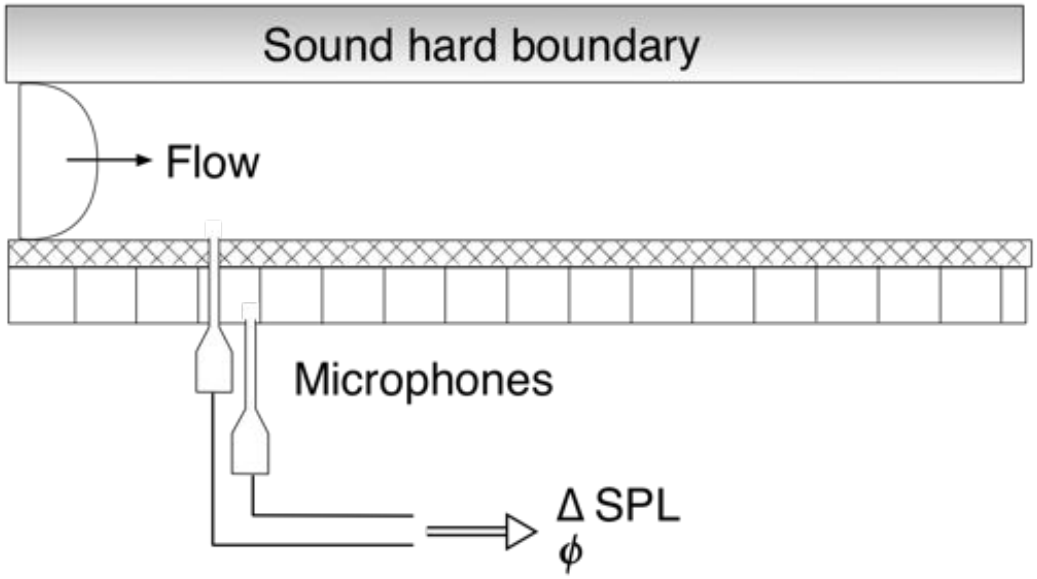

Figure 3-1. Illustration of the general setup for the *in-situ* method, adapted from Dean, P.D. 1974. An In Situ Method Of Wall Acoustic Impedance Measurement In Flow Ducts. Journal of Sound and Vibration. Volume 34. (Page 101, Figure 5).

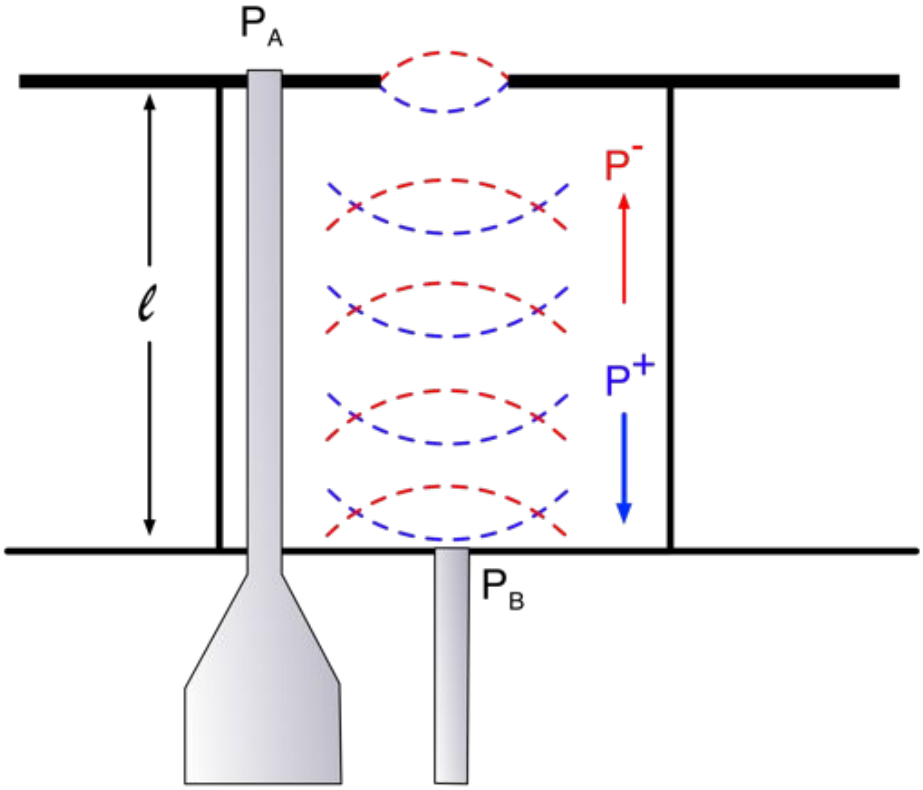

Figure 3-2. Close up view illustrating the assumed pressure field in a locally reactive acoustic liner cell.

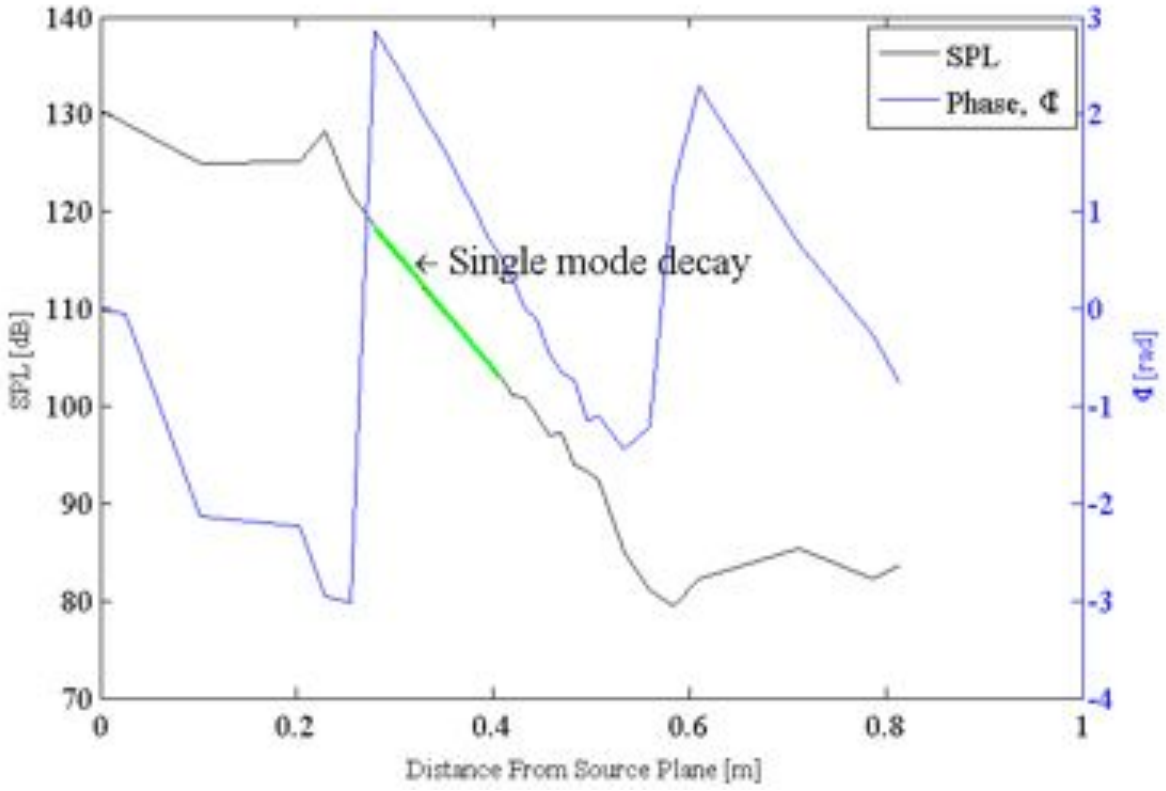

Figure 3-3. Linear SPL and phase decay in the presence of an acoustic liner demonstrated by experimental data from Jones *et al.* (2004*b*).

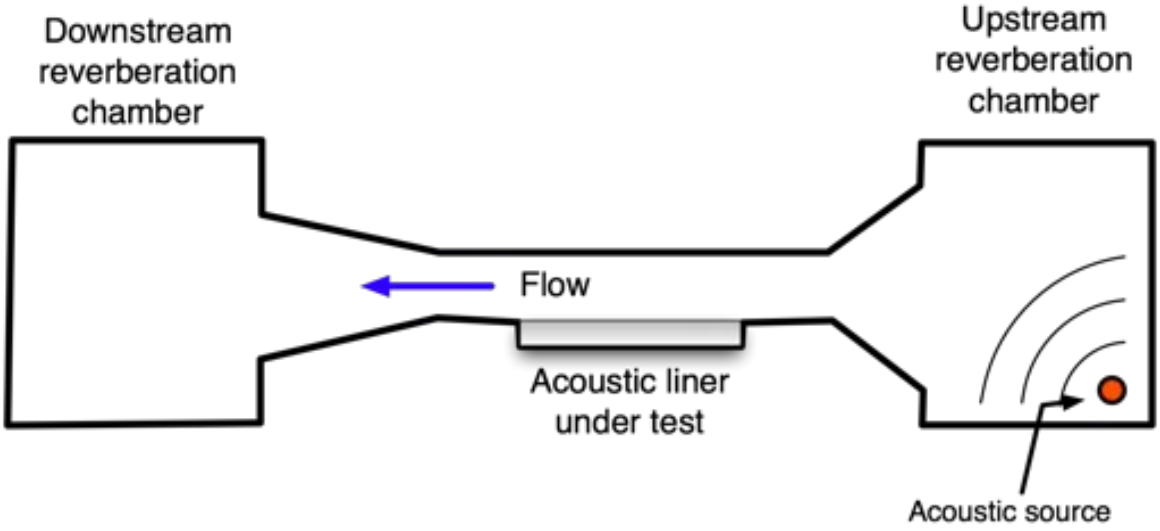

Figure 3-4. The BF Goodrich test facility, adapted from Syed, A. A. et al, 2002. The Steady Flow Resistance of Perforated Sheet Materials in High Speed Grazing Flows. NASA Technical Report NASA/CR-2002-211749. (Page 31, Figure 3).

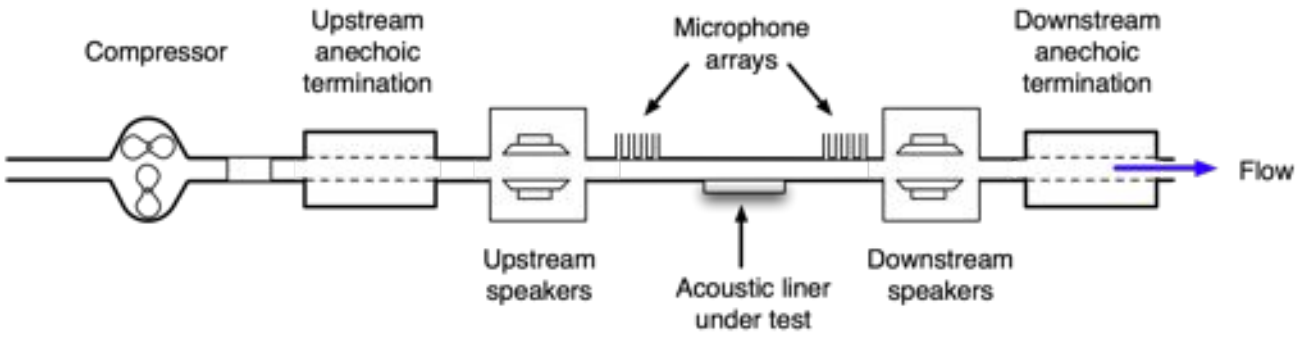

Figure 3-5. The flow duct at the University of Maine, France, adapted from Auregan et al. 2004. Measurement of Liner Impedance with Flow by an Inverse Method. 10^{th} AIAA/CEAS Aeroacoustics Conference. AIAA 2004-2838. (Page 4, Figure 5).

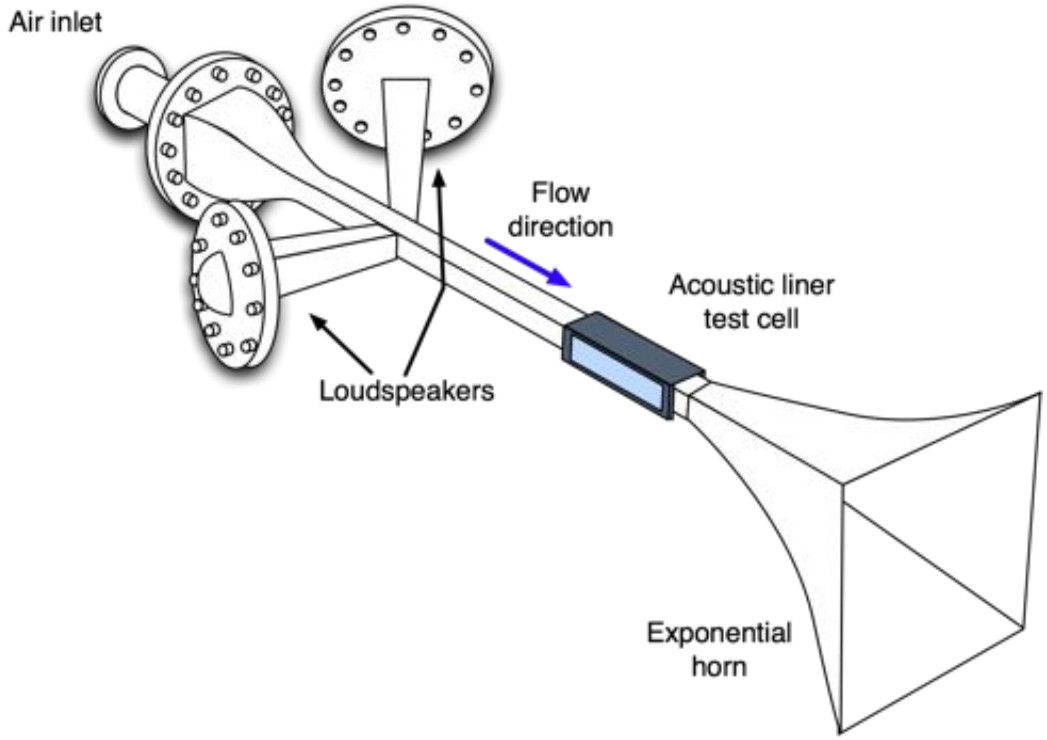

Figure 3-6. The ONERA B2A, adapted from Lavielle et al. 2006. Measurement of liner acoustic impedance in a shear layer of a subsonic flow by Laser Doppler Velocimetry. SAPEM 2005. (Page 234, Figure 1).

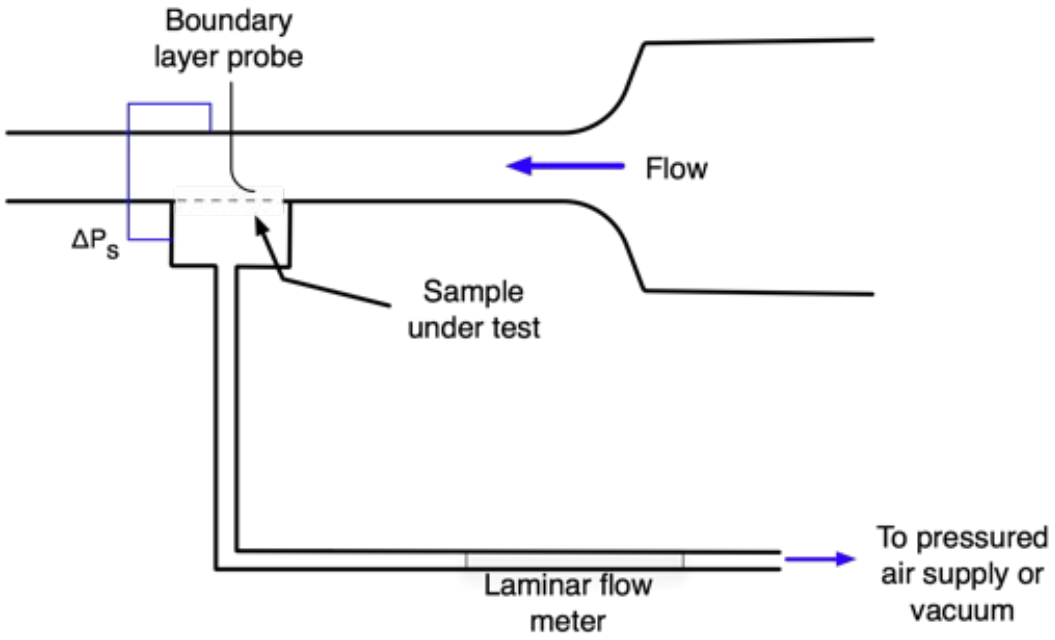

Figure 3-7. The General Electric DC flow duct, adapted from Syed, A. A. et al, 2002. The Steady Flow Resistance of Perforated Sheet Materials in High Speed Grazing Flows. NASA Technical Report NASA/CR-2002-211749. (Page 34, Figure 4c).

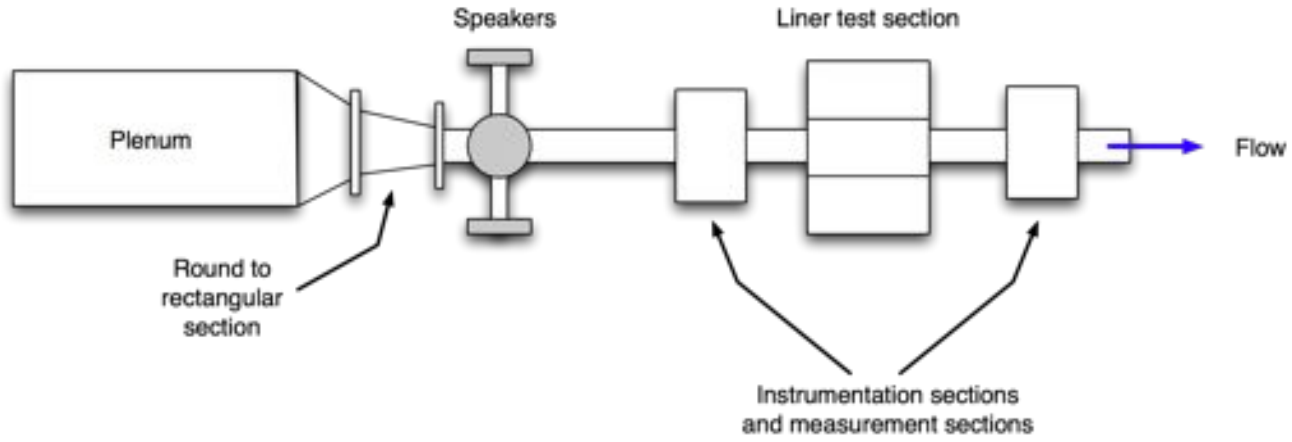

Figure 3-8. The GTRI Liner Flow Duct Facility, adapted from Ahuja et. al. 1997. A Unique Test Facility to Measure Liner Performance With a Summary of Initial Test Results. NASA CR 201667. (Page 38, Figure 2-1).

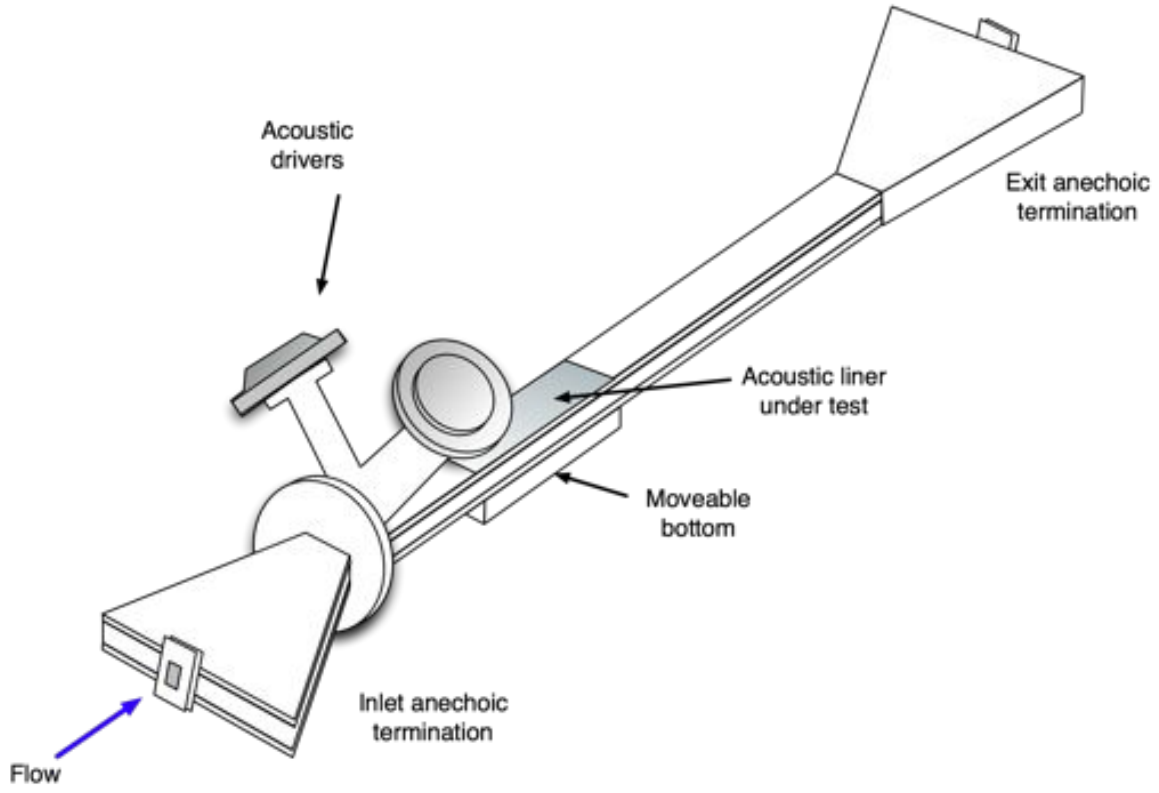

Figure 3-9. The UTRC Grazing Flow Facility, adapted from Simonich et al. 2006. 12^{th} AIAA/CEAS Aeroacoustics Conference. Development and Qualification of an In-Situ Grazing Flow Impedance Measurement Facility. AIAA 2006-2640. (Page 2, Figure 1).

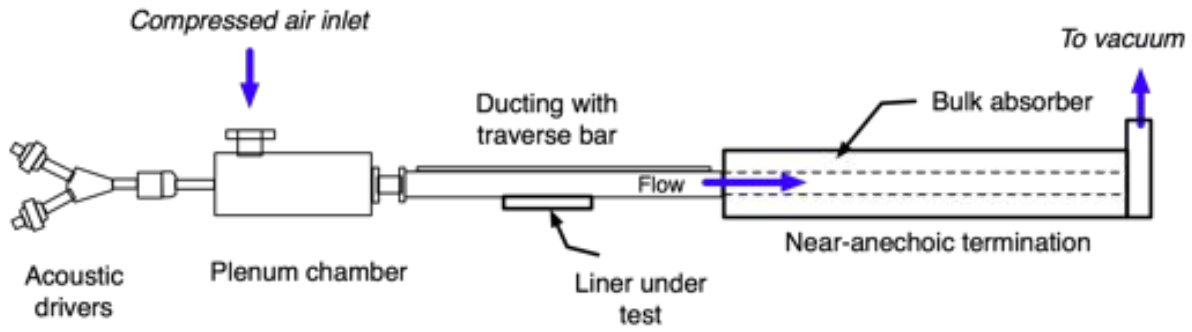

Figure 3-10. The FIT at NASA LaRC.

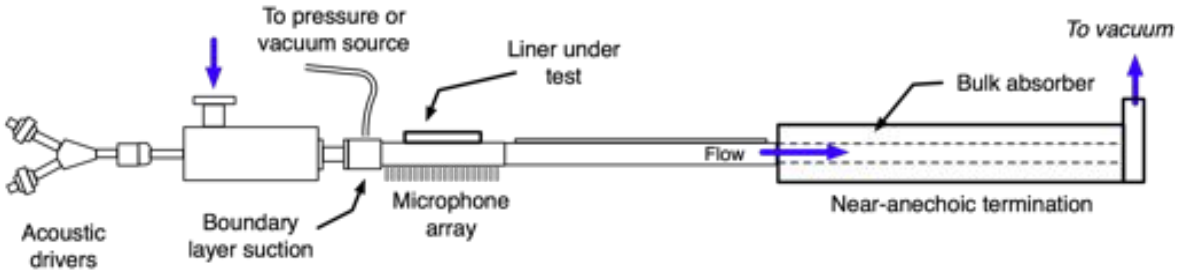

Figure 3-11. The GIT at NASA LaRC.

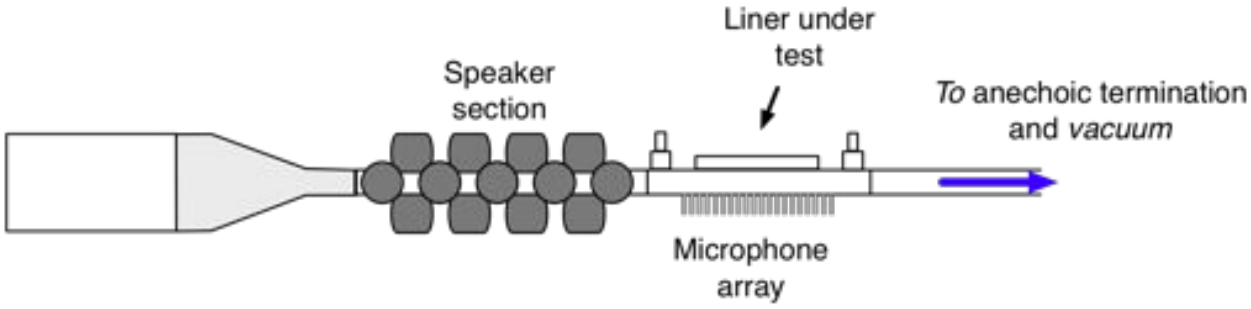

Figure 3-12. The GFIT at NASA LaRC.

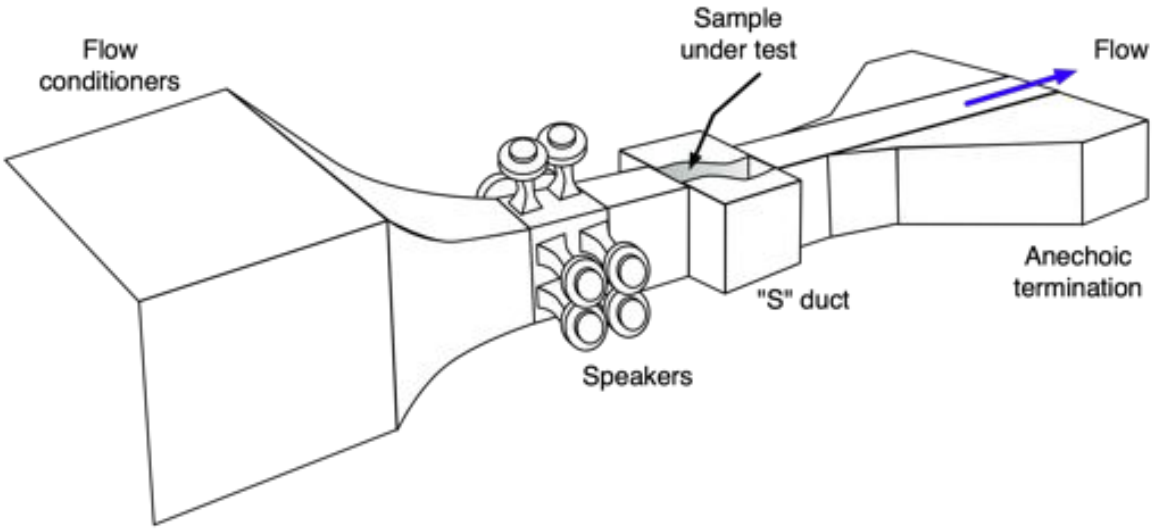

Figure 3-13. The CDTR at NASA LaRC.

CHAPTER 4
DESIGN AND IMPLEMENTATION

Chapter 3 reviewed current and past facilities and relevant studies to the GFID facility design, with topics focusing on turbulent channel flow investigations, impedance eduction methods, and identification of acoustic flow facilities. In Section 3.3 a comparison of known acoustic liner test facilities served to develop design concepts for the current facility. Five of the 17 acoustic liner test facilities presented are at universities, and no current US university facilities are active.

Modern aircraft engines convect air across acoustic liner surfaces within the nacelle at speeds near $M = 0.7$ and produce acoustic sound pressure levels in excess of 160 dB (Smith 2004). The eventual goal of the GFID is to match or exceed these conditions; however the initial objective is to reach $M = 0.5$, and attain SPL values at 130 dB. The means to accomplish this task were made possible by the generous donation of several components of the former GIT liner facility by NASA LaRC (Section 3.3.4) to the University of Florida (UF) in December of 2008.

The GFID facility is a combination of a high-speed wind tunnel and an acoustic plane wave test facility. Due to often divergent design paths, certain compromises were made during the design phase on each front toward the common goal without sacrificing vital measurement capabilities related to each type of facility. This chapter strategically analyzes the individual components that make up the GFID in order of downstream flow: air source and piping, stagnation chamber, acoustic source section, test section, ducting, anechoic termination, and exhaust ducting. Design choices were made to accommodate existing geometry and work within the constraints of budget.

4.1 Air Handling

4.1.1 Air Supply, Flow Valve and Flow Silencer

The GFID is a blow-down facility for initial testing up to $M = 0.5$. The system is fed by a 210 $psig$ source composed of two pressure tanks rated for 225 $psig$ with a total

volume of 1016 ft^3 (28.77 m^3). The tanks are filled by a Sullair LS-20T air compressor outputting 1760 $ACFM$ (1.005 $^{kg}/_{s}$) at 210 $psig$. A schematic of the air and electrical connections is illustrated in Figure 4-1.

A Fisher 667 diaphragm actuator regulates the pressure to functional levels for the facility. The valve itself is set to allow a maximum of 20 $psig$ when fully open and fine adjustments are made via a Fisher 3582 stem positioner. The regulator valve had to be hand-calibrated for the specific application, loading, and pressure drop of the entire system. The valve was calibrated such that the maximum output would allow flow up to $M = 0.7$ to accommodate future testing, bypassing future recalibration. All piping from the compressor to the stagnation chamber is 2 $in.$ unless stated otherwise.

Downstream of the valve, a Universal Silencer U5C-4 inline flow silencer, illustrated in Figure 4-2 was installed to reduce internal broadband noise levels from upstream contamination including flow noise from pipe bends, the flow valve, as well as structural noise from the compressor or other air handing units. The 57 $in.$ long steel-cased unit has a 4 $in.$ internal diameter lined with perforated metal covering 3 $in.$ of broadband acoustic insulation. The piping setup was designed to minimize head loss by reducing the use of bends and short radius curves.

4.1.2 Stagnation Chamber and Nozzle

The inline silencer is connected downstream to a 12 $in.$ steel schedule 40 T-junction via a 3 $in.$ pipe. The large internal volume of the T-junction allows for stagnation conditions to be met. A cross-sectional view of the stagnation chamber is illustrated in Figure 4-3. The inlet pipe is oriented to expel the flow toward the aft wall with a 6 $in.$ separation distance. The sensors used for stagnation pressure, Omega PX303-100A5V pressure transducer, and stagnation temperature, Omega RTD-806 3-wire RTD, were screw-mounted into the rear wall for measurement of stagnation properties. Additionally, atomized seed for optical flow measurements can be introduced via a port in the back wall of the stagnation chamber where it is mixed with in the incoming flow.

At the front of the stagnation chamber, the flow passes through honeycomb flow straighteners installed 21 *in.* from the rear wall and 16 *in.* upstream of the nozzle exit. The stainless steel honeycomb straighteners are made of 0.25 *in.* hexagonal cells 3 *in.* long. The straighteners reduce lateral flow motion by forcing stream tubes through the honeycomb cells stretching the vorticity (Rae & Pope 1999). Axial turbulence reduction is generally reduced through a series of flow screens and settling chambers within a stagnation chamber. Due to the heavy use of oil based seeding introduced within the stagnation chamber, axial flow screen installation was postponed.

To mate the stagnation chamber with the existing ducting, a two-stage nozzle was implemented, shown in Figure 4-4. The first stage is a steel schedule-40 reducer, decreasing the outer diameter from 12 *in.* to 6 *in.* over an 8 *in.* length. The second stage nozzle both reduces and changes the geometry by modifying the interior walls from a 6 *in.* diameter circle to a 2×2 *in.* square over a 6 *in.* length for an area ratio of 12. The nozzle was "printed" via stereo lithography rapid prototyping using high strength Accura-60 polycarbonate to accommodate the duct geometry and maximize strength.

The secondary nozzle contains a four-port static pressure ring 1 *in.* from where the area is 2×2 *in.*, equal to the reused NASA duct area. The four pressure ports are connected in parallel by 0.040 *in.* vinyl tubing to average the pressure distribution across the four walls. A single tube connects the pressure ring to an Omega PX409-005G10V pressure transducer. The nozzle exit was outfitted with "zig-zag" trip-tape, $3/8$ *in.* wide by $1/64$ *in.* thick to promote transition to a turbulent flow regime (Rae & Pope 1999).

4.1.3 Data Acquisition

All sensors used for measurement and control of general tunnel operation were acquired by a National Instruments (NI) cDAQ-9178 eight-port USB chassis. Input used a single four-port NI 9129 universal cDAQ card which acquires the stagnation temperature, stagnation pressure, and the static pressure sensor signals. The various signals were recorded in a custom NI LabVIEW-based interface and displayed real-time for the user.

The interface also performs the tunnel Mach number control via a proportional integral (PI) controller by adjusting the output voltage with typical settings of $P = 1.4$ and $I = 0.4$. A $0 - 10\ V$ incremental voltage output from a NI 9263 cDAQ card adjusted the pressure of a Marsh-Bellofram T2000 transducer from $3 - 15\ psi$. The variable pressure line was attached to the pneumatic regulator valve on the Fisher stem-positioner to adjust the valve opening to achieve the desired run condition.

Using the sensors for measuring stagnation pressure, p_0, stagnation temperature, T_0, and the calculated Mach number, Ma, the mass flow rate, $\dot{m}$, can be determined from the isentropic relationship

$$\dot{m} = \frac{p_0}{\sqrt{RT_0}} A\sqrt{\gamma} M \left(1 + \frac{\gamma - 1}{2} M^2\right)^{-\frac{\gamma+1}{2(\gamma-1)}}, \tag{4–1}$$

where R is the ideal gas constant for air, γ the ratio of specific heats, and A is the cross sectional area of the nozzle (John & Keith 2006). The mass flow rates within a 95% confidence range were measured for Mach numbers from $M = 0.1 - 0.5$ and are tabulated in Table 4-1. Note that the uncertainty value is statistical only as the isentropic calculation disregards viscous effects and thus Equation 4–1 overestimates the mass flow rate. Comparing these values to the maximum output of the compressor, 1.005 $^{kg}/_{s}$, it is clear that the compressor is able to produce a sufficient mass flow rate to sustain continuous flow up to the tested $M = 0.5$.

4.2 Acoustic Source

Acoustic excitation within the duct is used in an effort to mimic both the frequency content and amplitude of the BPF observed within an aircraft nacelle entrance previously discussed in Chapter 1. Acoustic excitation within the GFID was generated by a single BMS 4592ND dual-compression driver with an output range from $300 - 22,000\ Hz$ driven by a Crown $XLS1500$ power amplifier (BMS 2010). The drive signal was delivered to the amplifier by either a dedicated function generator or a Brüel & Kjær Pulse system,

depending on the experiment. Full details of each experimental setup are included in Chapter 5.

The speaker was installed immediately downstream of the nozzle within a specially designed duct section, shown in Figure 4-5. The 10 $in.$ long aluminum acoustic duct was designed with a removable speaker interface plate, where the speaker is mounted normal to the flow within a sidewall. The speaker face was offset 0.25 $in.$ from the flow. To fill the resulting cavity, a piece of aluminum foam 0.249 $in.$ thick with density 10 ppi (pores per inch) covered by a fine stainless steel mesh was installed. The mesh guides the flow over the surface yet allows the acoustics to pass through with negligible acoustic losses assumed. The aluminum foam provides a rigid permeable structure for the mesh.

The initial goal of the acoustic setup was to reach levels of 130 dB at specific frequencies to match experiments performed in the literature. Chapter 5 will demonstrate that the single driver setup was capable of reaching the desired values. However the eventual goal of attaining sound pressure levels in excess of 160 dB will require a redesign with additional speakers and amplifiers.

4.3 Ducting

The original GIT ducting remained as part of the GFID facility providing additional flow development length and multiple installation locations. The ducting was constructed of stainless steel walls, with a minimum thickness of 1 $in.$ In total, the 105 $in.$ (4.13 m) long duct is the combination of three individual duct pieces of length 48 $in.$, 29 $in.$, and 28 $in.$ Each component utilizes a common junction connection system illustrated in Fig. 4-9, allowing for the components to be installed in any order. This junction connection was replicated on all connections of fabricated sections. Steel alignment pins, 0.200 $in.$ diameter, ensure a smooth transition between facility components.

The ducting came with a microphone traverse bar that was used as part of the original FIT implementation at NASA (Jones *et al.* 2001). Even though the upgrade to the GIT replaced the traverse bar with stationary microphones, the traverse bar remained

as a stationary piece to fill the gap (Jones *et al.* 2004*a*). To allow the test section to be installed in-between any two duct pieces, the traverse bar was removed and each duct pieces has the traverse track permanently sealed with a custom stainless steel filler piece. The fabricated pieces also eliminated potential leakage through the top of the duct.

4.4 Test Section

The test section is a multi-use piece able to be installed between any two duct pieces. A photograph of the test section is shown in Figure 4-6. Constructed of black anodized 6061 aluminum to reduce surface glare for optical measurements, the test section was used for both fluid dynamic and acoustic measurements. The test section design contains two symmetry planes, horizontal and vertical. Symmetric about the horizontal symmetry plane, the top and bottom of the test section each have three ports, one centrally located acoustic liner installation port, and two outer auxiliary ports, each located one duct diameter (2 *in.*) away from the edge of the central liner port. The auxiliary ports are 0.076×0.076 *in* (3×3 *in*) square holes. The simple geometry allows for installation of individual sensors or quick access to the tunnel interior. The central acoustic liner installation port is designed to fit acoustic liners of dimensions 51×610 *mm* (16.36×2.51 *in.*), over eight duct diameters in length. Acrylic plugs filled the space when no liner was present. The dimensions match those used by the GFIT facility described in Section 3.3.4 at NASA LaRC for cross-facility collaboration (Jones *et al.* 2010). The liners used for testing are described in Chapter 5.

Various acoustic tests were performed necessitating the auxiliary ports to hold microphones. Two aluminum inserts, shown in Figure 4-7, were fabricated allowing for two 1/4 *in.* microphones to be installed within a circular rotation mount necessary for the two-microphone test in Section 5.3. Angle markers of 1° increments were installed on the edges of one quadrant.

The two sidewalls, shown in Figure 4-8 allowed for large 29 *in.* length opening for measurements upstream, downstream, and in the immediate vicinity of the acoustic liner.

Currently, three side walls have been fabricated for specific uses: a static pressure tap insert, and optically clear window, and a linear microphone array wall. Additional dummy polycarbonate walls were also made to reduce unnecessary use and potential damage to the specialized walls and inserts.

4.4.1 Optical Window

The multipurpose test section was designed to allow for optical-based fluid dynamic measurements, providing unrestricted optical access for either a laser or cameras. While plate glass is generally recommended for wind tunnel applications, the cost of manufacturing a metal frame was cost prohibitive; therefore, optical-grade 1.125 $in.$ thick Makrolon WG polycarbonate was used. The polycarbonate allowed for high strength while maintaining optical clarity. The window thickness was found to be an issue for large angles of incidence for LDV measurements. An analysis of the effects of the thick window are detailed in Section 5.1.2.

4.4.2 Static Pressure Wall

Static pressure within the test section was measured using 29 centerline pressure taps with 1 $in.$ spacing. A photograph of the static pressure insert is shown in the top of Figure 4-8. The taps were counterbored into the aluminum plate such that a 0.032 $in.$ thru-hole on the inside face connected to 0.040 in stainless steel pressure tap press-fit and epoxied in place. A post-drill "facing" pass of an end mill was performed to remove any drilling burrs without the need to round the internal tap corners.

4.4.3 Linear Microphone Array

A linear microphone array wall insert was fabricated from aluminum with ten, 1/4 $in.$ microphone ports with 0.85 in spacing along the centerline of the duct. An illustration of the installed microphone array is shown in Figure 5-22 and additionally photographed without microphones in Figure 4-8. Centerline measurements assume a plane mode; therefore testing with this plate is limited to frequencies below the higher-order mode cut-on at 3.37 kHz. Microphone holders, on loan from The Boeing Corporation, allowed

for screenless 1/4 " microphones to be installed flush with the interior surface of the tunnel wall to minimize flow noise.

4.5 Termination

Many of the impedance eduction methods presented in Section 3.2 rely on an assumption of progressive acoustics waves exclusively propagating in the streamwise direction. In reality this condition is impractical to physically realize, particularly at low frequencies where large wavelengths require excessive cell depths. Breakdowns in this assumption can lead to increased computational time for parameter convergence or failure in educing the desired parameter altogether (Jing *et al.* 2008).

An anechoic termination was fabricated that both reduces upstream acoustic reflections while simultaneously decreasing flow velocity. NASA LaRC originally designed the termination where it is currently implemented as part of the GFIT facility. The internal cross-section of the termination linearly increases from the GFID duct geometry of 2×2 *in.* to 8.125×9.125 *in.* over a 120 *in.* length. The gradual increase in the cross-sectional area decreases the flow speed. In the case of the maximum tested flow speed of $M = 0.5$ (171.5 $^{m}/_{s}$) at the nozzle, conservation of mass calculations reveal that the flow decreases to 9.4 $^{m}/_{s}$ at the termination exit.

Illustrated in Figure 4-10, the walls are a three-piece laminate construction of a felt metal facesheet, honeycomb, and aluminum hard-wall back plate forming a highly resistive locally reactive acoustic liner. The wire mesh is a 0.0625 *in* stainless steel sheet of woven wires, cold-rolled to a nominal static resistance of 320 *cgs rayls*. The stainless steel honeycomb cells are 3/8 *in.* with a varying cavity depth from 0.125 *in.* to 6.090 *in.* The honeycomb is aligned normal to the walls acting both as a cavity as well as a structural component. The ends of the honeycomb were epoxied to a 0.031 *in.* thick aluminum backplate sealing the end of the cavity. This construction was repeated on all four sides and the structure was wrapped in several layers of fiberglass. The final structure has an octagonal exterior shape with the corner volumes filled with high-density spray foam for

structural integrity. Section 5.3 presents the results of tests performed on the anechoic termination.

All velocity-based testing in Chapter 5 required the use of an atomized oil for flow seeding. The oil used in the LDV experiments is a Phantom Smoke Oil 135 from Pea Soup Ltd, a refined mineral oil. Concern arose over the accumulation of oil in the metal mesh of the interior walls of the anechoic termination and the inability to clean it, thereby reducing the long-term efficacy of the acoustic reflection reduction properties. A second hard-wall diffuser of identical internal dimensions was fabricated of 0.175 $in.$ thick fiberglass limited only to testing when seeding was necessary, such as LDV.

4.6 Exhaust Ducting

Downstream of the termination the flow is steered out of the test room and building to the outdoor environment through a duct of cross-sectional area equal to the termination exit, as illustrated in Figure 4-11. The duct was fabricated of sheet metal with entrance flanges matching the hole pattern of the termination. The duct is constructed of two parts, where the straight downstream duct slides concentrically into the curved upstream duct, to allow for adjustments if necessary. A coarse metal grating was installed at the duct exit obstructing debris from entering.

4.7 The GFID Layout

The full drawing of all GFID sections is illustrated in Figure 4-12. In all, the GFID is 34 ft long from the inline silencer to the exhaust exit and extends 4 ft off the wall for a total footprint of 136 $sq.\ ft.$ Additional room is necessary for computer control, storage of the alternate termination, and various instrumentation.

While not discussed in each section, sealing leaks between all adjacent sections, as well as from any seem or joint is a nontrivial issue for both blowdown facilities and acoustic ducts. If left untreated the gaps could lead to a drop in flow velocity and/or reduction in acoustic energy propagating down the duct as well as undesired acoustic scattering. When possible, rubber o-rings were installed on all compression fit pieces such

as optical windows and installation ports. All exposed seams were covered with Silicone RTV. Additional coverage at often removed interfaces were sealed with off-the-shelf Silly Putty.

4.8 Design Conclusion

This chapter described the layout and detailed the components of the GFID in streamwise order. Section 4.1 described the air source, piping system, nozzle, and velocity control of the system using LabVIEW for real-time thermodynamic property monitoring, recording, and tunnel control. The acoustic source was outlined in Section 4.2. Accurate source excitation matching tonal content and sound pressure levels is vital for acoustic liner testing and improvements should be made on this stage to increase levels. Section 4.3 detailed the three pieces of ducting from the GIT facility which were reused providing added length between the nozzle and the test section for increase flow development and multiple test section installation locations. Section 4.4 described the modular test section and the current testing capabilities, including static pressure, optical flow measurements, and a linear microphone array. The anechoic termination, described in Section 4.5, is vital for acoustic testing by reducing upstream propagating modes. Due to the current use of oil-based seeding for LDV, the application of anechoic termination is limited to acoustic testing without flow measurements. Chapter 5 describes the setup and results of experiments characterizing the GFID and the testing of acoustic liner impedance. Full technical drawings of all UF designed parts are included in Appendix D.

Table 4-1. GFID mass flow rates as a function of Mach number.

Set Mach Number	Mass Flow Rate $[^{kg}/_{s}]$
0.1	0.100 - 0.113
0.2	0.210 - 0.219
0.3	0.319 - 0.327
0.4	0.429 - 0.439
0.5	0.541 - 0.553

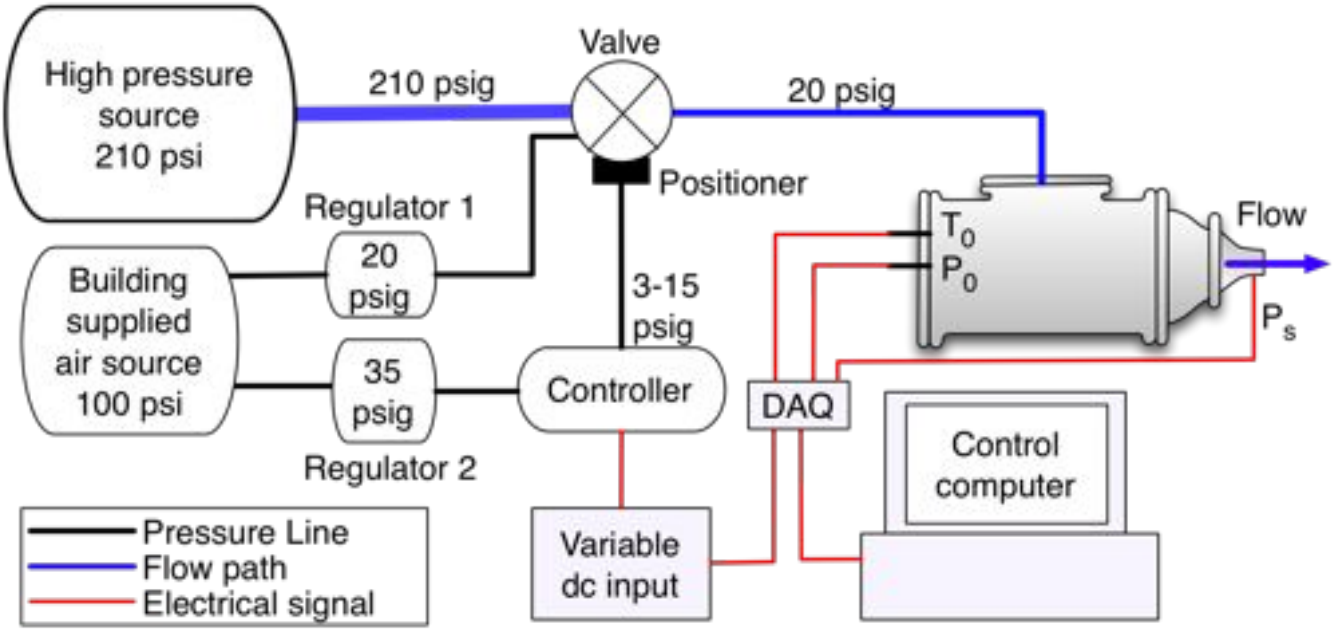

Figure 4-1. GFID air supply schematic indicating pneumatic lines, electrical connections, and flow paths.

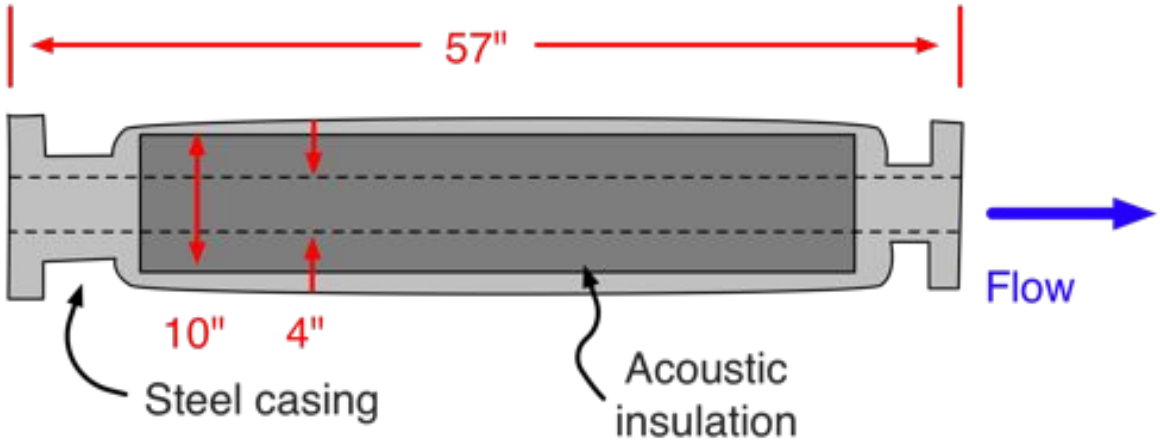

Figure 4-2. Internal view of the Universal Silencer U5C-4 flow silencer for reducing flow noise and structural line noise.

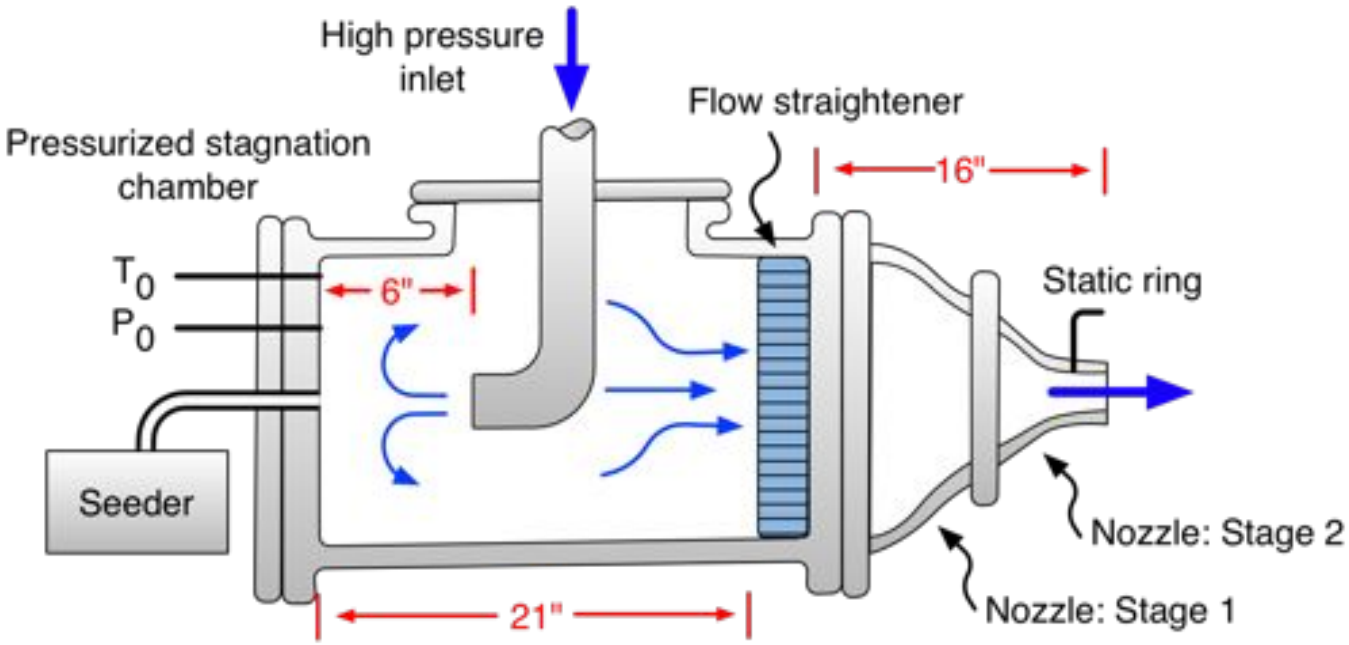

Figure 4-3. The GFID plenum uses a two-stage nozzle. Seed particles are introduced for homogeneous mixing.

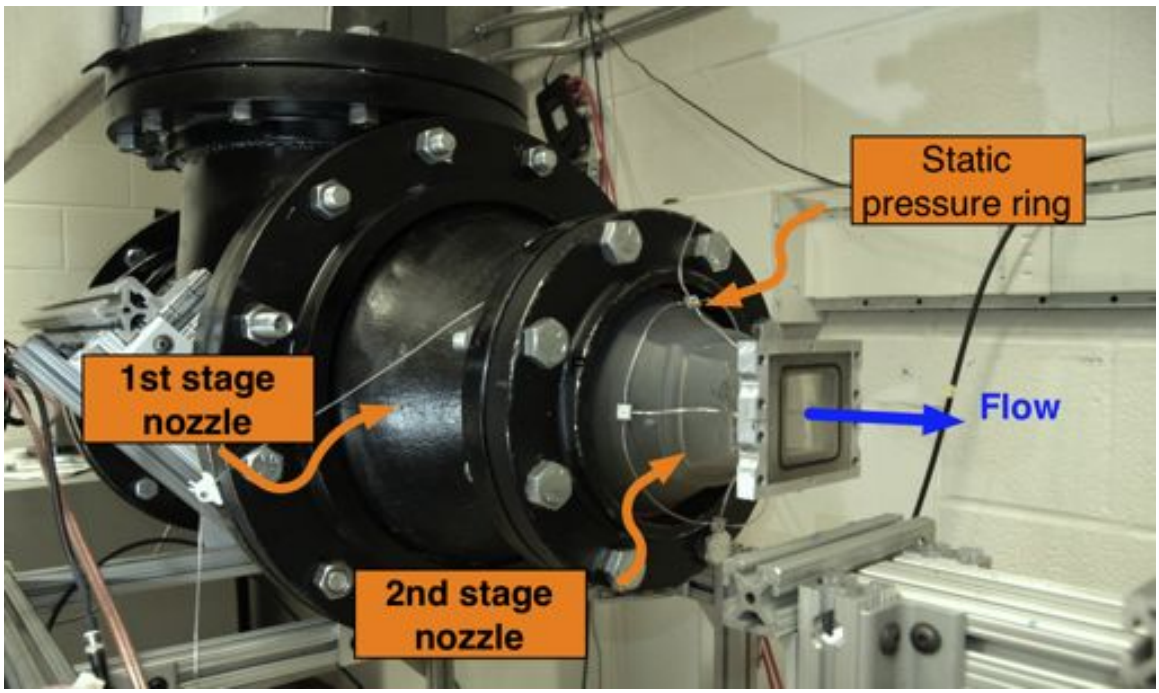

Figure 4-4. Diagram of the GFID stagnation chamber. The inlet pipe is turned toward the aft wall forcing stagnation conditions and enhancing homogeneous mixing of seed particle. The chamber uses a two-stage nozzle to maintain flow quality and modify the shape.

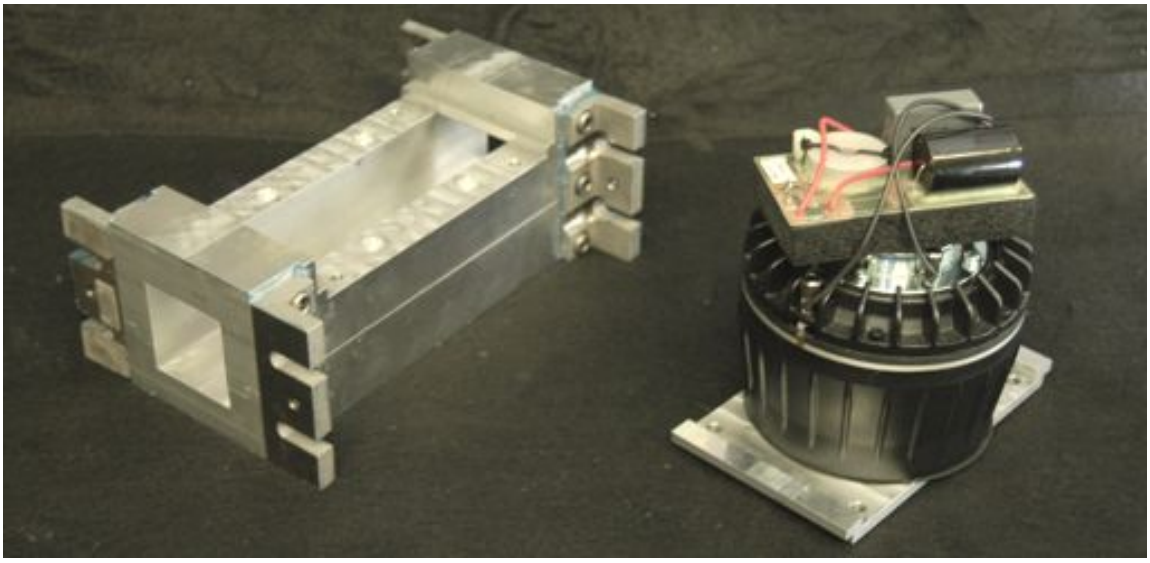

Figure 4-5. Acoustic duct section (Left) with speaker mounted to speaker plate (Right).

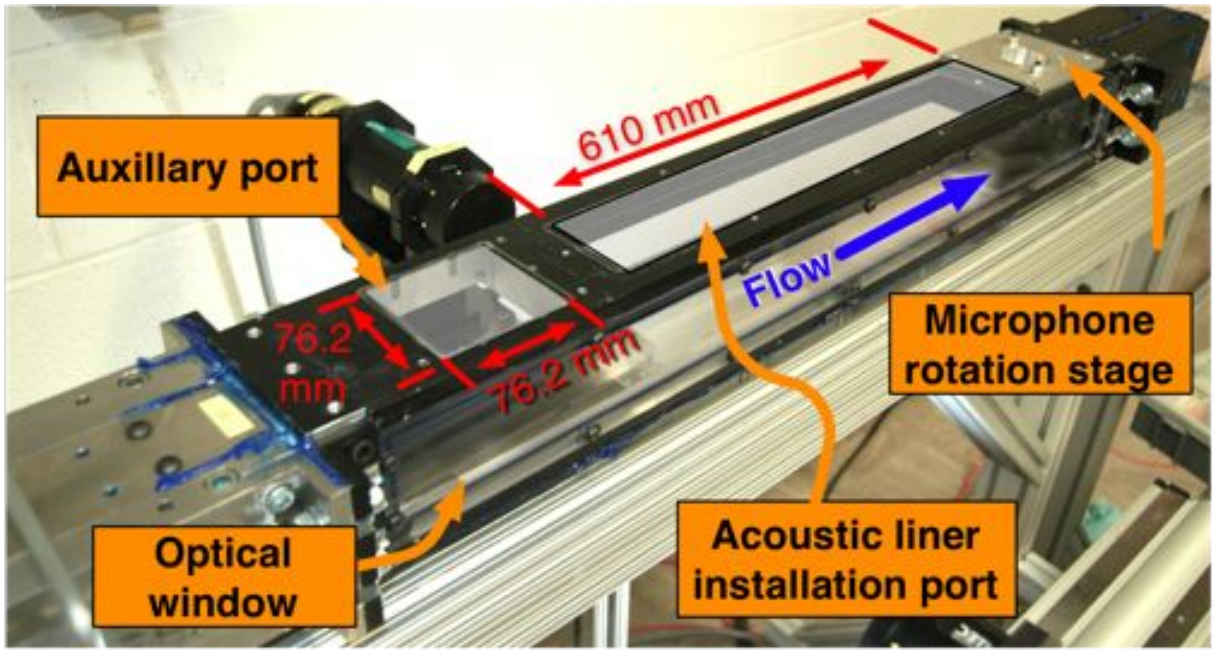

Figure 4-6. The GFID test section has acoustic liner installation ports on top and bottom and four auxiliary ports for microphones and additional sensors.

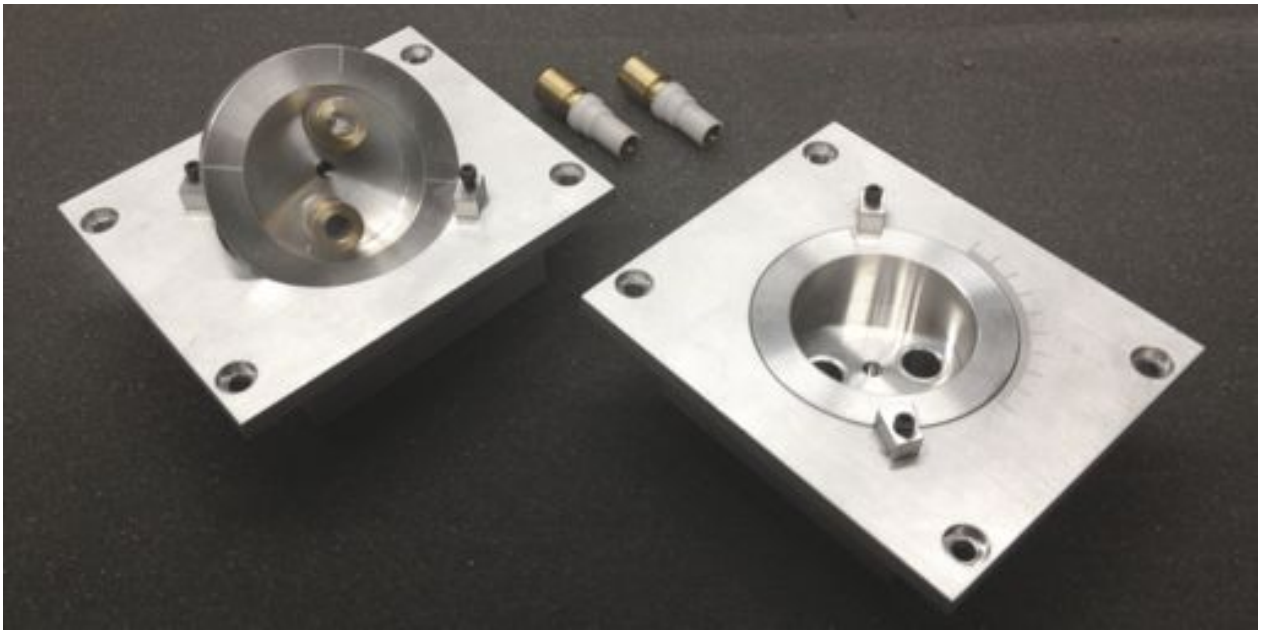

Figure 4-7. Photograph of the two microphone rotational plug for test section auxiliary ports with microphone holders.

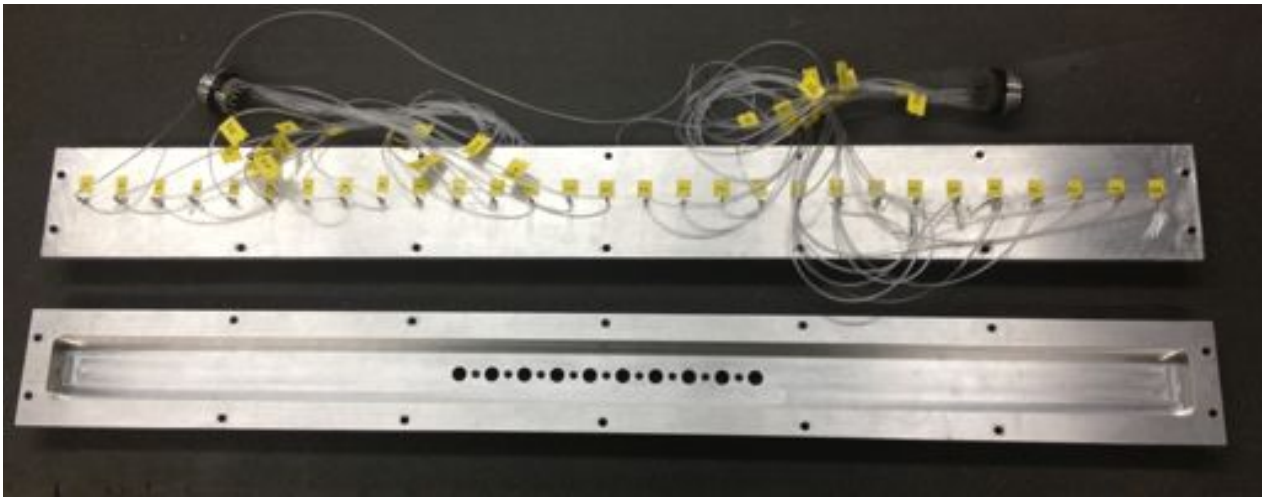

Figure 4-8. Static pressure tap insert (top) and linear microphone array wall (bottom).

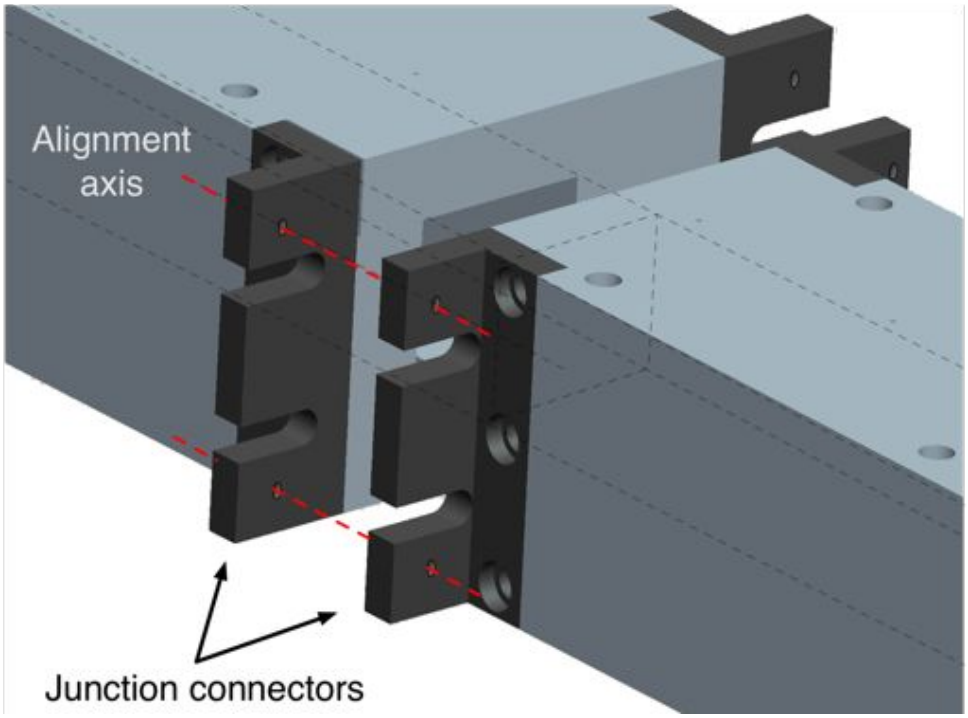

Figure 4-9. Common GFID connectors joining each adjacent section.

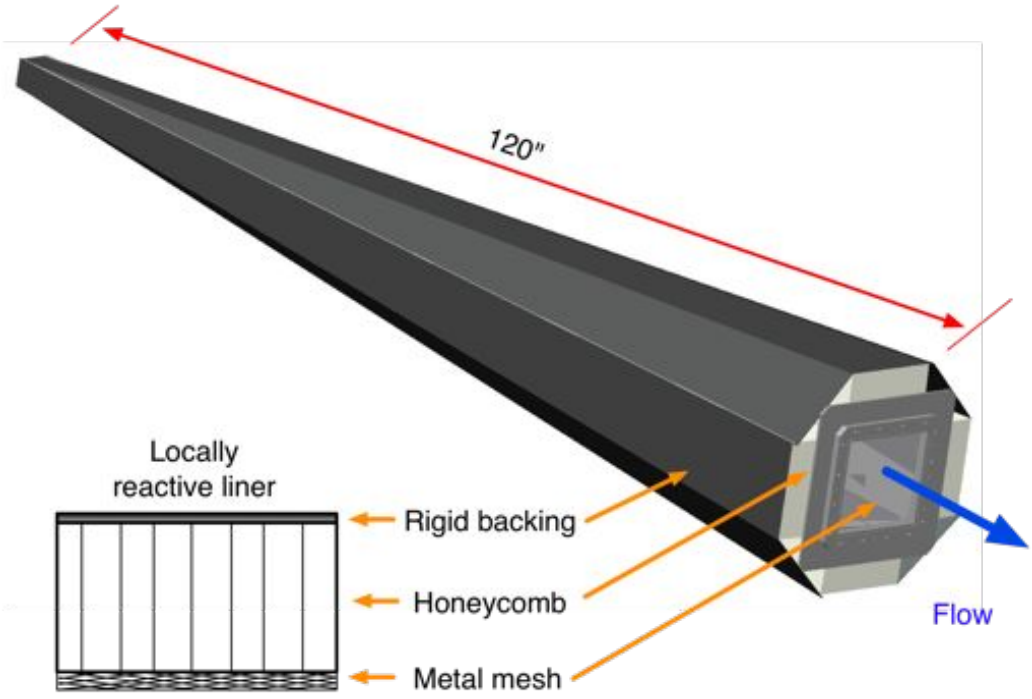

Figure 4-10. GFID near-anechoic termination composed of linear reactive acoustic liner walls to mitigate upstream propagating noise.

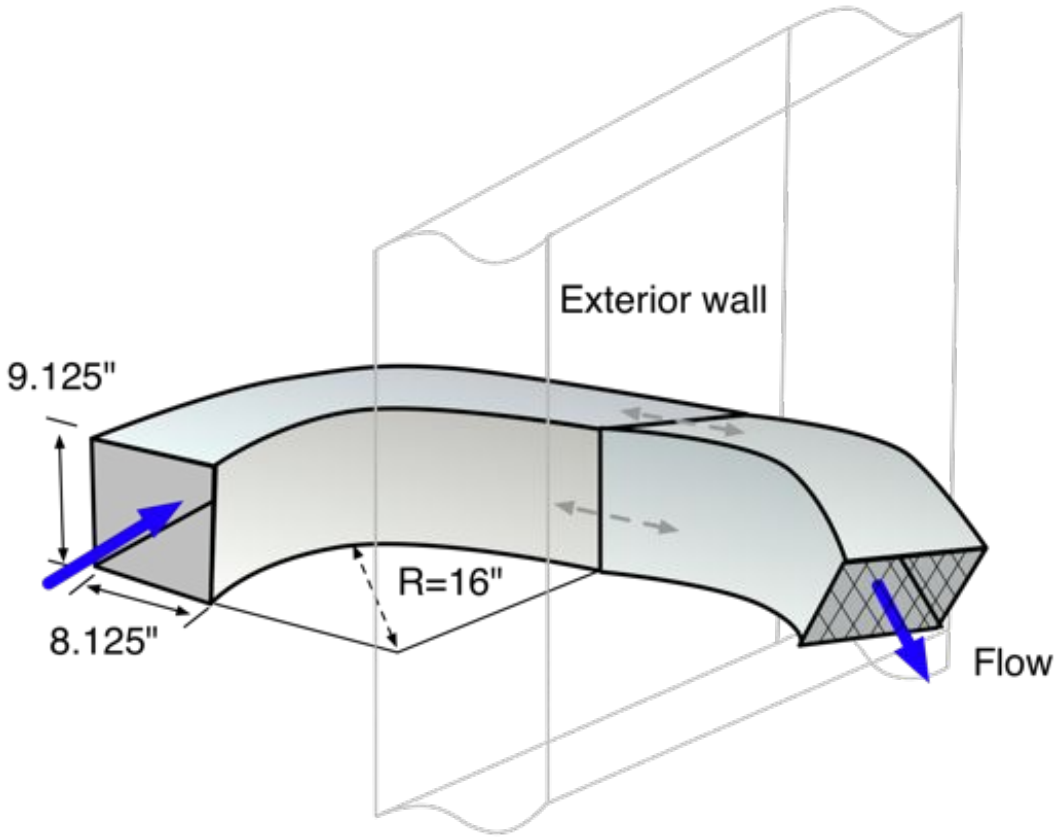

Figure 4-11. The GFID exhaust ducting expels the flow to the building exterior.

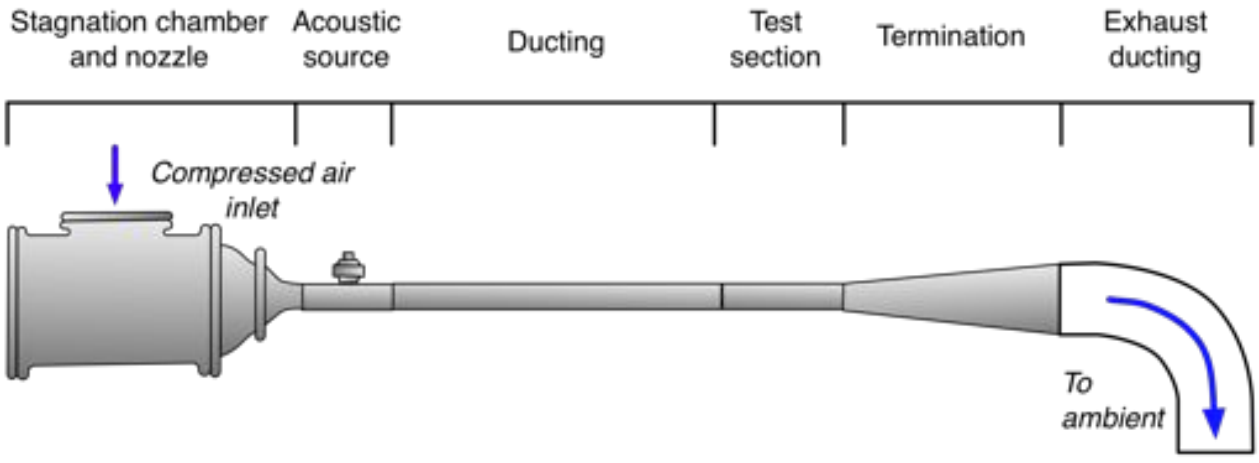

Figure 4-12. An illustration of the GFID by section, not drawn to scale.

CHAPTER 5
FACILITY CHARACTERIZATION AND PROCESS VALIDATION

This chapter will lay out the methodologies and results of the fluid dynamic and acoustic investigation of the GFID as a high Reynolds number turbulent channel flow and a grazing flow impedance facility. The experiments were chosen to specifically highlight key aspects of the flow and acoustic testing, demonstrating the performance of the GFID compared against the available literature. Section 5.1 outlines setup for fluid dynamic testing in the GFID, with a specific focus and background on the application of laser Doppler velocimetry as the primary velocity measurement technique. Section 5.2 presents the experimental results and discussion of the fluid dynamic characterization of the GFID. The characterization focuses on two sections of the tunnel: the upstream entrance region for developing flow studies and the downstream fully developed region. Similarly, acoustic characterization is presented in Section 5.3 to determine the testing limitations imposed by upstream propagating reflections within the facility that may hinder certain impedance eduction techniques. Section 5.4 attempts to educe the impedance of an untested acoustic liner via the application of the single mode method through a data-processing validation process based on experimental results taken at both UF and NASA LaRC. The chapter concludes with Section 5.5, presenting an experimental analysis of the drag influence of the acoustic liner using three indirect velocity-based techniques. Results and discussion are included in each section.

5.1 Fluid Testing Experimental Setup

Several techniques are available to measure the velocities of interest. Compared to larger wind tunnels, the relatively small 2 $in.$ $\times$ 2 $in.$ cross section of the GFID is more sensitive to blockage from intrusive measurement probes. As flow development is of primary interest, physical probes would need to be traversed to predetermined grid locations. Traversable wall sections are prone to leakage and increased complexity. To this end, non-intrusive measurement techniques, such as particle image velocimetry (PIV) and

laser Doppler velocimetry (LDV), are preferred to intrusive techniques such as hot-wire anemometry, pitot probes, and boundary layer rake. Ultimately LDV was chosen due to a higher spatial resolution, high data rates, and a relatively simpler experimental setup compared to PIV.

5.1.1 Basic Principals of Laser Doppler Velocimetry (LDV)

Laser Doppler velocimetry (LDV) is a non-intrusive point measurement technique that directly measures the Doppler shift of a tracer particle passing through the small intersecting volume defined at the intersection of multiple focused laser beams. The intersecting volume defines an optical anemometer probe of fixed location in reference to the transmitting and receiving optics and thus is referred to as the "probe volume". The principle behind the most common implementation of LDV, illustrated in Figure 5-1, is based on two monochromatic laser beams of wavelength, λ_1, crossing at a beam separation angle, θ, at the focal length of the transmitting optics. An interference fringe pattern is established in the probe volume, with fringe spacing δ_f, due to constructive and destructive interference of the intersecting wavefronts (Albrecht *et al.* 2003)

$$\delta_f = \frac{\lambda_1}{2\sin\left(\theta/2\right)}. \tag{5–1}$$

The intensity of light scattered by a particle passing through the probe volume is dependent on the receiving angle of the collector relative to the optical axis. All LDV velocity data in this thesis was captured in back-scatter mode, illustrated in Figure 5-1, where the scattered light is captured along the path of the transmitted beam. Light collected opposite the transmission path is called "forward scatter", possessing a higher reflected intensity at the expense of increased complexity due to a separate receiver and intricate alignment (Albrecht *et al.* 2003). The collected light scattered by the particle is directed via multi-mode optical fibers (multi-mode to accommodate multiple colors, one for each velocity component) to a photo-multiplier tube (PMT) where it is converted into an electric current. The subsequent Doppler shift frequency, f_d, from the passing particle

is related to the particle velocity component, v_p, perpendicular to the bisector of the two incident beams, (Dynamics 2000)

$$v_p = \left| \frac{\lambda_1}{2 \sin(\theta/2)} f_d \right|. \tag{5–2}$$

However, a particle passing through the probe volume will generate a Doppler shift of f_d for either a positive or negative particle displacement, illustrated in Figure 5-2A.

In order to eliminate the directional ambiguity, a constant frequency shift, f_0, is added to one of the monochromatic beams by an opto-acoustic modulator, called a Bragg cell (Albrecht *et al.* 2003). Without a Bragg cell, a zero velocity results in a null Doppler frequency. The addition of the induced frequency shift results in a zero velocity equal to the offset frequency, as illustrated in Figure 5-2B, and a negative velocity can be acquired

$$f_d \cong \left| \frac{2 \sin(\theta/2)}{\lambda} v_p + f_0 \right|. \tag{5–3}$$

Noting the upper and lower limits of a signal processor, Equation 5–4 can be extended to solve for the velocity limits of a particular system (Dynamics 2000)

$$-\left| \frac{(f_0 - f_{min})\,\lambda}{2 \sin(\theta/2)} \right| < v_p < \left| \frac{(f_{max} - f_0)\,\lambda}{2 \sin(\theta/2)} \right|. \tag{5–4}$$

The process described above for a single velocity can be extended to measure all three velocity components of a single particle simultaneously using two additional laser sources of wavelengths λ_2 and λ_3, (note: $\lambda_1 \neq \lambda_2 \neq \lambda_3$). A single multimode Argon-ion (Ar:Ion) laser is commonly used to generate the three wavelengths simultaneously corresponding to three dominant spectral peaks from the Ar:Ion laser source, 514 nm, 488 nm, and 476 nm, respectively. From the Ar:Ion laser, the multimode beam is separated into the individual wavelengths listed above and directed to individual fiber optics. The Dantec transmission box used for this thesis is illustrated in Figure 5-3A demonstrating the light paths and Bragg cell signal input. Each wavelength has two fibers, one of which has a constant $f_0 = 40\ MHz$ frequency shift added via the Bragg cell. The wavelength specific fibers

leaving the transmission box are split between two probe heads where the transmitting optics are held.

The primary head contains the four beams of the two primary wavelengths, 514 nm and 488 nm, while the secondary probe head outputs two beams at 476 nm. Illustrated in Figure 5-4, the primary probe head is generally configured with the four beams outputting from a square orientation with wavelength pairs aligned opposite each other, commonly referred to as "4-beam mode". However, in order to resolve wall-bounded flows the probe can be reconfigured, as illustrated in Figure 5-3B, to ensure one of the incident beams is not clipped by a wall or body. The reconfigured "3-beam mode" probe head has the green and blue beams aligned 180° apart and a combination of the two is located 90° to them both. The received scattered light is bandpass filtered and each wavelength is directed toward an individual PMT.

The beam separation angle, θ, in Figure 5-1 is a function of the separation distance between the exit position of the two beams, as well as the focal length, f, of the transmitting optics. Therefore the lens choice and beam configuration will determine the velocity range of a particular setup from Equation 5–4. The UF signal processor has a reported upper limit of $f_{max} = 180\ MHz$ and an inferred lower limit of $f_{min} = 15.85\ MHz$ (Jensen & Bertolucci 2012). These values are used to solve for the upper and lower velocity limit of the Dantec system signal processor used and are shown in Figure 5-5 and tabulated in Tables 5-1 and 5-2. The limits are based on the available lens focal lengths available for the UF system of 120 mm and 400 mm, however only the 120 mm lens was used for the present experiments due to improved spatial resolution.

Probe Volume Dimensions

The detection of particles within the probe volume has several contributing factors including wavelength, probe volume size, particle size, concentration, and type, and optical path, amongst others. Several of these topics are touched in the remainder of this section. The size of the probe volume itself has one of the largest influences on data rate at the

expense of spatial resolution associated with larger probe volumes. The probe volume size is defined by three dimensions, the width, dx, the height, dy, and the length, dz. The width and height of the probe volume are nearly always equal (Dynamics 2000).Each of the dimensions is dependent upon the beam waist diameter, a_0, defined as

$$a_0 = \frac{4f\lambda}{\pi E d_I}, \tag{5–5}$$

where f is the transmitting optics focal length, d_I and λ are the incident beam diameter and wavelength, respectively (Dynamics 2000). Although not applicable to this study, the beam expansion ratio E, is unity unless a beam expander for larger optics is installed. For the 120 mm and 400 mm lenses available, the beam waists are 56.6 μm and 189 μm. Assuming equal height and width, the dimensions of the probe volume are defined by

$$dx = dy = \frac{a_0}{\cos\left(\theta/2\right)}, \tag{5–6}$$

and,

$$dz = \frac{a_0}{\sin\left(\theta/2\right)}. \tag{5–7}$$

Applying Equations 5–6 and 5–7 for the 120 mm in 2/4-beam mode results in $dx = dy =$ 57.3 μm and $dz = 361.9$ μm.

Estimation of moments

LDV measurements are inherently tied to the random sampling of seed particles passing through the probe volume. The rate at which the particles pass through the probe volume is a function of the volume flux of seed particles. As higher speed flows have a larger volume flux for a fixed region, LDV measurements of averaged quantities are inherently biased toward high speed flows; this is referred to as a "velocity bias". In order to compare flows of unequal sample rates, the measured quantities need to be weighted. While there are several possible expressions for the weighting factor, g_i, newer LDV systems allow for accurate measurements of the transit time, τ_i, the length of the time

required for each particle measured to pass through the probe volume, which is inversely proportional to the magnitude of the vector velocity (Albrecht *et al.* 2003).

Using the transit time as the weighting factor, each velocity sample, u_i, is weighted and the mean flow velocity and standard deviation are respectively expressed as

$$\hat{\bar{u}} = \frac{\sum_{i=1}^{N} u_i g_i}{\sum_{i=1}^{N} g_i} \tag{5–8}$$

and

$$\hat{\sigma}_u = \sqrt{\frac{\sum_{i=1}^{N} \left(u_i - \hat{\bar{u}}\right)^2 g_i}{\sum_{i=1}^{N} g_i}}. \tag{5–9}$$

The $\left(\hat{}\right)$ symbol indicates that the equation expresses an estimation of the calculated quantity (Albrecht *et al.* 2003).

Seeding and Limits

Detection of a particle by the PMTs within the system is a function of incident laser intensity, particle size, relative refractive indices of the particle material and flow medium, particle shape, and receiving angle (Albrecht *et al.* 2003). The particle size dictates the effectiveness of the particle to scatter light, and thus the benefit of the seeding particle for use with LDV. The particle size is related to the incident wavelength, λ, through the non-dimensional Mie parameter, which in air can be simplified to

$$\alpha = \frac{\pi d_p}{\lambda}, \tag{5–10}$$

where d_p is the particle diameter (Albrecht *et al.* 2003). All LDV measurements in this thesis use a Pea Soup PS31 oil-based seeder to produce a dry atomized oil smoke particle. The seeder requires a proprietary Phantom Smoke Oil 135, a highly refined mineral oil with a reported particle diameter of $d_p = 0.3\mu m$, and thus has a Mei parameter between

$1.83 - 1.98$ for the output wavelengths of the laser. The particles generated are assumed to be of equal size, or monodisperse, spherical, and non-absorptive.

The seed particles can be thought of as small spheres that ideally move with the flow. However, as the size of the particles increases, a relative slip velocity between the true fluid motion and the motion of the particle occurs. The slip between the seeding particles and the surrounding fluid, s, is defined as

$$s = \frac{u_f - u_p}{u_f}, \tag{5–11}$$

where u_f and u_p are the fluid and particle velocities, respectively. This is especially important when dealing with high speed turbulent flows as the particle size acts as a low-pass filter for both turbulent and spectral analysis (Albrecht *et al.* 2003). The particle diameter and material properties define the cut-off frequency for which the particles can accurately follow the flow. If the density of the particles, ρ_p, is much larger than that of the surrounding fluid, the particle diameter, d_p, can be related to the cut-off frequency, f_c, through

$$d_p < \sqrt{\frac{18\nu}{\rho_p f_c}\frac{1}{2\pi}\sqrt{\frac{1}{(1-s)^2} - 1}}, \tag{5–12}$$

where ν is the kinematic viscosity of air (Albrecht *et al.* 2003). Figure 5-6 illustrates Equation 5–12 over a range of sizes applicable to the proposed experiment showing two common seeding materials and allowing for a 1% slip error. The vertical line indicates the cut-on frequency of higher order acoustic modes dictated by the tunnel geometry of $3.37\ kHz$ for $M = 0$, defined by Equation 2–8. Based on Figure 5-6, the particle produced by the mineral oil based Pea Soup seeder can be accurately used for frequencies above $10\ kHz$.

5.1.2 Laser Doppler Velocimetry Experimental Setup

This section will outline how LDV measurements were used for GFID fluid dynamic characterization. The alignment of the LDV system to the GFID is described. The

limitations of the system and those imposed by the GFID are outlined specifically for application to this thesis and in general to apply to future experiments.

The LDV probe head was positioned by a 3-axis Parker traverse allowing for precise movements with 3 μm repeatability, controlled via a custom LabVIEW user interface capable of communicating with the provided LDV software, Dantec BSA. The three axes were aligned with the tunnel coordinate system at each test section installation location. The longest axis, a Parker 406XR-1250, had 1250 mm of travel and was aligned streamwise with the x-direction. The other two axes, both a Parker 404XR-300 with 300 mm of travel and 3 μm resolution, were aligned with the cross-tunnel directions. The traverse was rigidly attached to the GFID stand to maintain alignment.

While care was taken when attaching the traverse to the GFID stand for alignment, a finite offset angle is unavoidable. Precise knowledge of probe location for both near-wall and centerline measures requires the traverse motion to track the coordinate system of the tunnel defined by the inherent geometry. A laser displacement sensor (LDS), Keyence LK-G97, was attached to the traverse and the distance to a flat tunnel surface was measured as the traverse was moved along a single axis. The analog data was recorded via LabVIEW and the separation distance plotted. The resultant angle was found through a linear fit of the data. The tests were repeated for all three axes and the resultant slopes were used as a translation of all motion requests to the traverse, both manual and automated through the BSA software.

Using the LDS allowed for the traverse motion to be aligned to the tunnel coordinate system, however, the probe head itself is not. The probe laser emitters are factory aligned such that all beams cross at a fixed location defined by the lens focal length. As a result, alignment of the probe's individual beams are unnecessary. However, alignment of the probe head to the tunnel coordinate system is essential for measuring the true velocity. Several steps are involved in aligning the probe head to the test section. Aligning to the tunnel floor ensures that the plane of two laser beams is equal to the tunnel floor plane.

Illustrated in Figure 5-7, an alignment procedure was implemented where two beams emanating from the probe head are set at low power and directed at the interface of a thin opaque shim resting on the tunnel floor. The probe head is carefully rotated until the light passing underneath the shim at both points is of equal intensity.

The reflection of the beams off of the front of the window are used for additional alignment to ensure that probe head is normal to the test section. Beam reflections off of the window surface will fall on the front lens of the probe and independent pitch and yaw adjustments were made to the probe head until the secondary and tertiary reflections were aligned with the primary emitting beams.

Finally, with the probe head aligned to the tunnel it was necessary to define the zero location of the traverse relative to the tunnel coordinate system. This requires that three locations are accurately known, the floor, the sidewall, and the upstream vertical edge of the test section. The tunnel floor was previously aligned using the opaque shim. To locate the interior surface of the test section a technique outlined by Dynamics (2000) is applied. With the laser outputting at low power, the probe volume is incrementally stepped in the z-direction until the monitored anode current is maximized, with care to not overload the PMT. Just as the processor will have the highest signal when a particle passes through the center of the probe volume, so too will a solid object, and thus the interior surface of the window will reflect the most light. This process was able to determine the tunnel edge to $\pm$ 10μm. With location of the sidewall, floor, and test section entrance known to the traverse, the centerline of the tunnel can be defined as numeric offsets of these features.

Experimental setup

As will be discussed in Section 5.2, two types of experiments were performed: centerline measurements, and cross-duct measurements. All centerline data used a 4-beam configuration for measuring 2D velocity data oriented such that both the green and blue overlapping probe volumes measured a positive velocity, as illustrated in Figure 5-4A.

The cross-duct profiles required near-wall measurements on both the top and bottom wall. Generally, near-wall measurements are made using a 3-beam probe configuration, illustrated in Figure 5-4B. However, as a 3-beam configuration is aligned to a surface such that no beams are cropped, the benefits of the second velocity component from 3-beam configuration are negated on the upper wall unless the the probe head was rotated 180°. The necessary rotation step could undo the intricate alignment of the probe head. Additionally, due to the nature of the 3-beam confirmation, one vector must always measure a negative velocity. As listed in listed in Table 5-1, the low velocity limit of $-54.26\ {}^{m}/_{s}$ would be limiting for many of the flows tested in this thesis. To utilize the spatial resolution of the 120 mm lens for near wall measurements when performing cross-duct profiles, 1-D velocity measurements of the streamwise velocity component were made using just the 514 nm beam.

The cross duct profiles only measure the local velocity value but were not affected by fluctuations in free stream conditions. The stationary secondary LDV probe head with wavelength 476 nm was setup opposite the primary head and aligned to measured the centerline velocity. Velocity can only be sampled when both probes registered a signal within a 250 μs window. The reference velocity, u_{ref} is then used to smooth out the tunnel fluctuations of the mean flow

$$u_i = u_{i,t} \times \left(\frac{\overline{u_{ref_i}}}{u_{ref_i}} \right), \tag{5–13}$$

where the subscript i refers to an individual sample.

Effect of window thickness

Originally, all three components of velocity were to be measured simultaneously by using both probe heads and aligning to a pin hole. However, initial experiments through the test section optical window presented in Section 4.4 demonstrated very low and often null data rates. While lower data rates are expected for 3D LDV due to the small region of overlapping probe volumes, the window was determined to be a primary factor. To

better understand the issue and the influence of the window on the measurements, an optical model was set up based on Snell's law.

The model was based on tracing two beams emanating from the probe head, illustrated in Figure 5-8, and accounted for the angle shifts at the incident and transmitting interfaces of the window of finite thickness according to Snell's Law,

$$n_2 \sin \alpha_2 = n_1 \sin \alpha_1. \tag{5–14}$$

Snell's Law is a simple equation based on the index of refraction of two mediums, in this case air ($n = 1.00$) and the polycarbonate window ($n = 1.59$). The beams, shown in solid blue line in Figure 5-8, are traced until they cross. Similarly, a third beam path from the center of the lens, illustrated as a dashed line, was calculated to indicate the path of light reflected by a particle to the receiving optics and thus the offset distance, d.

A sample ray diagram for the case of 2-/4-beam 120 mm lens configuration with an $\alpha = 60°$ offset angle is shown in Figure 5-9. The model was used to analyze both the 120 mm and 400 mm lenses for all angles from $\alpha = 45° - 90°$ as measured from the window such that 90° corresponds to normal incidence. The results are shown in Figures 5-10A-D. There exists a maximum angle α, beyond which the two probe heads would physically interfere with each other. This value is indicated by the vertical red dotted line. The angle at which the separation distance, d, overlaps with the probe volume width by at least 50% to generate a potential measurement is indicated by the horizontal black line (Jensen & Bertolucci 2012).

Based on Figures 5-10A-D, it is evident that the 120 mm lens is unable to be used in a 3D measurement setup with the current window. The offset angles required for either a 4-beam or 3-beam configuration, 86° and 82° respectively, are both beyond the maximum angle without probe head interference. In contrast, the use of the 400 mm focal length lens is applicable for all angles, due to the smaller associated beam separation angle resulting from longer focal lengths.

The 400 mm lens would always be a more appropriate choice for performing 3D velocity measurements through the current window. However, this thesis was more concerned with the characterization of the facility toward the application to acoustic liners, including development of the centerline velocity as well as cross-duct velocity profiles, specifically with the aim of near-wall velocity profile based shear measurements, discussed in Section 5.5. As previously demonstrated through Equation 5–5, the associated probe volumes of the 120 mm and 400 mm lenses are 56.6 μm and 189 μm respectively, and thus the better spatial resolution achieved with the 120 mm was more applicable to the current goal.

Velocity Data Reduction

As depicted by the direction of the arrows in Figure 5-4, the LDV processor records a positive velocity in the direction of the frequency shift applied by the Bragg cell and outputs a velocity without reference to the actual coordinate system. A coordinate transformation must be applied to the data to transform it to velocity within the correct coordinate system. For centerline velocity measurements, the probe head was oriented as shown in Figure 5-4A, permitting both the green and blue probe to measure a positive velocity of equal magnitude. The raw data is recorded as two channels, corresponding to the two probe colors. The green is recorded as "LDA1" and the blue as "LDA2". The raw channels are transformed to tunnel coordinate system via the generic transformation matrix

$$\begin{bmatrix} U \\ V \end{bmatrix} = \begin{bmatrix} \sin\phi & \cos\phi \\ -\cos\phi & \sin\phi \end{bmatrix} \times \begin{bmatrix} LDA1 \\ LDA2 \end{bmatrix}. \tag{5–15}$$

The 1D bulk velocity and control volume measurement used the single green probe and was aligned with the tunnel floor, discussed in Section 5.1.2, therefore no transformation matrix was necessary.

Outlier rejection was executed via a multivariate "adjusted outlyingness" approach proposed by Hubert & Van der Veeken (2008). For the 1D velocity data, both the local

and reference velocities were used as inputs. The clean data is subjected to transit time weighting previously described in Equations 5–8 and 5–9 to account for the velocity bias of the mean and standard deviation of the measured velocities.

The control volume approach to calculating drag presented in Section 5.5.3 required that the density be known. The density is based on the measured isentropic properties

$$\rho = \rho_0 \left(1 + \frac{\gamma - 1}{2} M^2\right)^{\gamma - 1}. \tag{5–16}$$

The stagnation density, ρ_0, is calculated from the ideal gas equation. Unlike a fan driven tunnel, the flow properties of a blowdown facility can be time dependent due to upstream compressors and air holding tanks out of the control of the tunnel. To accurately account for the true value of density and other flow properties, a LabVIEW code was written to sample the tunnel run conditions along with a time stamp. The code was run simultaneously to the LDV measurements to guarantee that the two times recorded for each measurement were from the same internal computer clock. After outlier rejection was applied to the velocity data, the remaining data was time matched to the nearest set of flow properties. The tunnel control only samples at a constant 5 Hz, however LDV sampling is dependent on seeding density and can reach several thousand samples per second. As a result, there may be several velocity samples that match to the same sampled flow property.

5.2 Fluid Dynamic Characterization

The front of an aircraft's engine nacelle generally accommodates acoustic liners to attenuate the forward propagating noise from the engine's fan and compression stages. Unlike the bounded flow within the GFID, full-scale engine nacelle acoustic liners are subject to developing flow over the liner face that continues up to the fan stage and may never reach a fully developed conditions. The developing flow within this region gives rise to a modification of the boundary condition and thus is an important flow feature of acoustic liner research. However, establishing and testing acoustic liner impedance under

fully developed conditions within the GFID allows for a known environment to reduce measurement inconsistencies and provide common flow characteristics that can be easily replicated by alternate facilities and numerical studies.

The fluid dynamic assessment to characterize the GFID was split between two locations, illustrated in Figure 5-11, each dedicated to a specific flow regime: the entrance region and the fully developed region. The test section was installed at $^{x}/_{D_h} = 0 - 19$ for entrance region tests with optical access between $^{x}/_{D_h} = 2.5 - 16.5$ and moved downstream to $^{x}/_{D_h} = 58.5 - 77.5$, with a viewable range from $^{x}/_{D_h} = 60 - 74$, for fully developed region testing.

A test Reynolds number based on bulk velocity of $Re_{D_h} = 2.25E5$ was chosen to meet three requirements. This regime allows for direct comparison with high Reynolds number turbulence channel flow studies and comparisons to other facilities found in the literature. Additionally, to minimize effects due to compressibility, the speed was chosen such that the local Mach number was less than 0.3 at all duct locations (John & Keith 2006). Finally, in anticipation of acoustic liner drag assessment in Section 5.5, the velocity needed to be as high as possible to maximize the shear influence.

5.2.1 Entrance region

The flow within the entrance region of the GFID was experimentally assessed from $^{x}/_{D_h} = 2.5 - 16.5$ at $Re_{D_h} = 2.25E5$. Two separate experiments were performed in the entrance region analyzing the relation of tunnel bulk velocity and the centerline velocity as compared to similar facilities and run conditions.

The bulk velocity, also referred to as the average velocity, is the result of integrating the local streamwise velocity over the cross-sectional area. The bulk velocity in incompressible flow is constant for all axial distances and thus is convenient to use as a velocity scale for comparing Reynolds numbers of the various channel flows. The bulk velocity was measured using a 2D LDV probe at $^{x}/_{D_h} = 2.5$ as shown in Figure 5-4, corresponding to the furthest upstream position that is optically accessible without blocking one of the

incident laser beams with the window's edge. A 30-point vertical profile was measured at the centerline of the tunnel with $20,000$ velocity samples at each measurement position. The velocity measurements were limited to the range of ${}^{y}/_{D_h} = 0.09 - 0.91$ due to cropping of incident laser beams by the tunnel floor and/or ceiling. Measurement position spacing was defined by two regions, an inner core which spanned the majority of the sampled space at $\pm 18\ mm$ about the centerline in $2\ mm$ increments and the outer region with $0.5\ mm$ increments from $\pm 18.5 - 21\ mm$.

The mean velocity points are shown in Figure 5-12 overlaid by the bulk velocity value of $66.63 \pm 0.37\ {}^{m}/_{s}$, the width of which indicates the 95% confidence interval. The bulk velocity overlaps the majority of the velocity point measurements demonstrating the flow is mostly uniform with the tapering effects of a boundary layer near the outer edges.

Centerline velocity was sampled along the central axis of the tunnel, at $y = z = 25.4\ mm$, from ${}^{x}/_{D_h} = 2.5 - 16.5$ with $25.4\ mm$ between measurement locations. The data are shown in Figure 5-13 with the measured centerline velocity normalized by the bulk velocity as a function downstream distance in terms of duct diameter. For comparison, the measured data is displayed along with data extracted from two experimental high Reynolds number turbulent channel flow studies from Gessner *et al.* (1977) and Melling & Whitelaw (1976) with bulk velocity Reynolds numbers of $Re_{D_h} = 2.5E5$ and $Re_{D_h} = 4.2E4$, respectively.

Even though the three data sets in Figure 5-13 have turbulent Reynolds numbers, direct comparison is difficult because each set has a unique axial starting location and all three display dissimilar centerline velocity axial growth rates. Recall from Chapter 3, Anselmet *et al.* (2009) postulated high-Reynolds number turbulent channel flow entrance region data will collapse when plotted as

$$\frac{U_c}{U_b} = \frac{{}^{X}/_{D_h}}{\left({}^{U_b x}/_{\nu}\right)^{1/5}}. \tag{5–17}$$

Equation 5–17 was applied to the three data sets and the results are shown in Figure 5-14. All three data sets display a linear increase with distance; the two comparison sets maintain the linear trend up to $^{(x/D_h)}/_{(U_b x/\nu)^{1/5}} = 1.5$ which Anselmet *et al.* (2009) described as the limit of the entrance region. Based on this value, the entrance region of the GFID would extend to $^{x}/_{D_h} = 36.2$.

Anselmet *et al.* (2009) reported a slope of 0.185 to best fit the data, displayed by the dashed black line in Figure 5-14. Represented by the solid black line, the data from Gessner *et al.* (1977) was independently fit in a least-squares sense to Equation 5–17 with a resultant slope of 0.167 ± 0.05. Similarly, the GFID entrance region data resulted in a fitted slope of 0.145 ± 0.039. Linear regression was only applied to the Gessner *et al.* (1977) comparative data due to the far upstream starting position compared to Melling & Whitelaw (1976).

The Monte-Carlo simulation generates a distribution of potential values dependent on the distribution of input variables, as described by Coleman & Steele (2009). Variable distributions are generated as an assumed normal or uniform distributions about the provided mean value. The bulk and centerline velocities were assumed normally distributed with matching standard deviations. The uniformly distributed position was accounted for as the sum of three potential uncertainties: the $y = 0$ position of the floor via laser alignment, the repeatability in traverse motion, and the duct height.

The velocity measurements within the entrance region of the GFID reasonably matched the conditions of similar facilities. By matching the proper dimensionless parameters set forth by Anselmet *et al.* (2009), which are associated with the growth of the centerline velocity, the test section with an installed acoustic liner can be appropriately placed for a specific flow characteristic.

5.2.2 Fully developed region

The determination of the fully developed conditions in the strictest sense requires that all flow variables are unchanging with additional streamwise distance. For turbulent

Reynolds number flows in pipes and channels of order $Re_{D_h} = 10^5$, this value can be as high as $x/D_h = 70 - 100$ for higher-order turbulence quantities. Although shear effects, such as boundary layers, generally converge near $x/D_h = 30$, most mean quantities are essentially considered fully developed beyond this point (Zagarola & Smits 1998). This is in agreement with the calculated entrance length value of $x/D_h = 36.2$ determined in Section 5.2.1.

All measurements were made with a plexiglass insert installed in the acoustic liner installation port, referred to here as a "clean" test section. The clean test section allowed for a clearer assessment of the facility influence on the flow. Flow assessment was based on three measured quantities to establish baseline fully developed conditions. First, the centerline velocity is measured to demonstrate that the boundary layers on the enclosing walls have converged and the flow is no longer accelerating. Second, cross duct velocity profiles were sampled at multiple streamwise distances for direct comparison. Lastly, the static pressure within the test section is examined at multiple run conditions.

As illustrated in Figure 5-11, the test section was installed with the upstream edge at $x/D_h = 58.5$, the furthest downstream installation available, allowing for maximum flow development. Velocity measurements were made via a 1D LDV probe with a 120 mm lens allowing for near wall measurements to better resolve the higher velocity gradients compared to the entrance region. The results presented here are also used in Section 5.5 for quantifying the shear effect of the acoustic liner installation.

The centerline velocity was measured with the probe aligned at $y = z = 25.4\ mm$ with 25.4 mm spacing between points. Replicating the entrance length test, 28 spatial location were sampled with 20,000 samples per location. The measured data are shown in Figure 5-15 with error bounds displaying a near constant value of $U_c/U_b = 1.25$. The value agrees with the reported range of $U_c/U_b = 1.1 - 1.3$ for high Reynolds number turbulent channel flows (Anselmet *et al.* 2009). Therefore, the developing boundary layers have converged and are no longer accelerating an inviscid core.

Shear effects, including boundary layers, are subject to the effects of turbulence and consequentially take longer than mean centerline velocity to reach a steady state value. Mean 1D velocity profiles were measured at two streamwise locations of $^{x}/_{D_h} = 63$ and 72, chosen to measure the flow one duct diameter upstream and downstream of the liner where the effect of the liner on the boundary layer may be evident. This test was repeated with an acoustic liner installed for a comparative study, included in Section 5.5. The cross-duct profiles were composed of 63 sample locations over two regions: the sparse central core and a dense near-wall region with 1 mm and 0.5 mm spacing, respectively.

The full cross-duct profiles are shown in Figure 5-16A with uncertainty bounds represented by the lines of equivalent color. The two profiles match within experimental uncertainty demonstrating that viscous effects have diffused completely and the profiles are no longer developing with increased distance.

Additionally, the same data was compared to two turbulent channel flow cases from Gessner (1964) with Reynolds numbers $Re_{D_h} = 1.5E5$ and $Re_{D_h} = 3.0E5$ bounding the value tested in this thesis of $Re_{D_h} = 2.25E5$, shown in Figure 5-16B. Gessner (1964) only presented a half duct profile for each, hence the GFID data was rescaled to the same dimensions for direct comparison. Again, the data match within experimental uncertainty at both the lower and higher Reynolds number cases.

The uncertainty bounds illustrated in Figure 5-16 stem from a Monte-Carlo analysis of the measured velocity. The Monte-Carlo approach is based on that presented by (Coleman & Steele 2009) accounting for the bias error of and the measured velocities. While there can be several sources of bias error in LDV measurements, including particle response, probe volume size, residence time, and geometric errors (Semaan 2010). On the geometric error has yet to be acknowledged in this chapter. The geometric error accounts for the assumed measured location to the actual location. The difference in these two points is a function of the traverse, machining tolerances, and method of alignment. The traverse has a reported repeatability of 3 μm, machining tolerances were ± 0.005 $in.$, and

the alignment of the probe volume to the surface account for an uncertainty of half the probe volume thickness. The sum of these errors are the bias errors used for uncertainty calculations and are assumed uniformly distributed. The Monte-Carlo method uses the mean and standard deviation of each measured quantity to build a distribution, uniform for bias error and normal for LDV velocity samples. The distribution is then sampled randomly to calculate desired quantities; the velocity profiles in this case.

Finally, the static pressure was measured along the test section length. For internal flows, a constant pressure drop across a finite distance is indicative of fully developed flow. In addition, static pressure measurements can be helpful in assessing leakage and small disturbances that may otherwise be hidden within turbulent streamwise velocity. Due to the relative simplicity and speed of the test, measurements were made at not only the test Reynolds number, $Re_{D_h} = 2.25E5$ corresponding to a $M = 0.22$ flow, but also $M = 0.3,\ 0.4$ and 0.5 as these values could provide insight for future testing at higher speeds.

Measurements were made using the static pressure wall insert described in Section 4.4 and are shown in Figure 4-8. Due to limited measurement capabilities, the 29 static pressure taps were sampled in two sets for each run condition illustrated in Figure 5-17; taps $2-15$ and $16-29$ measuring set 1 (upstream) and set 2 (downstream), respectively. The setup was switched to the other set without turning off the tunnel to maintain settled run conditions. The most upstream pressure tap, port 1, was reserved for both sets as a reference port for each differential measurement. Each static pressure set was sampled via a 1 psi differential Pressure Systems Inc. (PSI) pressure scanner. In turn, port 1 is measured via a PSI $5\,psi$ differential pressure scanner referencing the tunnel static pressure ring at the nozzle. Pressures were sampled at 5 Hz synced to the GFID tunnel controller for simultaneous recording of tunnel conditions.

The local measured pressure at each port, p_i was converted to a coefficient of pressure, C_p, through the ratio of the pressure drop from the static ring at the nozzle

to local port, by the dynamic pressure

$$C_p = \frac{(P_i - P_\infty)}{\frac{\gamma}{2} P_\infty M^2}. \tag{5–18}$$

The compressible version of the dynamic pressure was used to account for potential compressibility effects from the higher Mach number tests and is equivalent to the traditional definition $q = \frac{1}{2}\rho V^2$ at incompressible run conditions (John & Keith 2006).

The results are shown in Figure 5-18 displaying the 29 measured values as a function of downstream distance with calculated uncertainties displaying a seemingly linear downward trend. The data show a small deviation from the trend near $x/D_h = 71.5$, which increases at higher Mach numbers. This location corresponds to the downstream acoustic liner installation port edge. Linear regression of each of the four Mach numbers was applied and the resultant R^2 value is displayed in the legend of the Figure 5-18. All the data sets are well fit by the linear regression with R^2 values of 0.96 or greater, indicating the pressure drop is linear, and the pressure and shear have reached an equilibrium.

The flow measured at a test section installation at $x/D_h = 58.5$ was demonstrated to be fully developed. Three experiments examined the streamwise development of centerline velocity, comparative velocity profiles, and a linear pressure gradient within the test section. With the fully developed assumption confirmed, acoustic testing at this location can be performed under a known flow environment.

5.3 Acoustic Characterization

5.3.1 Near-Anechoic Reflection Experiment

Acoustic characterization of the GFID centers on the evaluation of the primary assumption in many of the impedance eduction methods presented in Section 3.2, that the pressure field in the duct is composed of a plane progressive wave. The assumption is critical for several eduction methods, although difficult to physically realize due to potential impedance mismatches at the boundaries and area changes in the duct. The wind tunnel and acoustic waveguide combination inherent to the GFID design necessitates

a diffuser to slow the high speed flow, requiring an expansion of the cross-sectional area. Similarly, turns in the exhaust ducting and other non-idealities all present potential reflection sources that can propagate upstream, increasing the noise floor and contaminating measurements.

The anechoic diffuser introduced in Section 4.5 was fabricated to reduce the upstream acoustic propagation generated by downstream reflection sources. The effectiveness of the termination was experimentally determined by measuring the reflection coefficient of the anechoic diffuser, essentially a relative measure of the reflected acoustic energy. For comparison the hard wall fiberglass diffuser, exclusively utilized for all LDV measurements, was also tested.

Recall from Section 4.5 and illustrated in Figure 4-10, that the internal boundaries of the anechoic diffuser are themselves locally reactive acoustic liners. The variable honeycomb depth increases with downstream distance and thus higher frequencies are attenuated first. Low frequency attenuation corresponding with large honeycomb depths increases further downstream. Even though attenuation is a function of frequency and axial distance, no microphones can be installed in the diffuser itself. Instead, all measurements are made upstream within the test section, and the diffuser is lumped as a single unknown impedance at the sample plane indicated in Figure 5-19. The effectiveness of the termination will be quantified by measuring the reflected acoustic energy, determined by the reflection coefficient using the two-microphone method (TMM) (E1055-98 1998).

The measurement was carried out with a clean test section, i.e. no acoustic liner installed, and the test section was installed at the furthest downstream position of the GFID. Two Brüel & Kjær 4938 1/4 $in.$ microphones were installed in the downstream auxiliary port and a portable Brüel & Kjær Pulse Analyzer System was used for both data acquisition as well as acoustic signal generation via a Crown $XLS1500$ amplifier. A periodic-random signal was generated between $300 - 3500\ Hz$ with $8\ Hz$ bin

width. Output gain was adjusted such that the measured pressure at the test frequency was a minimum of 10 dB above the noise floor, as per the test protocol described in (E1055-98 1998). The microphones were then rotated 180° and the test was repeated in this "switched" configuration, eliminating the need for microphone phase calibration.

The acoustic pressures at the two microphones, P_1 and P_2, were sampled as a function of frequency, $\omega = 2\pi f$, and are expressed as

$$P_1(\ell + s, \omega) = P^+ \left(e^{j\kappa(\ell+s)} + Re^{-j\kappa(\ell+s)} \right), \tag{5–19}$$

and

$$P_2(\ell, \omega) = P^+ \left(e^{j\kappa\ell} + Re^{-j\kappa\ell} \right), \tag{5–20}$$

respectively. The reflection coefficient, R, is written in terms of the transfer function, $\hat{H}_{12}$, between P_1 and P_2,

$$R = \frac{H_{12}(\omega) - e^{-j\kappa s}}{e^{j\kappa s} - H_{12}(\omega)} e^{j2\kappa(s+\ell)}. \tag{5–21}$$

Figure 5-20 shows the reflection coefficient, R, versus frequency for both the fiberglass diffuser and the anechoic diffuser. The vertical thickness of each color illustrates the 95% confidence interval of the measurement as determined by a Monte-Carlo simulation based on geometric and ambient thermodynamic conditions described in Schultz (2006). The anechoic diffuser demonstrates a reflection coefficient nearly half that of the hard wall fiberglass diffuser with the highest reflection coefficients at low frequencies. The frequency dependent reflection coefficient demonstrates a maximum of 0.19 at 300 Hz decreasing to less than 0.13 for higher frequencies. In contrast to the anechoic diffuser, the hard wall fiberglass diffuser displays much larger reflection coefficients, upwards of 0.40 at 324 Hz. Additionally, the hard wall diffuser is highly frequency dependent demonstrating large spikes in the data, potentially due to a structural resonance of the relatively thin-wall fiberglass of 0.175 in. In both cases, the cut-on frequency of the first higher-order mode of the facility is evident near 3400 Hz.

5.3.2 Description of the Acoustic Liners

All acoustic experiments used one of two locally reactive acoustic liners, shown in Figure 5-21, borrowed from the NASA LaRC Liner Physics Group. During testing, the liners are installed in the top acoustic liner installation port of the test section, described in Section 4.4, and held in place by a custom fabricated liner holder secured on the top by eight screws. An illustration of the installation and primary dimensions are shown in Figure 5-22.

The first liner is a conventional perforate acoustic liner composed of a three stacked layers. The top layer is a perforate facesheet, shown in detail in Figure 5-23A. The aluminum facesheet is 0.20 $in.$ thick, with 0.045 $in.$ diameter holes in a staggered hole pattern with 0.125 $in.$ hole-to-hole spacing. Both liners have exterior dimensions of 2.50×16.36 $in.$, overlapping the walls of the test section by 0.25 $in.$ on each side to reduce edge effects on the flow.

The second liner has identical outer dimensions as the perforate liner, but uses a dense woven stainless steel wire mesh facesheet, shown in close-up view in Figure 5-23B. Unlike the perforate liner, the wire mesh facesheet is not permanently bonded to the honeycomb cells. During testing, the wire mesh was held in place by applying a spray adhesive to the small top surface of the honeycomb cells to keep the facesheet in place. Tape was applied to the leading and trailing edges of the liner to eliminate the possibility of air penetrating underneath the liner.

5.4 Impedance Eduction Using the Single Mode Method

As described in Chapter 3, there are many models and algorithms available for impedance eduction. The "infinite waveguide method" developed by Armstrong (1974), and later used under the name of the single mode method (SMM) in Jones *et al.* (2004*b*) by NASA was chosen and used for impedance eduction in this investigation due to the simplicity and accuracy in the presence of a plane progressive wave (Jones *et al.* 2004*b*).

The anechoic termination, tested in Section 5.3, minimizes upstream acoustic propagation, aiding the assumption of a single mode by restricting upstream reflections.

The SMM is the sole impedance eduction technique used in this thesis. Additionally, this thesis is the first study to use the particular wire mesh acoustic liner and thus no other published results are available for comparison. Therefore additional steps were put in place to validate the method and build confidence in the results. The process is based on two comparative evaluations using experimental data from both UF and NASA LaRC facilities prior to applying the method to the GFID. First, educed impedance of the wire mesh with zero mean flow in the GFID using the SMM is compared to testing the same liner under normal incidence conditions. The normal incidence test was performed in a separate normal incidence waveguide using the two-microphone method (TMM), an impedance testing standard E1055-98 (1998). Therefore, it was deemed important that the present data be compared to data with trusted results even though this represents a limited case by negating the Mach number dependance of the SMM. For the second step, the SMM is applied to published benchmark grazing flow data from Jones *et al.* (2005) and the results are compared with the paper's two advanced FEM-based methods for impedance eduction. With the confidence that the data reduction process provided accurate results from the process validation steps, the impedance of the wire mesh sample is educed as a function of test frequency. The wire mesh liner experimental data is shown for all frequencies and Mach numbers followed by the steps used to validate the processing method. Each evaluation method is described with results following.

5.4.1 Experimental Setup and Application of the Single Mode Method

The SMM educes the impedance of an acoustic liner by measuring the cross spectrum over the liner relative to an upstream reference microphone. The studies published by Armstrong (1974) and Jones *et al.* (2004*b*), presented in Section 3.2.2, both used two microphones for their experiments, a stationary microphone upstream of the liner, and a second microphone installed in a traversable section of the wall opposite the liner. The

GFID test section was designed with discrete microphone locations in lieu of a traverse bar to reduce air leakage inherent to a sliding traverse (Jones *et al.* 2004*a*). While a traverse bar has more flexibility over microphone sample locations, the GFID's multiple microphones have the advantage of allowing shorter run times through simultaneous sampling, maintaining more consistent run conditions over the course of the experiment.

Ten flush-mounted microphones were installed in the aluminum microphone wall of the GFID, positioning the microphones along the horizontal mid-plane of the tunnel of the wall spanning the central 8.5 $in.$ of the 16.36 $in.$ long liner with 0.85 $in.$ spacing between microphones, as depicted in Figure 5-22. Measurements were made along the central portion of the acoustic liner to minimize contamination from evanescent modes generated at the leading and trailing edges due to impedance mismatches. A reference microphone was installed at the upstream side of the rotational two-microphone holder within the upstream auxiliary port, four hydraulic duct diameters upstream of the leading edge of the liner. Including the reference microphone, a total of 11 $^1/_4$ $in.$ microphones were used: nine GRAS $40BE$ and two Brüel & Kjær 4939. All microphones were individually calibrated outside of the tunnel using a 94 dB 1000 Hz signal generated by a Brüel & Kjær 4231 pistonphone sound calibrator and were within 1% of manufacturer calibrated specifications. The pistonphone only allows for amplitude calibration.

Data acquisition was performed by LabVIEW running on a National Instruments (NI) PXI$-1042Q$ chassis via a 16 channel NI PXI-4498 DAQ card, simultaneously sampling all microphones. An Agilent $33220A$ function generator provided the waveform to the amplifier and speaker for acoustic excitation at discrete frequencies from f=$500 - 3000$ Hz in 500 Hz increments. The function generator amplitude was adjusted until 130 dB was measured by the reference microphone, recreating the conditions described by Jones *et al.* (2005). All frequencies were tested at four bulk Mach numbers: $M = 0.0,\ 0.1,\ 0.3,\ 0.5$. Data are acquired at a sampling frequency of 10,000 Hz for 30 seconds. The data are

split into 300 blocks of 1000 samples each, resulting in a 10 Hz bin width. The blocks are averaged using a Hanning window with a 75% overlap.

Figures 5-24 - 5-27 show the measured complex pressure for all tested Mach numbers, respectively as combined plots of unwrapped relative phase in blue and the sound pressure level (ref. 20 μPa) in green, versus the distance from the leading edge of the liner. Recall from Equation 3–15, that the SMM assumes a single dominant mode propagating in the positive x-direction. If these conditions are met, both the relative phase and SPL will exhibit a linear decay demonstrating a loss of acoustic energy, where in the $e^{j\omega t}$ system chosen manifests as a negative slope of both values with increased distance.

The measured data predominantly follows the expected downward trend excluding a few cases in which the SPL demonstrates a deviation from a linear trend. While each case will be discussed with the applied linear fits and resultant educed impedance in Section 5.4.4, the $f = 500\ Hz$ case merits note. Qualitatively, it is evident that across all run conditions, including quiescent, the $f = 500\ Hz$ case displays a reasonably linear relative phase whereas the SPL values are erratic with no discernible downward trends; even intensifying at some locations. Increased SPL values imply a breakdown of necessary model assumptions, including the presence of upstream propagating waves. However, similar results at $f = 500\ Hz$ were observed and discussed in the literature by Jones *et al.* (2005) and were attributed to possible longitudinal standing waves. With the inability of the model to handle such cases, the $f = 500\ Hz$ cases are absent from subsequent plots and discussions.

As the pressure was sampled at discrete locations, the two terms which make up the axial wavenumber, κ_x, are easily calculated from Equation 3–15. The two terms in Equation 3–15 assume a constant slope and thus the data were fit to a line in a least-squares sense. A few of the cases demonstrated a rise in SPL near the downstream end of the installed liner and so only the linear region was used for linear regression. Unlike the $f = 500\ Hz$ case, these cases are considered limited but not failures as

they all contain a portion of the data demonstrating the downward trend indicative of the expected attenuation. Upon calculating the axial wavenumber for each case, the impedance value was then extracted from Equations 3–16 and 3–17. Both impedance results presented and the implementation of the SMM performed here will be referred to as "UF SMM" for the remainder of this thesis. Table 5-3 provides the mean educed impedance values, the results are plotting with uncertainty for each method in their respective sections.

5.4.2 Validation of the Single Mode Method Via Normal Incidence Under Zero Mean Velocity

The first method compares the educed impedance for the case of zero mean flow against an ASTM standard for impedance eduction in a normal incidence impedance tube. The two-microphone method has the advantage of computational speed and simplicity, however the method inherently assumes a quiescent environment and thus any comparisons must be performed without flow.

The wire mesh acoustic liner was secured to the end of a normal incidence tube (NIT) at UF, as illustrated in Figure 5-28. The NIT is a fully enclosed hard-walled acoustic waveguide sealed on one end by a speaker and the other by the sample under test. The NIT has a square 25.4×25.4 mm cross section and is 96 cm in length with 1 $in.$ thick aluminum walls. Excitation was provided by a BMS $4590P$ speaker up to the first cut-on mode of the waveguide at 6.7 kHz. Signal generation and data acquisition were performed by a Crown $XLS1500$ amplifier and a Brüel & Kjær Pulse Analyzer System. Input was periodic-random noise with $\delta_f = 8$ over the frequency range of 300 Hz to 6.7 kHz.

Following ASTM standard E1055-98 (1998), two Brüel & Kjær 4138 $^1/_8$ $in.$ microphones are installed in a microphone rotation plug, spaced $s = 20.7$ mm apart and $\ell = 32.1$ mm from the sample. The test was repeated with the two microphones rotated 180° to average out small amplitude and phase differences and the geometric mean of the two cases is used. The methodology behind the TMM was detailed in Section 5.3.

The complex specific acoustic impedance of the unknown sample, Z_N, is related to the characteristic impedance of the medium, Z_0, and the reflection coefficient

$$R = \frac{Z_N - Z_0}{Z_N + Z_0}. \tag{5–22}$$

The unknown specific acoustic impedance of the sample is normalized by the characteristic impedance of air, $\rho_0 c_0$, and can be split into the the real and imaginary components,

$$\zeta = \frac{Z_N}{\rho_0 c_0} = \theta + i\chi, \tag{5–23}$$

where θ is the normalized specific acoustic resistance and χ is the normalized specific acoustic reactance. The normalized acoustic impedance values using the TMM are compared to the $M = 0.0$ UF SMM case in Figure 5-29.

The plots demonstrate that the UF SMM matches the normalized impedance values of the TMM within experimental uncertainty. Both methods agree on the resonant frequency, f_{res}, of the liner under no flow conditions defined where the normalize reactance displays a positive zero-crossing at approximately $f_{res} = 2500\ Hz$. The comparison to the NIT provides initial confidence of the facility and data reduction process for a special case with no grazing flow.

5.4.3 Validation of the Single Mode Method Via Benchmark Data With Mean Flow

The second method employs the full SMM algorithm testing the Mach number dependency at multiple frequencies versus published benchmark data from Jones *et al.* (2005). The data are presented in Jones *et al.* (2005) as relative phase and SPL values measured with corresponding distance from the liner's leading edge.

The acoustic liner tested in Jones *et al.* (2005) was a high-resistance liner, designated the CT57. Instead of either a wire mesh or perforate facesheet atop honeycomb cells, the liner was composed of narrow 0.06 mm diameter ceramic tubes 85.6 mm deep, rigidly terminated by a hard wall back plate providing support and enabling a locally

reactive boundary condition by acoustically isolating each cell. The ceramic tubes, while not directly applicable to real-world engine nacelle applications, provide a linear response for a range of Mach numbers and sound pressure levels, which is useful for facility benchmarking and comparisons. The reader is directed to Jones *et al.* (2005) for additional details and discussion regarding the CT57.

The benchmark data was taken in the GIT facility detailed in Section 3.3.4. Jones *et al.* (2005) included data from the CT57 for three SPL values, six Mach numbers, and over the frequency range from $500 - 3000\ Hz$. In this thesis, only the $M = 0.255$ case at $130\ dB$ was used as the Mach number is nearest to the test conditions presented in Section 5.4.4. The results from the benchmark data using the UF SMM code were compared against the published impedance results generated by two FEM based approaches, the "2D-FEM", and the "Q3D-FEM". The results with corresponding measurement uncertainty of the UF SMM data are shown in Figure 5-30. Note that the uncertainty estimates shown are solely based on the 95% confidence of the linear regression as no information regarding run conditions was available for the benchmark case.

Similar to the GFID data, the $f = 500\ Hz$ case failed to produce a reasonable fit and was excluded from Figure 5-30 and ensuing discussion. The UF SMM code captures the overall trends of both the normalized resistance and reactance, although the normalized resistance is slightly over-predicted. The UF SMM does capture both the resonance and anti-resonance of the liner at the positive and negative zero-crossing of the normalized reactance, respectively at approximately $f = 1000\ Hz$ and $f = 2000\ Hz$. The largest discrepancy between all the methods occurs near the anti-resonance. Jones *et al.* (2005) noted that the two FEM-based models demonstrated a disparity at anti-resonance in contrast to the otherwise excellent matching.

The benchmark data provided a good comparison to published data taken in a well documented and trusted facility. The comparison provides confidence in the methodology

and implementation of the SMM algorithm and the GFID to move forward to educe an untested acoustic liner.

5.4.4 Experimental Impedance Eduction of a Wire Mesh Acoustic Liner in the Grazing Flow Impedance Duct

After validating the GFID data analysis process, the same method was applied to the remaining data taken in the GFID for the previously untested wire mesh liner. The results of the $M = 0.0$ case are repeated along with the flow cases of $M = 0.1,\ 0.3$ and 0.5, shown in Figure 5-31. The uncertainty estimates indicate the 95% confidence bounds of the extracted normalized complex impedance values including tunnel run conditions.

In Figure 5-31 the largest uncertainty across all Mach numbers occurs at $f = 1000\ Hz$, the lowest frequency case demonstrating a linear fit. However, the disparity between the $f = 1000\ Hz$ case and the remaining frequencies decreases with higher Mach number. Qualitatively, the raw $f = 1000\ Hz$ SPL trends shown in insert B of Figures 5-24 - 5-27 demonstrate the largest deviation from a linear trend with increased Mach number and thus the error in linear regression was higher. The $M = 0.5$ case across all frequencies demonstrates the largest error, although the normalized resistance stay within the positive domain.

Inspection of the raw data plotted in Figures 5-27 A-F demonstrate an increase in SPL toward the downstream end of the liner for all cases indicative of upstream propagating waves. Additionally, the higher shear effects associated with large relative Mach number may be invalidating the strict uniform flow assumption inherent to the model by introducing refraction effects near the walls (Nayfeh *et al.* 1975). To allow for additional insight and discussion of the trends and underlying physics of the normalized impedance results, the values are repeated in Figure 5-32 excluding the questionable $M = 0.5$ case.

The exclusion of the $M = 0.5$ in Figure 5-32 allows for rescaling of the data to more clearly emphasize trends. The normalized reactance decreases with increased

Mach number pushing the zero-crossing and implicative liner resonance, f_{res}, to higher frequencies from approximately $f_{res} = 2500$ for $M = 0.0$ to past $f_{res} = 3000\ Hz$ for $M = 0.3$. In contrast, the normalized resistance increased with higher Mach number, however was relatively insensitive to excitation frequency. The pressure field measured with the wire mesh liner installed provided a linear slope indicative of a more strongly dominant acoustic mode compared to the perforate liner and thus more applicable for the application of the SMM. Unlike the CT57 liner of the NASA benchmark data in Section 5.4.3, the anti-resonance was beyond the cut-on frequency of the GFID.

5.5 Drag Contribution By An Acoustic Liner With Acoustic Excitation

With the tunnel characterized and shown to be capable of educing the impedance of an acoustic liner under flow, an effort was made to quantify the influence of an acoustic liner subject to acoustic excitation on the shear stress of the surrounding flow. This influence was studied through three indirect velocity profile techniques using LDV velocity measurements: a centerline boundary layer curve fitting technique, momentum integral analysis of centerline cross-duct profiles, and a half-duct control volume analysis. Each of the experiments was performed both with and without an acoustic liner installed for direct comparison. All velocity measurements were performed at $^{x}/_{D_h} = 63$ and 72.

The LDV velocity measurements required oil based seeding and as a result neither the anechoic diffuser nor the wire mesh liner used for the acoustic impedance eduction tests were able to be used. Instead the previously described perforate acoustic liner, introduced in Section 5.3.2 was installed.

It was assumed that the largest influence of the liner would be determined through acoustic excitation at the liner resonant frequency. As the liner had not been tested in flow, the resonant frequency was unknown. Two GRAS $40BE$ $^1/_4$ $in.$ microphones were installed, one in each of the auxiliary ports, upstream and downstream of the installed acoustic liner. Acoustic excitation and data acquisition were provided by a Brüel & Kjær Pulse Analyzer System and a Crown $XLS1500$ amplifier with input of

periodic-random noise of 800 discrete frequencies from 300 Hz to 3.5 kHz. The test was operated at $Re_{D_h} = 2.25E5$. The coherence between the two microphones is plotted in Figure 5-33. The coherence displays a 500 Hz drop surrounding 1750 Hz. The lack of coherence between the two microphones indicates that the this frequency gap is subject to the most loss in acoustic energy. The value of $f = 1750$ Hz was assumed to be the resonant frequency and the all shear testing was performed at this value with a 130 dB (ref. 20 μPa) signal as measured by the upstream microphone.

5.5.1 Two-Dimensional Boundary layer approximation using Spalding Fit

The downstream boundary layer profile on the sample side was extracted from the cross-duct velocity profiles up to $y = {}^{D_h}/_2$. The extracted velocity values and associated wall-normal positions were input to a code that iteratively applied them to the Spalding turbulent boundary layer fit, Equation 2–25, solving for the friction velocity, $u^* = \sqrt{{}^{\tau_w}/_\rho}$, and wall offset distance. The process was added into a Monte-Carlo simulation to build up a distribution of friction velocities adjusting the normally distributed velocity and uniformly distributed position at each acquisition location (Coleman & Steele 2009). The Spalding fit is not applicable to the outer layer and thus only wall-normal positions corresponding to y^+ values less than 1000 were used for parameter extraction (White 2006).

The non-dimensional boundary layer profiles are shown in Figure 5-34, where the shaded regions indicates the uncertainty bounds from the Monte-Carlo simulation. Table 5-4 provides the values for variables extracted from the 2D boundary layer fit. The skin friction coefficient results for the hard wall and acoustic liner overlap within the experimental uncertainty.

5.5.2 Momentum-Integral

The second method uses the full cross-duct profile to approximate the skin friction coefficient with a variant of the classic momentum integral equation. Originally proposed by Kármán, the method is generally applied to flat plate boundary layers, however can be

used with internal flows when written as (Anselmet *et al.* 2009)

$$C_f = 2\frac{d\theta}{dx} - \theta\frac{H+2}{\rho U_c^2}\frac{dp}{dx}. \tag{5–24}$$

noting that θ and H are the boundary layer momentum thickness and shape factor, respectively. Unlike the boundary layer curve fit, this method takes into account the pressure drop across the liner.

The static pressure in the test section was measured, following the steps described in Section 5.2.2. The results are shown in Figure 5-35 overlaid with the data of Figure 5-18 when no liner was installed. The vertical dashed lines indicate the location of the leading and trailing edge of the acoustic liner. The static pressure measured both upstream and downstream of the liner appear to match the no liner case. However, across the liner there is a notable pressure difference between the two cases. The values of θ and H for Equation 5–24 are extracted from the downstream velocity profile under the substantiated assumption that the flow is fully developed.

The results from the momentum integral method are listed in Table 5-5. The skin friction values within the uncertainty range are largely meaningless as the encompass they non-real negative skin friction implying flow reversal as well as skin friction values indicative of a much higher speed flow. The results indicate that the method is more sensitive to large uncertainties in the input variables.

5.5.3 Control Volume Analysis

The final method to quantify the shear effect applied a control volume approach and integrated the momentum flux through two control surfaces bounding the acoustic liner, illustrated in Figure 5-36. The application of a control volume analysis was less dependent on near-wall influence compared to the cross-duct profile methods, as the majority of the momentum is located in the central core of the duct.

The control surfaces were defined by a grid pattern with spacing based on Gessner *et al.* (1977), illustrated in Figure 5-37, emphasizing the central core of the flow. Due

to the stable symmetry planes imposed from secondary flow patterns in a turbulent channel flow previously discussed in Chapter 2, only a single octet would be necessary to measure. However, as the influence of the acoustic liner on one wall is specifically under investigation no such assumption could be made and only the vertical symmetry plane which bisects the liner was assumed accurate.

The integral form of the conservation of momentum in the streamwise direction under a steady flow assumption can be expressed as,

$$\sum F_x = \tau_w A_\tau + P_1 A_1 - P_2 A_2 = \iint_{cs_1} -u_{x1}\rho_1 v_1 \cdot dA_1 + \iint_{cs_2} u_{x2}\rho_2 v_2 \cdot dA_2, \tag{5–25}$$

where A_τ is the wetted area the shear stress acts upon. The numbered subscripts refer to the control surfaces illustrated in Figure 5-36. Equation 5–25 indicates that the shear force applied at the boundaries is balanced by the sum of the pressure drop and loss to momentum.

In a purely incompressible fully developed flow, the momentum terms would cancel out and pressure would balance shear stress directly. However, the measurement determines if the acoustic liner imposes an additional loss mechanism imposed by the acoustic liner under excitation. The pressure and momentum at the streamwise control surfaces act on areas A_1 and A_2 of dimensions $H \times H$, where H is the wall height and width of the square duct. The shear stress acts on all four walls over a distance L. Writing out the areas and noting that the velocity normal to the control surface and the relative velocity are equal at each location,

$$\sum F_x = \tau_w \left(4HL\right) + (P_1 - P_2)H^2 = 2\int_0^{H/2}\int_0^{H} \rho_2 u_2^2 dz dy - 2\int_0^{H/2}\int_0^{H} \rho_1 u_1^2 dz dy. \tag{5–26}$$

The assumed vertical symmetry plane at $y = {}^{H}/_{2}$ allows for integration on only half the duct width; this value is doubled to encompass the full duct cross-section. Equation 5–26

can be rewritten to isolate τ_w, and noting that $\Delta p = P_1 - P_2$,

$$\tau_w = \frac{-H^2}{4HL}\Delta p + \frac{2}{4HL}\left(\int_0^{H/2}\int_0^{H} \rho_2 u_2^2 dzdy - \int_0^{H/2}\int_0^{H} \rho_1 u_1^2 dzdy\right). \quad (5\text{–}27)$$

The shear stress is cast in terms of the non-dimensional coefficient of friction, C_f, by diving each term of Equation 5–27 by the dynamic pressure. The final simplified equation is then written as

$$C_f = \frac{H}{4L}\frac{-\Delta p}{\frac{\gamma}{2}p_\infty M^2} + \frac{1}{2HL}\frac{1}{\left(\frac{\gamma}{2}p_\infty M^2\right)}\left(\int_0^{H/2}\int_0^{H} \rho_2 v_2^2 dzdy - \int_0^{H/2}\int_0^{H} \rho_1 v_1^2 dzdy\right). \quad (5\text{–}28)$$

The measured velocity contours are displayed in Figure 5-38. The images illustrate the symmetric high-velocity central core with slight bulging out toward the duct corners indicative of secondary velocity flow effects. The same data is presented from an alternative perspective in Figure 5-39 with higher velocities both shown in color gradient and increased elevation. This view more clearly illustrates the secondary velocity effects at $^z/_{D_h} = 0.5$ and the central core velocity.

Similar to the 2D centerline profile, each position and velocity were perturbed to generate a distribution of samples. A no-slip velocity condition was imposed on tunnel boundaries and linearly fit to the nearest sampled location. Unlike the centerline, as the LDV probe volume was translated in both the y and z plane, the non-symmetric size of the 1D probe volume had to be take into account by allowing the z-dimension to be perturbed to the full 372 μm length of the probe volume while the y-dimension was only perturbed with 58 μm, as determined by Equations 5–7 and 5–6, respectively.

The results of the numerical integration are included in Table 5-6. Similar to the momentum-integral and boundary layer curve fit approaches, the skin friction values of the acoustic liner control volume and the hard wall do not demonstrate a discernible difference.

5.5.4 Concluding Remarks of Fluid Dynamic Results

The shear effect of an acoustic liner with resonant acoustic excitation was determined through three velocity profile-based techniques: a) curve fitting a 1D boundary layer profile, b) applying a momentum-integral analysis to a cross duct profiles up and downstream of the acoustic liner, and c) via a control volume analysis through a half-duct plane. The results of all shear experiments are listed in Tables 5-4, 5-5, and 5-6. The skin friction results of the three experiments with the acoustic liner installed and excited at the liner's resonant frequency overlap those of the hard-wall case within experimental error.

The indirect velocity profile methods applied were unable to demonstrate that the installation and excitation of the acoustic liner had any discernible effects to the shear contribution. As the shear influence of the acoustic liner is a function of the wetted area, a longer liner may have a larger impact. The future application of a direct or quasi-direct measurement of the shear stress by implementing a MEMS floating element sensor or oil-film interferometry may prove beneficial.

Table 5-1. Maximum negative velocity using the 120 mm lens

Probe configuration	Low Velocity [m/s]	High Velocity [m/s]
3-beam	-54.26	314.6
4-beam	-38.61	223.8

Table 5-2. Maximum negative velocity using the 400 mm lens

Probe configuration	Low Velocity [m/s]	High Velocity [m/s]
3-beam	-179.9	1043
4-beam	-127.2	737.7

Table 5-3. UF SMM educed impedance values of a wire mesh liner shown in Figure 5-31

	$M = 0.0$		$M = 0.1$		$M = 0.3$		$M = 0.5$	
Freq. $[Hz]$	ϕ	χ	ϕ	χ	ϕ	χ	ϕ	χ
1000	1.29	-1.11	1.07	-0.54	1.61	-1.35	7.52	-1.64
1500	0.88	-0.95	1.10	-1.46	1.86	-2.87	4.52	-3.31
2000	0.81	-0.48	1.06	-0.79	1.83	-1.71	2.21	-1.31
2500	0.79	-0.03	1.19	-0.09	2.02	-0.66	1.93	-1.41
3000	0.93	0.27	1.65	0.40	2.32	-0.14	2.60	-1.13

Table 5-4. 2D boundary layer approximation of friction velocity and shear stress

Wall configuration	Friction Velocity [m/s]	Shear stress [Pa]	$C_f \times 10^{-3}$
Hard Wall	3.08 - 3.32	11.22 - 13.04	3.30 - 3.92
Acoustic liner	3.05 - 3.25	11.37 - 12.25	3.36 - 3.91

Table 5-5. Momentum-integral analysis variable approximations

Wall configuration	$C_f \times 10^{-3}$
Hard Wall	-1.20 - 4.50
Acoustic liner	-1.04 - 5.76

Table 5-6. Control volume analysis for estimation of friction coefficient

Wall configuration	$C_f \times 10^{-3}$
Hard Wall	4.59 - 6.57
Acoustic liner	3.51 - 5.24

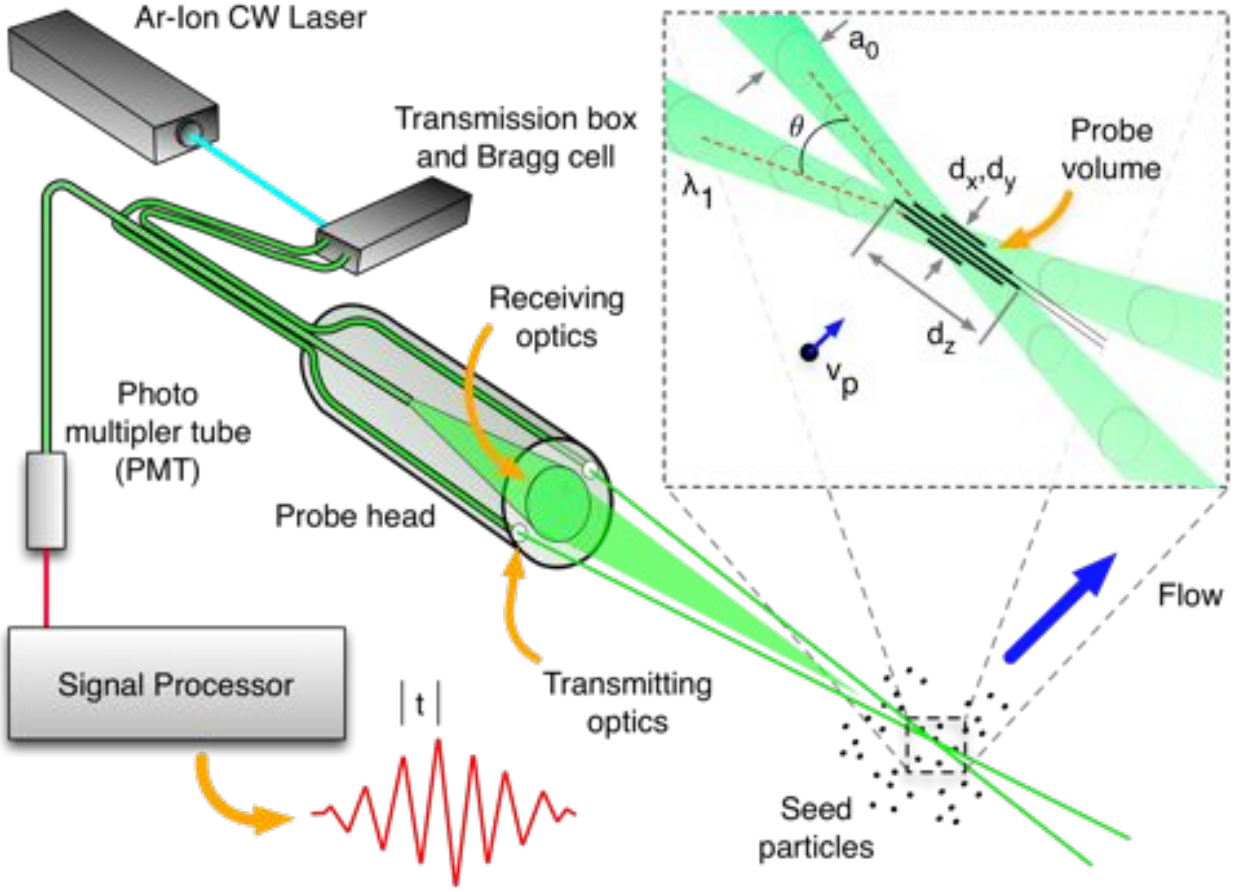

Figure 5-1. Basic principal and setup of laser Doppler velocimetry (LDV), adapted from Dantec Dynamics. Integrated Solutions in Laser Doppler Anemometry. Publication 318_v1.($Page 3, Figure 1$

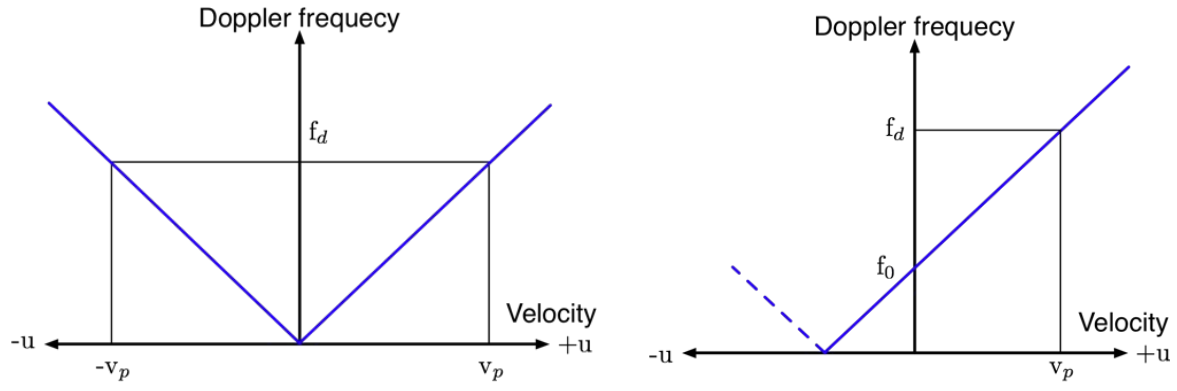

Figure 5-2. Doppler frequency workspace with resultant velocity.

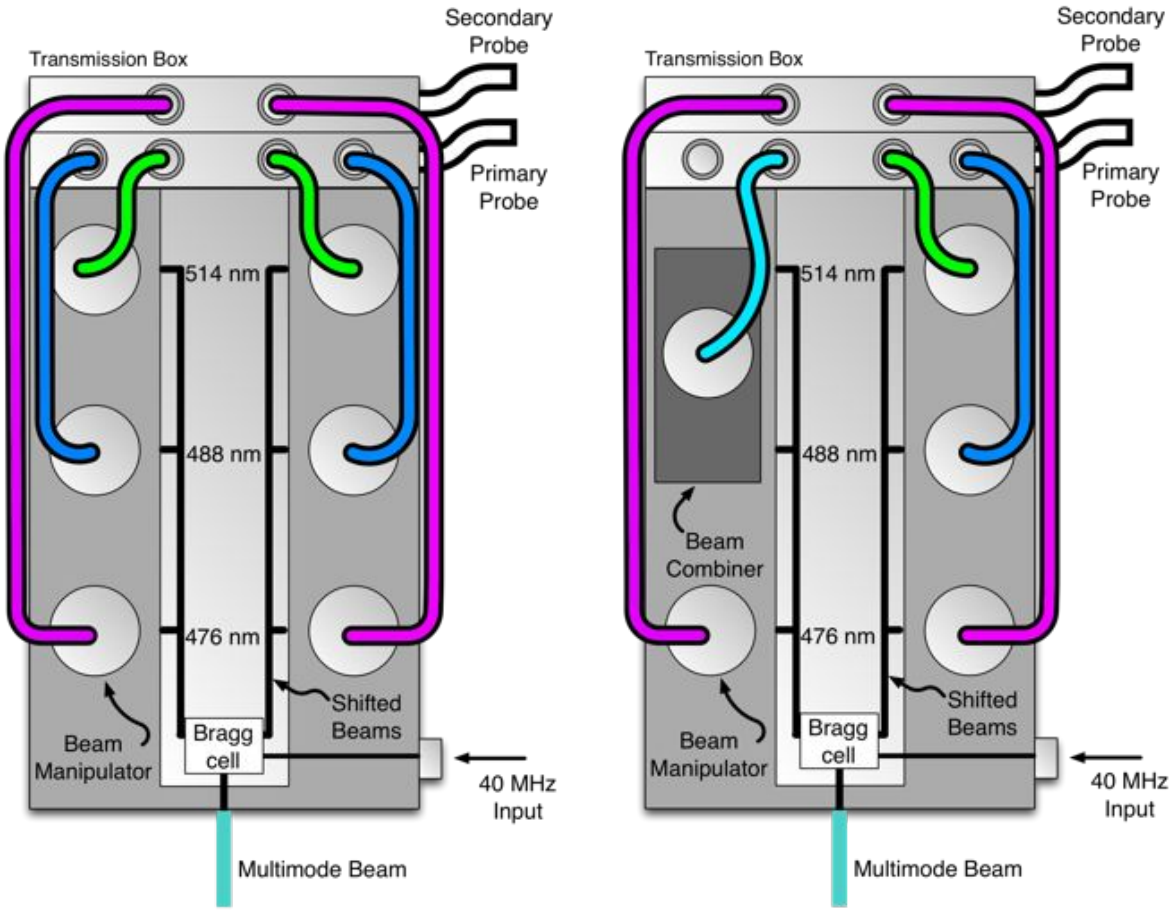

A B

Figure 5-3. Beam combiner comparison and workings.

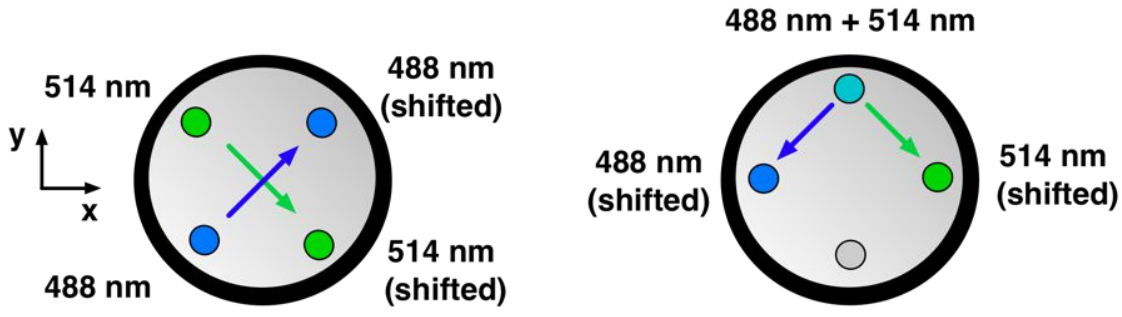

A B

Figure 5-4. 3-beam and 4-beam configuration of the primary probe head.

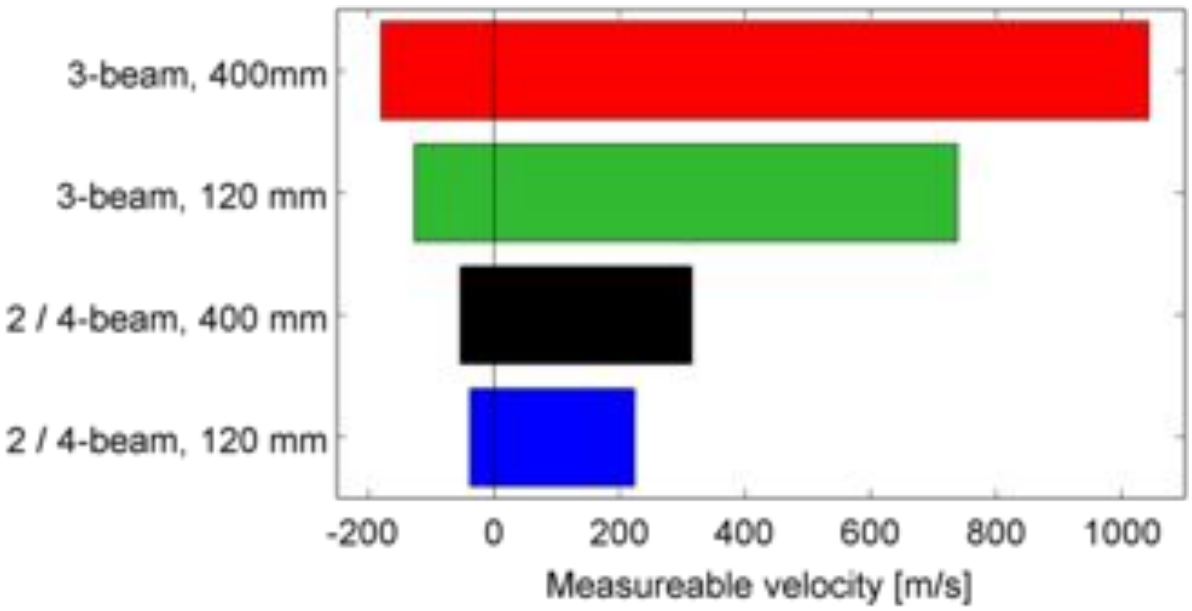

Figure 5-5. Velocity range for different probe configurations

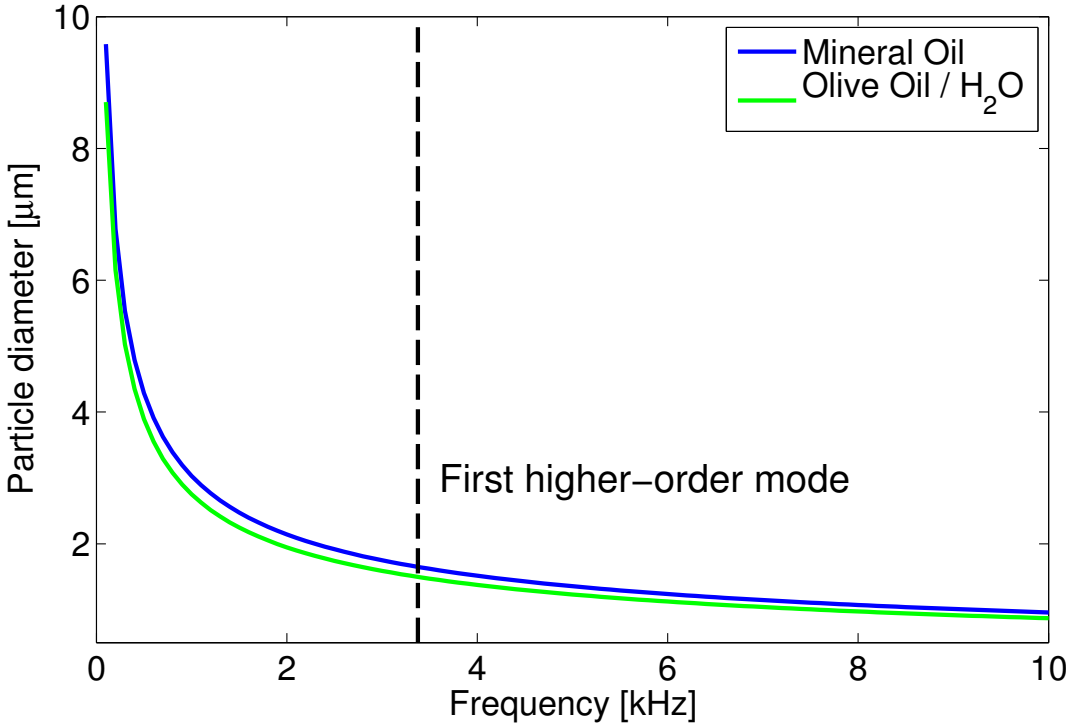

Figure 5-6. Cut-off frequency as a function of particle diameter.

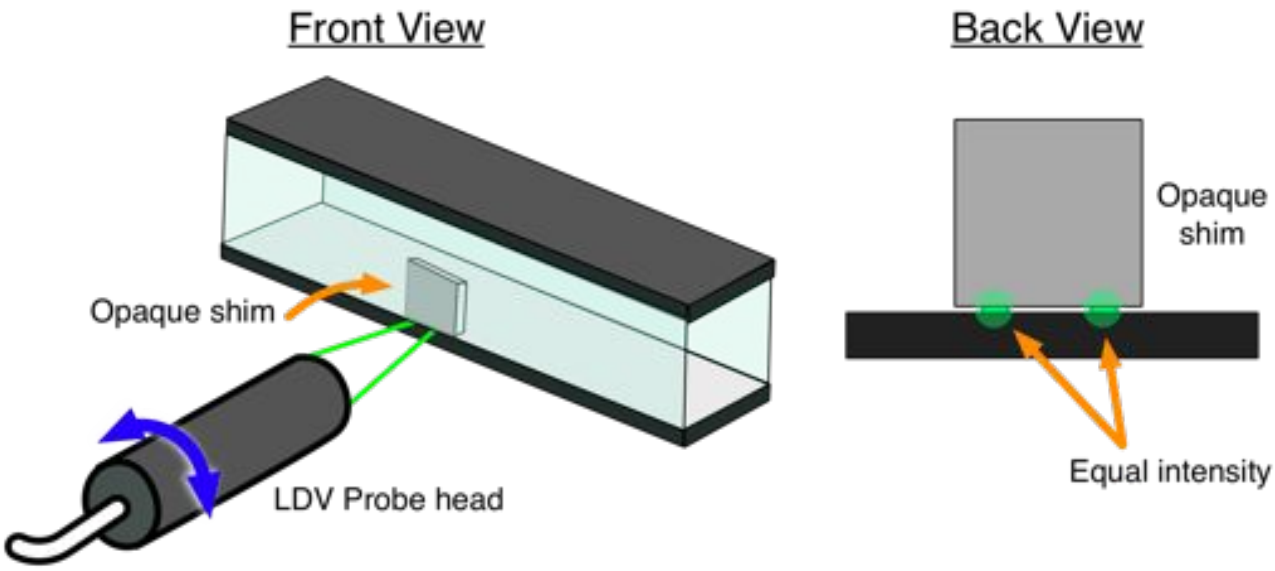

Figure 5-7. LDV alignment tunnel procedure using matched intensities of two laser beams a thin opaque shim to align the probe head plane to the test section floor.

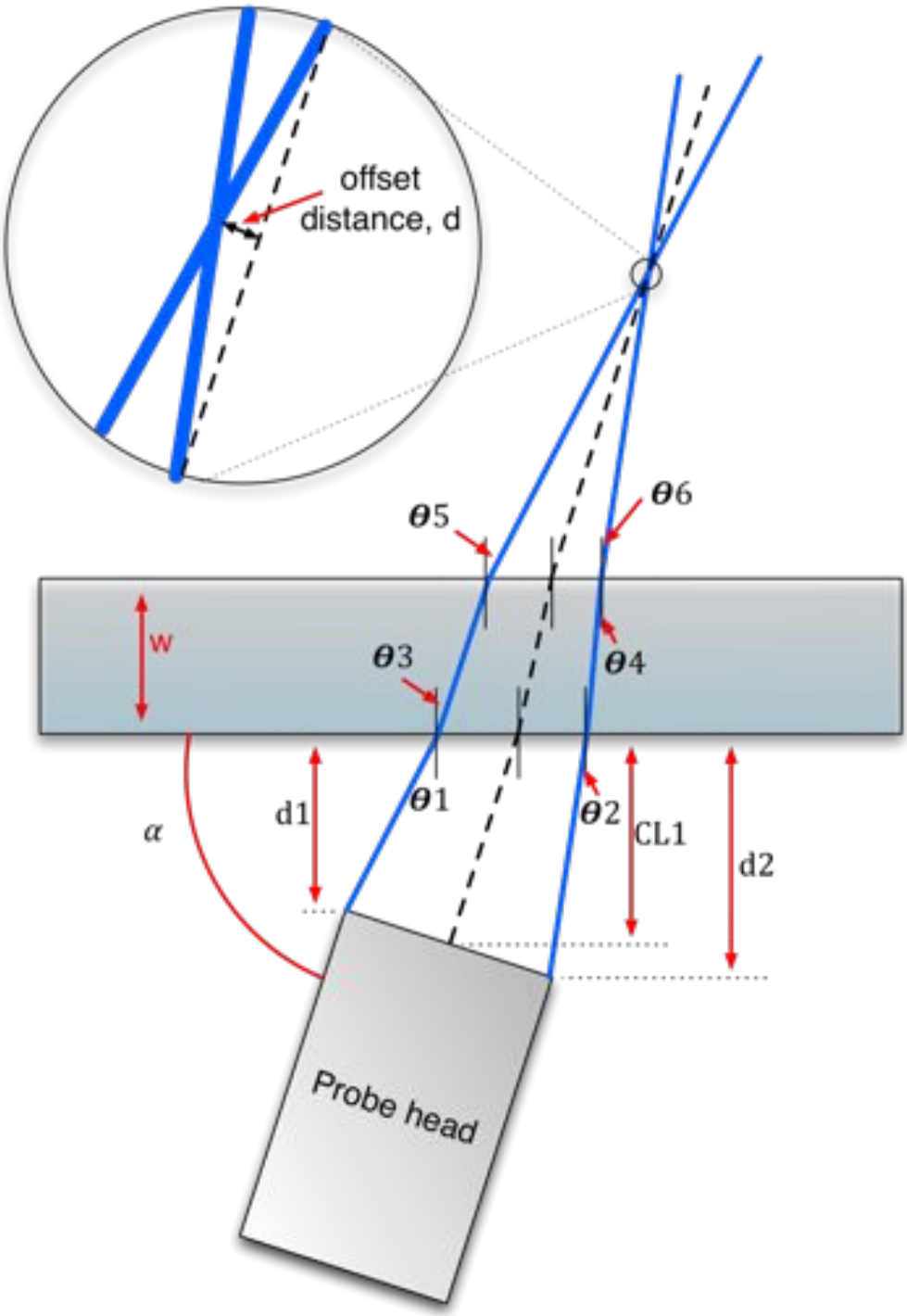

Figure 5-8. Illustration of the LDV beam paths through the optical window for an arbitrary offset angle, α. Each labeled angle and distance are calculated by the model to determine the offset distance of the off-axis probe volume to the expected probe location as determined by the receiving optics.

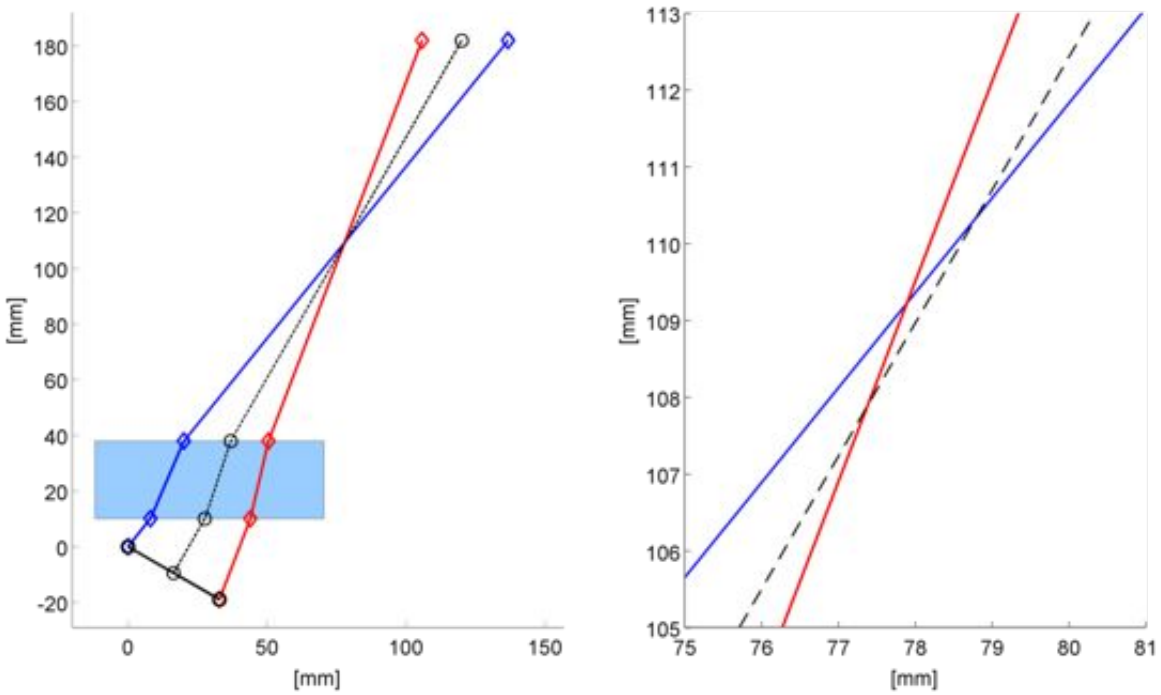

A B

Figure 5-9. A) The calculated beam paths with 38 mm spacing modeling the 2-beam or 4-beam probe head through a 120 mm focal length transmitting lens with a $\alpha = 60°$ offset angle. The simulated 27.94 mm thick window is displayed as the blue box matching the thickness of the GFID optical window. B) The cropped view of calculated beam paths showing the offset beam crossing to the expected location dictated by the focus of the receiving optics. All dimensions are based on reference location of the transmitting beam nearest to the window.

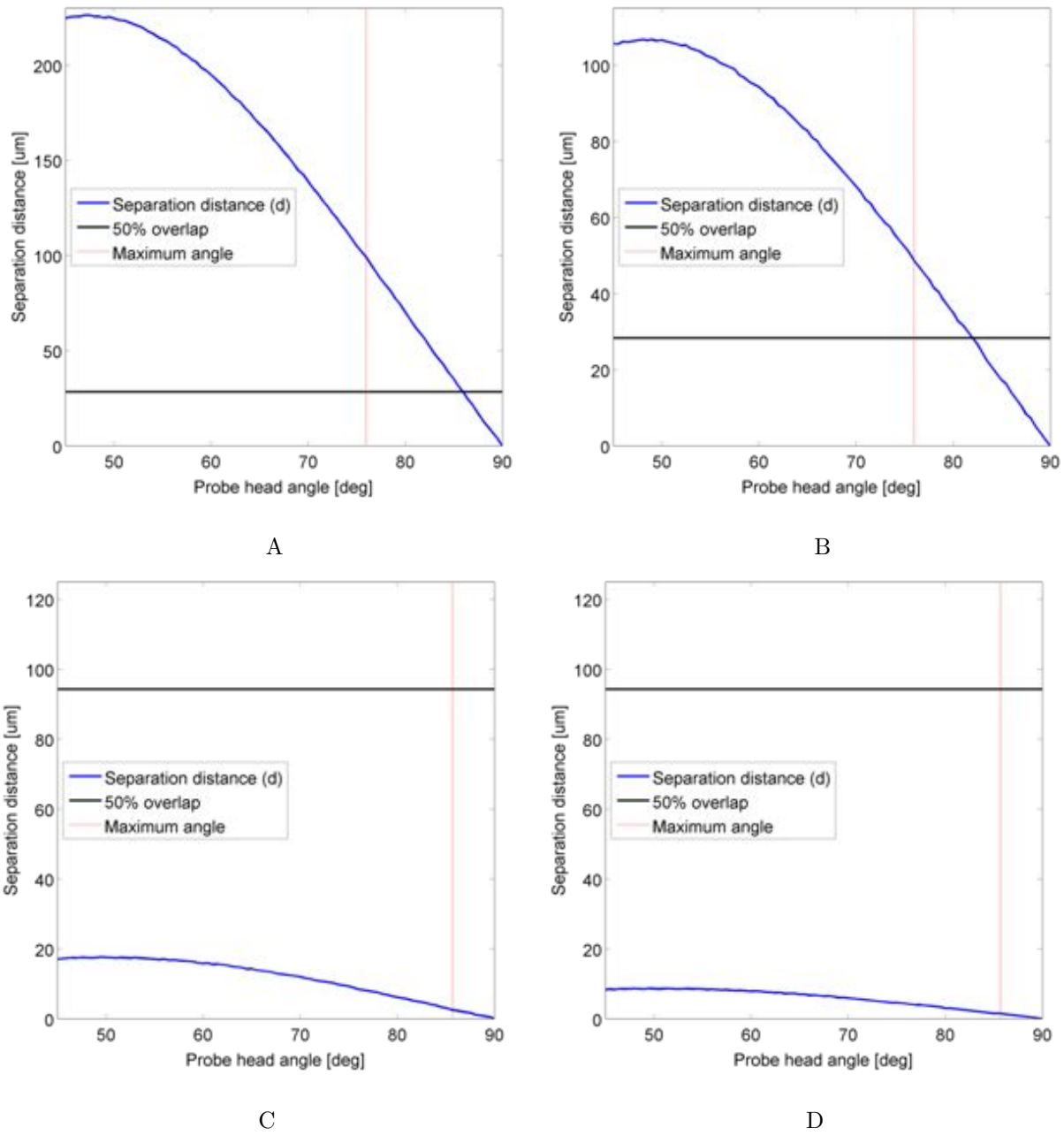

Figure 5-10. The separation distance between the true probe volume and the assume location based on receiving optic focus point. The vertical red line indicates the maximum angle, measured from the wall before the two probe heads could interact. The horizontal black lines indicates where the separation is at least 50% probe volume and this a signal is possible. Each plot is for a different transmitting lens focal length and probe head configuration combination of the following: A) 120 mm, 4-beam, B) 120 mm, 3-beam C) 400 mm, 4-beam, D) 400 mm, 3-beam.

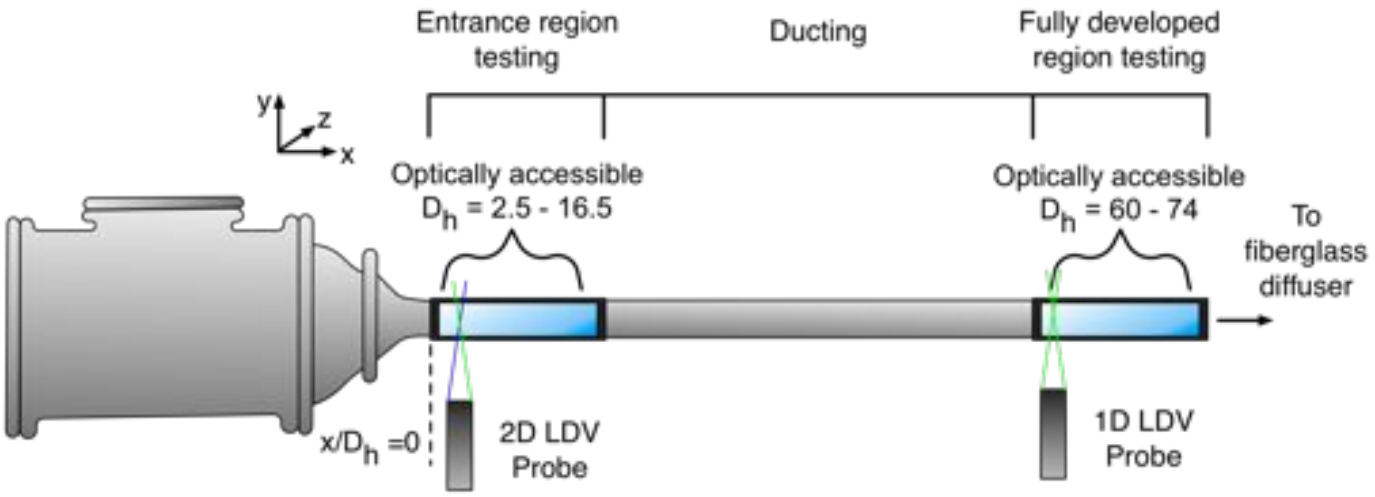

Figure 5-11. Test section installation location for entrance region measurements fully developed measurements downstream. The coordinate system is placed on the tunnel floor at the location marked as $x/D_h = 0$.

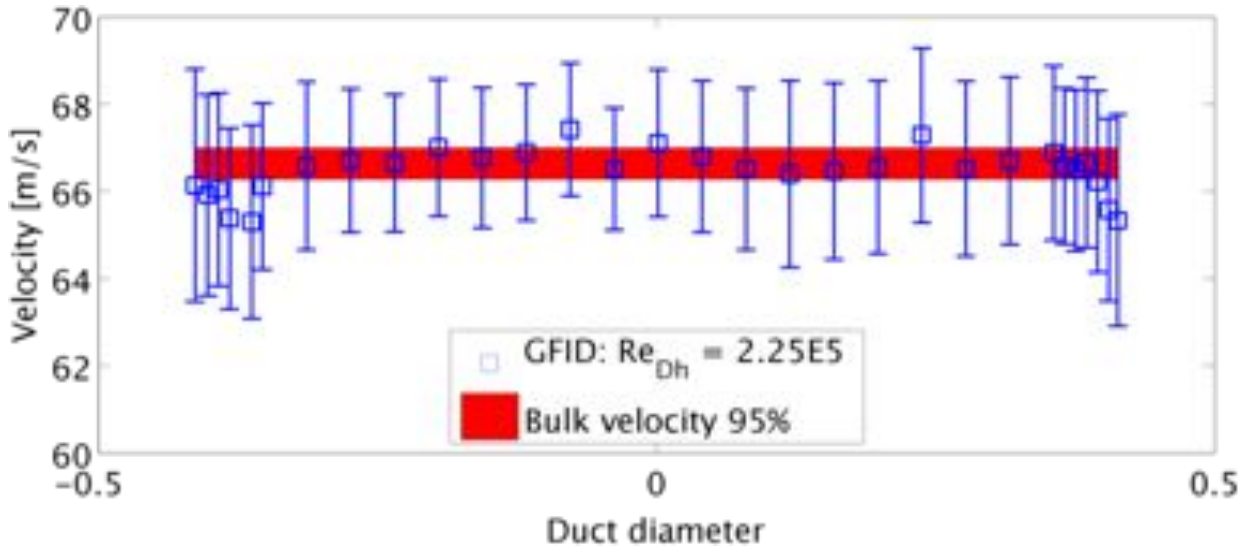

Figure 5-12. Cross duct velocity and integrated bulk velocity with corresponding errors measured at $x/D_h = 2.5$.

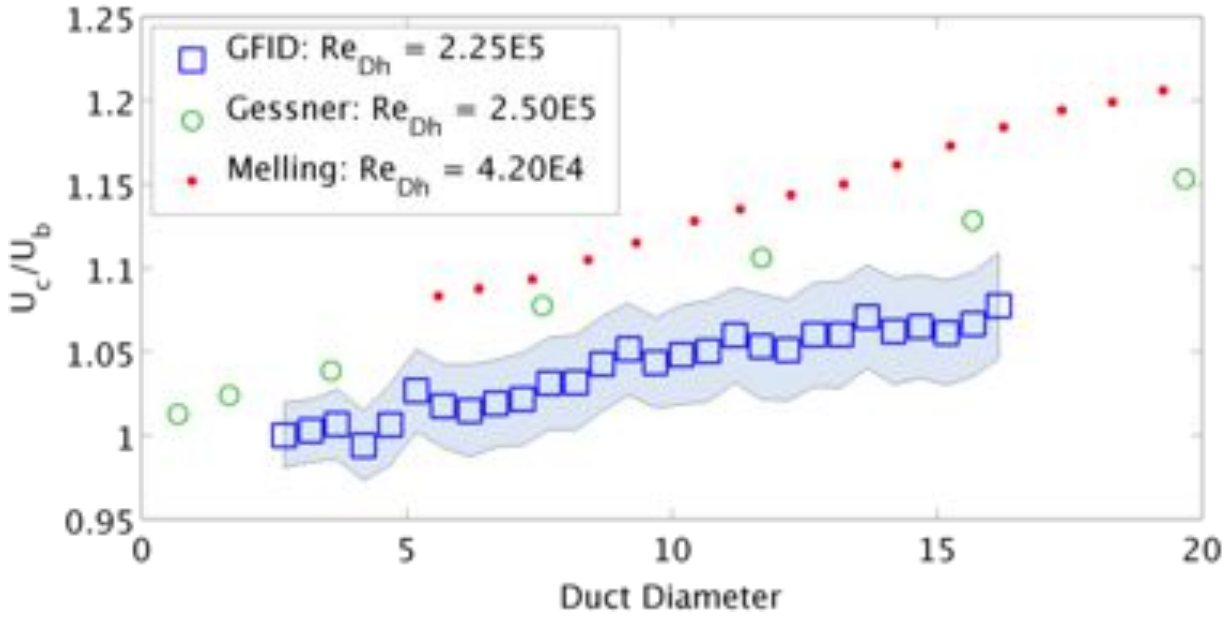

Figure 5-13. Centerline velocity normalized by bulk velocity as a function of downstream distance in of the entrance region of the GFID compared against similar data from Gessner *et al.* (1977) and Melling & Whitelaw (1976).

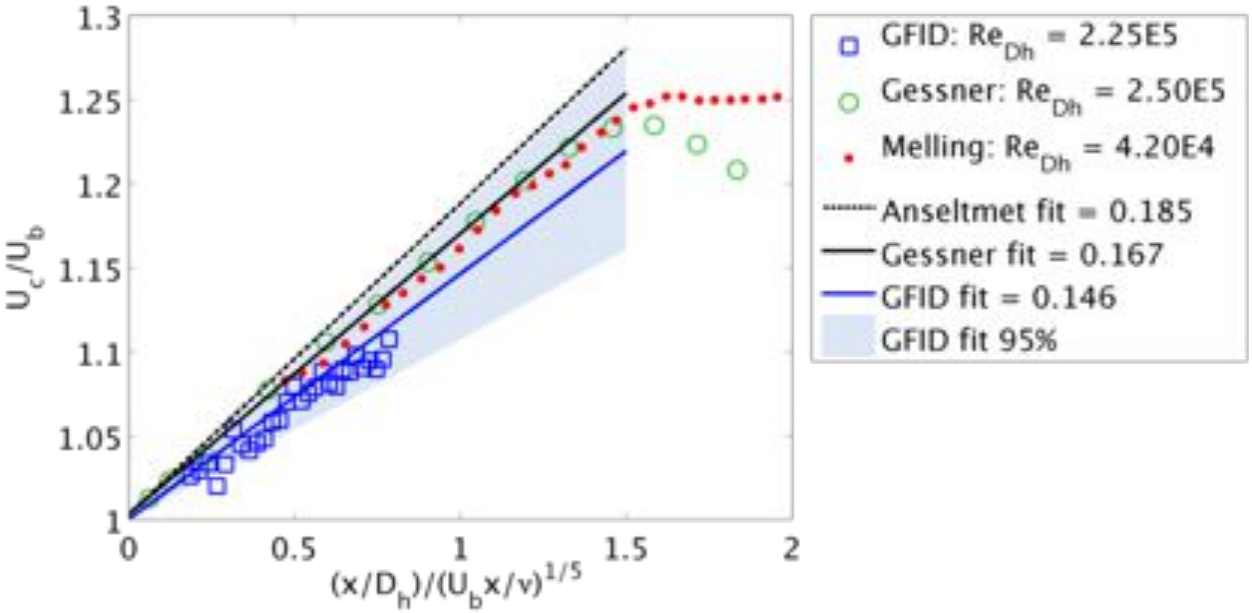

Figure 5-14. The GFID entrance region experimental velocity data expressed as ratio of centerline to bulk velocity as a function of function from Anselmet *et al.* (2009). Data and fit are compared to the similar experimental data from Gessner *et al.* (1977) and Melling & Whitelaw (1976).

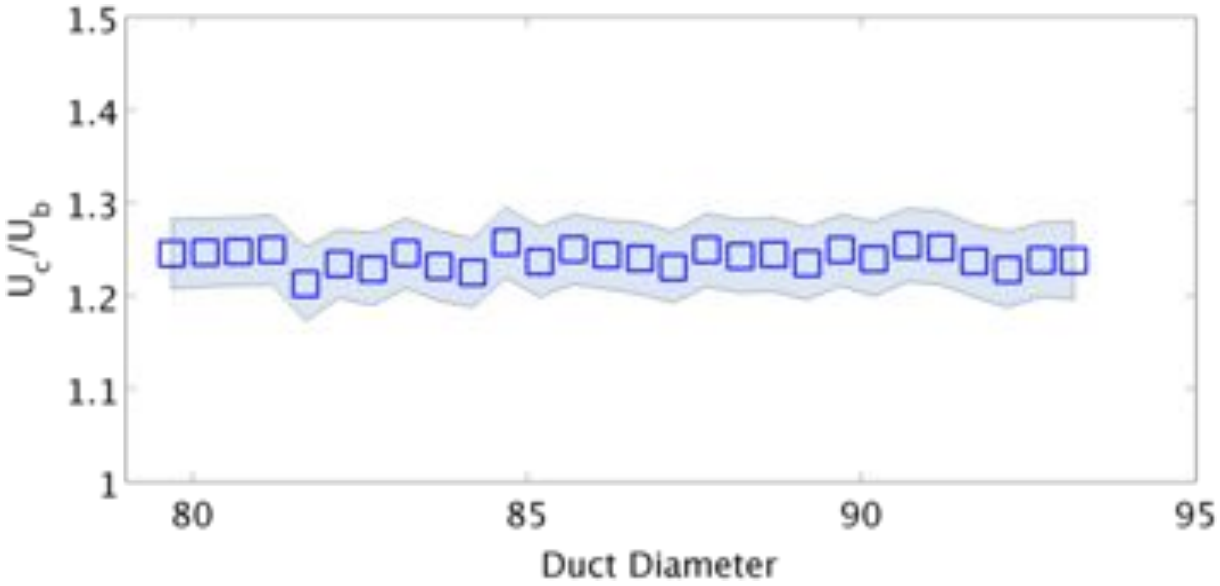

Figure 5-15. Normalized centerline velocity measurements in the fully developed region. Shaded region indicates the 95% confidence interval of the data.

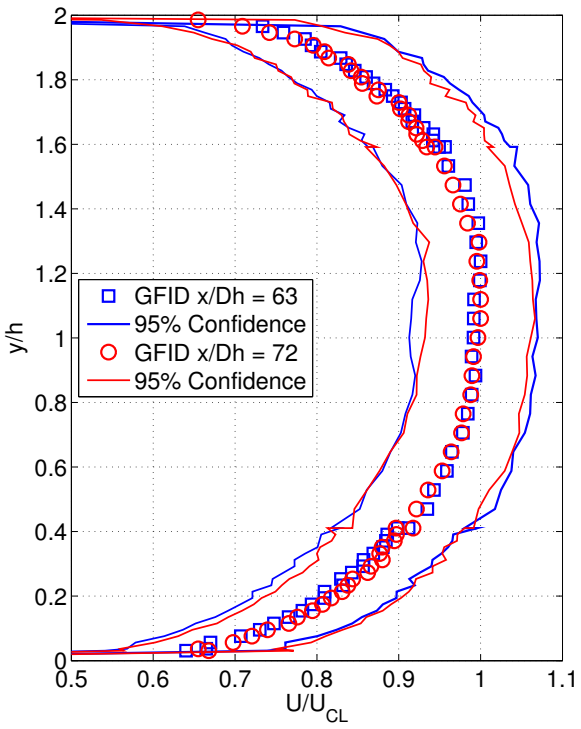

A B

Figure 5-16. (A) Full cross-duct velocity profiles at $^{x}/_{D_h} = 63$ and 72 demonstrating matched profiles within experimental uncertainty and (B) Half-duct velocity profiles at $^{x}/_{D_h} = 63$ and 72 compared to reference data of two high-Reynolds number fully developed channel flow from Gessner (1964).

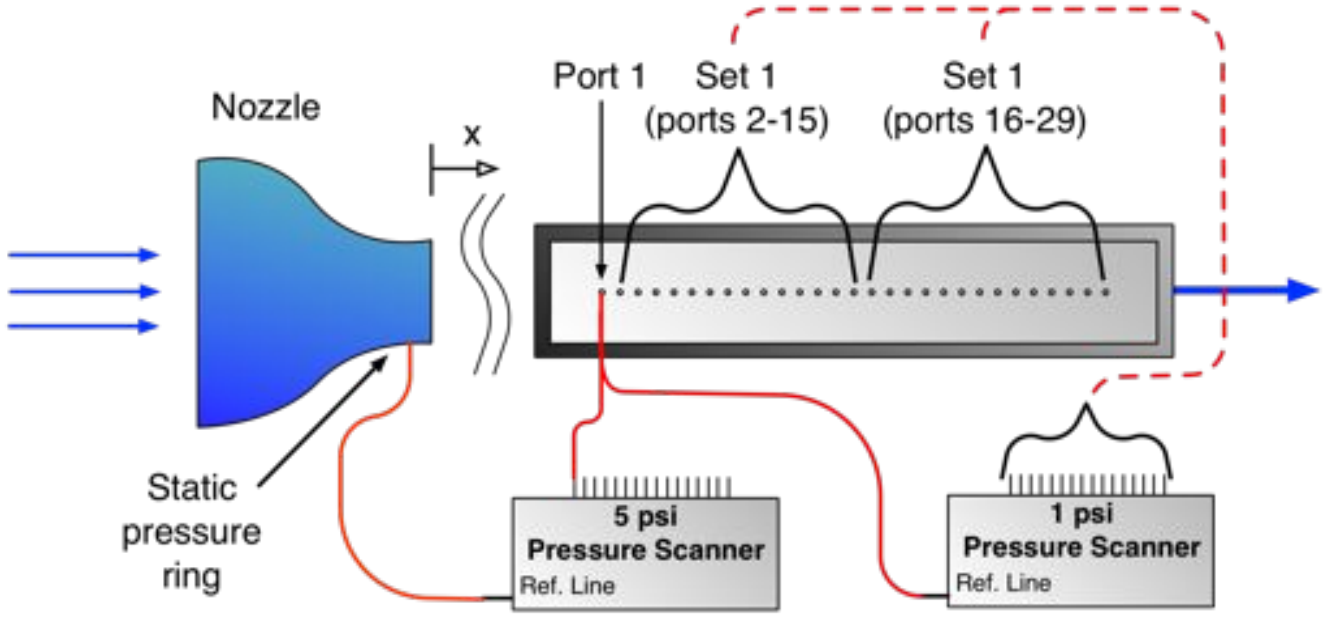

Figure 5-17. Experimental setup of the static pressure experiment where the pressure port window is sampled in two sets

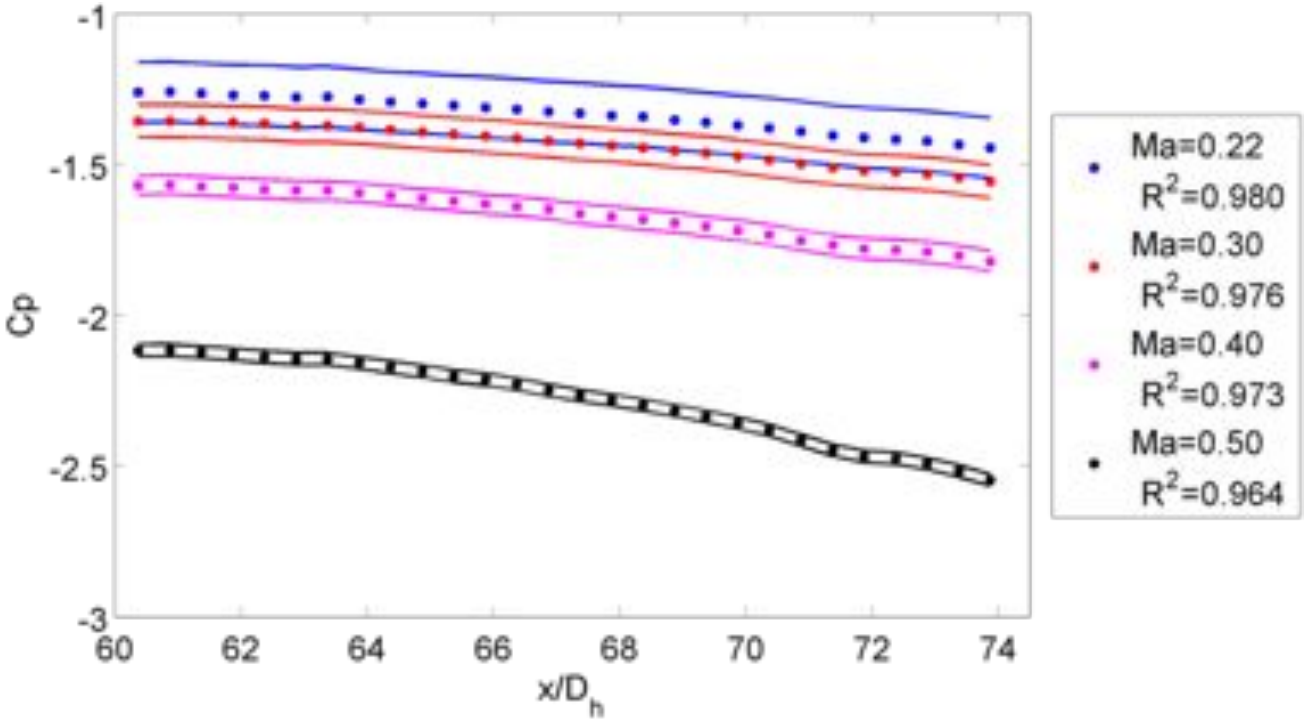

Figure 5-18. Cp as a function of Mach number with error bars.

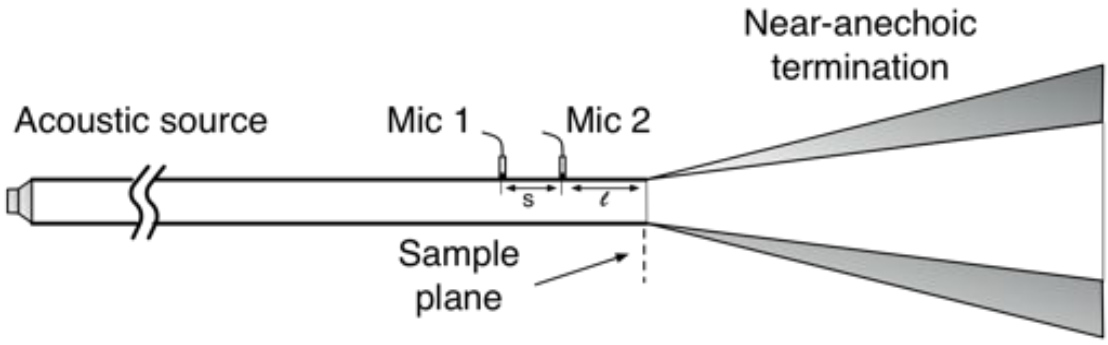

Figure 5-19. Experimental setup of the two-microphone method application for measuring the reflection coefficient of the anechoic diffuser.

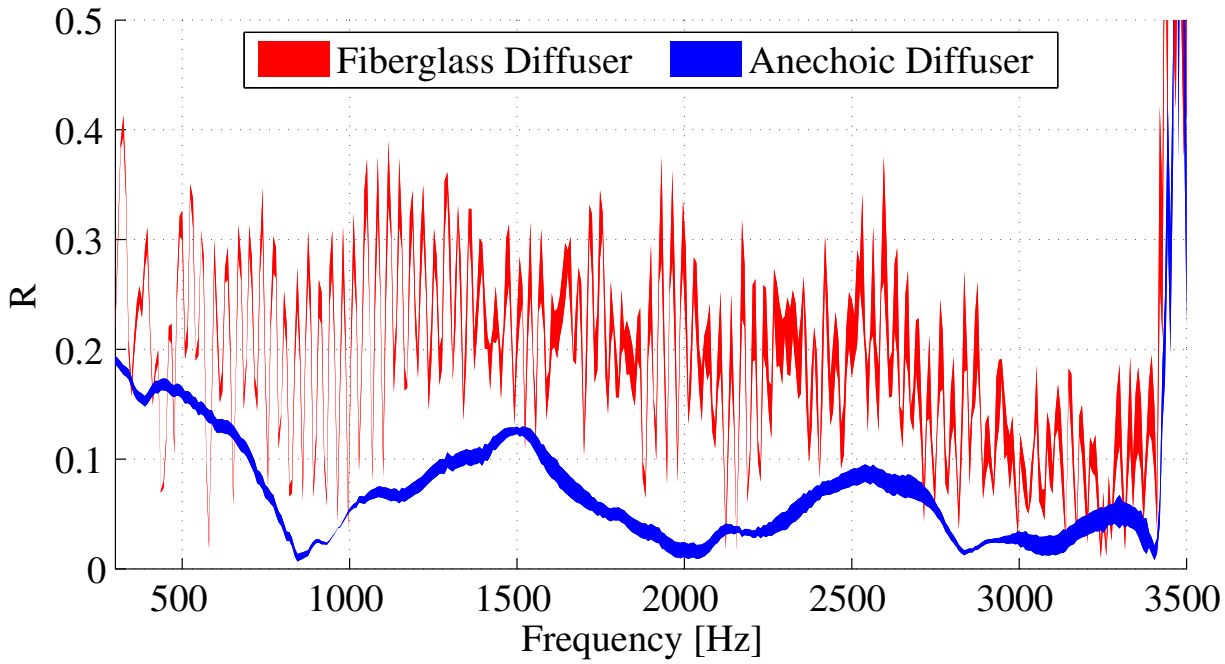

Figure 5-20. Reflection coefficient of the anechoic diffuser as compared to the hard walled fiberglass diffuser using the two-microphone method with periodic-random noise input.

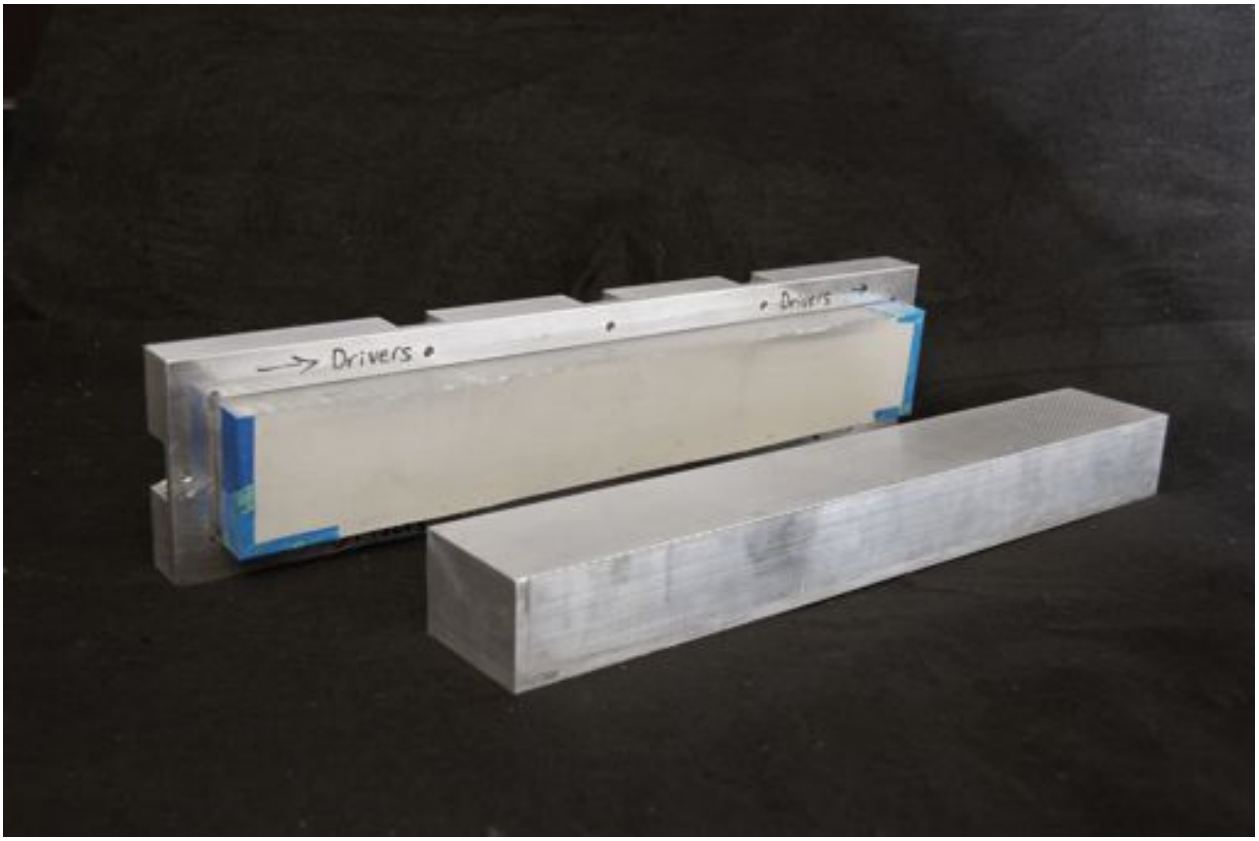

Figure 5-21. Photograph of the two acoustic liners tested, a resistive liner with highly resistive facesheet (background) and a perforated facesheet resonant liner (foreground). Both acoustic liners are 2.5×16.36 *in*.

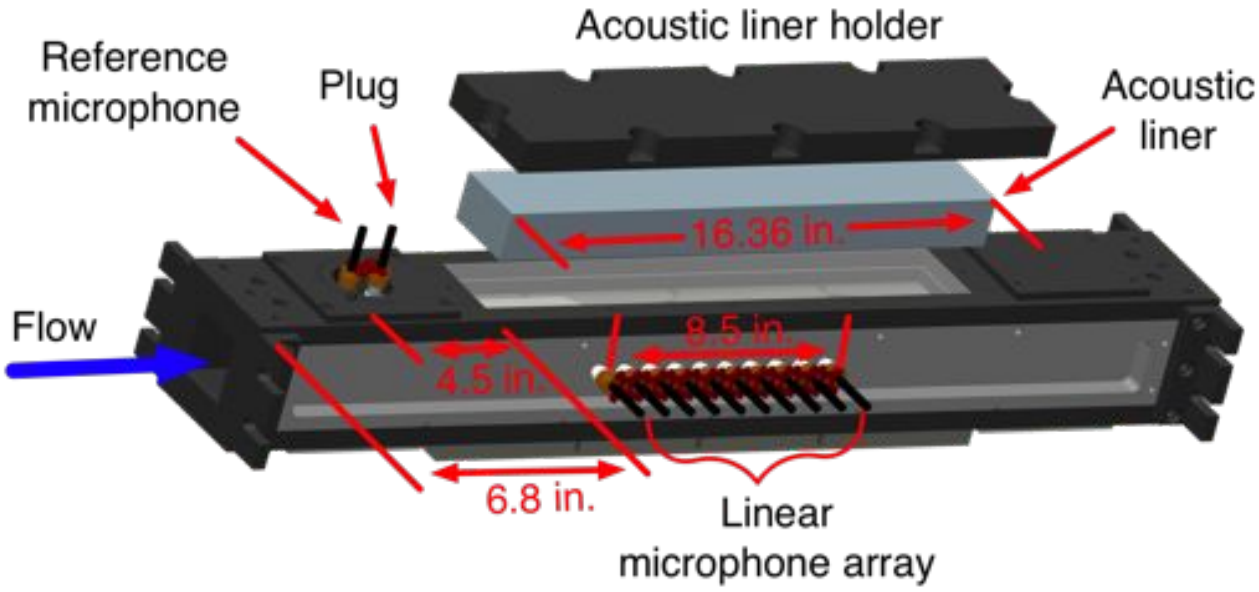

Figure 5-22. GFID test section with removable walls and replacement windows allow for full optical and sensor access.

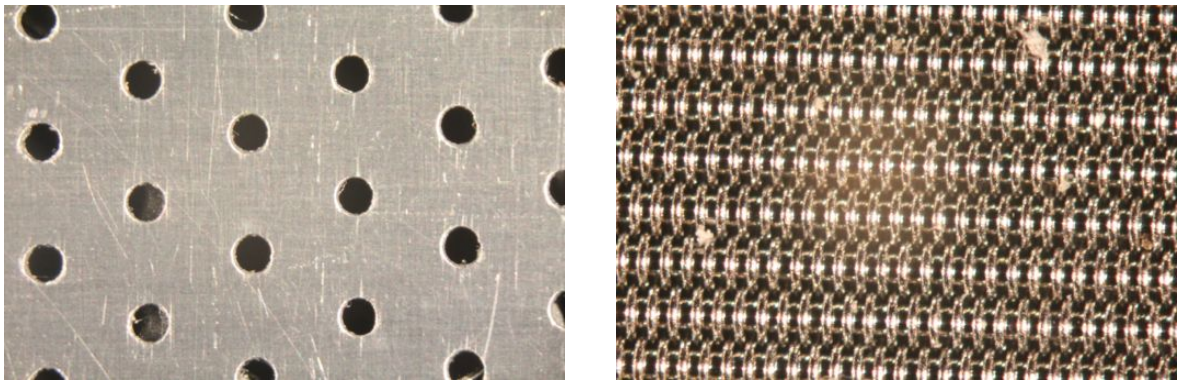

A B

Figure 5-23. Close up view of perforate (A) and wire mesh facesheet (B)

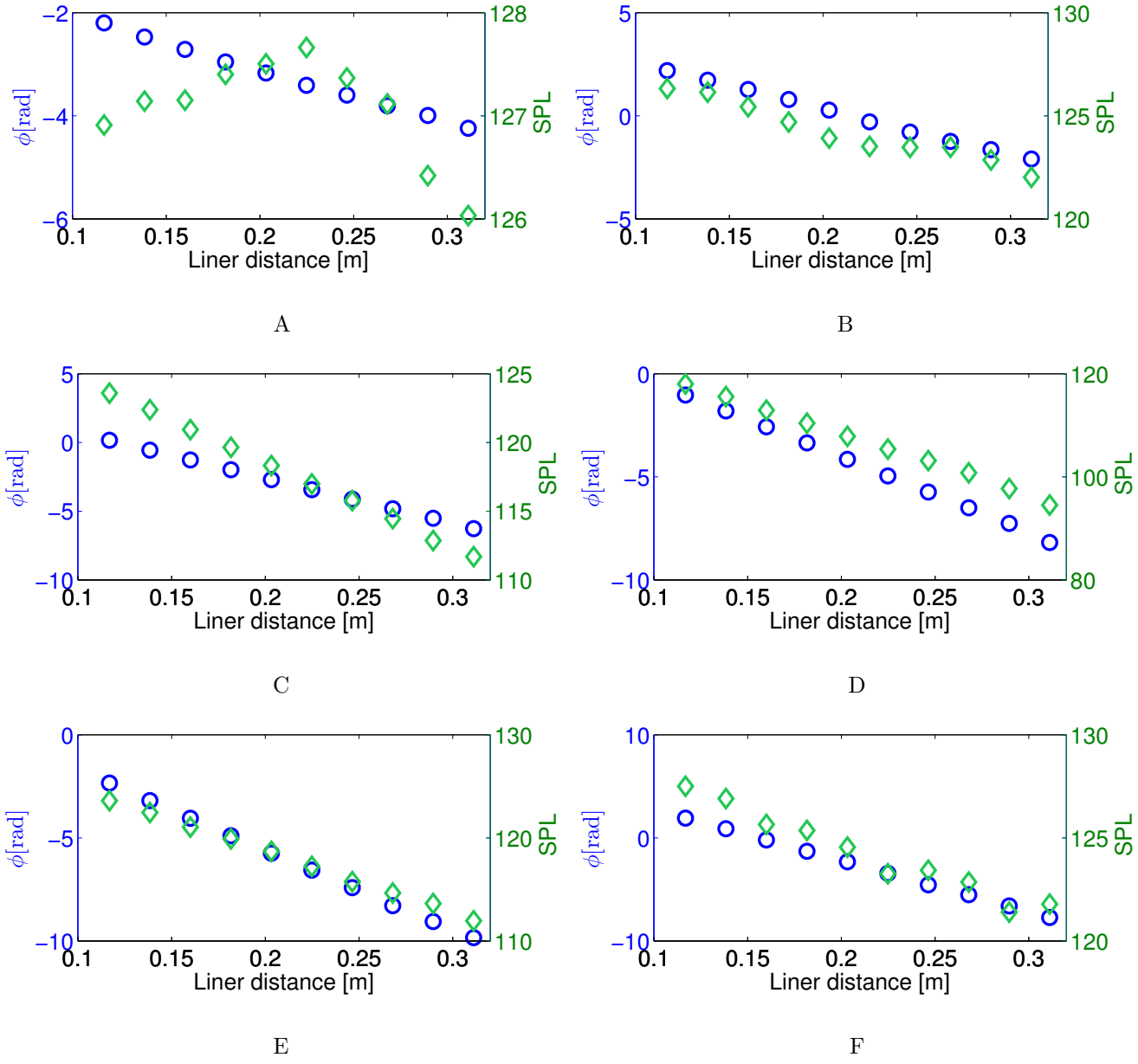

Figure 5-24. The phase (left axis and blue circles) and SPL (right axis and green diamonds) (ref. 20 μPa) for $M = 0.0$: (A) $f = 500\ Hz$, (B) $f = 1000\ Hz$, (C) $f = 1500\ Hz$, (D) $f = 2000\ Hz$, (E) $f = 2500\ Hz$, (F) $f = 3000\ Hz$

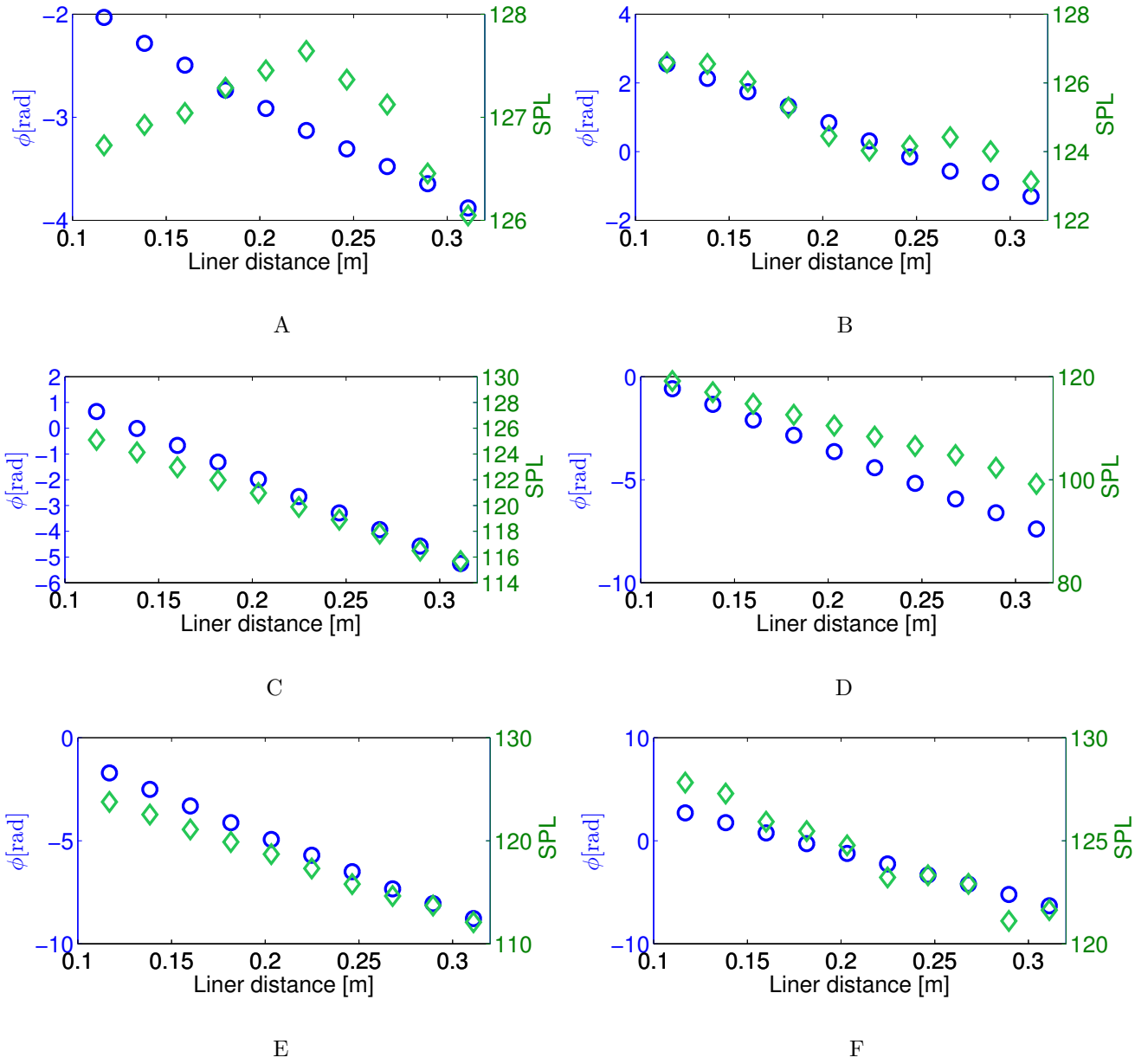

Figure 5-25. The phase (left axis and blue circles) and SPL (right axis and green diamonds) (ref. 20 μPa) for $M = 0.1$: (A) $f = 500\ Hz$, (B) $f = 1000\ Hz$, (C) $f = 1500\ Hz$, (D) $f = 2000\ Hz$, (E) $f = 2500\ Hz$, (F) $f = 3000\ Hz$

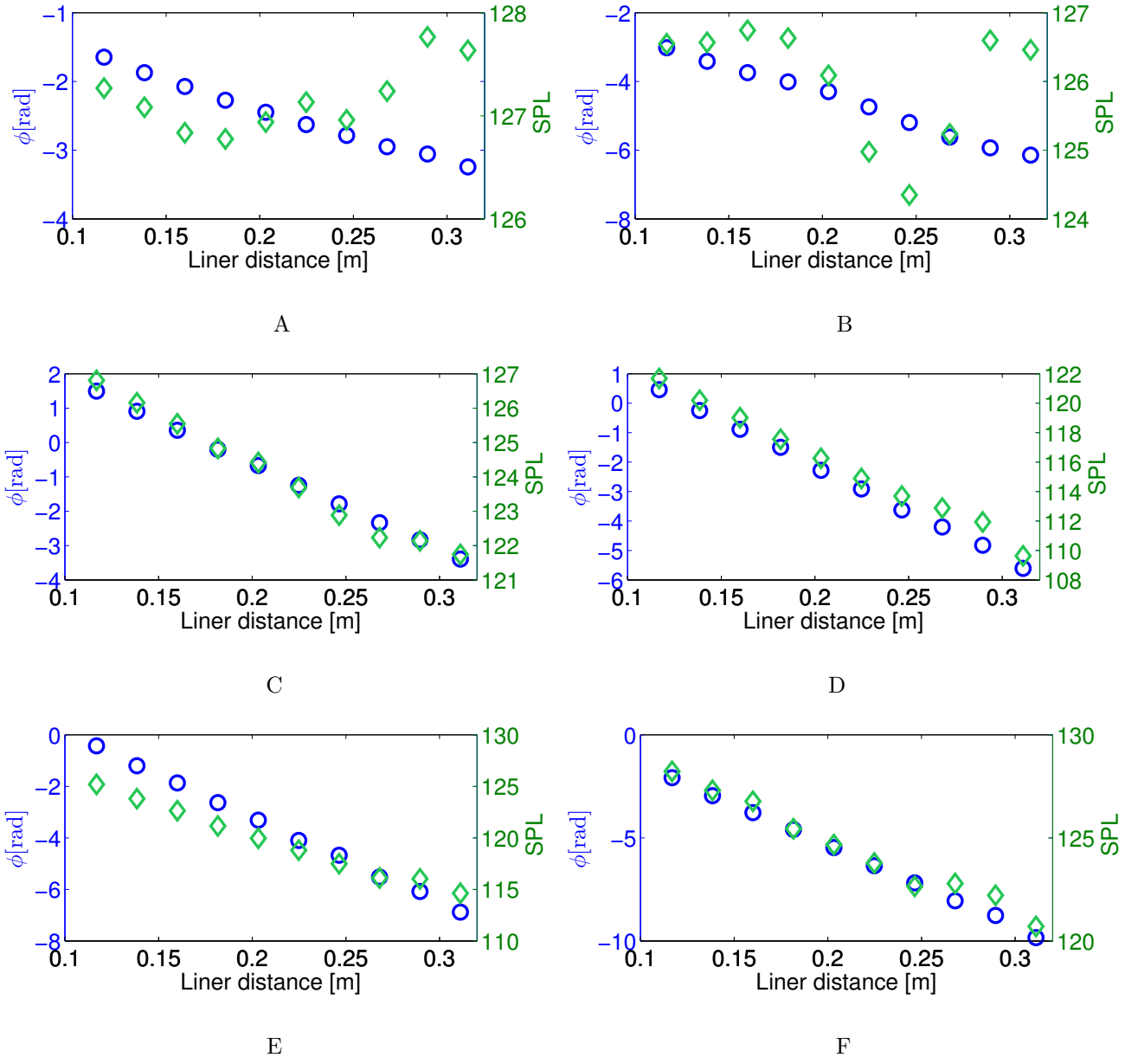

Figure 5-26. The phase (left axis and blue circles) and SPL (right axis and green diamonds) (ref. 20 μPa) for $M = 0.3$: (A) $f = 500\ Hz$, (B) $f = 1000\ Hz$, (C) $f = 1500\ Hz$, (D) $f = 2000\ Hz$, (E) $f = 2500\ Hz$, (F) $f = 3000\ Hz$

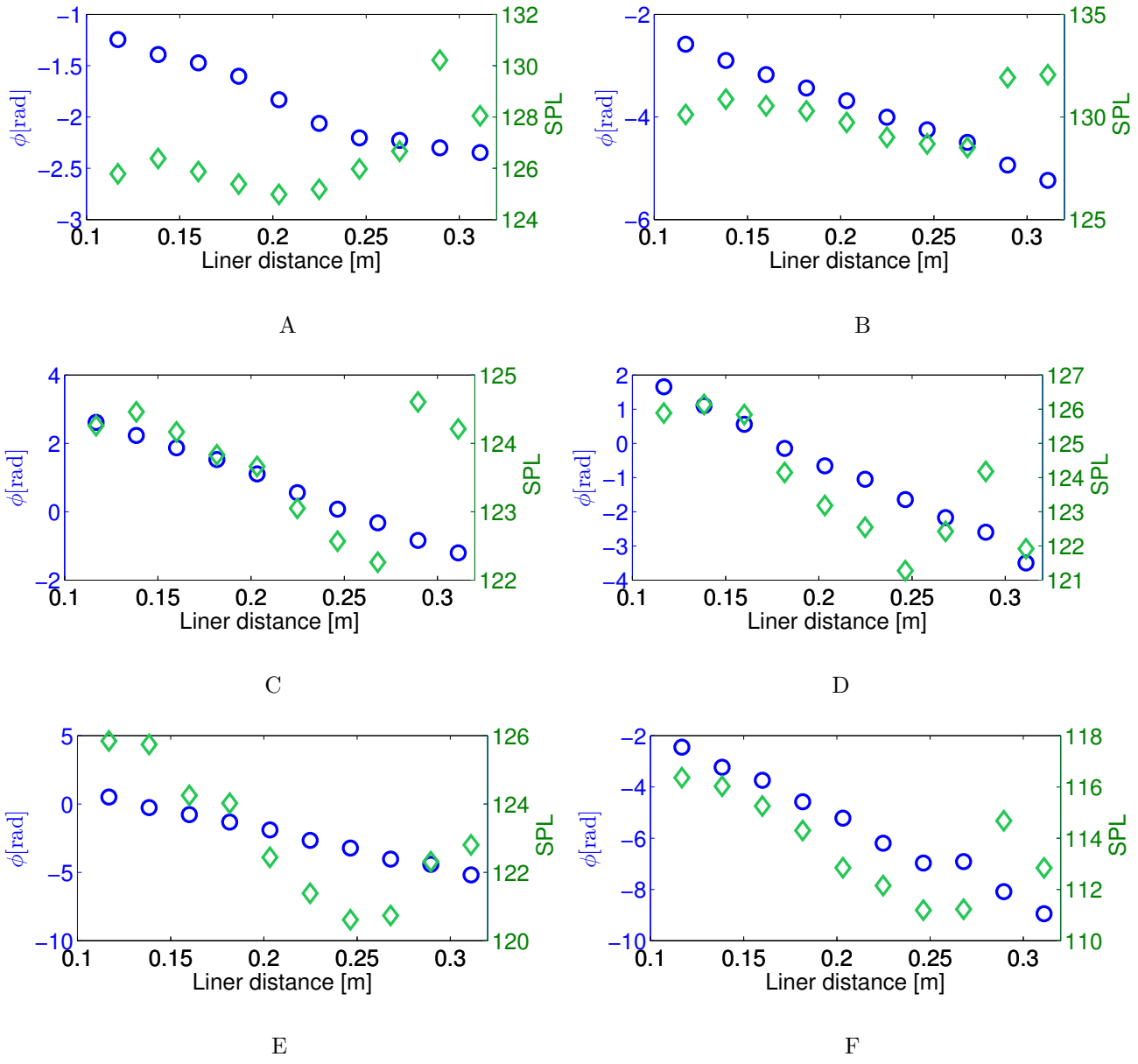

Figure 5-27. The phase (left axis and blue circles) and SPL (right axis and green diamonds) (ref. 20 μPa) for $M = 0.5$: (A) $f = 500\ Hz$, (B) $f = 1000\ Hz$, (C) $f = 1500\ Hz$, (D) $f = 2000\ Hz$, (E) $f = 2500\ Hz$, (F) $f = 3000\ Hz$

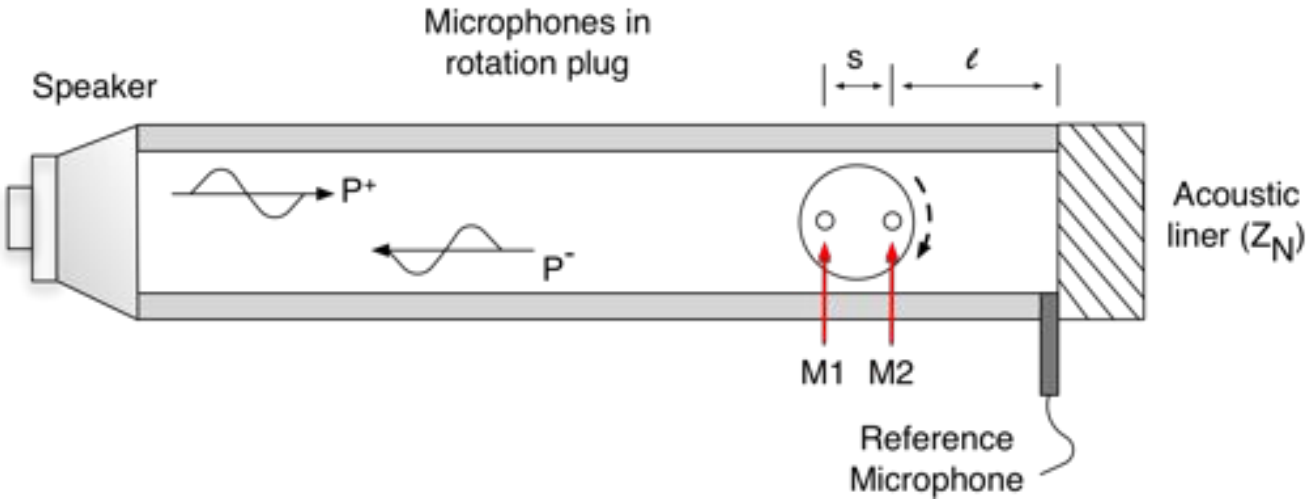

Figure 5-28. Experimental setup of the normal incidence tube (NIT) illustrating the two-microphone method of impedance eduction.

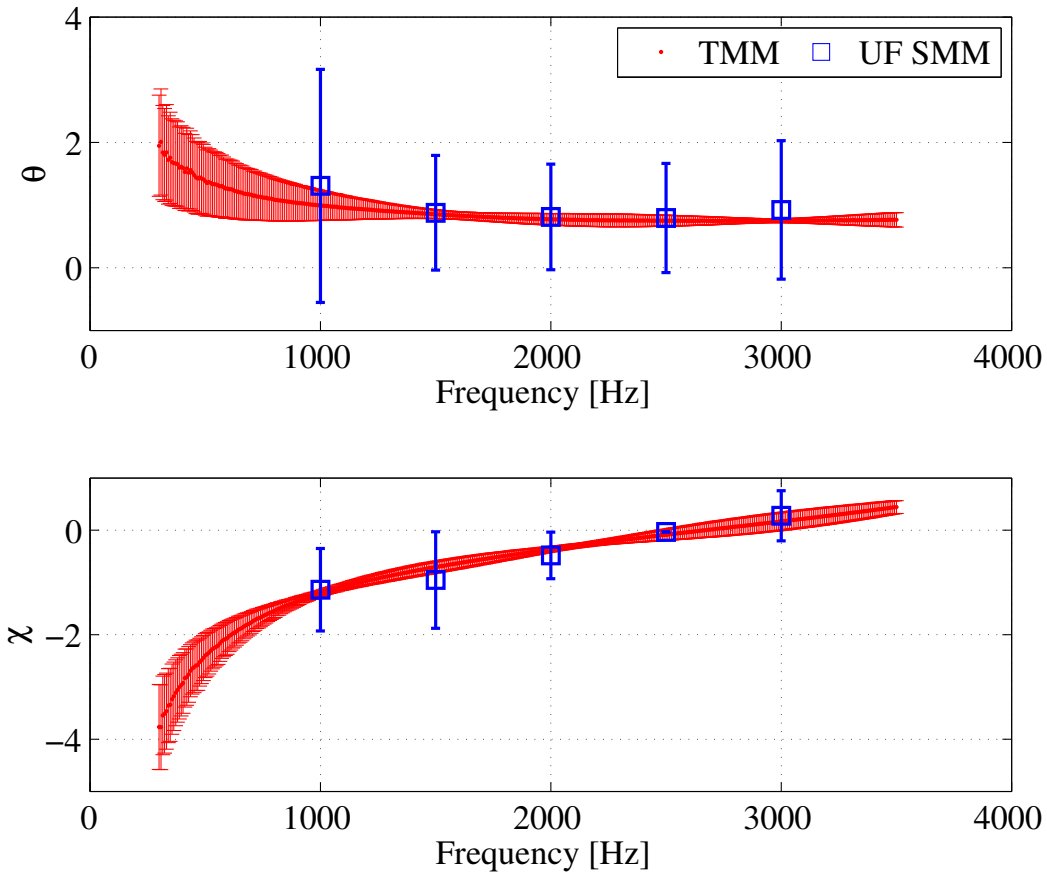

Figure 5-29. Normalized resistance (top) and reactance (bottom) of wire mesh acoustic liner results comparing the two-microphone method of the NIT to the GFID using the SMM.

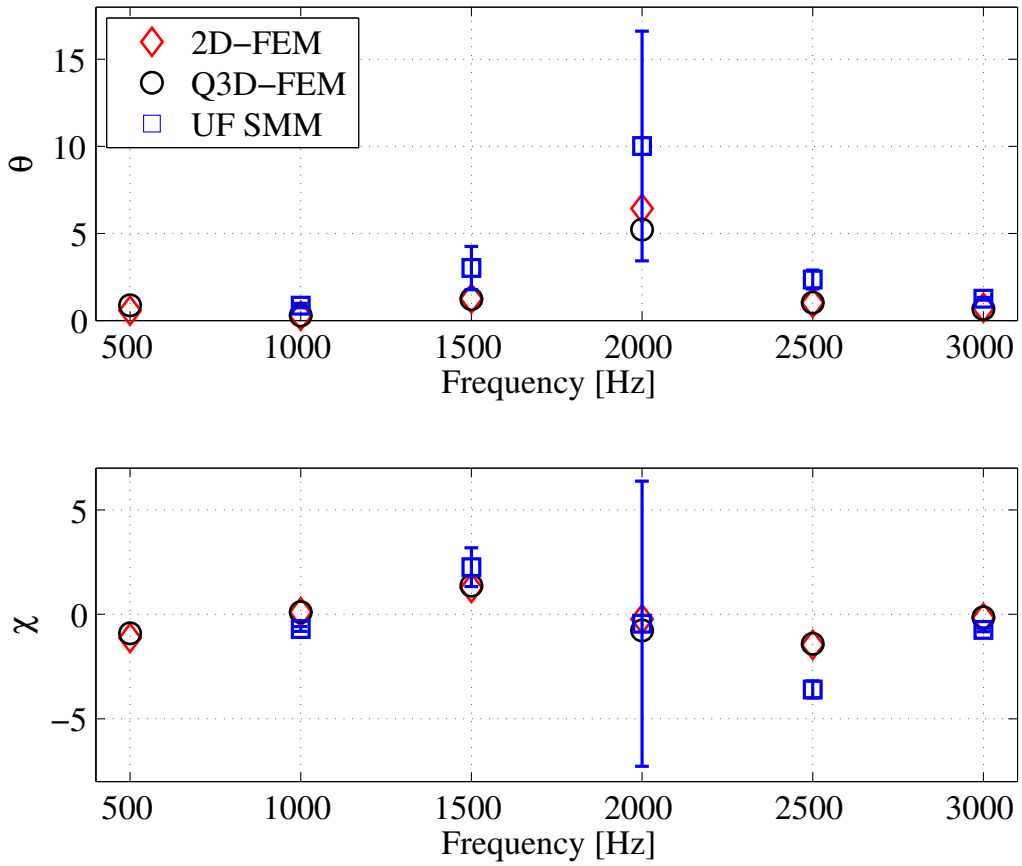

Figure 5-30. Comparison results of educed normalized specific acoustic impedance via the UF SMM, the 2D-FEM, and the Q3D-FEM impedance eduction techniques applied to benchmark data from Jones *et al.* (2005) of a tubular ceramic resistive liner tested at $M = 0.255$.

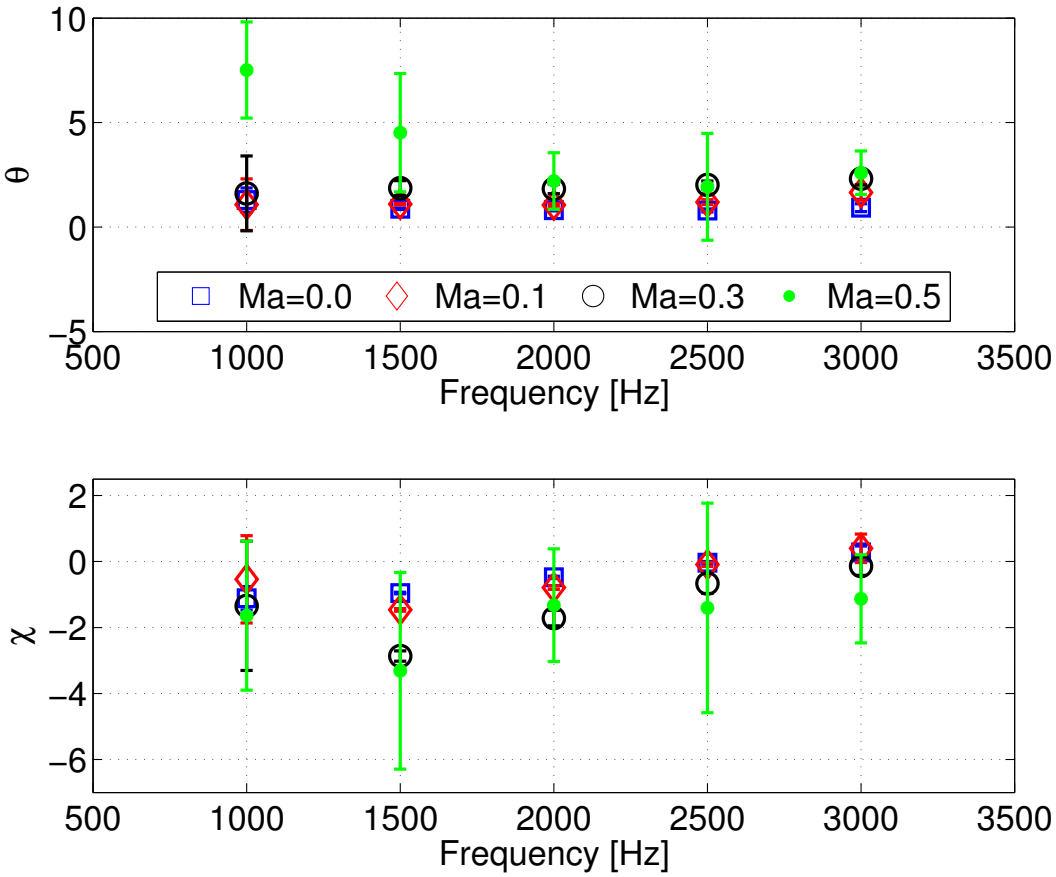

Figure 5-31. Normalized specific acoustic impedance of the wire mesh acoustic liner tested in the GFID at $M = 0.0,\ 0.1,\ 0.3,$ and 0.5. Impedance eduction performed via UF SMM.

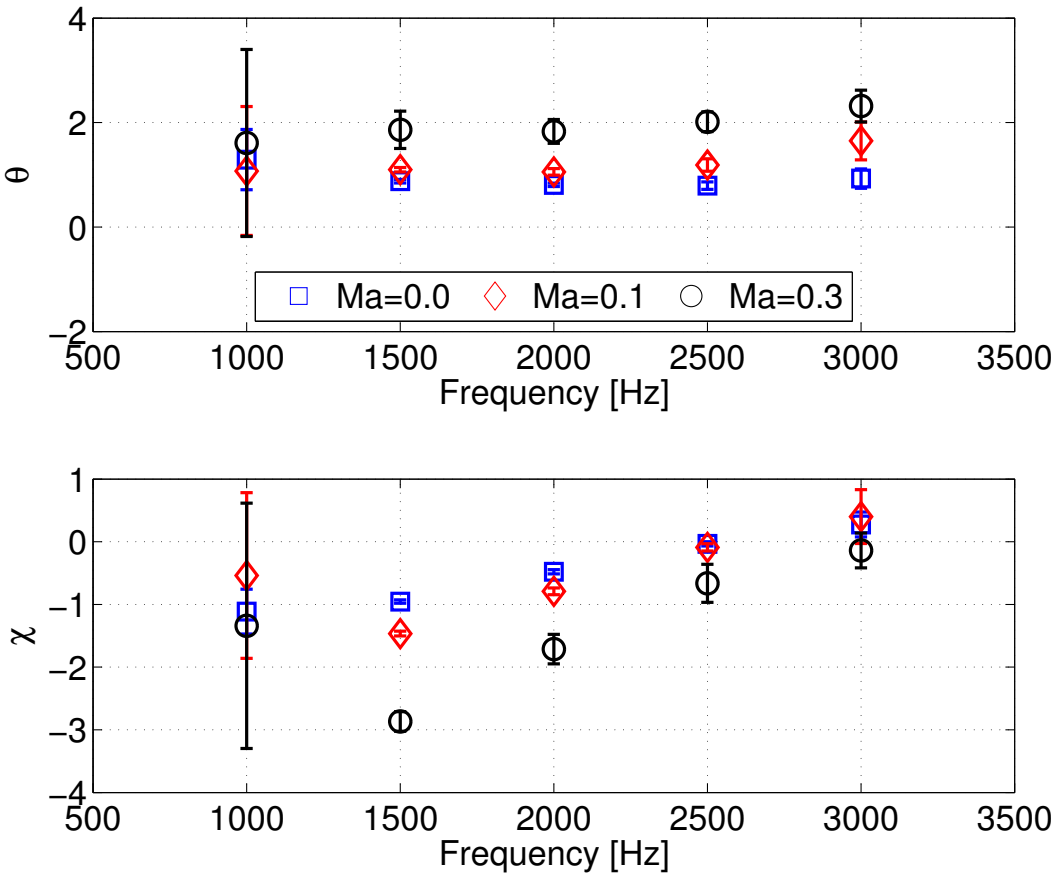

Figure 5-32. Normalized specific acoustic impedance of the wire mesh acoustic liner tested in the GFID at $M = 0.0,\ 0.1,$ and 0.3. Impedance eduction performed via UF SMM.

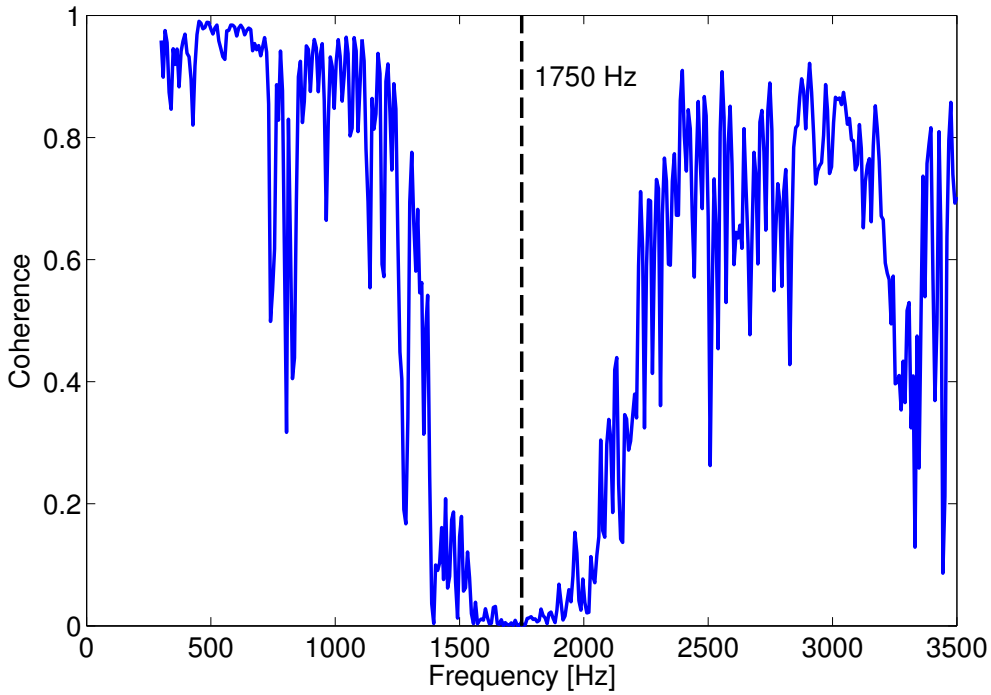

Figure 5-33. Coherence of perforate liner at M=0.22.

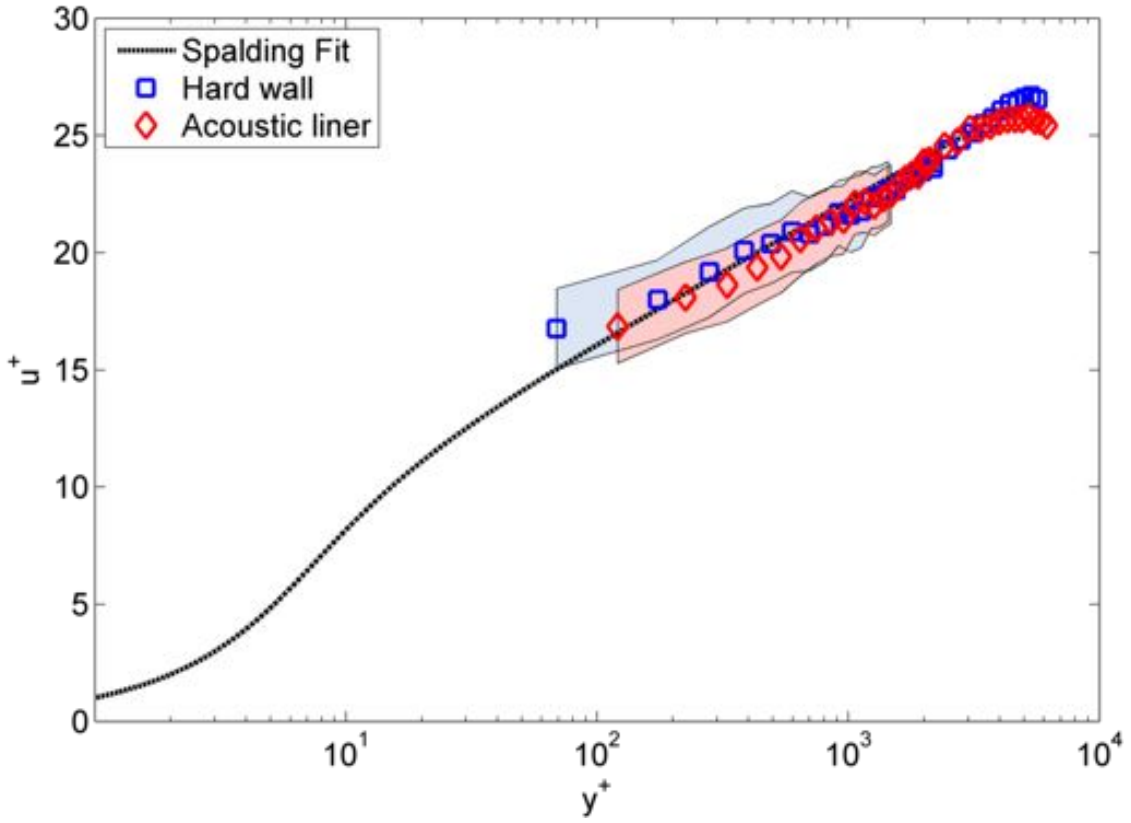

Figure 5-34. Spalding 2D boundary layer profile fit for hard wall and acoustic liner installation.

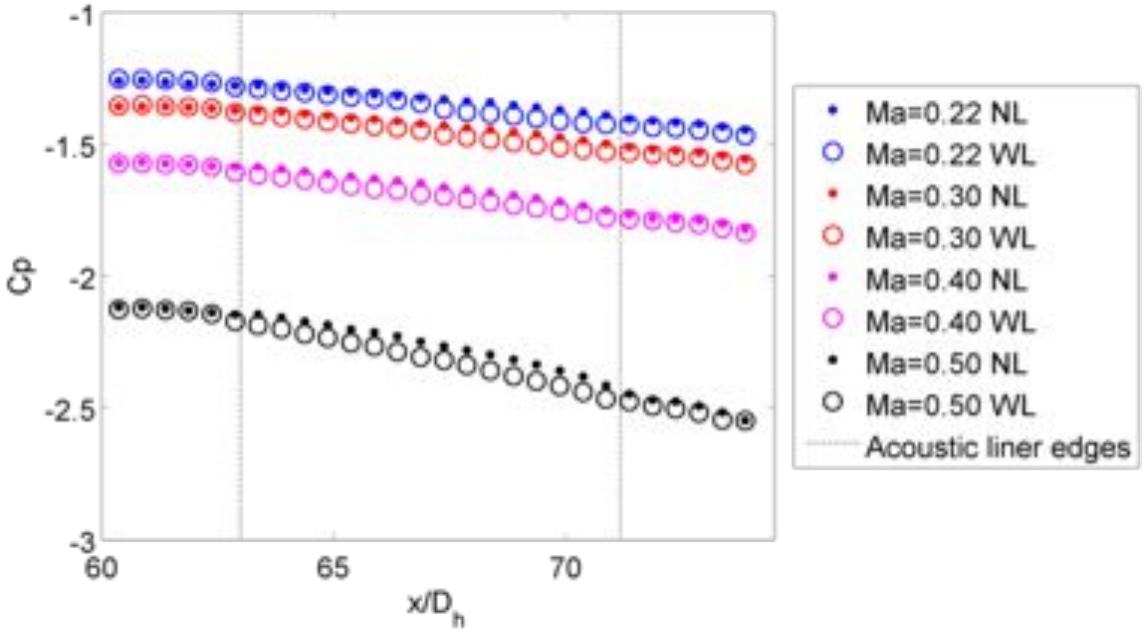

Figure 5-35. Pressure coefficient with liner.

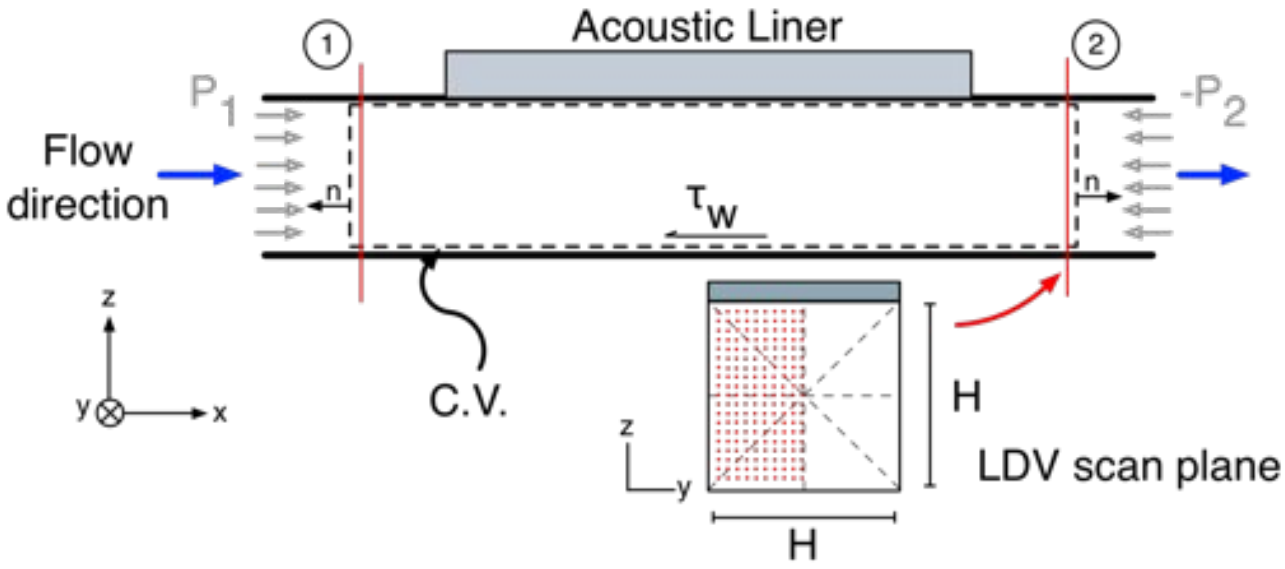

Figure 5-36. Schematic of the 2D control volume and physical setup.

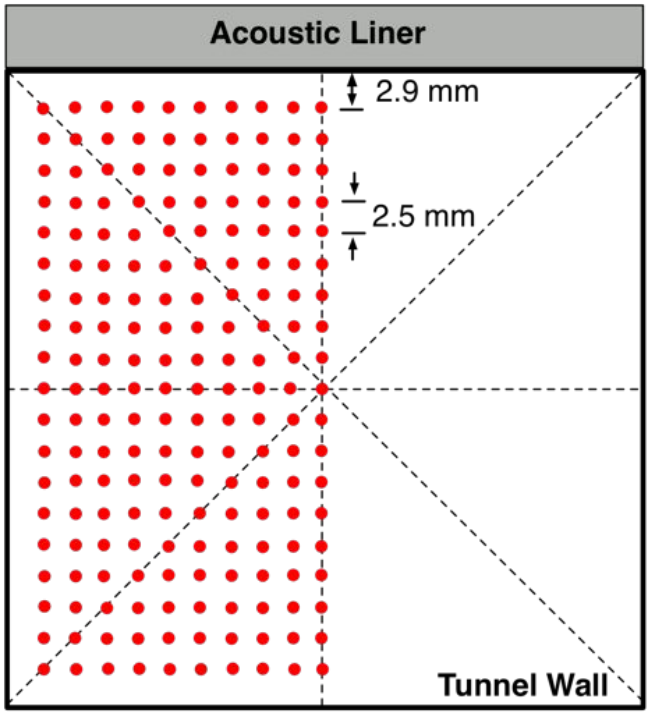

Figure 5-37. Grid pattern indicating 1D LDV measurement locations in the half-duct plane. Measurements were made at $x/D_h = 63$ and 72. Dashed lines indicate expected symmetry planes.

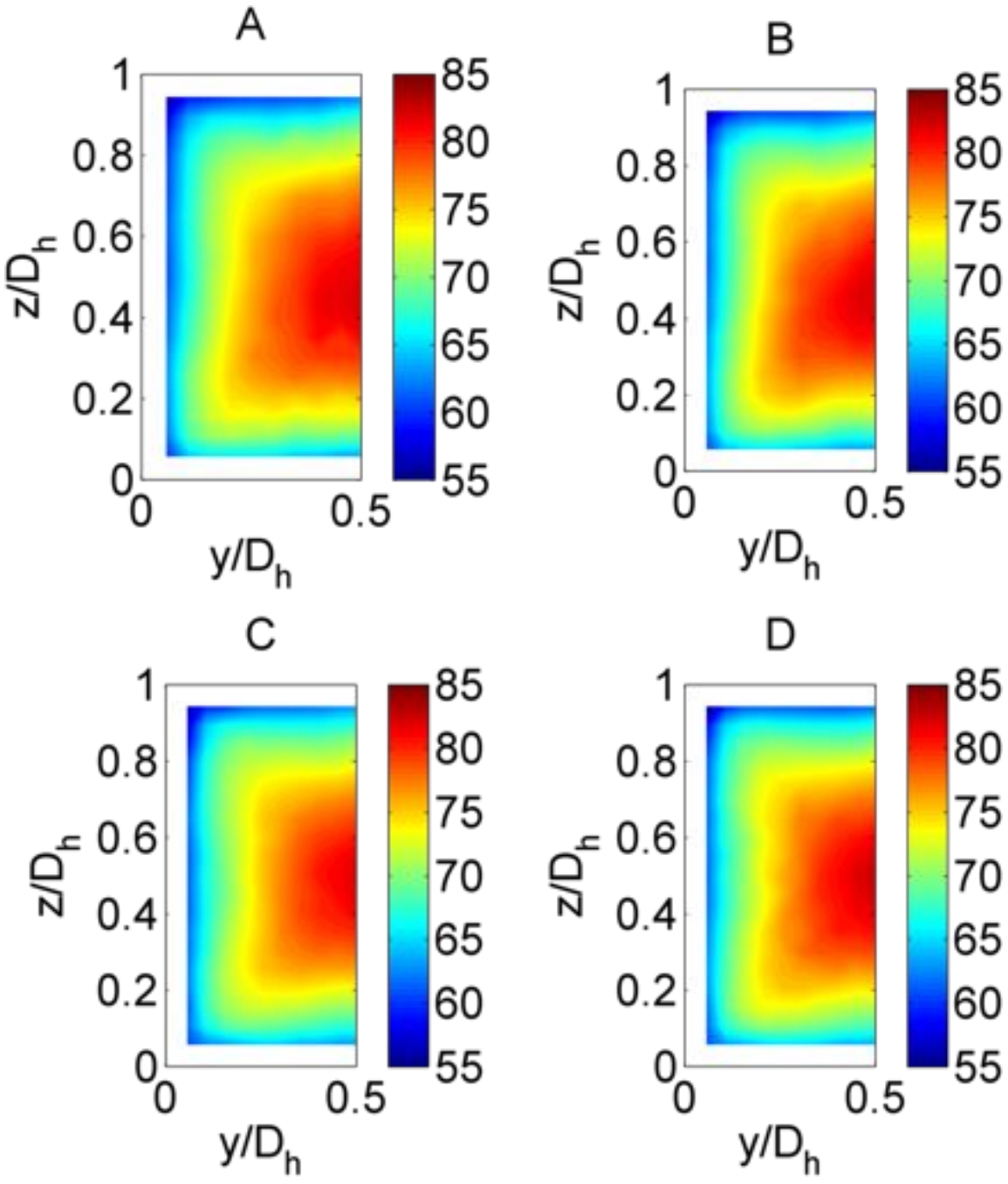

Figure 5-38. Control volume velocity [m/s] contour maps, A) Upstream hard wall, B) Upstream acoustic liner, C) Downstream hard wall, D) Downstream Acoustic liner.

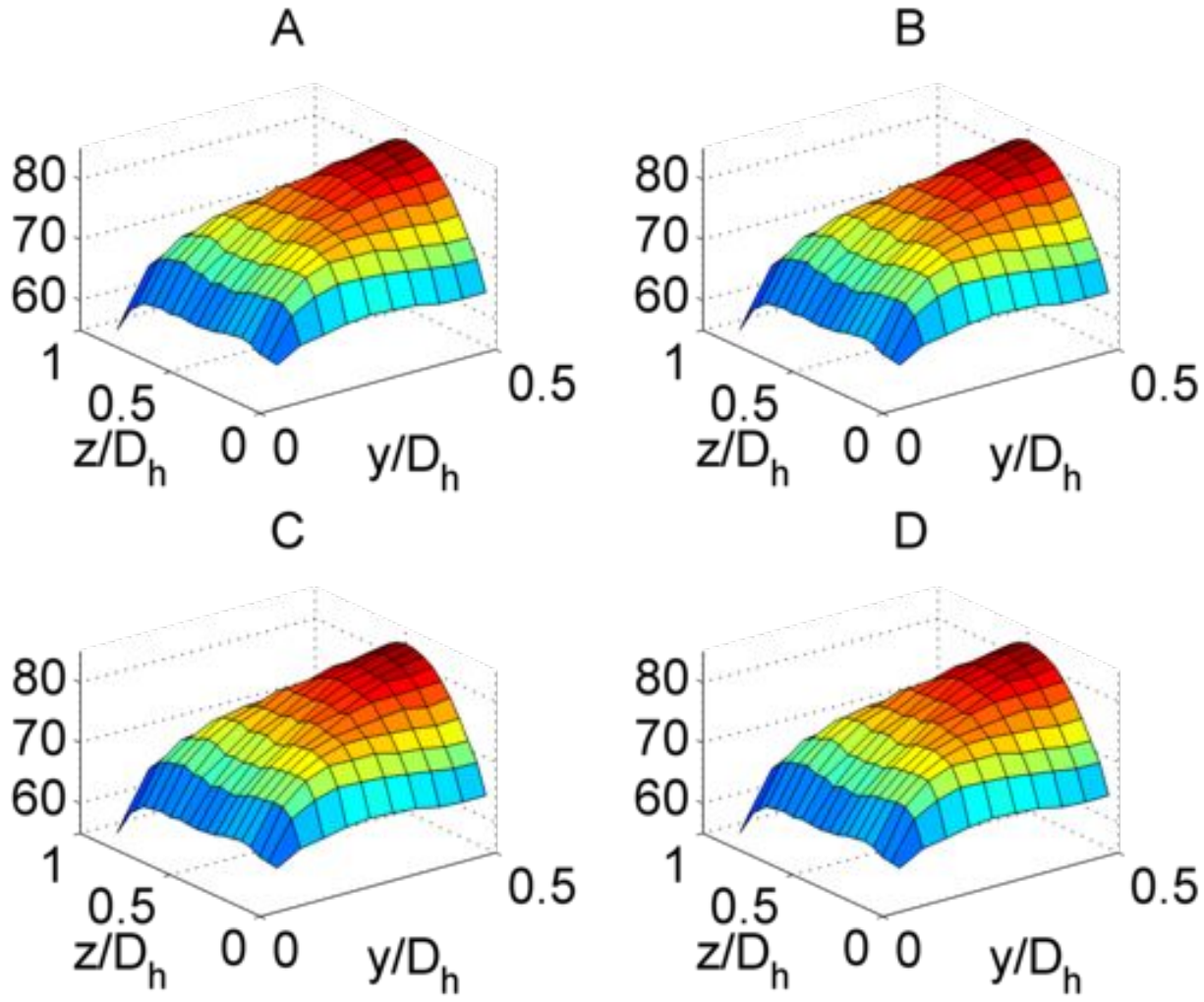

Figure 5-39. Control volume surface map velocity in [m/s], A) Upstream hard wall, B) Upstream acoustic liner, C) Downstream hard wall, D) Downstream Acoustic liner.

CHAPTER 6
CONCLUSION AND FUTURE WORK

Concluding this thesis, this chapter recaps the key points of the facility characterization, demonstration of ability to educe acoustic impedance of an acoustic liner, and detailing suggestions for future work. Improvements to facility design along with suggested implementations are described.

6.1 Facility Characterization

6.1.1 Fluid Dynamic Characterization

Experiments were performed to highlight the flow in two distinct regions of the tunnel, the entrance region immediately downstream of the nozzle, and a location far enough downstream to assume fully developed conditions. Both regions were tested and compared to published work.

The characterization of the entrance region centered on matching the growth of the accelerated central core flow to facilities of similar geometries and run conditions. Anselmet *et al.* (2009) proposed a non-dimensional scaling of entrance shown in Equation 5–17. The GFID data applied to Equation 5–17 yielded a slope of 0.145 ± 0.039, slightly under-predicting the reported value of Anselmet *et al.* (2009) of 0.185. However, independent analysis of the data from Gessner *et al.* (1977) resulted in a slope of 0.167 ± 0.05, in agreement with the GFID results. These findings indicate that the growth in the GFID entrance region is within the expected range for a high Reynolds number turbulent channel flow facility. Equation 5–17 can then be extended to estimate the entrance length of the GFID to $x/D_h = 36.2$.

Verification of downstream fully developed conditions were evaluated with the leading edge of the test section installed at $x/D_h = 58.5$. Analysis of the centerline and bulk velocity, as well as the streamwise static pressure all indicated that the mean flow was fully developed. The results allow for acoustic liner testing under known conditions

and simpler inputs for advanced impedance education analyses where the flow profile is considered.

6.1.2 Acoustic Characterization

A near-anechoic diffuser was fabricated to reduce upstream acoustic propagation. The reflection coefficient was demonstrated to be less than 13% over the frequency range of interest. In contrast, the hard-wall diffuser used for fluid dynamic studies was found to have reflection coefficients above 40% over the same range. Utilization of the anechoic diffuser however should be limited to acoustic testing when no flow seed is present, thereby reducing the potential of oil accumulation on the facesheet.

6.2 Research Impact

The primary goal of this thesis was to design, construct, a acoustic-flow bench and educe the impedance of an acoustic liner under grazing flow. The chosen impedance eduction method, the single mode method (SMM), as well as the ability to accurately extract impedance, were validated through a two step process using a wire mesh acoustic liner.

First, the wire mesh liner was tested in two facilities, the GFID with zero mean grazing flow using the SMM to educe the impedance, and in a normal incidence tube using the two microphone method. The impedance was matched between the two facilities across the frequency range tested.

The second step applied the SMM to published data from NASA with corresponding impedance results using two FEM-based eduction approaches. The SMM was able to match general trends of the FEM-results at the tested frequencies but yielded large errors near the anti-resonance of the acoustic liner.

Finally, the validated model was applied to experimental data from the GFID of the wire mesh liner over four Mach numbers and five discrete frequencies. Impedance results for the acoustic liner demonstrated both higher resistance values and increased resonant frequency with increasing Mach number. Impedance was unable to be determined from

the test data for a frequency of 500 Hz, regardless of Mach number. The experiment demonstrated the GFID capable of educing the impedance of an acoustic liner allowing for alternate methods to be applied to the data.

6.3 Future Work

During the design, fabrication, and testing within the GFID, potential areas of improvements were noted. The following sections will discuss potential improvements that could be made to the facility in Section 6.3.1 and improvements toward impedance education capabilities within the GFID in Section 6.3.2.

6.3.1 Facility Improvements

Stagnation chamber

The stagnation chamber is the most upstream component of the GFID and thus plays a large role in downstream flow influence. Additionally, the stagnation chamber houses stagnation property measurement sensors and introduces flow seeding. To help smooth out small fluctuations from the upstream flow valve, the stagnation chamber volume could be increased. An increased volume would reduce the initial flow speed and could be accomplished with pipe extension of equal diameter to the current stagnation chamber. This would also allow for the introduction of flow treatment such as flow screen and settling chambers for turbulence reduction.

The second stage nozzle is currently the only link between the large stagnation chamber and the massive GFID ducting. Care has been applied to reduce loading on the nozzle but improvement could be made through outfitting the nozzle within a metal cage structure to decouple the plastic nozzle from a downstream load, thereby reducing potential cracking or breakage of the nozzle.

Flow seeding

Flow seeding for optical based fluid dynamic measured are introduced at the aft end of the stagnation chamber. Extended run periods demonstrated that oil would pool at the base of the stagnation chamber, causing streaks downstream. A simple drain pipe would

allow for the removal of oil build-up without the need to dismantle the chamber, thereby reducing the potential for misalignment.

Additionally, the current seeder provided excellent particle size for LDV measurements, however limited measurement time due to window oil-accumulation. Future tests should explore the use of non-oil based seeding including dry seeding, which may require external collection, or water-based oil fluids for easy clean-up. Alternative seed approaches could eliminate the necessity of the hard-wall diffuser.

Acoustic excitation

The speaker used for excitation was able to generate discrete tones up to 130 dB (ref. 20 μPa) under speeds up to $M = 0.5$. Additional drivers and amplifiers will allow for higher SPL test conditions. Through inter-facility collaboration with the GFIT at NASA LaRC, SPL values may be able to reach and surpass values found in aircraft engine nacelles of 160 dB.

Test section

The test section was designed on a limited budget and through lessons learned several improvements are recommended. All windows were mounted to the test section through holes within the window material itself. The mounting holes are a stress concentration that is subject to cracking. New windows should utilize metal frames and float glass for improved optical performance and reduced window stress. The metal frames would allow for a thinner window material, thereby potentially reducing the restrictions imposed on 3D LDV measurements as noted in Section 5.1.2.

As the test section was used for all testing demonstrated throughout this thesis, the windows, auxiliary ports, and liner ports were mounted and unmounted many times. The excessive wear has worn down many of the tapped holes and it is recommended that each hole be outfitted with replaceable, stainless steel heli-coils.

Hard-wall diffuser

The large oscillations in the reflection coefficient of the hard-wall diffuser indicate a potential structural mode which may be due to the relatively thin walls and minimal mass of the diffuser. It is recommended that additional fiberglass wrapping be applied to the current diffuser or an inexpensive replacement hard wall diffuser be fabricated with additional stiffness. The hard wall diffuser should only be used until a suitable replacement flow seed can be acquired and demonstrated appropriate for fluids testing.

6.3.2 Advanced Impedance Eduction

As was demonstrated by this thesis, the GFID was used as a test bed for making acoustic measurements and educing the impedance of an acoustic liner under grazing flow conditions. The SMM was chosen due to the inherent simplicity, allowing for the GFID itself to be the forefront of the research and not a more complicated method. With the facility characterized the focus should shift toward advanced methods and increased accuracy over a larger range of run conditions. Alternate eduction methods should be explored including the Straightforward method and the Semi-direct method outline in Section 3.2. Both of these models are less sensitive to upstream acoustic propagation than the SMM and thus could be used at higher speeds. In addition, they have both been demonstrated to provide impedance results matching those of more advanced FEM based approaches.

6.3.3 Acoustic Liner Shear Stress Testings

The growing demand for aircraft noise reduction will place a greater necessity on the application of acoustic liners. The impact of an acoustic liner on the passing flow remains a topic of increasing interest. There are several methods for measuring shear stress of a flow and the reader is directed to Naughton & Sheplak (2002) for a thorough review.

In this thesis, three indirect measurement techniques using velocity profiles were explored but were unable to determine a measurable shear impact due to the acoustic liner. Indirect methods, such as velocity profile techniques, are attractive due to the

non-intrusive nature and ease of use. Future testing using velocity profile based techniques could employ multi-component velocity measurements and advanced control of the free stream velocity. Alternative methods such as PIV could be employed to reduce experimental acquisition time.

Future shear testing should also explore the use of both both quasi-direct and direct methods. The family of quasi-direct methods, such as oil-film interferometry (OFI) and micro pillar arrays, allow for shear stress of a flow to be inferred from the impact of shear on another measurable quantity. Both methods are applied at the boundary and thus have a greater potential to determine the actual impact from an acoustic liner. Similarly, direct methods such as force balances, and more recently MEMS based shear stress sensors could play a roll for average and point shear value assessment respectively.

The GFID has the ability to play a unique role toward advancing the research and application of acoustic liners through investigating the underlying physics and improved measurement methodology. Past and future collaboration with both corporate partners and government laboratories will allow the GFID to help design the next generation of acoustic liners and testing technology.

APPENDIX A
DERIVATION OF DUCT ACOUSTICS IN A QUIESCENT MEDIUM WITH SOUND HARD WALLS

Assumptions

- Linear
- Isentropic
- Homogeneous
- two-dimensional

Schematic

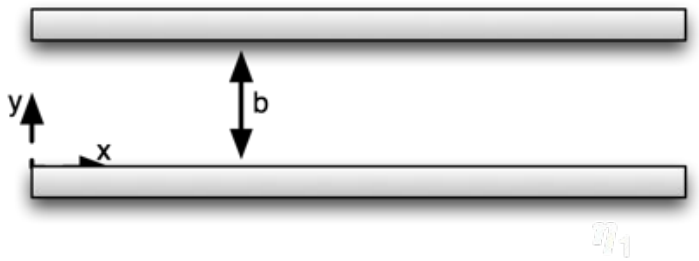

Analysis

Let

$$p'(x,y,t) = P(x,y,\omega)e^{j\omega t} \tag{A–1}$$

Given the pressure wave equation

$$\frac{1}{c_0}\frac{\partial^2 p'}{\partial t^2} - \nabla^2 p' = 0 \tag{A–2}$$

Plugging A–1 into A–2 results in

$$\frac{1}{c_0^2}\frac{\partial^2}{\partial t^2}\left(Pe^{j\omega t}\right) - \nabla^2\left(Pe^{j\omega t}\right) = 0$$

$$\frac{(j\omega)^2}{c_0^2} P e^{j\omega t} - e^{j\omega t}\nabla^2 P = 0 \tag{A–3}$$

Note:

- $j = \sqrt{-1} \Rightarrow j^2 = -1$
- $k = \frac{\omega}{c_0} \Rightarrow \left(\frac{\omega}{c_0}\right)^2 = k^2$

Eq. A–3 is rewritten as

$$-k^2 P e^{j\omega t} - e^{j\omega t}\nabla^2 P = 0$$

Divide out $-e^{j\omega t}$ from both sides

$$\nabla^2 P + k^2 P = 0 \tag{A–4}$$

Where k^2 is the dispersion relationship given by

$$k^2 = \left(\frac{\omega}{c_0}\right)^2 = k_x^2 + k_y^2$$

Assume a working form for the pressure to be the product of three univariable functions,

$$p'(x, y, t) = Y(y)X(x)e^{j\omega t}. \tag{A–5}$$

Applying a Separation of Variables approach, A–5 can be substituted into A–4

$$Y\frac{d^2X}{dx^2} + X\frac{d^2Y}{dy^2} + k^2XY = 0$$

Let X'' denote a second derivative, rewritten as

$$YX'' + XY'' = -k^2XY$$

Divide by the product XY

$$\frac{1}{X}X'' + \frac{1}{Y}Y'' = -k^2 \tag{A–6}$$

Note that the transverse y-direction is homogeneous and conversely, the propagating x-direction is non-homogeneous with boundary conditions applied at infinity

First solving the homogeneous direction

$$\frac{1}{Y}Y'' = -k^2 - \frac{X''}{X} = -k_y^2 = \text{constant}$$

Rewritten as

$$Y'' + k_y^2 Y = 0 \tag{A–7}$$

Equation A–7 under homogeneous boundary conditions results in the basis function to the solution of the sum of transcendental functions

$$Y(y) = C_1 \cos(k_y y) + C_2 \sin(k_y y) \tag{A–8}$$

Where C_1 and C_2 are constants. Acknowledging that transverse boundary conditions are expressed in terms of the derivative of pressure, take the derivative of A–8

$$Y'(y) = -k_y C_1 \sin(k_y y) + k_y C_2 \cos(k_y y)$$

Apply the first transverse boundary condition of no slip at the wall,

$$Y'(y=0) = 0 = -k_y C_1 \cancel{\sin(0)} + k_y C_2 \cos(0)$$

$$k_y C_2 = 0$$

$$k_y \neq 0$$

$$\therefore C_2 = 0$$

Apply the second transverse boundary condition

$$Y'(y=b) = 0 = -k_y C_1 \sin(k_y b)$$

$$k_y \text{ or } C \neq 0$$

$$\therefore \sin(k_y b) = 0$$

$$k_y b = n\pi$$

$$\boxed{k_y = \frac{n\pi}{b}} \quad \text{for n=0,1,2,3...}$$

Note that $n = 0$ is a trivial solution for the velocity field but does describe an important uniform pressure field.

The boxed result are the transverse eigenvalues, the transverse eigenfunctions are

$$\sin\left(n\pi\frac{y}{b}\right)$$

Recall,

$$k = \frac{\omega}{c_0} = \frac{2\pi f}{c_0}$$

$$\therefore \qquad fn = \frac{nkc_0}{2\pi} = \frac{nc_0}{2b} \Rightarrow \text{defines eigenfrequencies}$$

Here the integer value of n describes the pressure modes within the duct. The first eigenfrequency defines the cut-on frequency of the first higher order mode.

To conclude the transverse direction for the Separation of Variables, the basis function is rewritten

$$\boxed{Y(y) = C_1 \cos\left(\frac{n\pi y}{b}\right)} \tag{A–9}$$

Solve A–6 in the progressive x-direction

$$X'' + k_x^2 X = 0$$

yields the solution of a sum of exponential functions due to the prescribed boundary conditions at infinity.

$$X(x) = C_3 e^{-jk_x x} + C_4 e^{jk_x x} \tag{A–10}$$

The terms of eq. A–10 represent the progression of acoustic waves both away from the source and those progressing toward the source. The one-dimensional propagation assumption implies there is not a second source nor a reflective surface, therefore that C_4 goes to zero.

Note that

$$(k_x)_n = \sqrt{k^2 - k_y^2} = \sqrt{\left(\frac{\omega}{c_0}\right)^2 - \frac{n\pi}{b}}, \quad \text{for n=0,1,2,3...}$$

Because the progressive x-direction has non-homogeneous boundary conditions, the X and Y individual solutions must be combined first.

Combining the two independent basis functions, recalling that

$$p'(x,y,t) = X(x)Y(y)e^{j\omega t}$$

$$p' = \sum_{n=0}^{\infty} \cos\left(\frac{n\pi y}{b}\right) C_5 e^{-j(k_x)_n x} e^{j\omega t}$$

Where $C_5 = C_1 \times C_3$ For simplicity, C_5 is recast as the constant A. The final answer now becomes as follows with the change of variables.

$$\boxed{p' = \sum_{n=0}^{\infty} \cos\left(\frac{n\pi y}{b}\right) A e^{-j(k_x)_n x} e^{j\omega t}} \tag{A–11}$$

APPENDIX B
DERIVATION OF DUCT ACOUSTICS IN A QUIESCENT MEDIUM WITH PRESCRIBED IMPEDANCE BOUNDARY CONDITION

Assumptions

- Linear pressure propagation
- Isentropic flow
- Homogeneous medium
- Two-dimensional

Schematic

$$\eta_i = \frac{\rho_0 c_0}{Z_i}$$

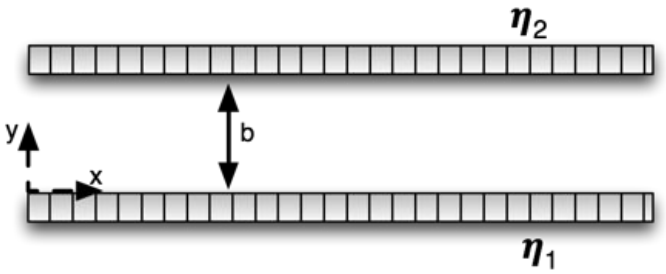

Analysis

Given

A rectangular duct with generalized acoustic liners at the boundaries, prescribed at y=0 and y=b. Similarly, the z-direction

The z-direction is neglected in this analysis but the theory can be extended or be superimposed with the hard walled case in Appendix A.

The locally reacting liners posses two difference impedance values, Z_{y1} at $y = 0$ and Z_{y2} at $y = b$.

The solution follows Ingard (1999) Duct Acoustics notes.

Boundary Conditions

The boundary conditions represent matching particle velocity at the surface.

BC 1:

$$\frac{1}{-j\omega\rho_0}\frac{\partial p}{\partial y} = \frac{P}{Z_1}\Big|_{y=0}$$

BC 2:

$$\frac{1}{-j\omega\rho_0}\frac{\partial p}{\partial y} = \frac{P}{-Z_2}\Big|_{y=b}$$

Note that the right-hand side of BC2 contains a negative sign denoting that the velocity is in the negative y-direction, outward normal from the wall.

Generalized Solution

Using a separation of variables approach, the problem can be decomposed into the product of two functions.

$$p' = Y(y)X(x)e^{j\omega t}$$

Where,

- Y(y) is a function describing the transverse spatial variation in the acoustic field.
- X(x) is a function describing the spatial variation in the direction of propagation.
- $e^{j\omega t}$ describes the time harmonic temporal variation of the acoustic field. Either the real or the imaginary component is used for analysis.

Transverse Direction,Y(y)

Because the problem is bounded at finite values, the solution can be written as the sum of transcendental functions.

$$Y(y) = A\sin(k_y y) + B\cos(k_y y),$$

or

$$Y(y) = A[cos(k_y y) + Rsin(k_y y)]$$

. Where A and B are constants, and $R = {}^{B}/_{A}$

At this time it is useful to introduce the reciprocal of impedance, the admittance is defined by

$$\eta_i = \frac{\rho_0 c_0}{Z_i}$$

.

Apply Boundary Conditions

Apply BC1

$$\rho_0 c_0 u_{y1} = -p\eta_1|_{y=0}$$

$$\cancel{\rho_0} c_0 \cancel{A} \frac{k_y}{j\omega\cancel{\rho_0}}[R\underbrace{cos(k_y 0)}_{1} - \cancel{\underbrace{sin(k_y 0)}_{0}}] = -\cancel{A}[\underbrace{cos(k_y 0)}_{1} + R\cancel{\underbrace{sin(k_y 0)}_{0}}]\eta_1$$

$$\frac{c_0}{\omega}\frac{k_y}{j}R = -\eta_1$$

Using the definition of the wave number and $1/j = -j$,

$$j\left(\frac{k_y}{k}\right)R = \eta_1$$

Solve for R,

$$R = \frac{\eta_1}{j}\left(\frac{k}{k_y}\right) \tag{B–1}$$

Apply BC2

$$\rho_0 c_0 u_{y2} = p\eta_2|_{y=b}$$

$$\cancel{\rho_0} c_0 \cancel{A} \frac{k_y}{j\omega\cancel{\rho_0}}[Rcos(k_y b) - sin(k_y b)] = \cancel{A}[cos(k_y b) + Rsin(k_y b)]\eta_2$$

$$\frac{c_0}{j\omega}k_y\frac{Rcos(k_y b) - sin(k_y b)}{cos(k_y b) + Rsin(k_y b)} = \eta_2$$

$$\left(\frac{k_y}{jk}\right)\frac{-sin(k_y b) + Rcos(k_y b)}{cos(k_y b) + Rsin(k_y b)} = \eta_2 \tag{B–2}$$

Plug in R,

$$\left(\frac{k_y}{jk}\right)\frac{-sin(k_y b) + \frac{\eta_1}{j}\left(\frac{k}{k_y}\right)cos(k_y b)}{cos(k_y b) + \frac{\eta_1}{j}\left(\frac{k}{k_y}\right)sin(k_y b)} = \eta_2$$

Divide each term by $cos\,(k_y b)$, and using the tangent function and $1/j = -j$

$$\left(\frac{k_y}{jk}\right)\frac{-tan(k_y b) - j\eta_1\left(\frac{k}{k_y}\right)}{1 - j\eta_1\left(\frac{k}{k_y}\right)tan(k_y b)} = \eta_2$$

$$-\left(\frac{k_y}{jk}\right)tan(k_y b)-\eta_1=\eta_2-j\eta_1\eta_2\left(\frac{k}{k_y}\right)tan(k_y b)$$

$$\eta_1+\eta_2=-\left(\frac{k_y}{jk}\right)tan(k_y b)+j\eta_1\eta_2\left(\frac{k}{k_y}\right)tan(k_y b)$$

$$\eta_1+\eta_2=j\left(\frac{k_y}{k}\right)tan(k_y b)\left[\eta_1\eta_2\left(\frac{k}{k_y}\right)^2+1\right]$$

$$\boxed{\left(\frac{k_y}{k}\right)tan(k_y b)=-j\frac{\eta_1+\eta_2}{1+\eta_1\eta_2\left(\frac{k}{k_y}\right)^2}}$$

APPENDIX C
DERIVATION OF THE CONVECTIVE WAVE EQUATION

Assumptions

- Linear
- Isentropic flow
- Homogeneous medium
- Incompressible
- Negligible body forces
- Irrotational
- 1-D propagation

Equations

- Continuity:

$$\rho_0 \nabla \cdot \vec{V} + \frac{D\rho}{Dt} = 0 \tag{C–1}$$

- Momentum:

$$\rho_0 \frac{D\vec{V}}{Dt} + \nabla P \tag{C–2}$$

- Equation of state:

$$c_0^2 = \frac{\partial \rho}{\partial p_s} \tag{C–3}$$

Plug Equation C–3 into Equation C–1 to get

$$\rho_0 \nabla \cdot \vec{V} + \frac{1}{c_0^2} \frac{}{DP} Dt = 0. \tag{C–4}$$

Take the spatial derivative of Equation C–2,

$$\rho_0 \frac{D\left(\nabla \cdot \vec{V}\right)}{Dt} + \nabla^2 P = 0. \tag{C–5}$$

Apply a total time derivative to Equation C–4 to get,

$$\rho_0 \frac{D}{Dt}\left(\nabla \cdot \vec{V}\right) + \frac{1}{c_0^2} \frac{D^2 P}{Dt^2} = 0 \tag{C–6}$$

Subtract Equation C–6 from Equation C–5 results in the convective wave equation,

$$\frac{1}{c_0^2}\frac{D^2P}{Dt} - \nabla^2 P = 0. \tag{C–7}$$

Equation C–7 can be rewritten as

$$\frac{D^2P}{Dt^2} - c_0^2\nabla^2 P = 0,$$

which can be further expanded,

$$\left(\frac{\partial}{\partial t} + \vec{V}\cdot\nabla\right)\left(\frac{\partial}{\partial t} + \vec{V}\cdot\nabla\right)P - c_0^2\nabla^2 P = 0,$$

$$\frac{\partial^2 P}{\partial t^2} + 2\vec{V}\cdot\frac{\partial P}{\partial t} + \left(\vec{V}\cdot\nabla\right)\left(\vec{V}\cdot\nabla\right)P - c_0^2\nabla^2 P = 0. \tag{C–8}$$

If a Cartesian coordinate system is assumed with the x-direction in the streamwise direction, Equation C–8 can be simplified as

$$\frac{\partial^2 P}{\partial t^2} + 2V\frac{\partial}{\partial x}\left(\frac{\partial P}{\partial t}\right) + U^2\frac{\partial^2 P}{\partial x^2} - c_0^2\nabla^2 P = 0. \tag{C–9}$$

Apply a separation of variables approach to the time function representing an acoustic source denoted by a complex exponential

$$P = X(x)Y(y)Z(z)e^{j\omega t}. \tag{C–10}$$

Plug Equation C–10 into Equation C–9 and noting the definition of the wavenumber and Mach number yeilds

$$-\kappa^2 + 2Mj\kappa\frac{X'}{X} + M^2\frac{X''}{X} - \frac{Z''}{Z} - \frac{Y''}{Y} - \frac{X''}{X} = 0. \tag{C–11}$$

Solving Equation C–11 for the transverse z-direction results in

$$Z'' + \kappa_z^2 Z \tag{C–12}$$

with solution

$$Z(z) = A_1\cos\kappa_z z + A_2\sin k_z z, \tag{C–13}$$

and similarly,

$$Y'' + \kappa_y^2 Y \tag{C–14}$$

$$Y(y) = B_1 \cos \kappa_y y + B_2 \sin k_y y. \tag{C–15}$$

Substitute Equations C–12 and C–14 into Equation C–11 yields

$$\frac{X''}{X}\left(1 - M^2\right) - 2M\left(j\kappa\right)\frac{X''}{X} + \left(\kappa - \kappa_z^2 - \kappa_y^2\right). \tag{C–16}$$

The propagation of axial acoustic energy is assumed to a progressive wave, the it can be assumed to be represented by

$$X = e^{j\kappa_x x}. \tag{C–17}$$

Apply Equation C–17 to Equation C–16

$$\left[-\kappa_x^2\left(1 - M^2\right) + 2M\kappa_x\kappa + \left(\kappa - \kappa_z^2 - \kappa_y^2\right)\right] e^{j\kappa_x x} = 0. \tag{C–18}$$

The solution to Equation C–19 is

$$\kappa_x = \frac{M\kappa + \sqrt{\kappa^2 - \left(1 - M^2\right)\kappa_y^2}}{(1 - M)^2}. \tag{C–19}$$

Rearranging and solving for the ratio of κ_y/κ yields

$$\frac{\kappa_y}{\kappa} = \left(\frac{1 - \left[(1 - M)^2\left(\frac{\kappa_x}{\kappa}\right) + M\right]^2}{(1 - M)^2}\right)^{1/2}. \tag{C–20}$$

APPENDIX D
TECHNICAL DRAWINGS

This appendix contains all the technical drawings made at UF for the GFID. Parts such as the near-anechoic diffuser were designed by NASA and thus only the specific parts adapted for the GFID are shown. The technical drawings are presented in downstream order starting with the second stage nozzle. Further details about the design and implantation of each piece are found in Chapter 4

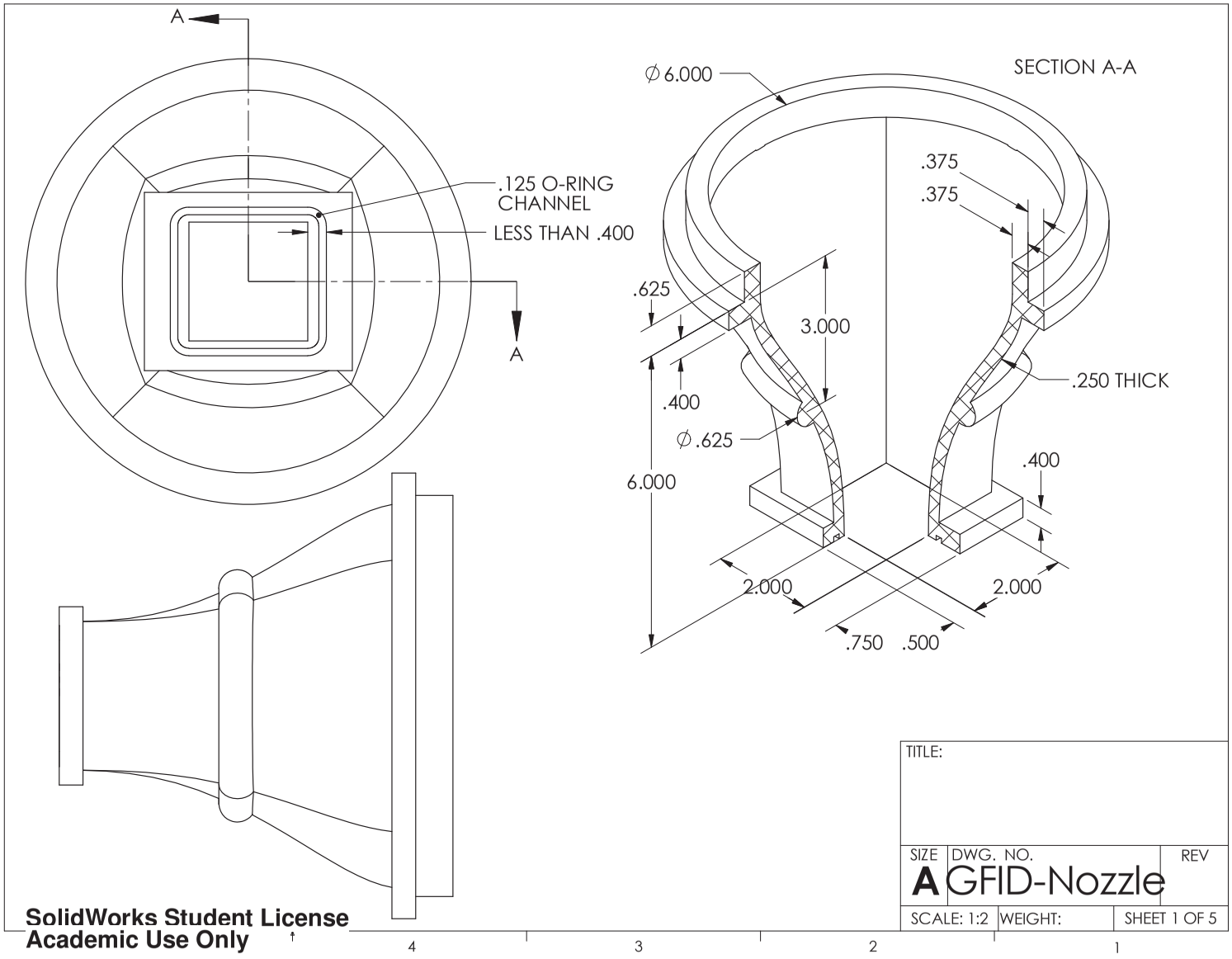

Figure D-1. Nozzle overall dimensions.

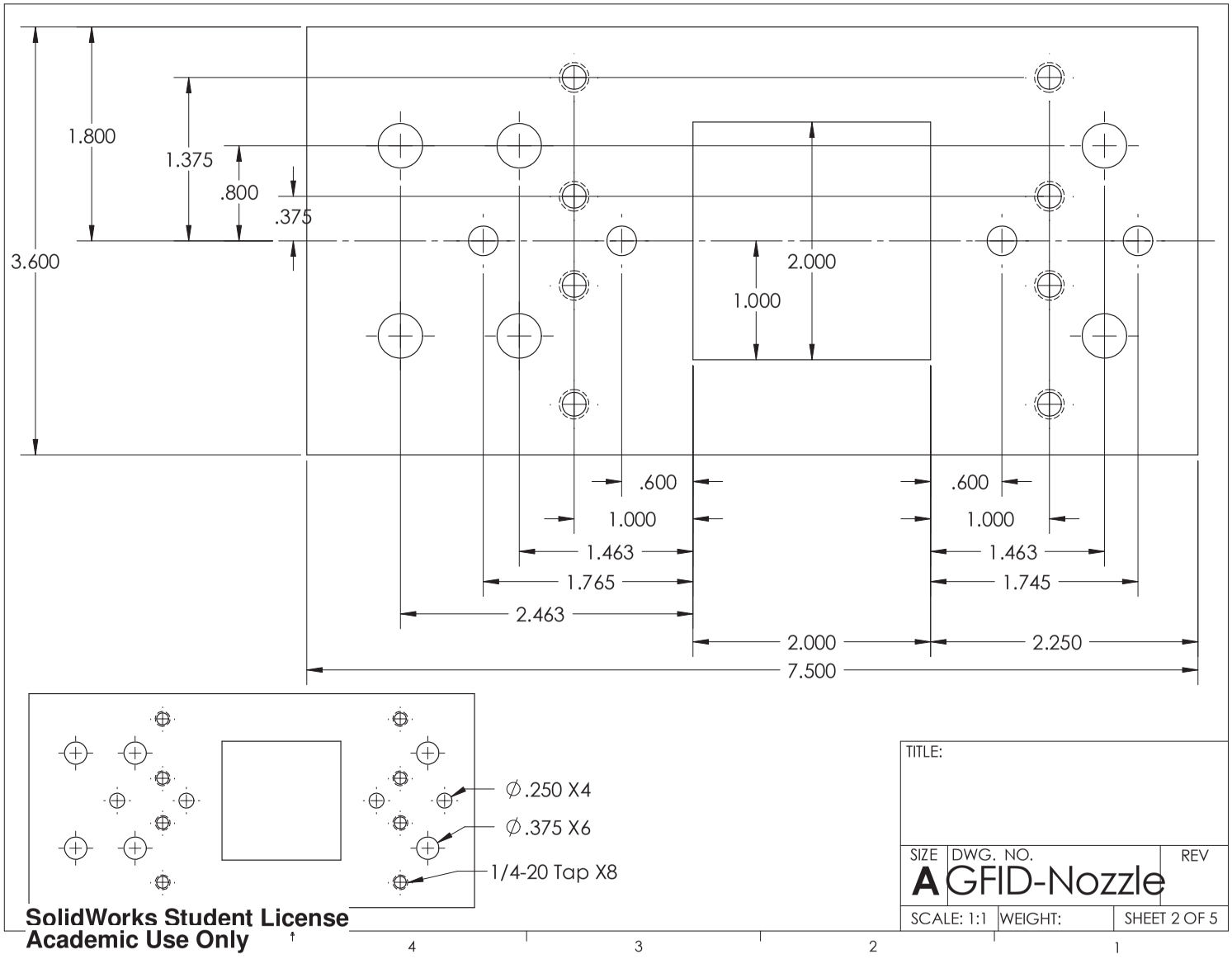

Figure D-2. Nozzle-ducting adapter and alignment plate.

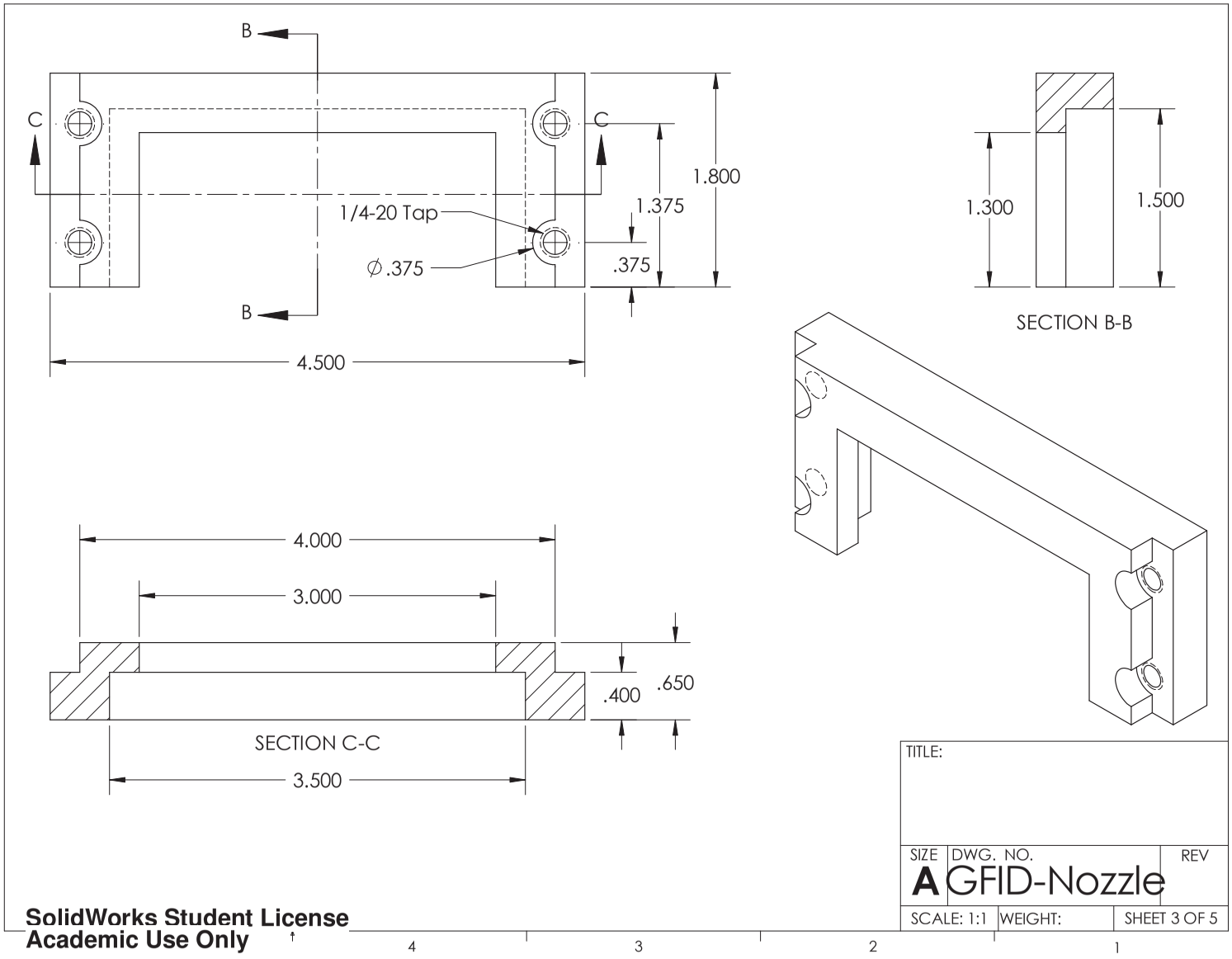

Figure D-3. Nozzle downstream flange.

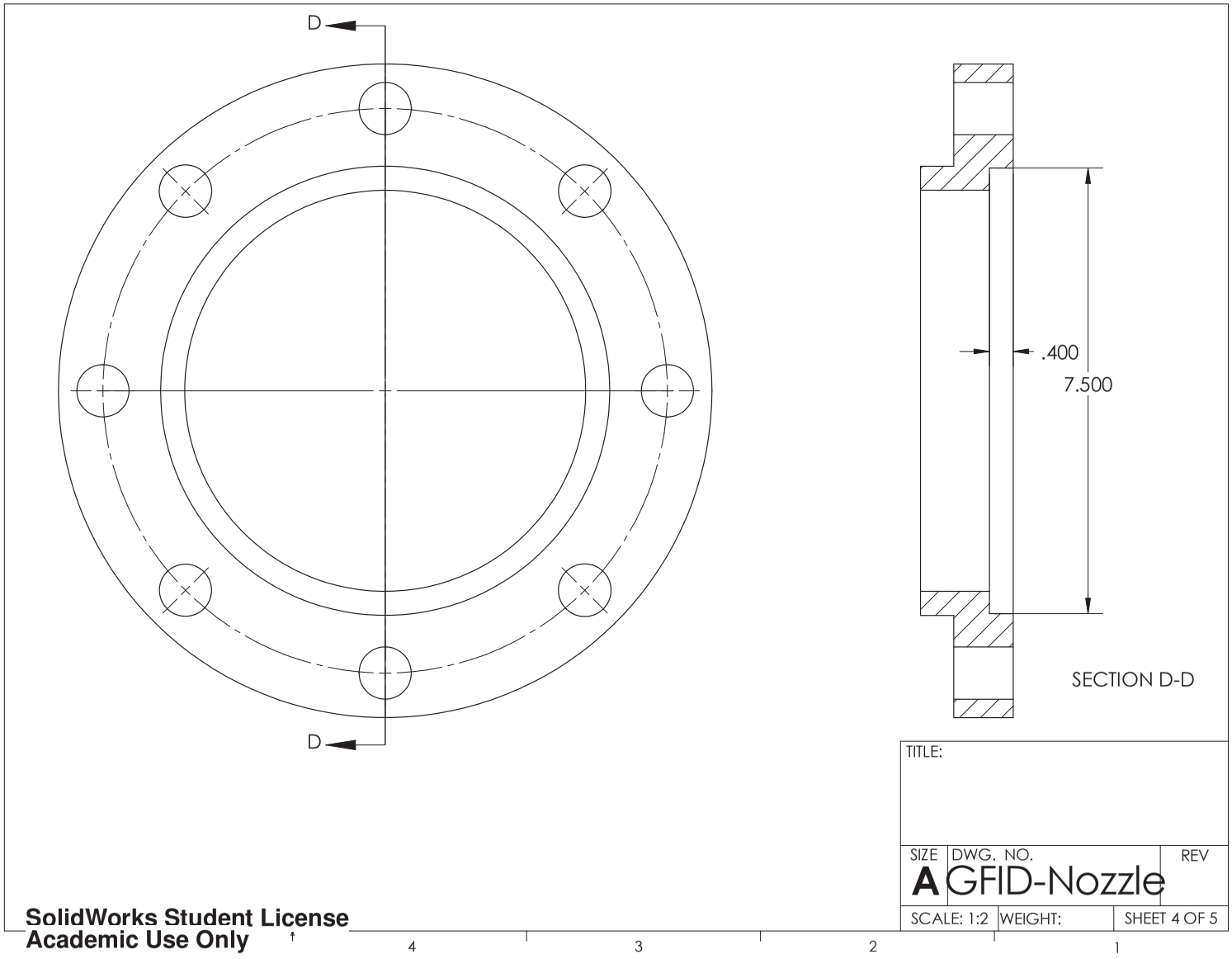

Figure D-4. Nozzle upstream flange.

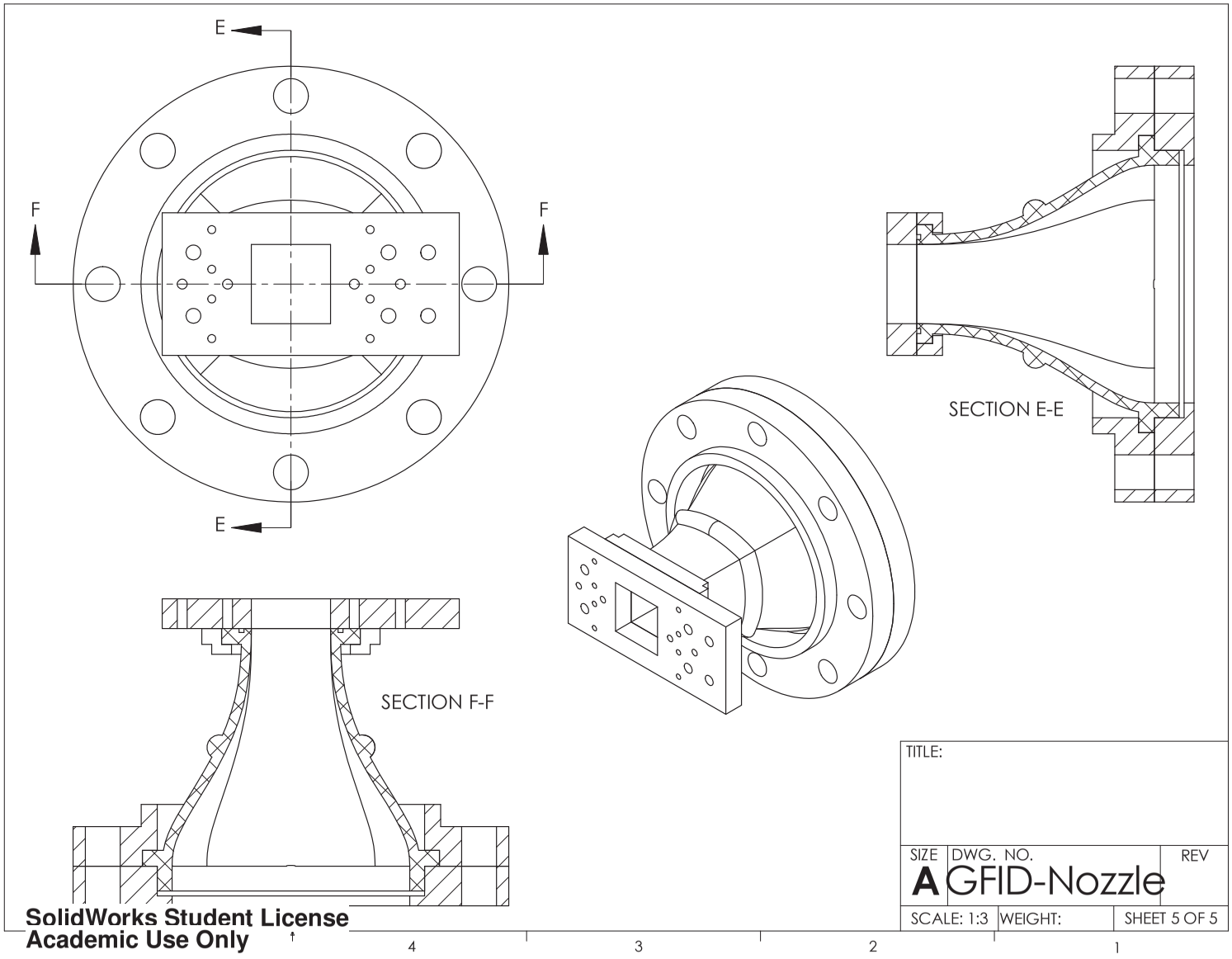

Figure D-5. Second stage nozzle assembly.

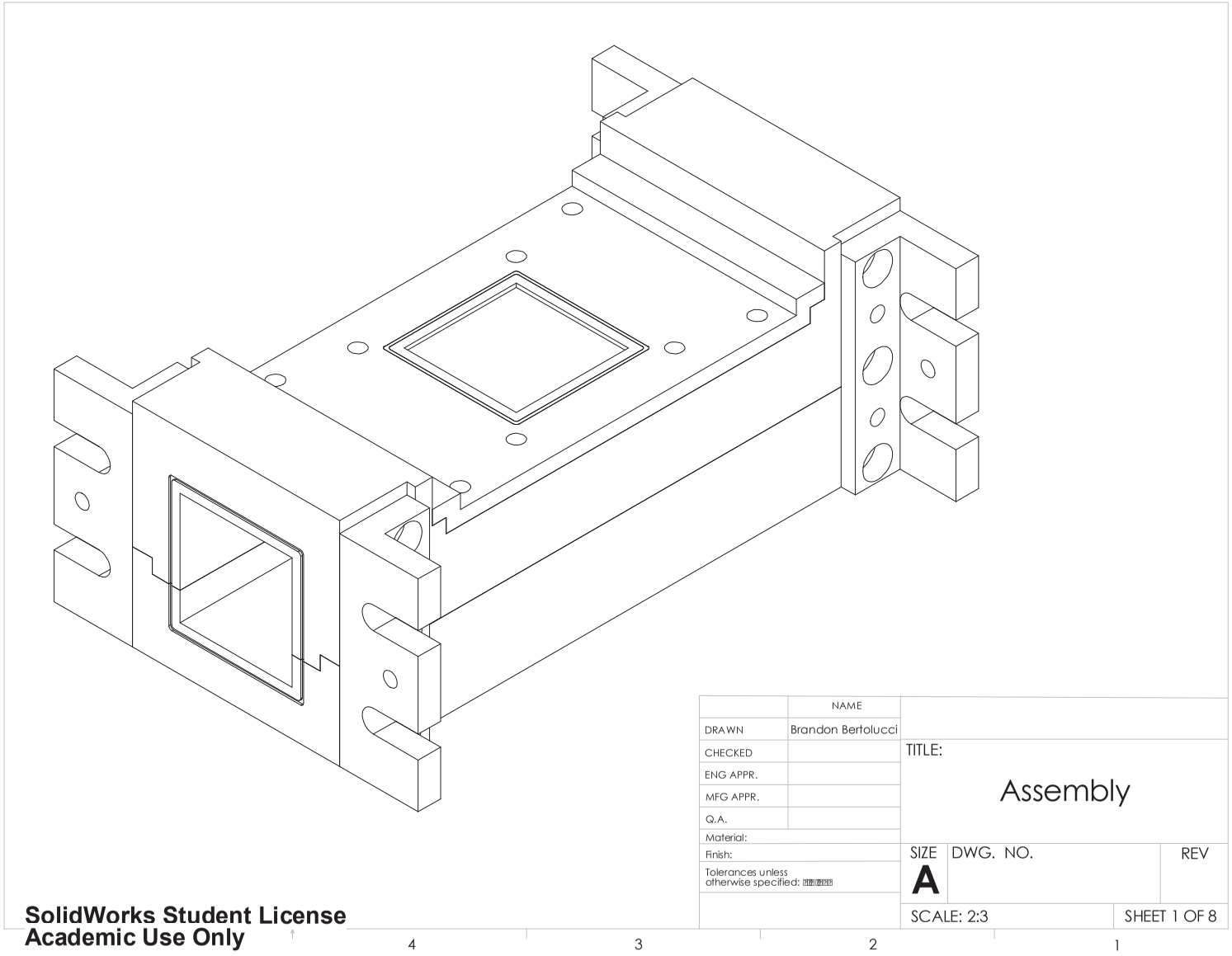

Figure D-6. Isometric solid view of speaker section with mounting brackets.

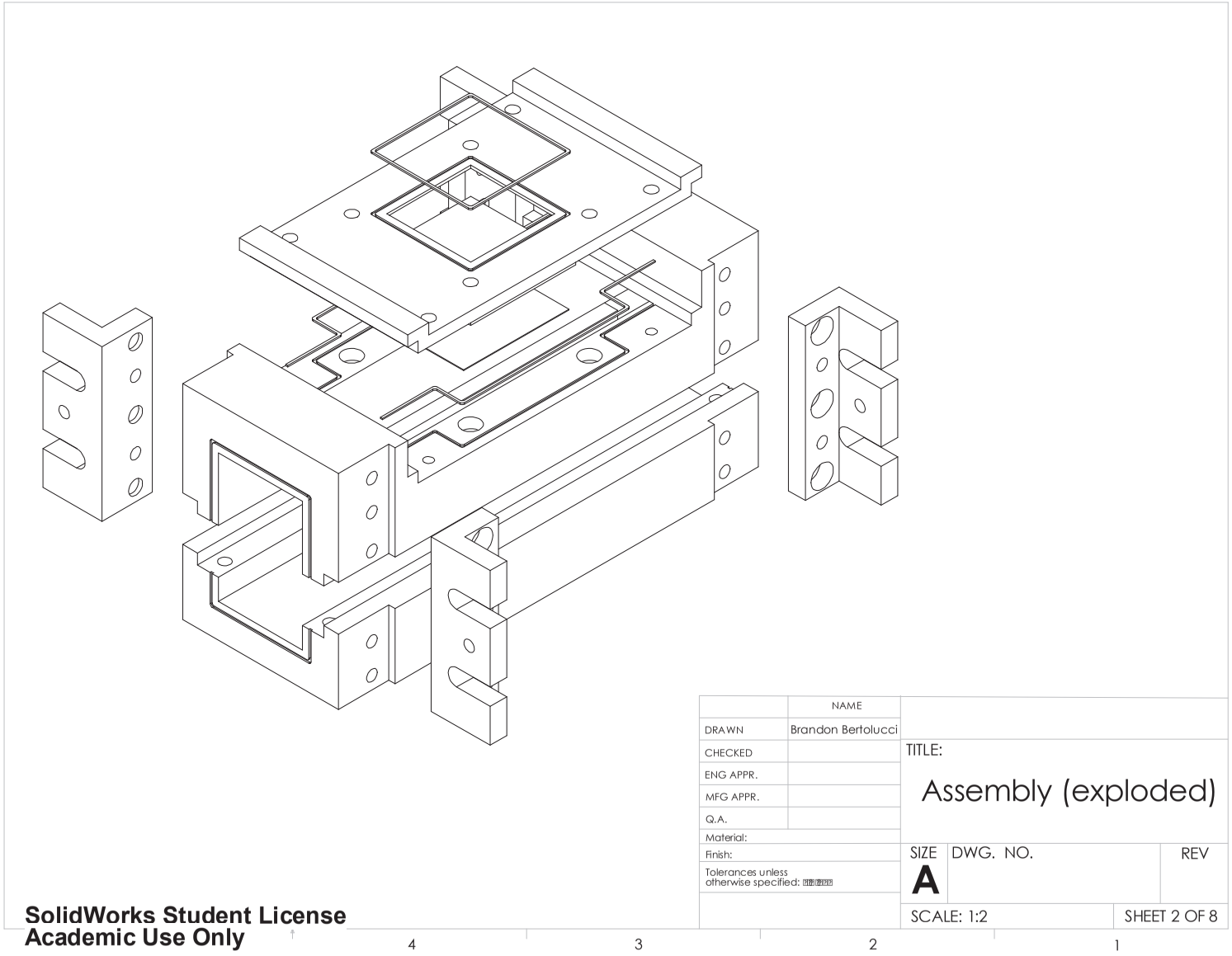

Figure D-7. Exploded isometric solid view of speaker section with mounting brackets.

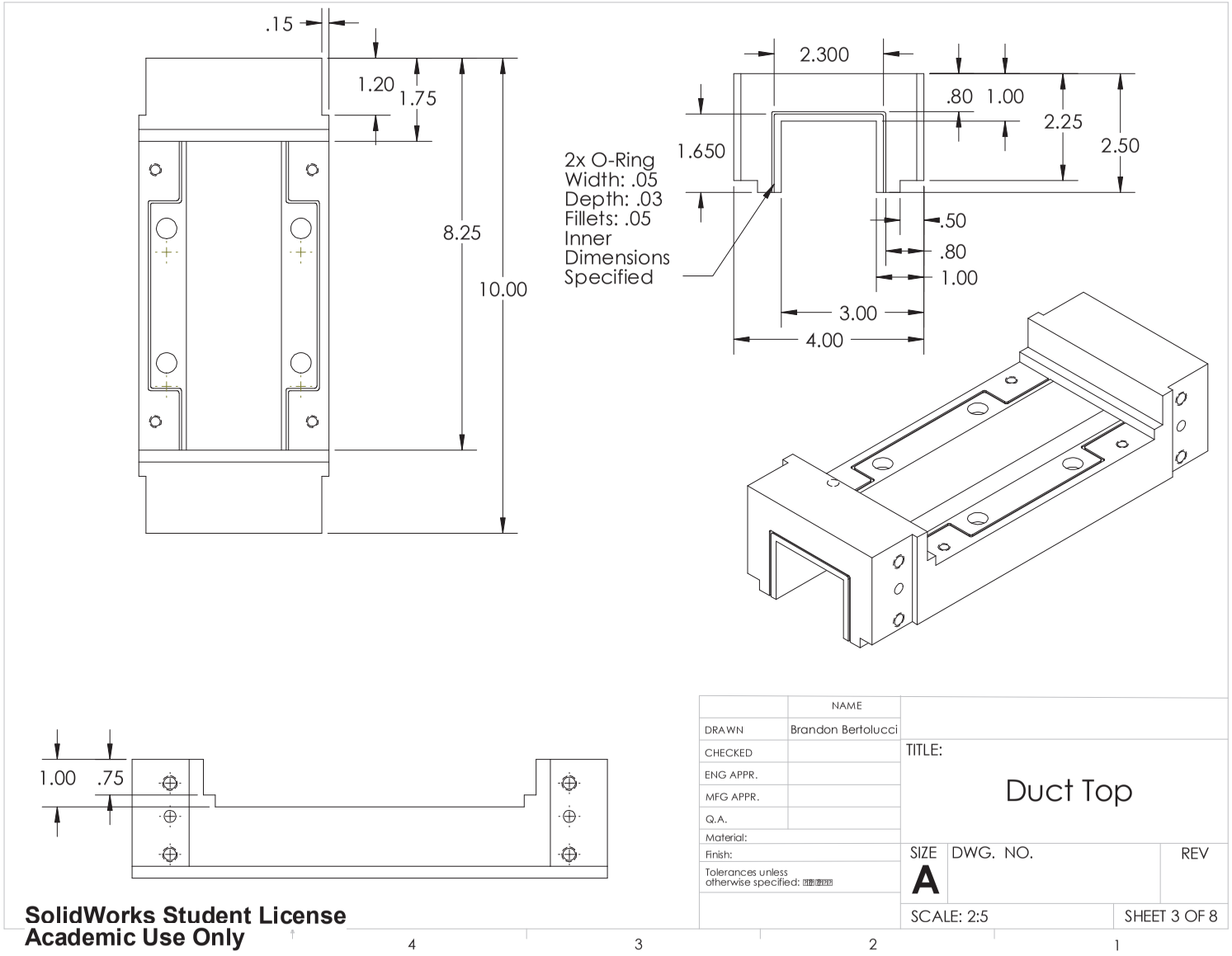

Figure D-8. Speaker section top view.

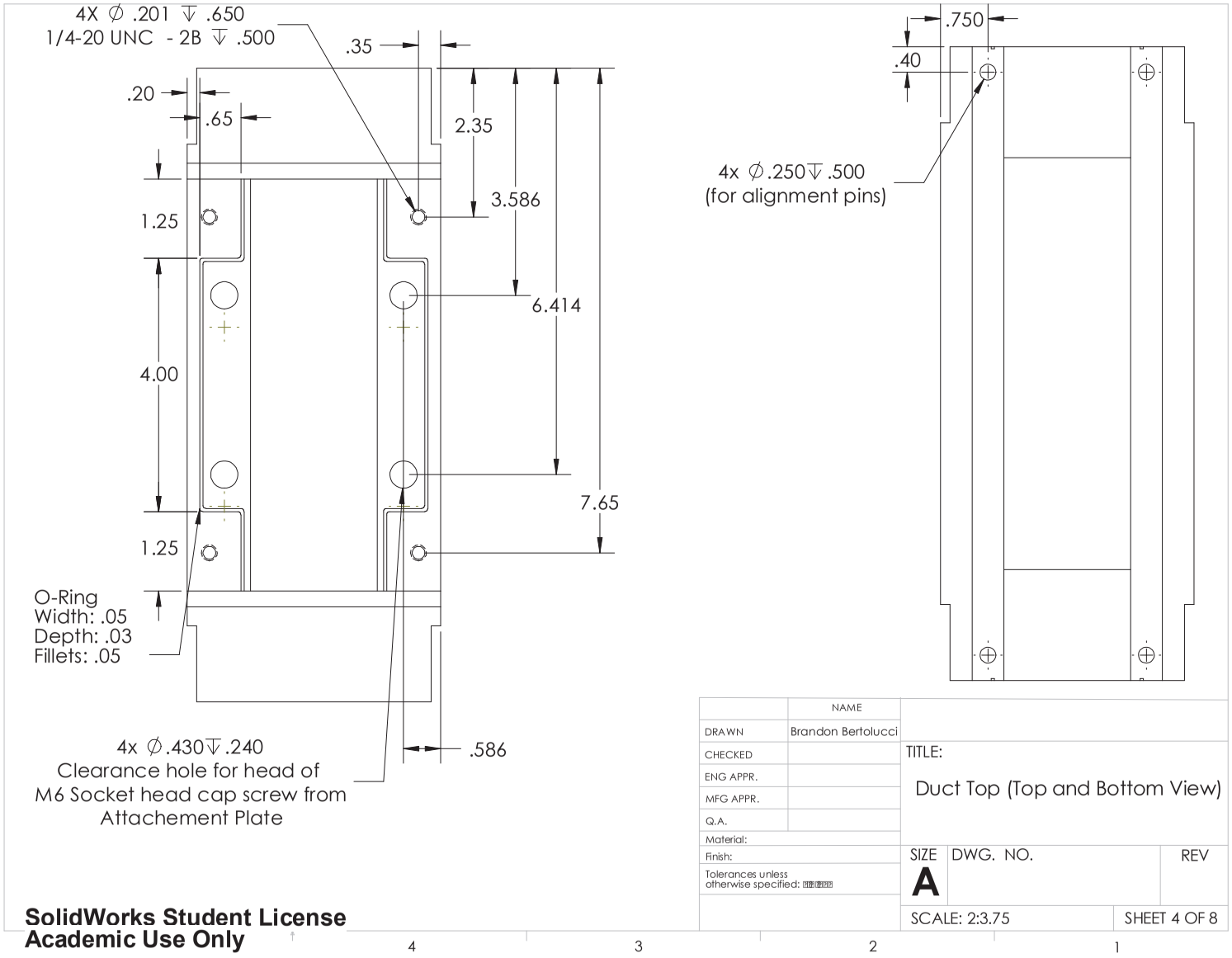

Figure D-9. Speaker section hole placement dimensions.

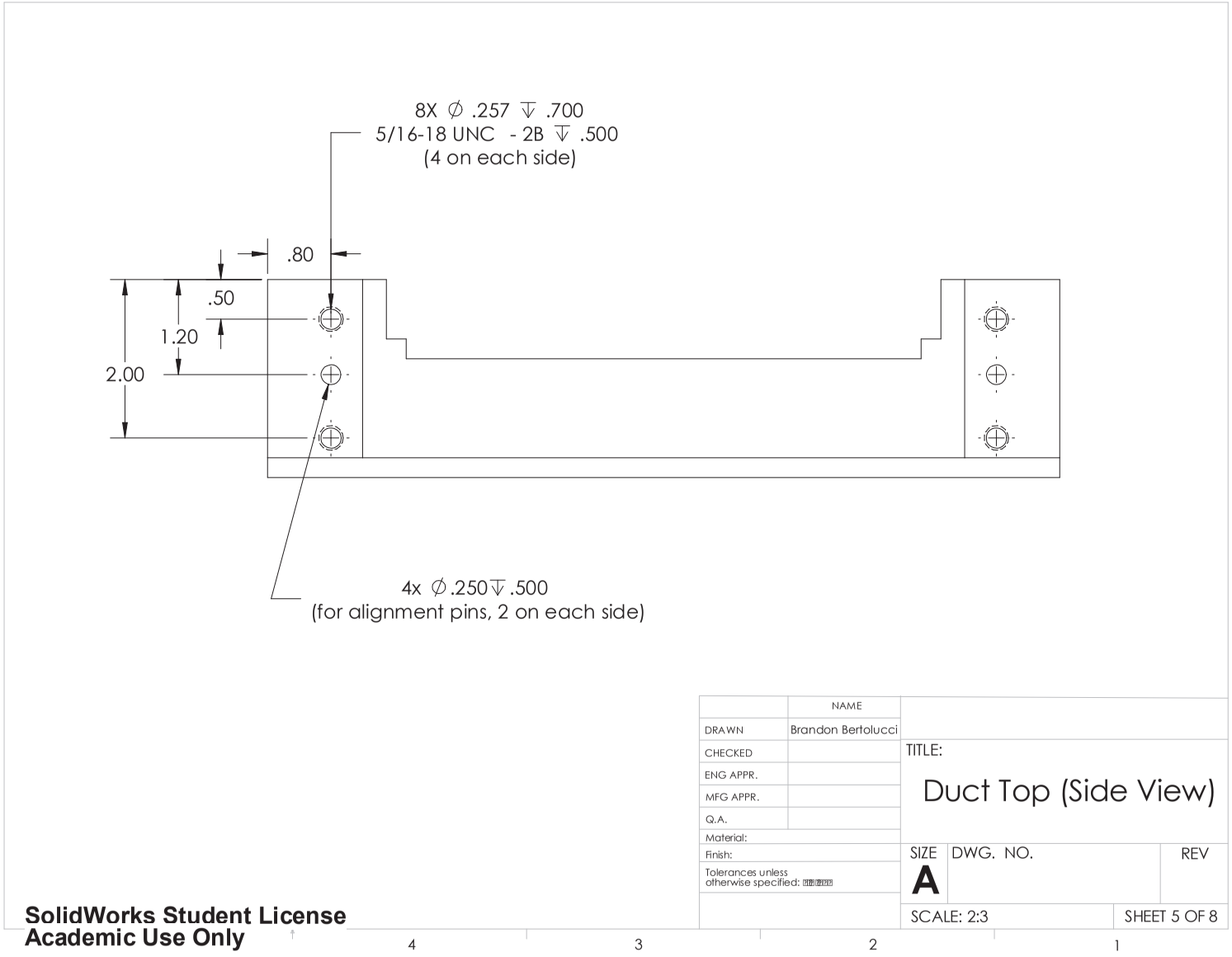

Figure D-10. Speaker section side alignment hole dimensions.

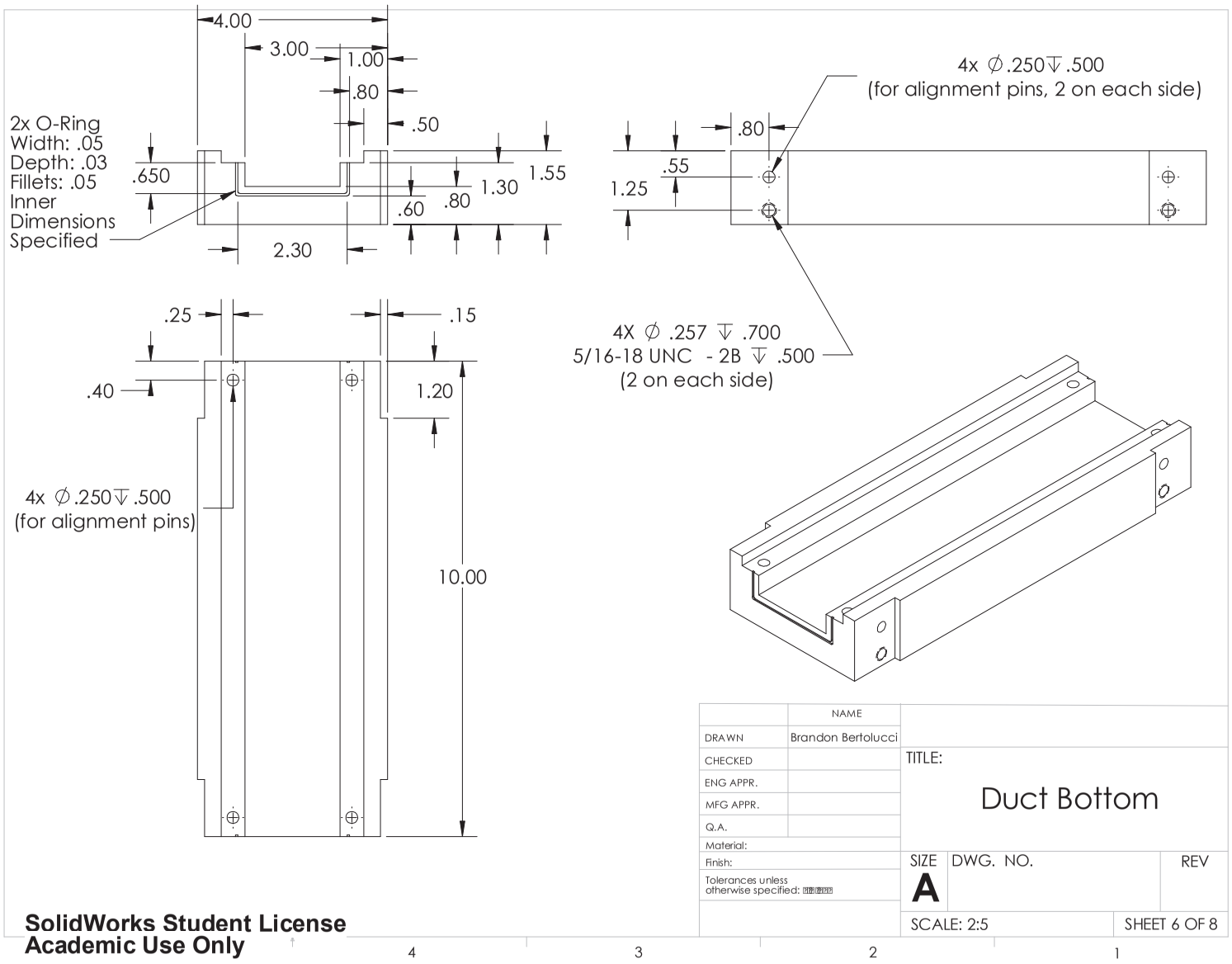

Figure D-11. Speaker section top dimensions.

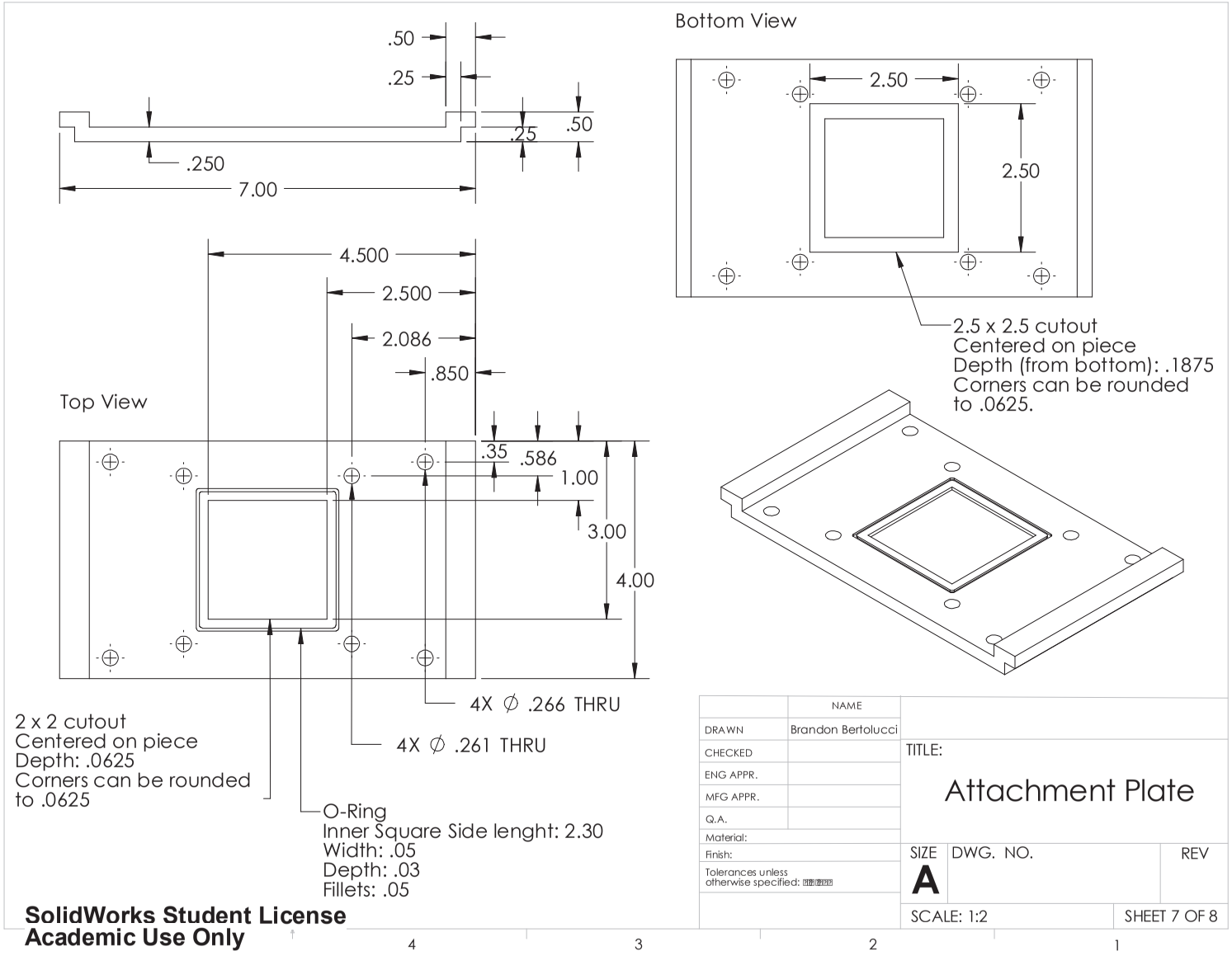

Figure D-12. Speaker cover plate dimensions.

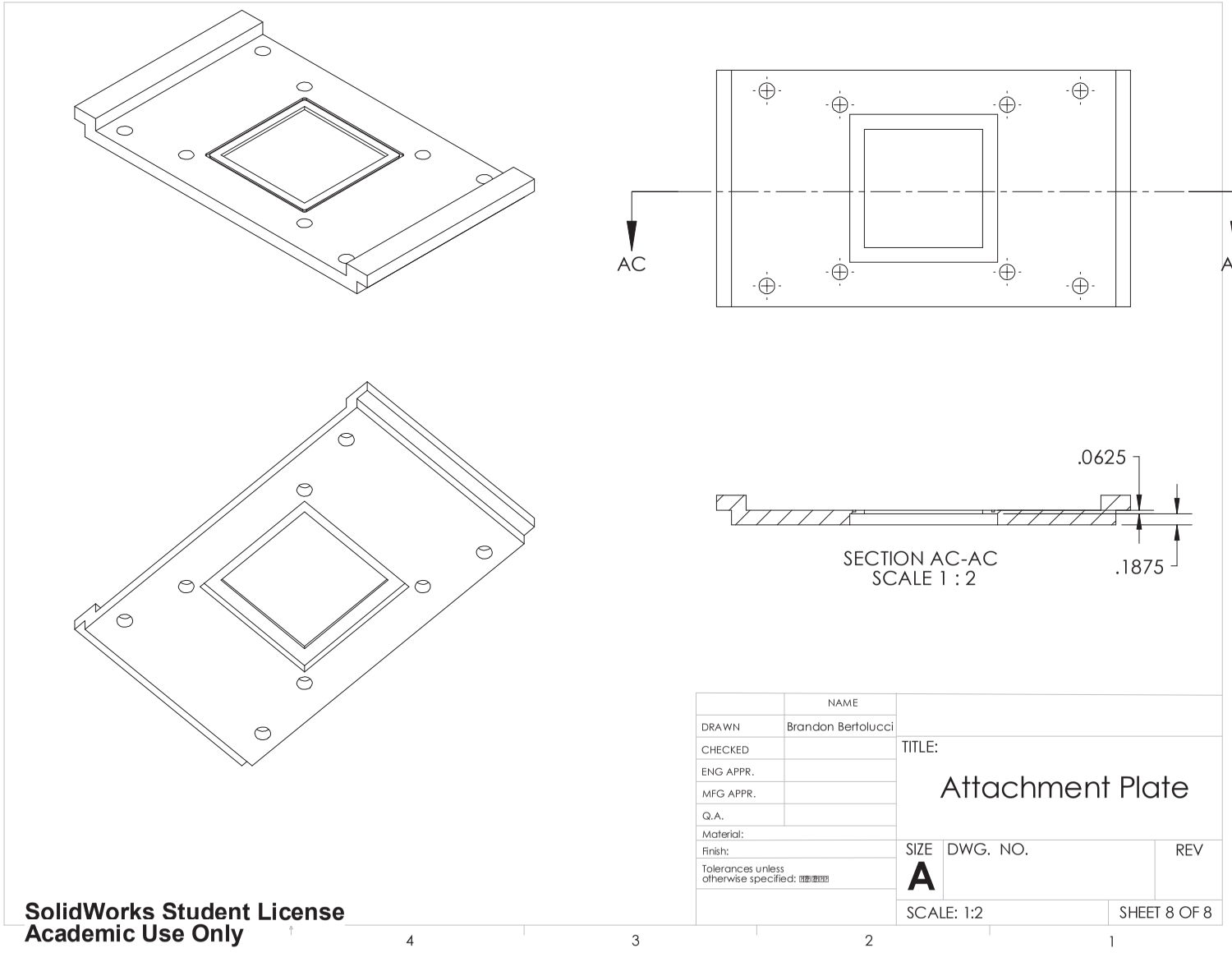

Figure D-13. Speaker cover plate isometric view.

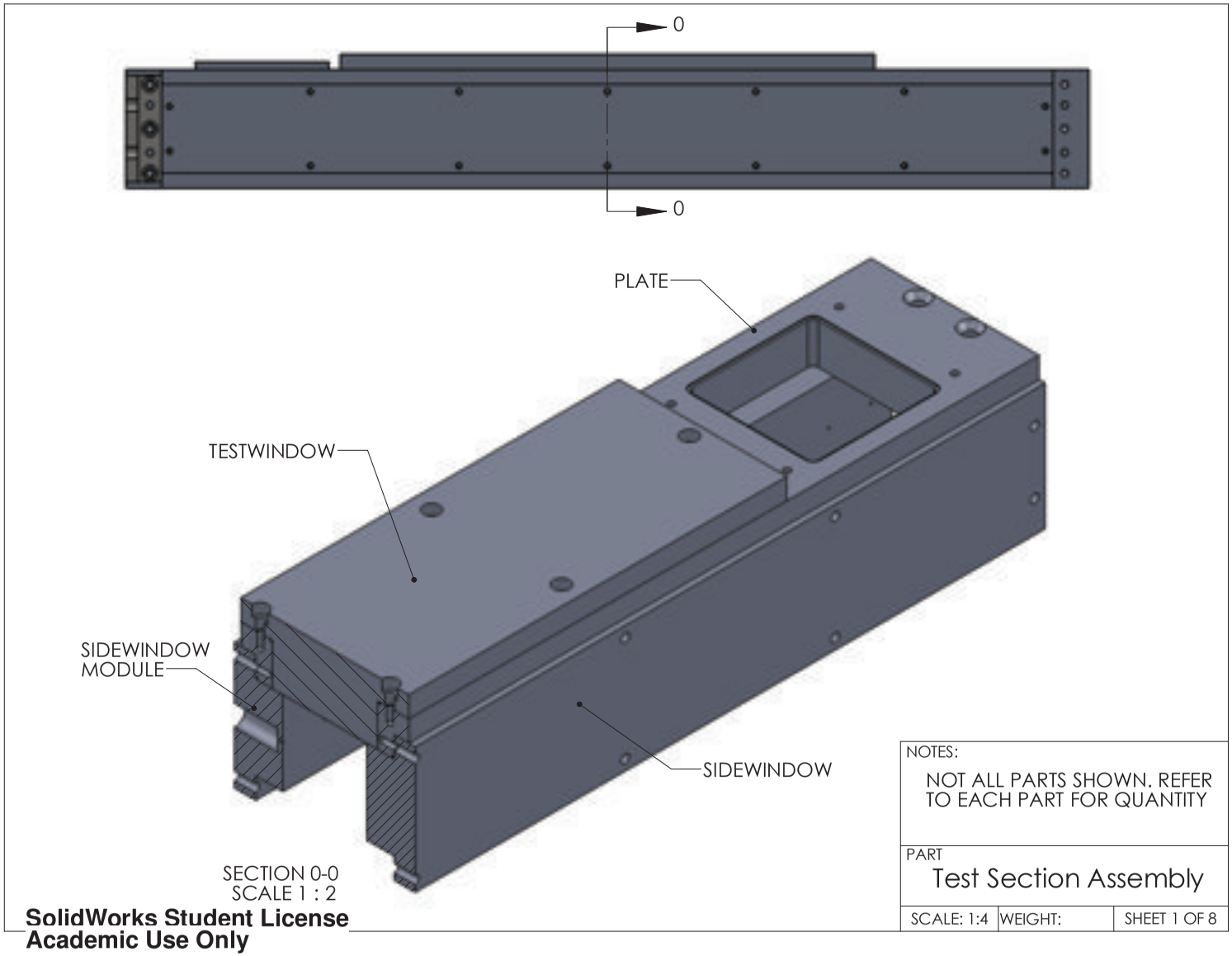

Figure D-14. Assembled test section cut away view of acoustic liner installation port and side windows.

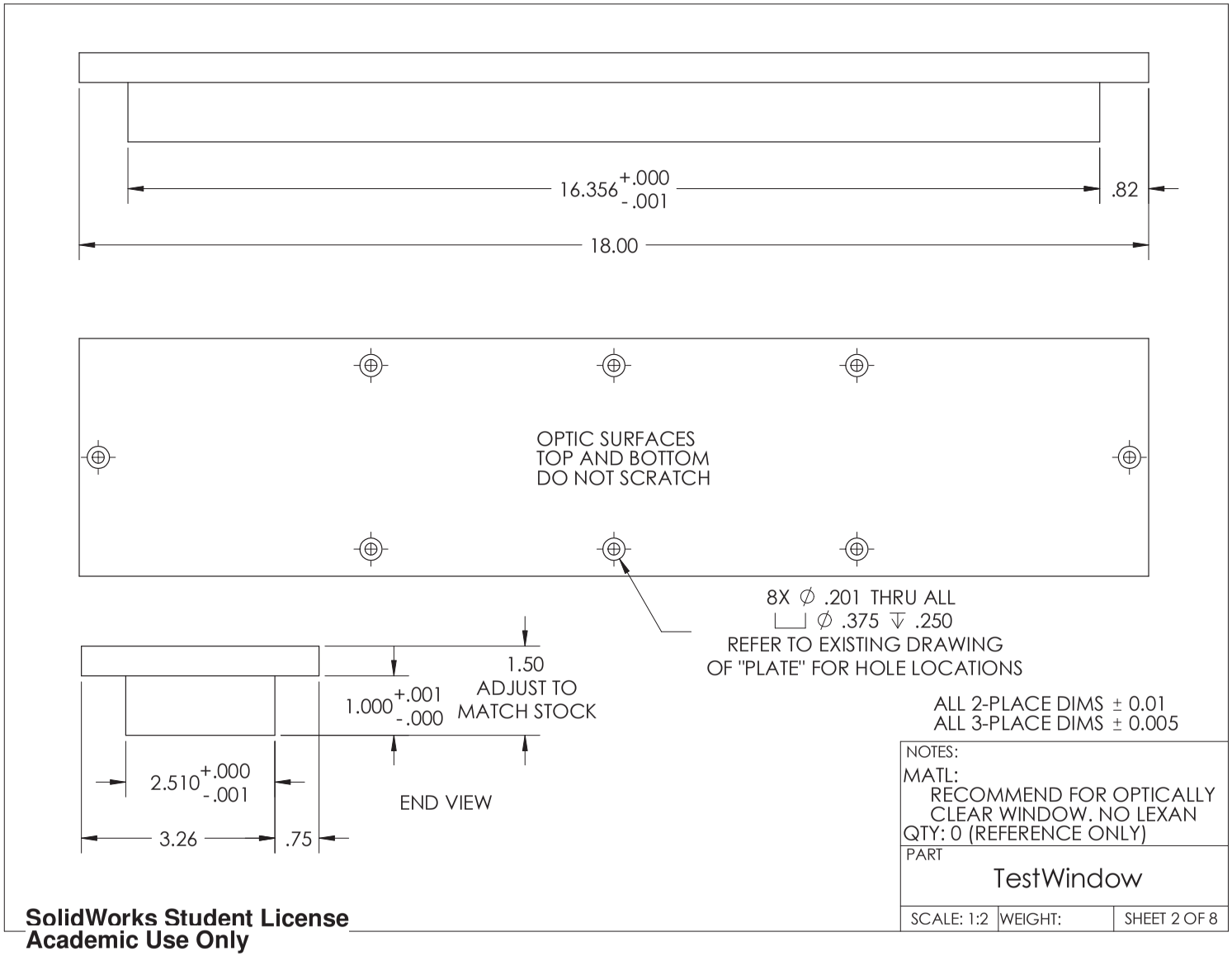

Figure D-15. Plexiglass hardball for acoustic liner installation port dimensions.

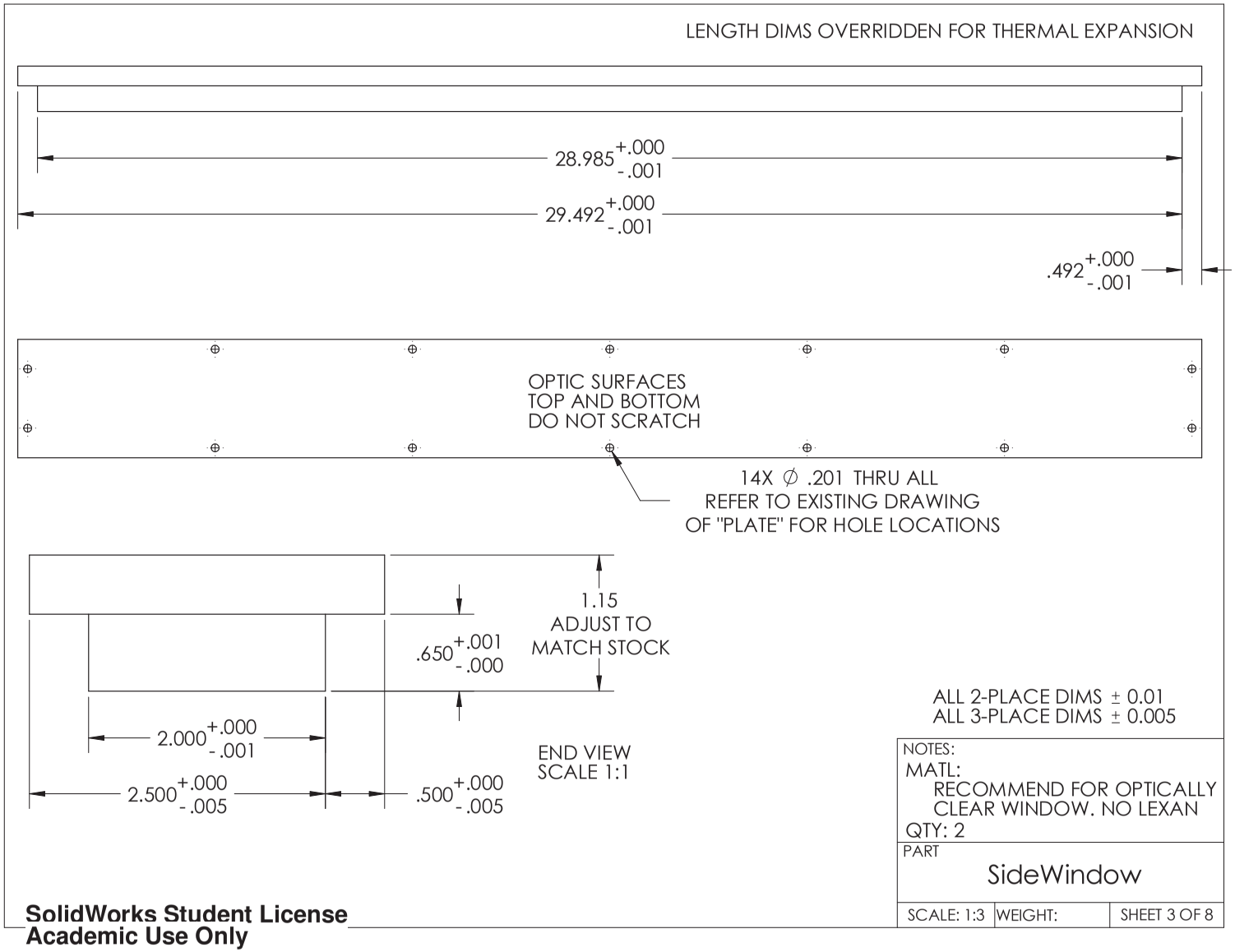

Figure D-16. Shared dimensions of test section side walls for use on optical windows, static pressure wall, and microphone array insert.

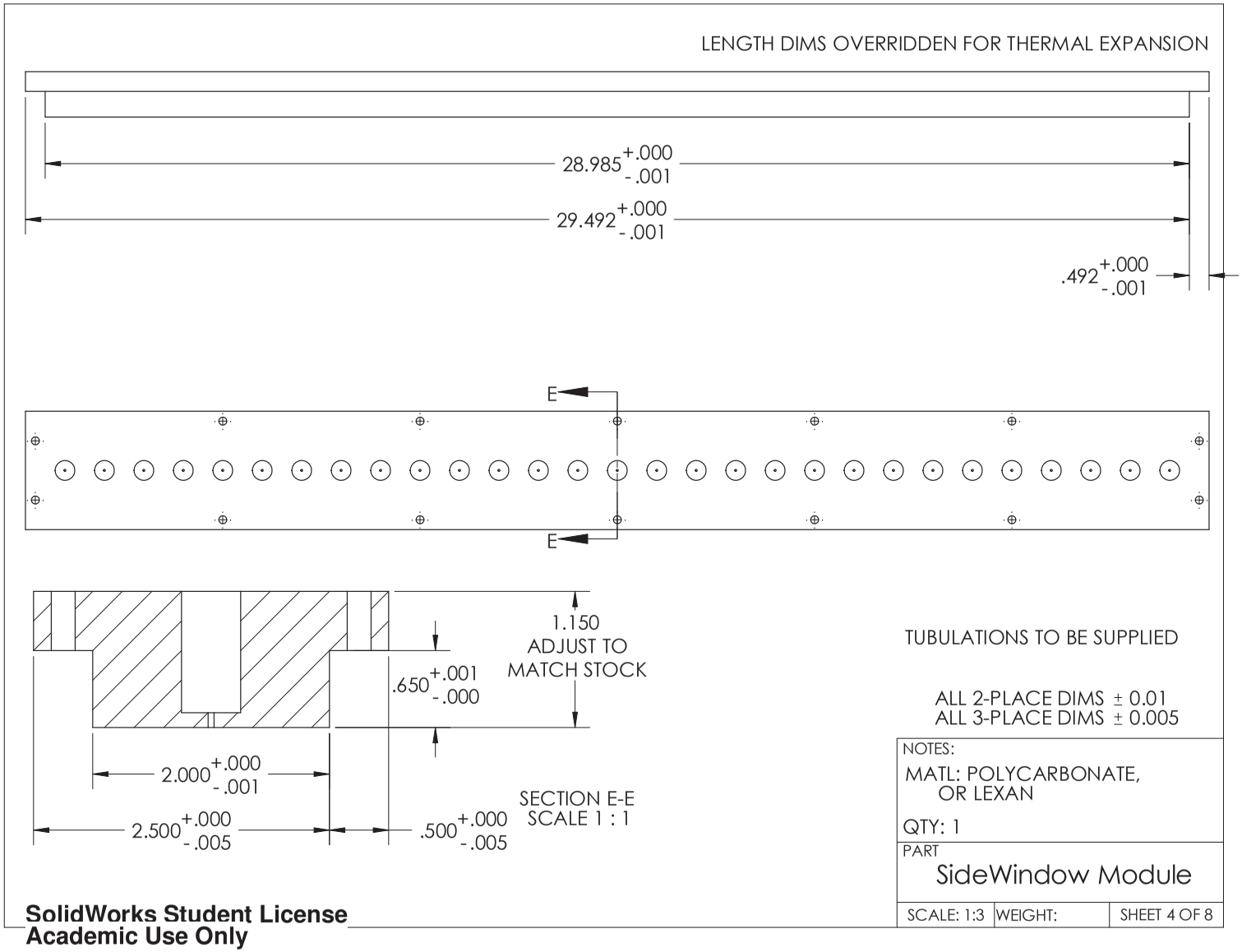

Figure D-17. Static pressure wall dimensions.

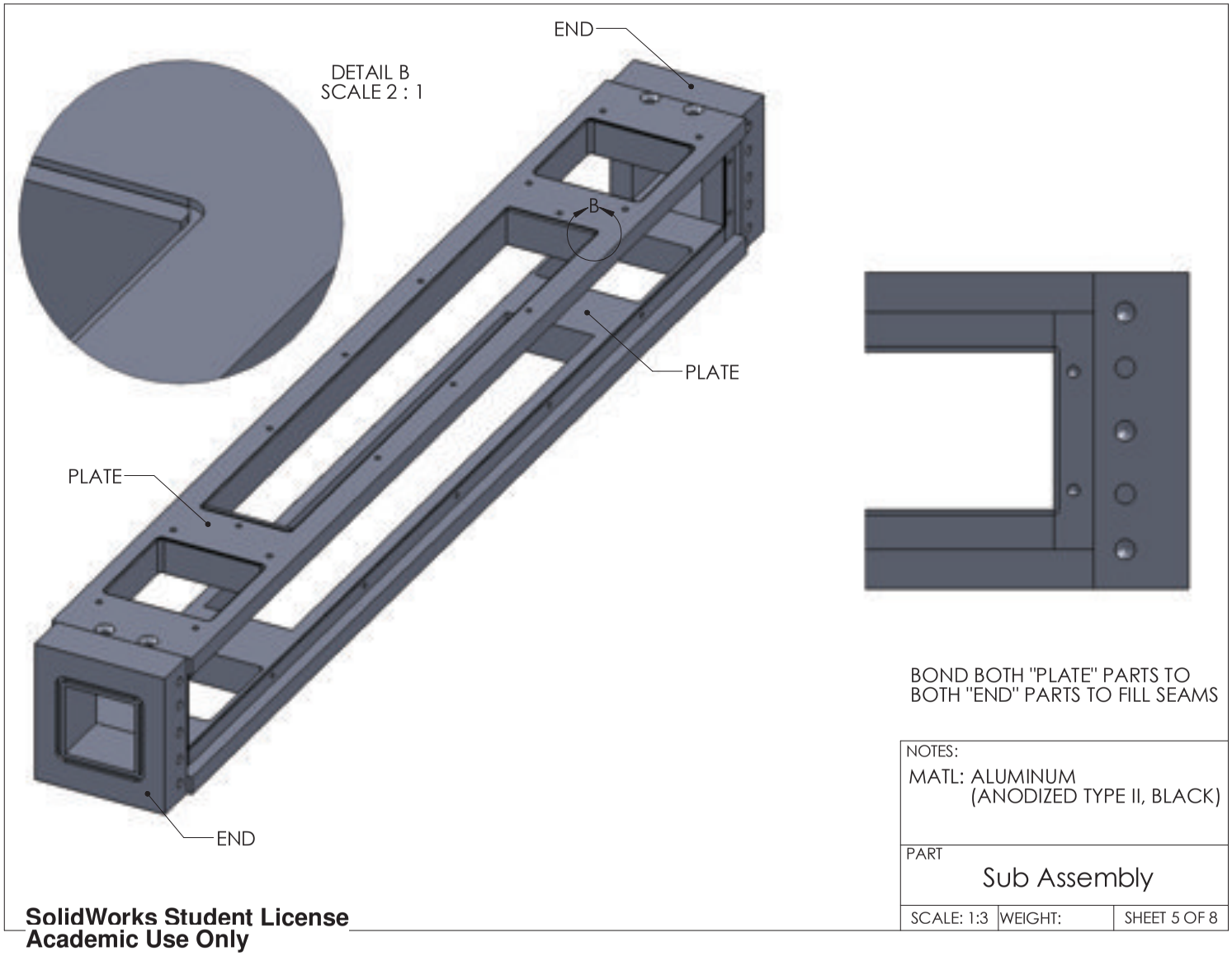

Figure D-18. Test section assembly skeleton isometric view.

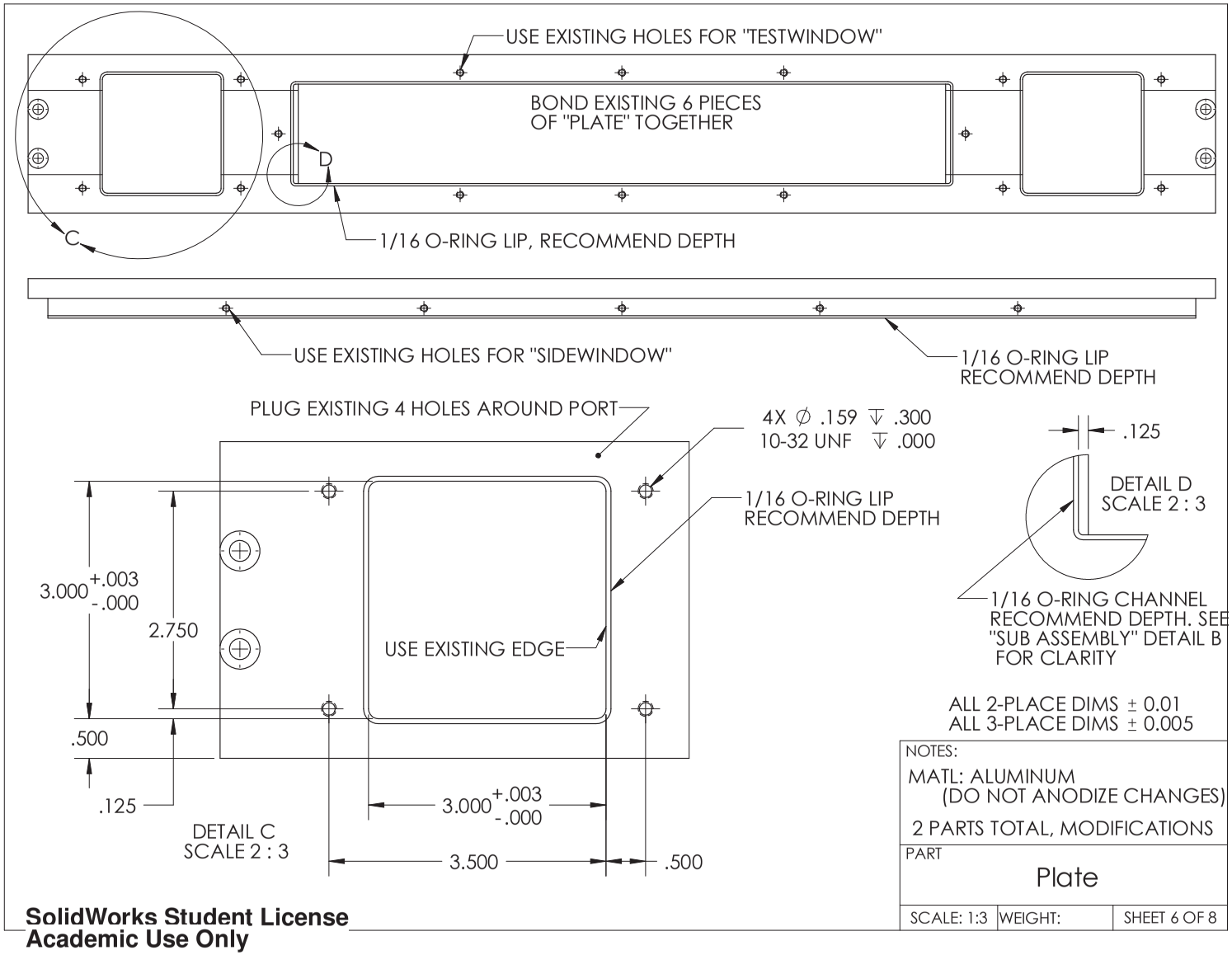

Figure D-19. Test section top wall permanent assembly.

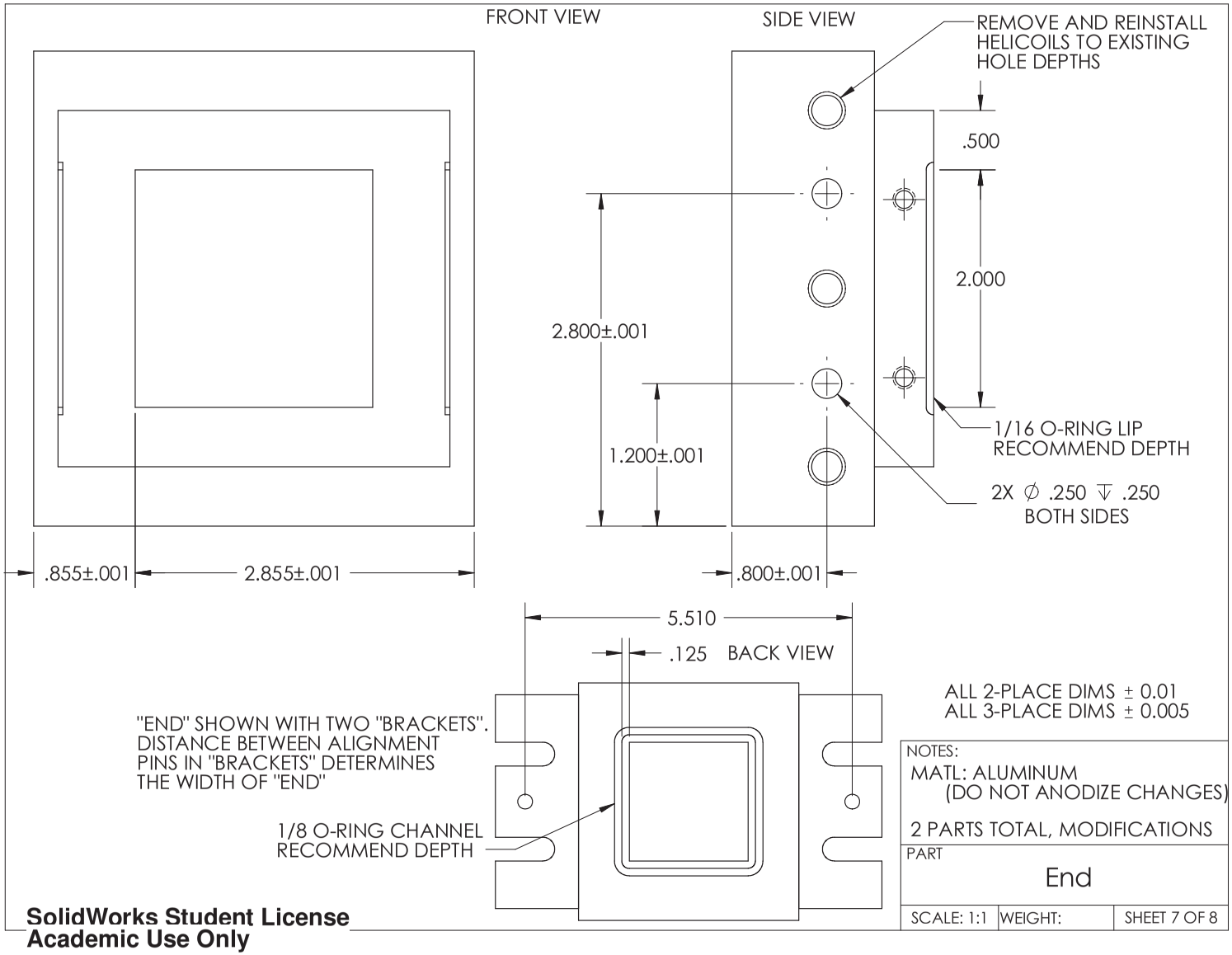

Figure D-20. Test section upstream and downstream end caps.

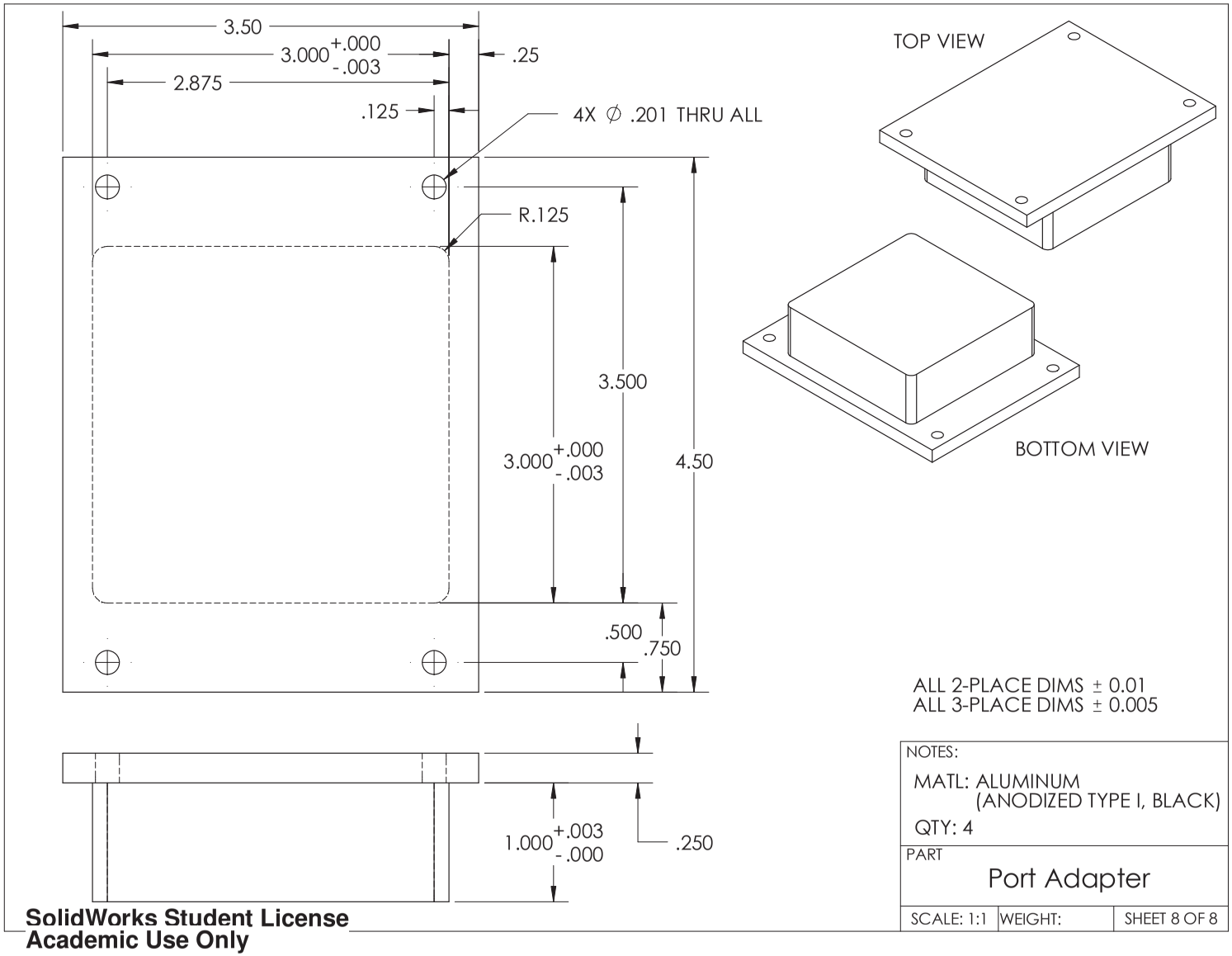

Figure D-21. Test section auxiliary plugs.

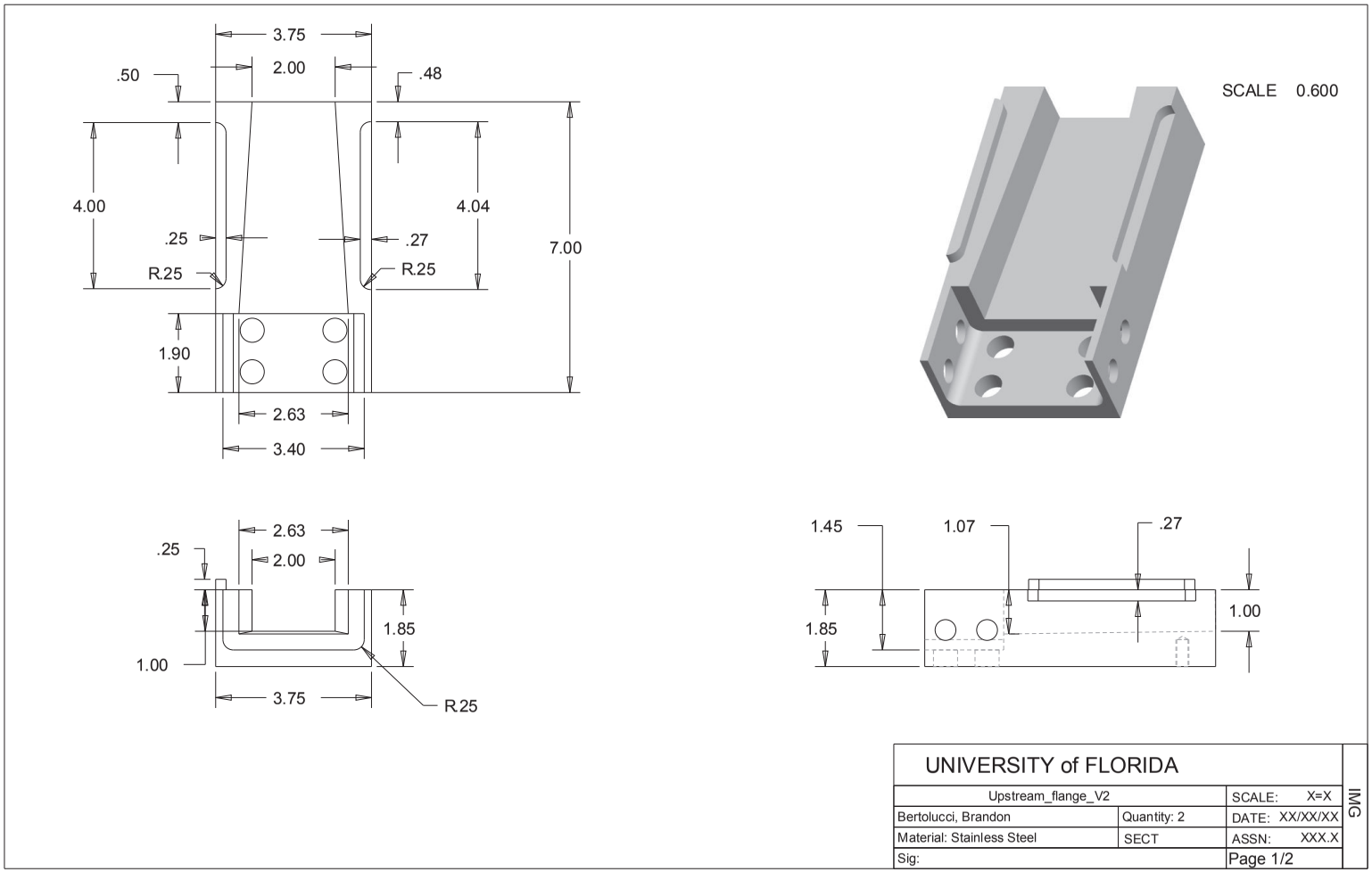

Figure D-22. Near-anechoic diffuser upstream flange overall dimensions. The two part is mirrored top to bottom.

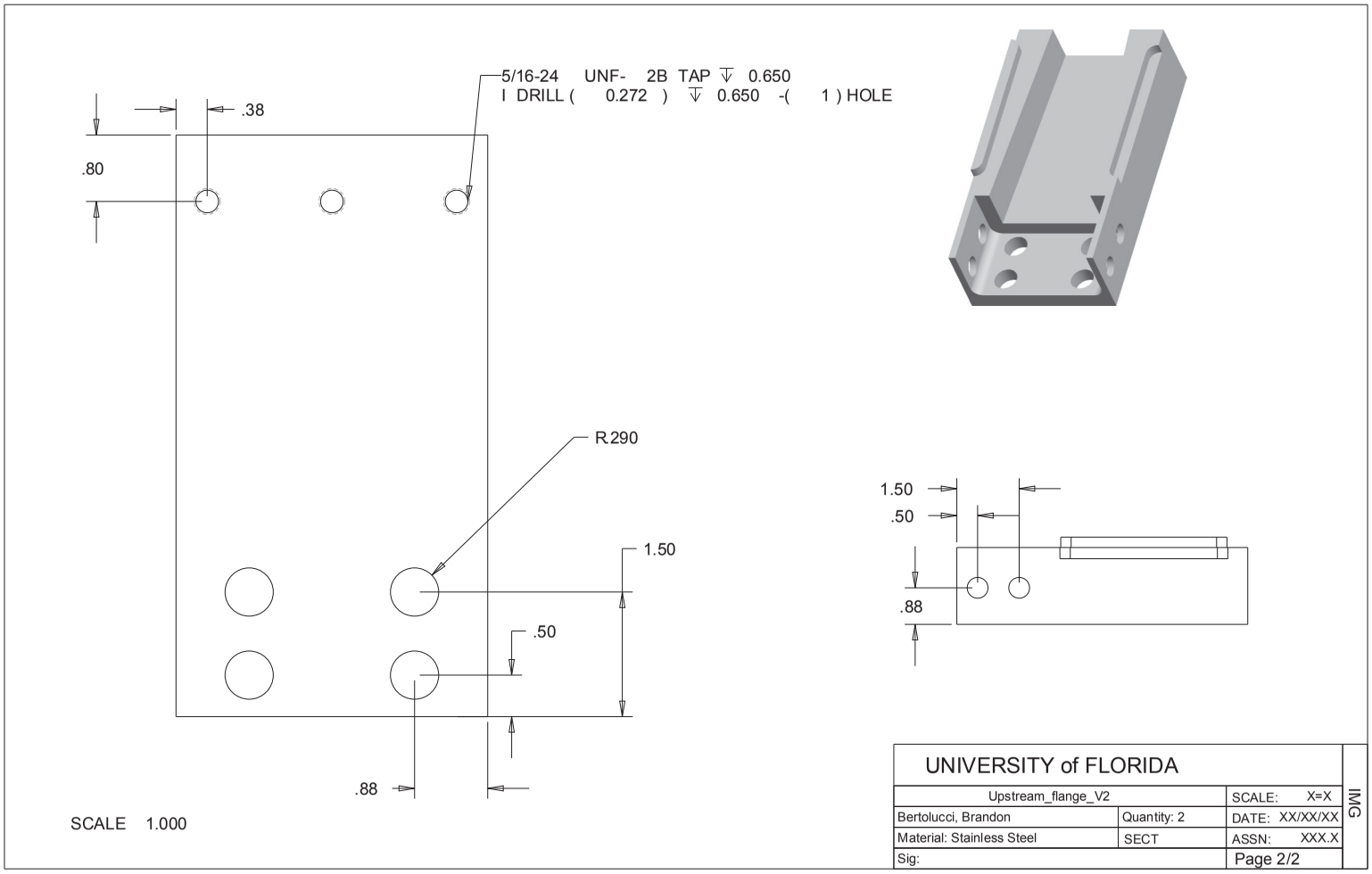

Figure D-23. Near-anechoic diffuser upstream flange hole placement.

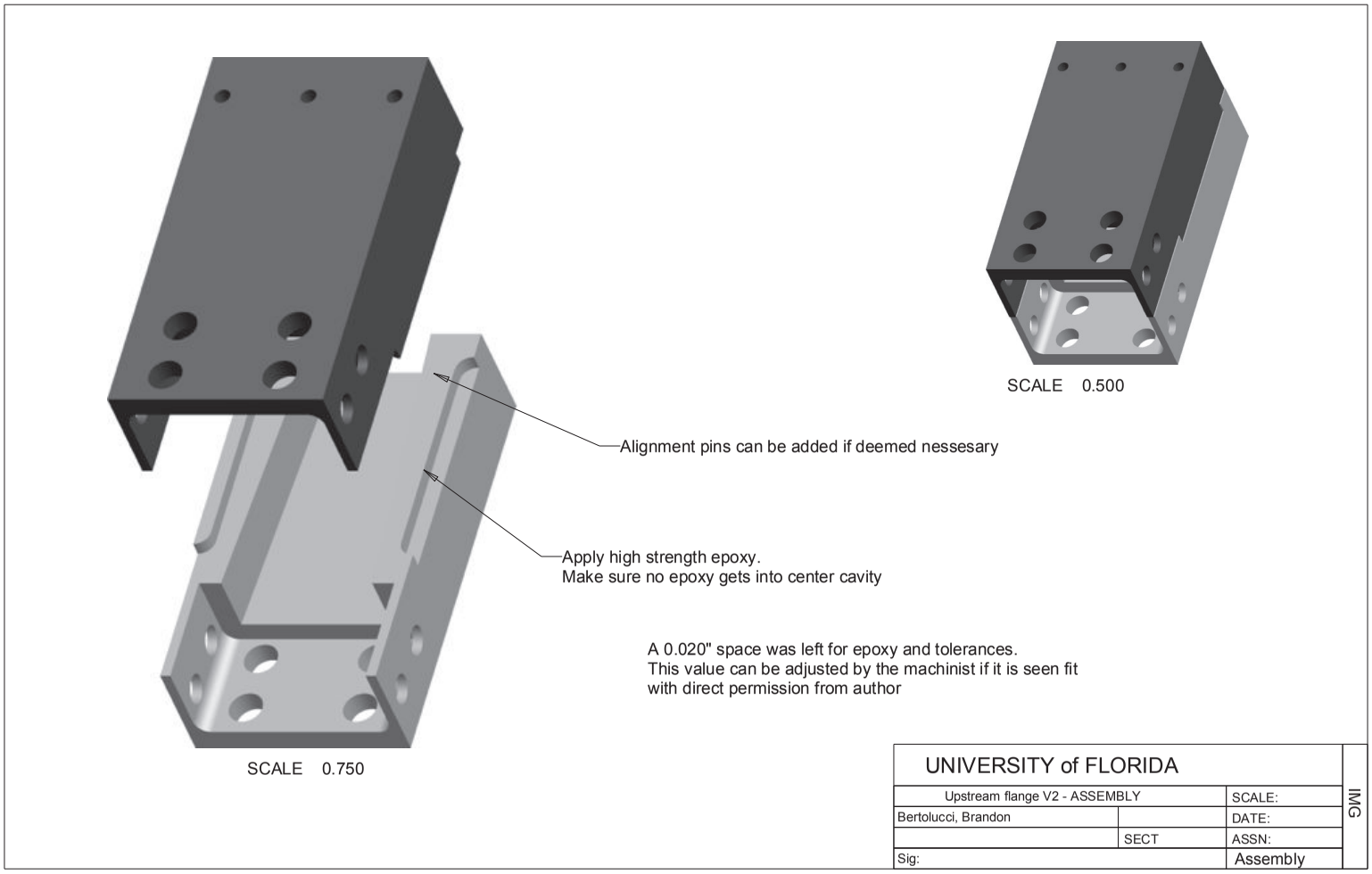

Figure D-24. Near-anechoic diffuser upstream assembly.

REFERENCES

Ahmed, S. & Brundrett, E. 1971 Turbulent flow in non-circular ducts. part 1: mean flow properties in the developing region of a square duct. *International Journal of Heat and Mass Transfer* **14**, 365–375.

Ahuja, K., Scott, M. & Gaeta, J. 2000 Flow Duct Data for Validation of Acoustic Liner Codes for Impedance Eduction. *Tech. Rep.* CR-2000-210634. GTRI.

Albrecht, H., Borys, M., Damaschke, N. & TROPEA, C. 2003 *Laser Doppler and phase Doppler measurement techniques*. Springer Verlag.

Anselmet, F., Ternat, F., Amielh, M., Boiron, O., Boyer, P. & Pietri, L. 2009 Axial development of the mean flow in the entrance region of turbulent pipe and duct flows. *Comptes Rendus Mécanique* **337** (8), 573–584.

Armstrong, D. L. 1974 Impedance measurements of acoustic duct liners with grazing flow. *The Journal of the Acoustical Society of America* **55** (S1), S59.

Auregan, Y. & Leroux, M. 2008 Experimental evidence of an instability over an impedance wall in a duct with flow. *arXiv.org* **physics.class-ph**.

Auregan, Y., Leroux, M. & Pagneux, V. 2004 Measurement of liner impedance with flow by an inverse method. *AIAA Paper 98-2611* pp. 2004–2838.

Batchelor, G. 2000 *An Introduction To Fluid Dynamics*. Cambridge Univ Pr.

Beranek, L. 1996 *Acoustics*. Acoustical Society of America.

Bielak, G., Premo, J. & Hersh, A. 1999 Advanced turbofan duct liner concepts. *NASA* (CR-1999-209002).

Blackstock, D. 2001 *Fundamentals Of Physical Acoustics*. John Wiley New York.

BMS 2010 2" Coaxial Neodymium Compression Driver.

Bronzaft, A. & Ahern, D. 1998 Aircraft noise: A potential health hazard. *Environment and Behavior* .

Brundrett, E. & Baines, W. 1964 The production and diffusion of vorticity in duct flow. *Journal of Fluid Mechanics Digital Archive* **19** (3), 375–394.

Casalino, D., Diozzi, F., Sannino, R. & Paonessa, A. 2007 Aircraft noise reduction technologies: A bibliographic review. *Aerospace Science and Technology* **12**, 1–17.

Coleman, H. W. & Steele, W. G. 2009 *Experimentation, Validation, and Uncertainty Analysis for Engineers*, 3rd edn. John Wiley and Sons.

Daggett, D., Brown, S. & Kawai, R. 2003 Ultra-Efficient Engine Diameter Study. *NASA CR* .

Dean, P. D. 1974 An In Situ Method Of Wall Acoustic Impedance Measurement In Flow Ducts. *Journal of Sound and Vibration* **34** (1), 97–130.

Dean, R. B. 1978 Reynolds Number Dependence of Skin Friction and Other Bulk Flow Variables in Two-Dimensional Rectangular Duct Flow. *Journal of Fluids Engineering* **100** (2), 215.

Dokumaci, E. 2005 Effect of sheared grazing mean flow on acoustic transmission in perforated pipe mufflers. *Journal of Sound and Vibration* .

Dowling, A. & Williams, J. 1983 *Sound And Sources Of Sound*. John Wiley New York.

Drouin, M., Gallman, J. & Olsen, R. 2006 Sound Level Effect on Perforated Panel Boundary Layer Growth. In *AIAA*.

Dynamics, D. 2000 *BSA Flow Software*, *Theory of Laser Anemometry*, vol. 3.

E1055-98, A. 1998 Impedance and Absorption of Acoustical Materials Using a Tube, Two Microphones and Digital Frequency Analysis System. *Tech. Rep.*.

Egan, M. 2007 *Architectural Acoustics*. J. Ross Publishing.

Elnady, T., Boden, H. & Elhadidi, B. 2009 Validation of an Inverse Semi-Analytical Technique to Educe Liner Impedance. In *AIAA Journal*, pp. 2836–2844. Ain Shams Univ, Sound & Vibrat Lab, Fac Engn, Design & Prod Engn Dept, Cairo 11517, Egypt.

Eversman, W. 1991 Theoretical models for duct acoustic propagation and radiation. *NASA Ref. Pub.* **2** (1258), 101–159.

Eversman, W. & Gallman, J. 2009 Impedance Eduction with an Extended Search Procedure. In *AIAA Paper 98-2611*. Miami, Fl.

Fage, A. 1936 On the Static Pressure in Fully-Developed Turbulent Flow. *Proceedings of the Royal Society of London. Series A* .

Fung, K. Y., Jing, X., Lu, Z. & Yang, X. 2009 Time-Domain In Situ Characterization of Acoustic Liners in a Flow Duct. *AIAA Journal* **47** (6), 1379–1387.

Gallman, J. & Kunze, R. 2002 Grazing flow acoustic impedance testing for the NASA AST program. *AIAA* (2002-2447).

Gallman, J., Kunze, R. & Breer, M. 2002 Measurement of the boundary layer growth due to transpiration flow through nacelle acoustic liners. *AIAA Paper 98-2611* (2002-3063).

Gessner, F. 1964 *Turbulence and Mean-Flow Characteristics of Fully-Developed Flow In Rectangular Channels*. PhD Thesis.

Gessner, F. 1973 The origin of secondary flow in turbulent flow along a corner. *Journal of Fluid Mechanics Digital Archive* **58** (01), 1–25.

Gessner, F. & Jones, J. 1965 On some aspects of fully-developed turbulent flow in rectangular channels. *Journal of Fluid Mechanics Digital Archive* **23** (4), 689–713.

Gessner, F., Po, J. & Emery, A. 1977 Measurements of developing turbulent flow in a square duct. *Symposium on Turbulent Shear Flows, University Park, Pa* p. 9.

Guynn, M., Berton, J., Fisher, K., Haller, J., Tong, M. & Thurman, D. 2009 Engine Concept Study for an Advanced Single-Aisle Transport. *NASA TM* .

Herkes, W., Olsen, R. & Uellenberg, S. 2006 The Quiet Technology Demonstrator Program: Flight Validation of Airplane Noise- .... *AIAA Paper 98-2611* (2006-2720).

Hillereau, N. 2004 Suppression Characteristics of Acoustic Liners with Porous Honeycomb. *ohiolink.edu* .

Hoagland, L. 1960 Fully developed turbulent flow in straight rectangular ducts. *MIT Thesis* .

Howarth, L. 1938 Concerning secondary flow in straight pipes. *Proceedings of the Cambridge Philosophical Society* **34** (03), 335–344.

Hubert, M. & Van der Veeken, S. 2008 Outlier detection for skewed data. *Journal of Chemometrics* **22** (3-4), 235–246.

Ingard, K. 1994 *Notes On Sound Absorption Technology*. Noise Control Foundation.

Ingard, K. 1999 *Notes on Duct Attenuators*.

Ingard, U. 1953 On the theory and design of acoustic resonators. *The Journal of the Acoustical Society of America* pp. 1037–1061.

Jensen, K. & Bertolucci, B. 2012 Dantec Processor limtations.

Jing, X., Peng, S. & Sun, X. 2008 A straightforward method for wall impedance eduction in a flow duct. *Journal Of The Acoustical Society Of America* **124** (1), 227–234.

John, J. & Keith, T. 2006 *Gas Dynamics*, 3rd edn. Prentice Hall.

Jones, M. 2011 On the Use of Experimental Methods to Improve Confidence in Educed Impedance. In *17th AIAA/CEAS Aeroacoustics Conference*. Portland, OR.

Jones, M., Parrott, T. & Watson, W. 2003 Comparison of Acoustic Impedance Eduction Techniques for Locally-Reacting Liners. *AIAA Paper 98-2611* pp. 2003–3306.

Jones, M., Parrott, T., Watson, W. & Gerhold, C. 2006 Development of experimental and computational aeroacoustic tools for advanced liner evaluation. In *Inter-Noise*. Honolulu, HI.

Jones, M., Watson, W. & Nark, D. 2010 Effects of Flow Profile on Educed Acoustic Liner Impedance. *AIAA Paper 98-2611* (2010-3763).

Jones, M., Watson, W. & Parrott, T. 2005 Benchmark Data for Evaluation of Aeroacoustic Propagation Codes with Grazing Flow. *AIAA Paper 98-2611* **2853**, 2005.

Jones, M., Watson, W., Parrott, T. & Smith, C. 2004*a* Design and Evaluation of Modifications to the NASA Langley Flow Impedance Tube. In *Design and Evaluation of Modifications to the NASA Langley Flow Impedance Tube*.

Jones, M., Watson, W., Tracy, M. & Parrott, T. 2001 Comparison of two acoustic waveguide methods for determining liner impedance. *AIAA Conference* **7th Aeroacoustics** (AIAA-2001-2266).

Jones, M., Watson, W., Tracy, M. & Parrott, T. 2004*b* Comparison of Two Waveguide Methods for Educing Liner Impedance in Grazing Flow. *AIAA Journal* **42** (2), 232–240.

Kays, W., Crawford, M. & Weigand, B. 2005 *Convective Heat And Mass Transfer*. McGraw-Hill Science.

Knipschild, P., Meijer, H. & Sallé, H. 1981 Aircraft noise and birth weight. *International Archives of Occupational and Environmental Health* **48** (131-136).

Kryter, K. 1959 Scaling human reactions to the sound from aircraft. *The Journal of the Acoustical Society of America* .

Kryter, K. 1990 Aircraft noise and social factors in psychiatric hospital admission rates. *Psychological Medicine* .

Laufer, J. 1948 Investigation of turbulent flow in a two-dimensional channel. *Cal Tech Thesis* .

Lavieille, M., Simon, F. & Micheli, F. 2006 Measurement of liner acoustic impedance in a shear layer of a subsonic flow by laser doppler velocimetry. *SAPEM* (7).

Leutheusser, H. 1984 Velocity Distribution And Skin Friction Resistance In Rectangular Ducts. *Journal Of Wind Engineering And Industrial Aerodynamics* **16** (2-3), 315–327.

Lighthill, M. 1952 On sound generated aerodynamically. I. General theory. *Proceedings of the Royal Society of London. Series A* .

Marsh, A. 1968 Study of Acoustical Treatments for JetEngine Nacelles. *The Journal of the Acoustical Society of America* **43** (5), 1137–1156.

Mathieu, J. & Scott, J. 2000 *An Introduction To Turbulent Flow*. Cambridge Univ Press.

Mattingly, J. 1996 *Elements Of Gas Turbine Propulsion*. McGraw-Hill New York.

Melling, A. & Whitelaw, J. 1976 Turbulent flow in a rectangular duct. *Journal of Fluid Mechanics Digital Archive* **78** (02), 289–315.

Melling, T. & Doak, P. 1971 Basic design considerations and theoretical analysis of double-reverberant chamber duct lining test facilities. *Journal of Sound and Vibration* **14** (1), 23–35.

Minotti, A., Simon, F. & Gantié, F. 2008 Characterization of an acoustic liner by means of Laser Doppler Velocimetry in a subsonic flow. *Aerospace Science and Technology* .

Motsinger, R. & Kraft, R. 1991 Design and performance of duct acoustic treatment. *NASA Ref. Pub.* **2** (1258), 165–206.

Mungur, P. & Gladwell, M. L. 1969 ACOUSTIC WAVE PROPAGATION IN A SHEARED FLUID CONTAINED IN A DUCT.pdf. *Journal of Sound and Vibration* **9** (1), 28–48.

Murray, P., Ferrante, P. & Scofano, A. 2005 Manufacturing process and boundary layer influences on perforate liner impedance. *AIAA* .

Musker, A. J. 1979 Explicit Expression for the Smooth Wall Velocity Distribution in a Turbulent Boundary Layer. *AIAA Journal* **17** (6), 655–657.

Naughton, J. & Sheplak, M. 2002 Modern developments in shear-stress measurement. *Progress in Aerospace Sciences* .

Nayfeh, A. H., Kaiser, J. & Telionis, D. P. 1975 Acoustics of aircraft engine-duct systems. *AIAA Journal* **13** (2), 130–153.

Panton, R. 2006 *Incompressible Flow*. Wiley India Pvt. Ltd.

Parrott, T. & Lester, H. 1980 Calculated and measured performance of a 'near ideal' locally reacting duct liner in grazing impedance. *AIAA Paper 98-2611* (80-0989).

Powell, C. & Fields, J. 1991 Human response to aircraft noise. In *Aeroacoustics of Flight Vehicles: Theory and Practice*. Acoustical Society of America.

Pridmore-Brown, D. 2006 Sound propagation in a fluid flowing through an attenuating duct. *Journal of Fluid Mechanics Digital Archive* **4**, 393–406.

Rae, W. & Pope, A. 1999 *Low-Speed Wind Tunnel Testing*, 3rd edn. Wiley New York.

Richter, Thiele, F., Heuwinkel, C. & Enghardt, L. 2008 Impedance deduction based on insertion loss measurements of liners under grazing flow conditions. *AIAA Paper 98-2611* (2008-3014).

Schlichting, H. & Gersten, K. 1968 *Boundary-Layer Theory*, 6th edn. McGraw - HIll.

Schultz, T. 2006 *Acoustic Impedance Testing For Aeroacoustic Applications*. PhD Thesis, University of Florida.

Semaan, R. 2010 *Experimental Investigations Of Swirling Jets*. PhD Thesis, University of Wyoming.

Simonich, J., Morin, B., Narayanan, S. & Patrick, W. 2006 Development and Qualification of an In-Situ Grazing Flow Impedance Measurement Facility. *AIAA Paper 98-2611* (2006-2640).

Smith, M. 2004 *Aircraft Noise*. Cambridge Univ. Press.

Spalding, D. 1965 A Unified Theory of Friction, Heat Transfer and Mass Transfer In the Turbulent Boundary Layer and Wall Jet. *Technical Report* (Her Majesty's Stationery Office, London.).

Stansfeld, S., Berglund, B., Clark, C. & Lopez, I. 2005 Aircraft and road traffic noise and children's cognition and health: a cross-national study. *The Lancet* .

Syed, A., Yu, J., Kwan, H. & Chien, E. 2002 The Steady Flow Resistance of Perforated Sheet Materials in High Speed Grazing Flows. *Tech. Rep.* 2002-211749.

Tack, D. H. & Lambert, R. F. 1965 Influence of Shear Flow on Sound Attenuation in a Lined Duct. *The Journal of the Acoustical Society of America* **38** (4), 655–666.

Tennekes, H. & Lumley, J. 1999 *A First Course In Turbulence*. MIT press.

Thiele, F., Busse, S., Heuwinkel, C. & Röhle, I. 2008 Impedance eduction from energy dissipation measurements with flow. *PAMM* .

Watson, W. & Jones, M. 2009 A Finite Element Theory for Predicting the Attenuation of Extended-Reacting Liners. *AIAA Conference* .

Watson, W., Jones, M. & Parrott, T. 2008 Investigation of an Anomaly Observed in Impedance Education Techniques. In *14 th AIAA/CEAS Aeroacoustics Conference*.

Watson, W., Jones, M. & Tanner, S. 1996 Validation of a Numerical Method for Extracting Liner Impedance. *NASA* .

Watson, W., Jones, M., Tanner, S. & Parrott, T. 1995 A Finite Element Propagation Model For Extracting Normal Incidence Impedance In Nonprogressive Acoustic Wave Fields. *NASA TM* (110160).

Watson, W., Tanner, S. & Parrott, T. 1998 Optimization method for educing variable-impedance liner properties. *AIAA Journal* **36** (1), 18–23.

Watson, W., Tracy, M., Jones, M. & Parrott, T. 2001 Impedance eduction in the presence of shear flow. In *AIAA*. Maastricht, Netherlands.

Wei, T. & Willmarth, W. 1989 Reynolds-number effects on the structure of a turbulent channel flow. *Journal of Fluid Mechanics Digital Archive* **204**, 57–95.

White, F. 2003 *Fluid Mechanics*. McGraw-Hill, New York.

White, F. 2006 *Viscous Fluid Flow*, 3rd edn. McGraw-Hill New York.

Wolter, J. 2005 Drag Measurements of Porous Plate Acoustic Liners. *AIAA Paper 98-2611* (2005-0803).

Young, A. 1989 *Boundary Layers*. BSP Professional Books.

Yu, J., Ruiz, M. & Kwan, H. 2008 Validation of Goodrich Perforate Liner Impedance Model Using NASA Langley Test Data. *AIAA* (2008-2930).

Zagarola, M. & Smits, A. J. 1998 Mean-flow scaling of turbulent pipe flow. *Journal of Fluid Mechanics* **373** (-1), 33–79.

BIOGRAPHICAL SKETCH

Brandon Bertolucci was born in Spokane, Wa. He graduated from Joel E. Ferris High School in 2001. Brandon received his Bachelor of Science in Mechanical Engineering from Oregon State University in 2005. Through his engineering studies he found a draw toward aerospace engineering and joined the IMG research group at the University of Florida under the advisement of Dr. Louis Cattafesta. After a series of small projects an opportunity to work closely with NASA on a facility development project arose and with newly appointed co-chair Dr. Sheplak he accepted the new project in his third year of graduate school. Completing his doctorate in the Fall of 2012, he accepted an aeroacoustics position at The Boeing Company in Seattle, Wa.